THE LINEAR STABILITY OF CHANNEL AND PIPE FLOWS BOUNDED BY COMPLIANT WALLS

A thesis submitted to the University of Manchester
for the degree of Doctor of Philosophy
in the Faculty of Science and Engineering

2002

Andrew Gibson
Department of Mathematics

(EAXJM)

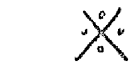

Th 23165

Contents

List of Figures

Abstract

The temporal linear stability of Newtonian flows is studied in channels and pipes bounded by compliant walls using a kinematic formulation. An existing kinematic method is extended to incorporate necessary and sufficient conditions for the existence of an instability which is physically realisable in any parallel shearing flow bounded by a simple-stretched-membrane wall. Consequently, bounds on the wall parameters (density, tension and damping) are found for which the above instability may arise.

The resulting kinematic extended eigenvalue problems are solved numerically for both channel and pipe flows. A Tchebychev collocation method is employed to evaluate the eigenfunctions and a Newton-Raphson method used to find the eigenvalue from an appropriate initial point.

Four classes of unstable numerical solution modes are found:

- Tollmien-Schlichting (TS) modes
- Kelvin-Helmholtz (KH) modes
- Transitional modes
- Resonant (R) modes

Analytical solutions are found for the long-wave and low Reynolds number limits. Instabilities in these regimes belong to the KH and R classes only.

For all solutions, methods of choosing wall parameters to eliminate instabilities are discussed and comparisons made with studies of the fully coupled fluid-wall systems.

Declaration

No portion of the work referred to in this thesis has been submitted in support of an application for another degree or qualification of this or any other university or other institution of learning.

Copyright

Acknowledgments

I would like to thank my supervisor, Dr. J.S.B. Gajjar and also Prof. P.K. Sen [1] for their help during my research and in the preparation of this thesis.

I would also like to thank my parents for their continuing support and the EPSRC for their financial assistance.

[1] Department of Applied Mechanics, Indian Institute of Technology, New Delhi 110016, India.

Chapter 1

Introduction

Much of the considerable interest in flows past flexible walls has stemmed from the experiments performed by Kramer in the 1950s and 1960s [38], [39], [40], [41], [42]. In his research, Kramer compared the drag on a rigid projectile with that on a similar projectile where sections of the outer shell were replaced by a flexible material. Projectiles of the same size and shape were towed through the sea by a boat. Despite the similarity in the geometry of the projectiles, a significant reduction in the drag was found for many of those with flexible walls.

Kramer attributed the improved efficiency of the flow to a reduction in the growth rate of the Tollmien-Schlichting waves which lead to transition in flow over rigid surfaces. Hence, with the correct choice of wall properties, the transition to turbulence could be postponed to higher Reynolds numbers or at the extreme bounds of possibility, eliminated altogether.

Some subsequent experimental studies, for example Smith and Blick [70], Fischer, Weinstein, Bushnell and Ash [20], were able to demonstrate a drag reduction in turbulent boundary-layer flows. However, early attempts to reproduce Kramer's results were unable to find any significant drag reductions in laminar flows. Differences in the experimental set up can explain the findings of such

studies, as illustrated by Carpenter and Garrad's comments [11] on the experiments by Puryear [59], Nisewanger [56], Ritter and Messum [61] and Ritter and Porteous [62]. It should be noted that in some of the above cases the introduction of a flexible wall actually resulted in an increase in the drag.

Kramer's claim that laminar flow could be maintained for higher Reynolds number flows using compliant walls was confirmed by Babenko and Kozlov [1] and by Gaster [24]. These experimental studies showed that indeed the growth rates of the Tollmien-Schlichting waves were reduced. In the case of Gaster's research the route to transition came from amplification of flutter disturbances in the wall surface itself.

Thus, it is now accepted that passive compliant walls can maintain laminar flows to higher Reynolds numbers and hence reduce the drag therein. Given that Gaster, Babenko and Kozlov used a visco-elastic wall material, unlike Kramer who used a composite wall which was essentially a spring-backed plate with a damping substrate fluid [11], it is clear that more than one type of wall is capable of exhibiting drag-reducing properties. However, given the large number of walls studied without drag-reducing properties, it is obvious that the choice of wall parameters, e.g. wall density, is critical to flow stabilisation.

The first theoretical studies to fully appreciate the complexity of the instabilities which arise in compliant-walled flows were undertaken by Benjamin [2], [3], [4] and Landahl [49]. They extended the existing linear hydrodynamic stability theory in flows over rigid walls derived by Tollmien [74], [75] and Schlichting [66]. This extension included the incorporation of the more complex boundary conditions obeyed by flows over flexible walls.

Benjamin [3] and Landahl [49] used a threefold classification for the instabilites they found. The instabilities belong to class A, class B or class C depending

on whether the energy required to activate them is negative, positive or zero, respectively. Those belonging to class A are similar to the Tollmien-Schlichting modes for flows past rigid walls. The class B modes depend only on the flexibility of the wall obey an essentially inviscid theory. Finally, class C instabilities occur for highly flexible walls and are also termed Kelvin-Helmholtz instabilities.

Since the modes of Tollmien-Schlichting type belonging to class A are destabilised by energy dissipation, damping effects in the flexible wall will cause these waves to grow more rapidly. Conversely, wall damping is beneficial in supressing the existence of any class B surface instabilities. Thus, Benjamin and Landahl showed that it was highly unlikely that a general-purpose flexible wall could be found which would lead to flow stabilisation for all Reynolds numbers.

Understandably, many subsequent studies concentrated on boundary-layer flow since Kramer's original experimental flows were of this type. Carpenter and Garrad [11] showed that the dynamics of Kramer's walls could be modelled by a relatively simple single equation relating the displacement of the wall and the perturbation of the pressure from its mean at any point along the length of the surface. They also used data from Kramer's papers to calculate the values of the wall parameters in the resulting model. They then went on to determine the effects of varying these parameters on the Tollmien-Schlichting instabilities (TSI) using a combination of an approximate theory and numerical solutions of the Orr-Sommerfeld equation.

Carpenter and Garrad followed this research with another paper [12], this time studying what they termed the flow-induced surface instabilites (FISI). These could be subdivided into static divergence (SD), travelling wave flutter (TWF) and a subclass of combined TSI/TWF modes. They used an inviscid theory combined with numerics to show that the SD modes are absolutely unstable, as are some of the TWF modes. However, the combined TSI/TWF modes, although

only convective, gave rise to the fastest-growing instabilities.

The above had built on the works of Landahl and Kaplan [50] and Gyorgyfalvy [31]. They had shown that although it was possible to make significant reductions in the drag via a reduction in the wave amplification rates, any particular wall would only be effective over a small range of values of the Reynolds number.

At about the same time as Carpenter and Garrad's studies on Kramer-type walls were published, Yeo [78] was researching boundary-layer flow over visco-elastic walls. Encouraging results were found with regard to overall flow stabilisation. The TSI were found to be stabilised by a thickening of the visco-elastic wall. The compliance-induced flow instabilities (CIFI), the same as Carpenter and Garrad's FISI, were stabilised by wall damping and the use of multi-layered visco-elastic walls with one stiffer, thinner layer above a thicker softer layer. Yeo suggested that by embedding such a plate-like layer in a thick wall, substantial reduction of disturbance growth might be obtained.

Yeo and Dowling [81] then extended Howard's semi-circle theorem [34] and Høiland's theorem [33] to invscid parallel-shearing basic flows over a generalised passive compliant wall. Yeo [80] also derived an equivalent of Fjørtoft's citerion [21] for the same type of basic flows over the same wall type.

Subsequent papers by Yeo [79], Yeo, Khoo and Chong [82] and Yeo, Khoo and Zhao [83] proceeded to look at the effects of wall anisotropy, the effects of boundary-layer growth and the existence of absolute instabilities, repsectively, all for boundary-layer flows over visco-elastic walls.

Many other aspects of boundary-layer flow over compliant surfaces have been studied. These include multi-deck approaches as employed by Carpenter and Gajjar [10], who were able to use the upper branch stability properties to find scalings for the TWF modes.

Starting with Landahl [49], there have also been numerous studies on the optimisation of the wall parameters to achieve the maximum stabilising effect on boundary-layer flow. This mantle was also taken up by Carpenter [9] who was able to show that, for water flows, a two-panel wall was able to outperform a single optimised panel. Carpenter used a Kramer-type wall but Dixon, Lucey and Carpenter [17] were able to show that visco-elastic walls also could be optimised. In addition, they confirmed Yeo's findings [78] that multi-layered visco-elastic walls out perform single-layered ones with two-and-a-half- and five-fold increases in the critical Reynolds numbers for single- and doubled-layered walls, respectively.

A most encouraging area not yet discussed is that of numerical simulations of boundary-layer flow over finite panels. Carpenter's paper [9] was on work in this area. An earlier study by Ellen [19] showed that the way in which the panels were attached to adjacent wall surfaces had a fundamental effect on the flow stabilisation properties. The later studies of Metcalfe, Rutland, Duncan and Riley [54] have looked at the use of active stabilisation and more recently Wiplier and Ehrenstein [76], [77] have looked at the use of spatial linear stability theory in conjunction with numerical simulations and discovered the existence of absolute instabilities in flows over Kramer-type walls. Most importantly, though Davies and Carpenter [16] have shown that finite panels of the order of a single wavelength in streamwise extent are capable of stabilising TS modes. In conjunction with Carpenter's results [9], this suggests that designing a multi-panelled wall with optimised parameters for the mean Reynolds number over each section is among the most promising means of improving flow stabilising surfaces in the future.

In addition to the potential transition-delaying aspect of using compliant walls in channel flow, there is another reason for studying flexible-channel flows. This

is the potential for collapse of compliant channels conveying fluid flows. Grotberg and Davis [27], Grotberg and Shee [30], Grotberg and Reiss [28], [29] and Larose and Grotberg [52], amongst others, have used flows through compliant channels to model the collapse of airways in the lung. This is thought to lead to wheezing.

However, we shall be concentrating more on the flow stabilisation properties of compliant walls when used in channel flows. Therefore, we shall review works in this area.

Hains and Price [32] were the first to consider the possibility of flow stabilisation in channel flows using compliant walls. They obtained the equivalent of Benjamin's results [3] for the TSI by numerically integrating the Orr-Sommerfeld equation.

Korotkin [37] then developed an analytic theory for compliant channel flows but failed to apply the correct streamwise boundary condition. Green and Ellen [26] also encountered some difficulties since they were unable to identify some of their instabilites as belonging to the TWF class.

Progress was made when Rotenberry and Saffman [64] demonstrated that an extension of Squire's theorem [72] could be made for channels with compliant walls which could be modelled as spring-backed plates. Thence, it was necessary only to study two-dimensional disturbances in order to know the overall stability of flows in such channels.

Later, Gajjar and Sibanda [22] adapted the multi-deck approach of Carpenter and Gajjar [10] for flows in compliant channels. Gajjar and Sibanda were able to demonstrate that such an approach was applicable to the TSI. They also were able to predict the existence of a fast travelling wave in the presence of high wall damping. Additionally, they showed that previous studies, for example Rotenberry [63] and Ehrenstein and Rossi [18], which retained only spring terms (neglecting inertia and tension) could be misleading. However, Gajjar and

Sibanda's asymptotic approach did not allow them to make a full decription of the FISI, though they were aware of this.

It was Davies and Carpenter [15] who brought the previous studies together and showed that all of the mode classes present in boundary-layer flow over a compliant flat plate are also present in compliant channel flow. They adopted the classification system employed by Carpenter and Garrad [11], [12] and thus found TSI, SD, TWF and combined TSI/TWF instabilities.

Davies and Carpenter studied disturbances whose stream function was symmetric about the channel centreline. They argued that this was sufficient for the TSI since the symmetric TSI are less stable than the anti-symmetric TSI. However, they were aware that anti-symmetric FISI might cause transition to occur at lower Reynolds numbers. Recently, Nagata and Cole [55] have shown that anti-symmetric instabilities may well cause transition to occur at lower Reynolds numbers than would the symmetric modes on their own. However, their findings have yet to be confirmed in the literature.

Fully developed flow in a rigid pipe has been shown to be linearly stable by Corcos and Sellars [13], Gill [25], Salwen and Grosch [65], and Garg and Rouleau [23], for example. The papers by Davey and Nguyen [14], Itoh [35] and Sen, Venkateswarlu and Maji [68] have also shown that fully devloped pipe flow is stable to sufficiently small finite-amplitude disturbances. Therefore, the study of flows in compliant pipes is mainly linked with biological applications such as the aforementioned collapse of airways in the lung studied by Grotberg and Davis [27], Grotberg and Shee [30], Grotberg and Reiss [28], [29] and Larose and Grotberg [52], using channel flows.

Experiments by Krindel and Silberberg [43] showed that the behaviour of the flow in gel-walled tubes differed considerably from the flow in rigid tubes.

Similarly, many modes of instability were observed by Bertram [5], [6] during the collapse of flexible tubes due to a difference between the internal and external pressures. These instabilities were later classified by Betram, Raymond and Pedley [7].

Subsequently, the collapsing tube problem was studied theoretically by Reyn [60] and Jensen and Pedley [36], who found good agreement between the theory and the experimental observations.

Kumaran [45], [44], [46] studied the stability of axisymmetric disturbances for a tube modelled on Krindel and Silberberg's experimental tubes. A rigid cylindrical outer casing was lined on the inside by a visco-elastic material with fluid flow at the core of the tube. The first of Kumaran's papers [45] studied the viscous flow in such a pipe and found that instabilities could arise as a result of the basic-flow shear at the fluid-solid interface. The second paper [44] then looked at the problem for high Reynolds numbers. The third paper [46] derived the equivalent results for axisymmetric modes in invscid compliant-pipe flow that Yeo and Dowling [81] and Yeo [80] had found for inviscid compliant-channel flow.

Later Kumaran studies looked at the effects of varying the elastic shear modulus, the wall viscosity and the wall thickness for intermediate Reynolds number flows [47] and also at the asymptotic nature of the wall modes for high Reynolds numbers.

Shankar and Kumaran [69] have subsequently extended Kumaran's conditions for inviscid flows [46] to include non-axisymmetric disturbances.

All the above studies simultaneously formulated and solved both the solid and fluid problems, which are coupled by the continuity conditions at the solid-fluid interface. However, Sen and Arora [67] took a radically different approach to formulating the linear stability problem of boundary-layer flow over a compliant

surface. They obtained the so called "Kinematic Problem" by introducing an extra parameter, ϕ_w, which corresponded to the complex amplitude of the stream function at the wall for two-dimensional disturbances. Accordingly, the boundary conditions for the fluid at the compliant wall were then formulated in terms of ϕ_w.

Under this formulation, all values of ϕ_w gave rise to disturbances which were valid for the fluid bounded by a wall response of the same wave-number and phase velocity. However, not all values of ϕ_w necessarily gave rise to solutions which obey the necessary dynamical continuity conditions at the solid-fluid interface, i.e. at the compliant wall, for a given wall model. Hence, the boundary conditions imposed were purely kinematic, as suggested above. Therefore, by considering all values of ϕ_w, a superset of the physically realisable solutions were obtained.

This enabled the two systems to be decoupled. The fluid problem could then be solved independently, knowing that any solution to the coupled system, for any wall, must also be a solution to the kinematic fluid problem.

Having obtained the solutions to the kinematic problem for all ϕ_w, the solutions relevant to a particular wall model could then be found from the dynamical conditions at the solid-fluid interface. This was done by using a concept known as the admittance, which is used in acoustics to indicate the response of a solid to an incoming sound wave. Landahl [49] was the first to use it in flows over compliant surfaces and many subsequent studies have followed his lead. The admittance is generally defined as $-V'/P'$, where V' is the normal velocity of the fluid/solid at the fluid-solid interface and P' is the pressure perturbation from the basic flow. This is easily found from the solutions of the fluid problem. This was matched by Sen and Arora to the admittance for the solid wall which could be calculated, for a generic set of wall parameters, from its governing equation. In this way, the wall parameters required to produce the given fluid solution could be back

calculated and checked to determine whether they were physically realistic. For the simple stretched membrane model used by Sen and Arora, this meant that the mass per unit area, the tension and for a passive wall, the damping must all be positive.

With the above method, Sen and Arora were able to find four classes of instability, which they named the Tollmien-Schlichting (TS) class, the Kelvin-Helmholtz (KH) class, the Transitional class and the Resonant class. The TS modes were the same as the TSI of Carpenter and Garrad's nomenclature [11], [12] and the R modes were a flutter instability. However, the Transitional and KH instabilities were not so easy to identify with previous studies' classifications. The KH modes share some properties with Carpenter and Garrad's SD instabilities and the Transitional modes can exhibit very large growth rates like the combined TSI/TWF instabilities but further study is required to make the necessary links.

As previously mentioned, many studies have attributed the drag reducing properties of compliant walls to a delay in transition to a higher Reynolds number, Re. Although no single theory has been developed to describe the transition to turbulence for a general flow, the following is relevant to transition in rigid-walled channels and/or pipes.

For a rigid-walled channel, the flow is of plane-Poiseuille type and is stable to infinitesimal disturbances for low Re. However, two-dimensional disturbances develop in the flow as Re is increased to approximately $5772 = Re_{cr}$ [58]. This flow regime is in turn susceptible to three-dimensional dimensional oscillations [73]. Weakly non-linear theory shows that small but finite amplitude oscillations of this type are governed by a Stuart-Landau equation [51]:

$$\frac{d|A|^2}{dt} = 2\gamma|A|^2 - \alpha|A|^4 . \tag{1.1}$$

Here, $|A|$ is the amplitude and γ is the growth rate of the oscillation, and α is

the Landau constant.

The fixed point of equation (1.1) yields $|A|_\infty = (2\gamma/\alpha)^{\frac{1}{2}}$, the amplitude of the oscillation for large t. This shows that the small but finite amplitude oscillations exist and are stable for $Re > Re'_{cr}$ where $Re'_{cr} < Re_{cr}$ (typically, $Re'_{cr} = O(10^2)$ for channel flows [51], [73]). Therefore, the critical Reynolds number for finite amplitude initial disturbances is lower than that for infinitesimal initial disturbances. This can lead to hysteresis: if the flow is controlled so that finite amplitude oscillations are eliminated as Re is increased then plane-Poiseuille flow will become unstable as Re passes Re_{cr}. If Re is then held at just above Re_{cr} and the perturbations are allowed to develop then their amplitude will tend towards $|A|_\infty$ after a sufficiently long time. The oscillations are now finite in amplitude and so if the Reynolds number is reduced then steady plane-Poiseuille flow will only be regained once Re falls below Re'_{cr}, not Re_{cr}.

The weakly non-linear theory is only valid for Re up to just greater than Re_{cr}, and hence, like the linear theory for infinitesimal disturbances, it is insufficient to describe the transition to turbulence. It is at this point (i.e. for Re significantly greater than Re_{cr}) that no general theory exists. However, one proposed mechanism for transition is that of a succession of period doubling bifurcations of the finite amplitude oscillations, the details of which are given in Landau and Lifshitz [51]. This theory does describe the rapid cascade of frequencies which occurs in practice as Re is increased, with turbulence setting in as a transitional Reynolds number, Re_{tr} say, is passed.

The route to transition in a pipe is similar to that in a channel, with one or two differences. Steady Hagen-Poiseuille flow is stable to infinitesimal and sufficiently small finite-amplitude disturbances, as mentioned above. Therefore, only initial disturbances larger than this will grow with time. Thus, the flow will experience a sudden increase in the drag. Conversely, channel flow where

the linear modes are excited first will experience a smooth increase in the drag. Another difference in the flows is that there is no Squire's theorem for the pipe and so it cannot be assumed that two-dimensional disturbances will be the least stable in Hagen-Poiseuille flow.

The above shows that linear theory is insufficient in itself to predict the transition to turbulence in channel and pipe flows. However, it also shows that linear theory is still important in predicting the growth of sufficiently small disturbances and hence in providing the first step in understanding the process of transition in such flows.

1.1 Aims Of Thesis

We wish to apply Sen and Arora's [67] kinematic approach to the problems of channel and pipe flows bounded by compliant walls. The instabilities found in these problems will be compared with those for boundary-layer flow over a compliant surface. This comparison will include the effects that introducing wall compliance has on the TSI and the classification of the instabilities.

Landahl's results [49] suggested that some instabilities may persist for low Reynolds number flows. Despite this, very little research has been performed for such regimes. Only Kumaran [45] appears to have looked at instabilities in viscous flows over compliant surfaces for boundary layers, channels or pipes. An additional aim, therefore, is to study the potential for instabilities in compliant channels and pipes for very low Reynolds number flows.

Chapter 2

The Kinematic Approach

In this chapter we develop some of the more general ideas and concepts which we shall employ in formulating the temporal linear stability problem for both channel and pipe flow bounded by normally compliant walls. The numerical approach to solving the resulting equations and some aspects of the interpretation of the solutions are also considered here.

2.1 Boundary Conditions

As mentioned in chapter 1, Sen and Arora [67] took a radically different approach, compared to previous studies, when formulating the linear stability problem of boundary-layer flow over a compliant surface. Since we shall be applying the same kinematic formulation to both the problems of the linear stability of channel and pipe flows bounded by compliant walls, it seems prudent to introduce the mathematical concepts once, in isolation. The specific cases of channel and pipe flow then may be dealt with much more briefly when they are encountered.

In order to proceed, we need to assume a wall geometry and basic flow that

are more general than but which apply to both the compliant channel and pipe. We shall need to make certain further assumptions which are also given below.

We shall start by assuming that we can find a co-ordinate system such that the x_* axis is aligned with the basic flow, which is uni-directional. Furthermore, we shall assume that the y_* axis is normal to the wall in its undisturbed state, so that the equation of the wall at rest can be written in the form $y_* = y_0$, a constant. The remaining axis, which we shall label the z_* axis, is such that x_*, y_*, z_* form a right-handed, orthogonal co-ordinate system.

Next, we shall assume that we are considering a Newtonian fluid and hence its flow is governed by the Navier-Stokes equations. It also will be assumed that we are looking for disturbances to a shearing basic flow of the form:

$$\boldsymbol{u_B} = u_B(y_*)\hat{\boldsymbol{x}}_*\,, \tag{2.1a}$$

$$p_B = \frac{dp_B}{dx_*}x_* + p_0\,, \tag{2.1b}$$

where dp_B/dx is the constant pressure gradient driving the flow and p_0 is a constant background pressure, which can be taken to be zero without loss of generality. Here, $\hat{\boldsymbol{x}}_*$ is a unit vector in the x_* direction and the velocity must obey the no-slip condition at the compliant wall in its undisturbed state, i.e. $u_B(y_0) = 0$. A flow consistent with these assumptions can be seen in figure 2.1.

Finally, we shall assume that the equations governing small disturbances from the basic flow permit solutions of the form:

$$\left(u'_{x_*}, u'_{y_*}, u'_{z_*}, p'\right) = A\left(u(y_*), v(y_*), w(y_*), p(y_*)\right) e^{i(\alpha(x_*-ct_*)+\beta z_*)} \tag{2.2}$$

and that these governing equations may be written in the form:

$$i\alpha Re(u_B - c)u + Re(Du_B)v = -i\alpha Re\, p + L_1(y_*, u)\,, \tag{2.3a}$$

$$i\alpha Re(u_B - c)v = -Re\, Dp + L_2(y_*, v, w)\,, \tag{2.3b}$$

$$i\alpha Re(u_B - c)w = f_1(y_*)Re\, p + L_3(y_*, v, w)\,, \tag{2.3c}$$

$$i\alpha\, u + L_4(y_*, v) + f_2(y_*)w = 0\,. \tag{2.3d}$$

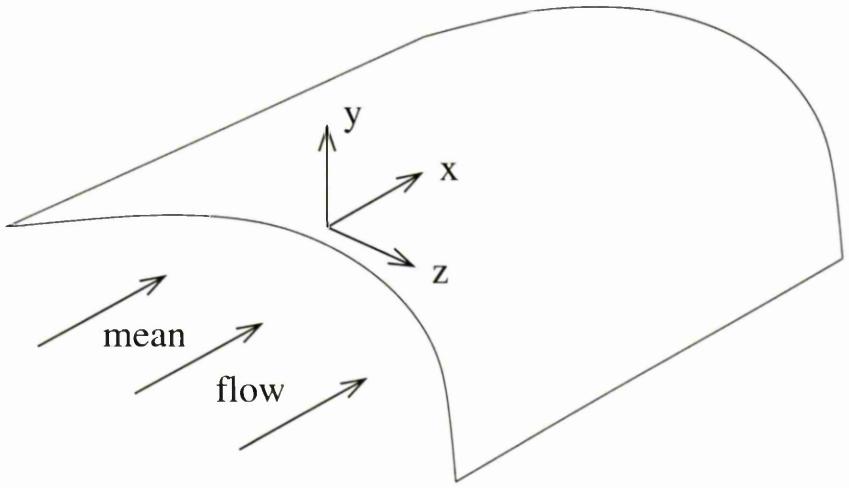

Figure 2.1: Basic flow for a generalised geometry.

Here, u'_{x_*}, u'_{y_*} and u'_{z_*} are the three velocity components of the disturbance, p' is the pressure disturbance and Re is the constant Reynolds number for the flow. Here also, α and β are respectively the x_* and z_* components of the wave number, c is the phase velocity of the wave, u, v, w and p are complex amplitude functions and $A \ll 1$ is a positive real constant which ensures that the disturbances are small enough to be governed by a linear theory. The functions, f_1 and f_2 are known, L_1, L_2 and L_3 are linear differential operators which are second order in the total derivative, $D = d/dy_*$ and L_4 is a linear differential operator which is first order in D.

For two-dimensional disturbances, i.e. when $w(y_*) = \beta = 0$, it is possible to find the solutions in terms of a stream function, ψ, which automatically obeys the relevant form of the continuity equation (2.3d) for such perturbations. We shall assume that, in our geometry, the equations defining the stream function

are of the form:

$$u'_{x_*} = f_*(y_*)\frac{\partial \psi}{\partial y}\,, \tag{2.4a}$$

$$u'_{y_*} = -f_*(y_*)\frac{\partial \psi}{\partial x}\,, \tag{2.4b}$$

where, f_* is a known function which is 1 at $y = y_0$. Hence, given the normal mode decomposition for u'_{x_*} and u'_{y_*}, the stream function must also have a normal mode decomposition, which we shall write as

$$\psi = A\phi(y_*)e^{i\alpha(x_*-ct_*)}\,. \tag{2.5}$$

Here, ϕ is the complex amplitude of the stream function and as before $A \ll 1$ is the real number indicating the small size of the disturbances. Combining equation (2.5) with our expressions (2.2), (2.4a) and (2.4b), for u'_{x_*} and u'_{y_*}, the relations

$$u(y_*) = f_*(y_*)D\phi(y_*)\,, \tag{2.6a}$$

$$v(y_*) = -i\alpha f_*(y_*)\phi(y_*)\,, \tag{2.6b}$$

are obtained, where again $D = d/dy_*$.

Expressions (2.6) allow us to introduce the parameter, ϕ_w, as employed by Sen and Arora [67]. The kinematic boundary conditions at the compliant wall then may be formulated in terms of ϕ_w. In order to do this we need to consider the displacement of the compliant wall with respect to its undisturbed position, $y_* = y_0$. This must take a similar normal mode form to the stream function and hence we may write the equation of the compliant surface, y_{*s}, as

$$y_{*s} = y_0 + Aae^{i(\alpha(x_*-ct_*)}\,, \tag{2.7}$$

where a is the complex amplitude of the wall displacement. Now, given that $\phi_w = \phi(y_{*s})$, we obtain

$$\phi(y_0) = \phi_w\,, \tag{2.8}$$

to leading order in powers of A. This enables us, henceforth, to evaluate the stream function at the wall in its rest state rather than in its disturbed state.

The first boundary condition that we shall obtain is the kinematic condition which equates the normal velocity component of the fluid at the wall, $u'_{y_*}|_{y_*=y_{*_s}}$ to the normal velocity of the compliant wall itself, $\partial y_{*_s}/\partial t_*$. From our stream-function representation of v (2.6b) we obtain the normal velocity of the fluid at the wall,

$$v(y_{*_s}) = -i\alpha f_*(y_{*_s})\phi_w \,.$$

If we Taylor expand about $y_* = y_0$ and then linearise this expression with respect to A, using equation (2.7), we find that

$$v(y_0) = -i\alpha f_*(y_0)\phi_w = -i\alpha\phi_w \,. \tag{2.9}$$

Using expression (2.7) for y_{*_s}, we obtain $\partial y_{*_s}/\partial t_* = -i\alpha Aac\exp(i\alpha(x_* - ct_*))$ as the normal velocity of the wall. Thus, equating the normal fluid and wall velocities and linearising with respect to A yields

$$v(y_0) = -i\alpha ac \tag{2.10}$$

and hence, we can deduce that

$$\phi_w = ac\,, \tag{2.11}$$

which enables us to eliminate the unknown, a from all subsequent formulae.

The other condition at the compliant wall is given by the no-slip condition for the streamwise velocity component, $u_B + u'_{x_*} = 0$ at $y_* = y_{*_s}$. Again using our decomposition for y_{*_s} (2.7) and expanding about $y_* = y_0$ in powers of A, we obtain $u(y_0) = -aDu_B(y_0)$. Substituting (2.11) for a, we arrive at the second wall condition

$$u(y_0) = -\frac{\phi_w Du_B(y_0)}{c} \,. \tag{2.12}$$

Thus, we have deduced the necessary boundary conditions at the compliant wall for a two-dimensional perturbation from the basic flow (2.1). These are expressions (2.9) and (2.12), which correspond to the normal and streamwise velocity components of the disturbance, respectively.

We can extend this method of formulating the boundary conditions to three-dimensional disturbances, i.e. for $w(y_*), \beta \neq 0$, by defining a pseudo-stream-function, which we shall denote by ψ, as before. We shall define ψ using a normal mode decomposition identical to the two-dimensional decomposition (2.5), such that $\phi(y_*)$ is related to $v(y_*)$ via equation (2.6b). Hence, using equation (2.8) and linearising, as before, once again we obtain equation (2.9) as the boundary condition for the normal velocity at the compliant wall.

Further justification for this approach to formulating the boundary conditions for three-dimensional disturbances at the compliant surface can be gained by looking at equation (2.9). For the two-dimensional case, we specified the stream-function amplitude at the wall, ϕ_w and found $v(y_0)$ in terms of it, but we could just as well have specified $v(y_0)$ directly. For three-dimensional disturbances, we may also specify $v(y_0)$ directly and use equation (2.9) to write it in terms of the amplitude of a pseudo-stream-function, ϕ_w.

Since equation (2.10) is independent of the formulation of the boundary condition from the fluid side of the interface, we may, without further justification, use it to reproduce equation (2.11) for three-dimensional disturbances and hence again we may eliminate the amplitude of wall oscillation, a. It is then a trivial extension to show that again equation (2.12) is the relevant boundary condition for the streamwise velocity component of a three-dimensional disturbance.

For a three-dimensional disturbance there is a third velocity component for

which we need to find a boundary condition at the compliant wall. This, the boundary condition for the velocity amplitude function, w, is easily obtained from the no slip condition $u'_{z_*}|_{y_*=y_{*_s}} = 0$. Using the normal mode decompositions (2.2) and (2.7) for u'_{z_*} and y_{*_s} respectively, the condition becomes

$$w(y_0) = 0\,, \tag{2.13}$$

to leading order in A.

With the inclusion of the above condition it has been shown for both two- and three-dimensional disturbances, that the kinematic boundary conditions at a compliant wall can be formulated in terms of a parameter, ϕ_w. However, there are a few more analytical considerations which are relevant to both the channel and pipe problems and so again it seems prudent to deal with these together rather than in isolation.

The first of these considerations concerns a normalisation condition. The linear nature of the governing stability equations (2.3) implies that if a solution, $(u, v, w, p) = (u_*, v_*, w_*, p_*)$, is found for a given set of parameters α, β, Re and phase velocity, c, then so is $(u, v, w, p) = (\hat{u}_*, \hat{v}_*, \hat{w}_*, \hat{p}_*) = K_*(u_*, v_*, w_*, p_*)$, where K_* is any constant. Now, for the case of flow near a rigid wall, the boundary conditions for disturbances are homogeneous. It follows that if we fix the wave numbers α and β and the Reynolds number, Re, then we have an eigenvalue problem for the phase velocity, c, with associated eigenfunctions u, v, w and p. Therefore, in order to differentiate between eigenfunctions which are independent solutions and those that differ merely by a common factor, it is necessary to impose a further, normalisation condition. This may take one of many forms which include fixing the value of one of the eigenfunctions at a point where it is known to be non-zero.

However, our problem has homogeneous boundary conditions only for the specific case when $\phi_w = 0$ and hence is only an eigenvalue problem then. For non-rigid walls, i.e. for $\phi_w \neq 0$, the compliant problem can be thought of as an extended eigenvalue problem, as explained by Sen and Arora [67]. This is illustrated by considering the two solutions of the linear stability equations (2.3), namely (u_*, v_*, w_*, p_*) and $(\hat{u}_*, \hat{v}_*, \hat{w}_*, \hat{p}_*)$, above. The solution, (u_*, v_*, w_*, p_*), obeys the linear stability equations (2.3) with the fixed values of α, β, Re and phase velocity, c and must also obey the kinematic boundary conditions (2.9), (2.12) and (2.13), for some value $\phi_w = \phi_{w*}$, say. In order for the boundary conditions at the compliant wall to be consistent $(\hat{u}_*, \hat{v}_*, \hat{w}_*, \hat{p}_*)$ must obey the same linear stability equations (2.3), for the same parameters α, β, Re and phase velocity, c but with the wall stream function, $\phi_w = \hat{\phi}_{w*} = K_* \phi_{w*}$.

Since, for our kinematic formulation of the problem, ϕ_w can take any value in the complex plane, $(\hat{u}_*, \hat{v}_*, \hat{w}_*, \hat{p}_*)$, is also a valid solution to the same compliant problem. Hence, as for an eigenvalue problem, we need to apply a normalisation condition in order to differentiate between independent eigenfunction solutions and those which differ only by a constant factor. We shall use the type of normalisation condition mentioned above, whereby the value of one of the eigenfunctions is fixed at a point where it is known to be non-zero, though the details will be left until the relevant chapters.

The final consideration that we have to make in regard to the problem formulation pertains to the remaining boundary conditions for the eigenfunctions, u, v, w, p. For two-dimensional disturbances is it possible to eliminate the pressure from the stream-function formulation of the linear stability equations (2.3). The result is a fourth-order ordinary differential equation for ϕ which, in the

case of a Cartesian co-ordinate system, is the well known Orr-Sommerfeld equation [57], [71]. Hence, we require four boundary conditions in order to fix ϕ. For three-dimensional disturbances, equations (2.3) can be reduced to a sixth-order ordinary differential equation for one of the eigenfunctions and hence we need six boundary conditions in order to fix the solution. In either case, in order to fix a solution for the kinematic compliant problem, we require as many more conditions again as we have at a single compliant wall. In the case of channel flow, these conditions may take one of two forms: the velocity components may be specified at the other wall or in the case of the symmetric channel, i.e. where the other wall is also compliant, symmetry conditions for each of the velocity components may be specified. For the case of pipe flow, symmetry conditions are specified about the axis of the pipe for the velocity components. Again, the details for each case will be left to the relevant chapters.

The above completes the analytical aspects of the kinematic approach. However, when considering numerical solutions especially, it is not always possible to consider all values of ϕ_w, as required above. It is then convenient to decompose the complex amplitude into the form $\phi_w = |\phi_w| \exp(i\theta_w)$, where $|\phi_w|$ is the real modulus and θ_w is the real argument, of ϕ_w. By letting θ_w take values in the range $[0, 2\pi m]$ where m is the number of branches of the solution, and letting $|\phi_w|$ take values increasing from zero to some suitably large $|\phi_w|_{\max}$ (about 25 is large enough for boundary-layer flow), all the possible flow configurations can then be found.

2.2 Numerical Methods

2.2.1 The Tchebychev Collocation Method

For the compliant channel it is possible to non-dimensionalise the governing equations in such a way that, in their rest positions, the walls are at $y_* = -1$ and $y_* = 1$. Similarly, for the compliant pipe problem, it is possible to non-dimensionalise the governing equations so that axis of the pipe is at $y_* = 0$ and the wall is at $y_* = 1$. Using the transformation $y'_* = 2y_* - 1$, the solution domain can then be mapped from $(0, 1)$ to $(-1, 1)$ and hence both problems lend themselves readily to solution via a Tchebychev collocation method. This method, the details of which may be found in Canuto, Hussaini, Quarteroni and Zang [8], relies on the ability to expand any smooth function, f say, in the form

$$f(y_*) = \sum_{k=-\infty}^{\infty} \hat{f}_k T_k(y_*)\,,$$

over the interval $(-1, 1)$. Here, T_k is the kth Tchebychev polynomial of the first kind. In such a series, the expansion coefficients, $\hat{f}_k$ decay faster than any inverse power of k. This implies that truncation of the series after only a small number of terms should give an extremely accurate approximation for f. This property is known as the "spectral accuracy" of the Tchebychev collocation method.

We shall use expansions of the above type for each of our eigenfunctions u, v, w and p in order to solve the kinematic problem. The method we shall use will be to make an initial approximation to the phase-velocity eigenvalue, c and then to solve the linear stability equations (2.3) in conjunction with all the boundary conditions bar the streamwise condition (2.12) (since the problem is over specified unless c, is an eigenvalue and u, v, w and p are eigenfunctions). If c is close to the eigenvalue then the error in condition (2.12) will be small. If the error is below an acceptable tolerance, then we will assume that the errors in the eigenvalue, c and the eigenfunctions u, v, w and p are also within an acceptable tolerance and

so we shall take these to be our approximations to the solution. If however, the error is outside the accepted tolerance then we shall use a Newton-Raphson type of method on the condition (2.12) in order to refine our approximation to c, the details of which are given in the next subsection. By successive refinements of c we should eventually arrive at a solution to the kinematic problem.

Returning to our general function, f, the expansion coefficients, $\hat{f}_k$ depend on all the values of f in the interval $(-1, 1)$ and so they they cannot be calculated exactly. The solution to this problem is to find approximations, $\tilde{f}_k$, to a finite number of expansion coefficients, $\hat{f}_k$, by using the values of f at a finite number of selected points. The truncated terms have expansion coefficients which are approximated to be zero and hence the series expansion becomes $\tilde{f}(y_*) = \sum_{k=0}^{N} \tilde{f}_k T_k(y_*)$, where $N+1$ is the number of selected points.

This procedure defines a discrete transform between the values of f at the selected points in physical space and the set of approximate discrete expansion coefficients, $\tilde{f}_k$ in transform space.

There are many ways to implement the discrete transform procedure but as mentioned above, we shall use the collocation method. This requires that our approximation to f, namely $\tilde{f}$, is equal to f at each of the specified collocation points. Thus, $\tilde{f}$ is then the interpolating polynomial for the function, f at the collocation points.

Also, $\tilde{f}$ will obey the equations (2.3) plus the boundary and normalisation conditions at each of the collocation points if it is any of our approximations to the solutions for the quantities u, v, w and p.

Obviously then, we have

$$f(y_{*j}) = \sum_{k=0}^{N} \tilde{f}_k T_k(y_{*j}) \,,$$

where y_{*j} is the jth collocation point.

For convenience, we shall use the Tchebychev-Gauss-Lobatto points where

$$y_{*j} = \cos\left(\frac{\pi j}{N}\right) . \tag{2.14}$$

This choice of collocation points takes advantage of one of the properties of Tchebychev polynomials, namely $T_k(y_*) = \cos(k \cos^{-1} y_*)$ and hence

$$T_k(y_{*j}) = \cos\left(\frac{\pi jk}{N}\right) = C^{-1}_{j\,k}$$

at the jth collocation point. Here, C^{-1} is the transformation matrix from Tchebychev to physical space. The inverse transformation, i.e. from physical to Tchebychev space, is represented by the matrix

$$C_{j\,k} = \frac{2}{N\bar{c}_j\bar{c}_k} \cos\left(\frac{\pi jk}{N}\right) , \text{ where } \bar{c}_j = \begin{cases} 2 & j = 0 \text{ or } N, \\ 1 & 1 \le j \le N-1. \end{cases}$$

With this set of collocation points, we denote the value of u at y_{*j} by u_j, which we compute along with v_j and w_j, which are defined similarly. However, since we have no boundary conditions for the pressure, we use a pressure correction type of method and compute p at each of the points $y'_{*j'} = y_{*j+1/2}$ for $j = 0, \ldots, N-1$, instead of computing p at each of the y_{*j}. The matrix transforming from Tchebychev space to (half-point) physical space is given by

$$\left(C^{\frac{1}{2}}\right)^{-1}_{j\,k} = \cos\left(\frac{\pi\left(j+\frac{1}{2}\right)k}{N}\right)$$

and hence the inverse matrix, transforming from (half-point) physical space to Tchebychev space, is given by

$$C^{\frac{1}{2}}_{j\,k} = \frac{2}{N\bar{c}_j} \cos\left(\frac{\pi j\left(k+\frac{1}{2}\right)}{N}\right) .$$

So, now we have to find the $4N+3$ unknowns u_j, v_j and w_j for $j = 0, \ldots, N$ and $p_{j'}$ for $j' = 0, \ldots, N-1$. Hence, we need $4N+3$ equations to find a unique

solution. We obtain these equations from the momentum-derived stability equations (2.3) at each point, y_{*j} except for the points $y_{*j} = -1, 1$; plus the normalisation condition and the five boundary conditions where we exclude the streamwise condition (2.12) at a compliant wall; plus the continuity-derived stability equation (2.3d) at each of the half points, y'_{*j}.

Finally, in order to compute solutions to the linearised stability equations we need to know how to deal with derivatives. Following Canuto et. al. [8], this can be done in matrix form via the formula

$$(D_N f)(y_{*j}) = \sum_{l=0}^{N} (D_N)_{jl} f_l \,,$$

where, as before, f is any smooth function. For the Gauss-Lobatto points

$$(D_N)_{ij} = \begin{cases} \frac{\bar{c}_i}{\bar{c}_j} \frac{(-1)^{i+j}}{y_{*i} - y_{*j}} & i \neq j, \\ \frac{-y_{*j}}{2(1-y_{*j}{}^2)} & 1 \leq i = j \leq N-1, \\ \frac{2N^2+1}{6} & i = j = 0, \\ -\frac{2N^2+1}{6} & i = j = N. \end{cases} \tag{2.15}$$

We can now consider our solutions for u, v and w as the vectors $\boldsymbol{u}$, $\boldsymbol{v}$, $\boldsymbol{w}$, with the j-th component equal to the value of u, v, w at y_{*j}, for $j = 0, \ldots, N$, respectively. If also, we consider p as the vector $\boldsymbol{p}$, with j-th component equal to the value of p at $y_{*j+1/2}$, for $j = 0, \ldots, N-1$, then using the form of the boundary conditions along with equations (2.3), we can write our equations as

$$X1\boldsymbol{u} + Y1\boldsymbol{v} + W1\boldsymbol{p} = \boldsymbol{r1},$$

$$Y2\boldsymbol{v} + Z2\boldsymbol{w} + W2\boldsymbol{p} = \boldsymbol{r2},$$

$$Y3\boldsymbol{v} + Z3\boldsymbol{w} + W3\boldsymbol{p} = \boldsymbol{r3},$$

$$X4\boldsymbol{u} + Y4\boldsymbol{v} + Z4\boldsymbol{w} = \boldsymbol{r4}.$$

We can combine these four equations into a single matrix equation of the form

$$L\boldsymbol{\phi} = \boldsymbol{r}\,, \tag{2.16}$$

where

$$L = \begin{pmatrix} X1 & Y1 & 0 & W1 \\ 0 & Y2 & Z2 & W2 \\ 0 & Y3 & Z3 & W3 \\ X4 & Y4 & Z4 & 0 \end{pmatrix}, \boldsymbol{\phi} = \begin{pmatrix} \boldsymbol{u} \\ \boldsymbol{v} \\ \boldsymbol{w} \\ \boldsymbol{p} \end{pmatrix}, \boldsymbol{r} = \begin{pmatrix} \boldsymbol{r1} \\ \boldsymbol{r2} \\ \boldsymbol{r3} \\ \boldsymbol{r4} \end{pmatrix}.$$

Here, the only non-zero elements of $\boldsymbol{r}$ refer to the normalistion condition and the normal velocity boundary condition(s) (2.9) at a compliant wall.

We can find $\boldsymbol{\phi}$ by inverting the matrix L. This can be done by any one of a number of methods but we shall choose LU factorisation and implement it using the NAG library routine F04ADF.

2.2.2 The Newton-Raphson Iterative Method

Unless c is an eigenvalue of the problem, the relaxed boundary condition for the axial velocity at the compliant wall will not be obeyed. Eliminating ϕ_w from (2.12) and (2.9), this is equivalent to the condition

$$\chi(c) = c\; u(y_0) - \frac{Du_B(y_0)}{i\alpha} v(y_0) \neq 0\,. \tag{2.17}$$

However, if c is sufficiently close to the eigenvalue, we can find it iteratively using a Newton-Raphson technique. In this method, the Taylor expansion for $\chi(c+\Delta c)$, about c, is used to find the new approximation for the eigenvalue, $c+\Delta c$. The two term Taylor expansion for χ is

$$\chi(c+\Delta c) = \chi(c) + \Delta c \frac{\partial \chi}{\partial c} + O((\Delta c)^2)\,.$$

We wish to find Δc such that $\chi(c+\Delta c) = 0$, so to leading order in Δc

$$\Delta c = -\frac{\chi}{\frac{\partial \chi}{\partial c}}\,.$$

If our original estimate for c is sufficiently close to the eigenvalue then $c + \Delta c$ will be a closer approximation to it. However, the explicit form of $\partial\chi/\partial c$, calculated from equation (2.17) is

$$\frac{\partial\chi}{\partial c} = u(y_0) + c\frac{\partial u}{\partial c}(y_0) - \frac{Du_B(y_0)}{i\alpha}\frac{\partial v}{\partial c}(y_0)\,,$$

and so we need to find the values of $\partial u/\partial c|_{y_*=y_0}$ and $\partial v/\partial c|_{y_*=y_0}$. This can be done by partially differentiating equation (2.16) with respect to c to get

$$L\frac{\partial\phi}{\partial c} + \phi\frac{\partial L}{\partial c} = \frac{\partial r}{\partial c} = \mathbf{0}\,. \tag{2.18}$$

The elements of $\partial L/\partial c$ can be calculated from equation (2.16) and hence so can $\partial\phi/\partial c$ by inverting the above equation. We can then find $\partial u/\partial c|_{y_*=y_0}$ and $\partial v/\partial c|_{y_*=y_0}$ from the relevant elements of $\partial\phi/\partial c$ and hence we can calculate Δc and with it, the next approximation to the eigenvalue.

By iteratively using this whole procedure, we should find an accurate approximation to the phase velocity eigenvalue, c and the associated eigenfunction, ϕ, when the size of the adjustment to the phase velocity, $|\Delta c|$ is smaller than some suitable tolerance. We shall use a tolerance of $10^{-6}|c|$.

Before we start to generate results we will need to check the validity of our numerical scheme. In chapters 3 & 4 we shall do this in two ways:

- We shall check the eigensolutions which we obtain for $\phi_w = 0$ with those previously obtained for rigid flows.
- We shall check the eigensolutions which we obtain for non-zero ϕ_w with the analytical results derived later.

2.3 Physical Realisability

2.3.1 Introduction Of The Wall Dynamics

We are now in a position to find numerical solutions to the kinematic problem. However, in chapter 1 we mentioned that the kinematic formulation only takes account of the necessary kinematic conditions at a compliant surface and so the solutions to the kinematic problem form a superset of those which occur in reality. Physically realisable modes must also obey the necessary dynamical conditions at the fluid-solid interface. This requires us to introduce the dynamics of the wall, at this stage, in order to make the reduction from kinematic to physically realisable solutions.

We shall choose to use the example of the simple stretched membrane in order to study physically realisable modes. Using this wall model will allow a comparison with many earlier works, including those of Landahl [49], Davies & Carpenter [15] and Sen & Arora [67], which studied wall models of a similar type. The equation of motion obeyed by the simple stretched membrane may be written in non-dimensional form as

$$m\frac{\partial^2 y_{*s}}{\partial t^2} - T\frac{\partial^2 y_{*s}}{\partial x^2} + \bar{d}\frac{\partial y_{*s}}{\partial t} = -p'_w\,, \tag{2.19}$$

where m is the (non-dimensional) mass per unit area of the wall, T is the (non-dimensional) tension per unit length applied to the wall, $\bar{d}$ is a (non-dimensional) damping coefficient based on a unit area of the wall and p'_w is the pressure perturbation at the wall. The following analysis may be extended to other, more complex, stretched membrane models by following the analysis of Sen and Arora [67].

The theoretical basis for the use of such models for Kramer's wall was laid down by Carpenter and Garrad [11], who showed that $m = O(1)$ for Kramer's walls and hence the wall density is usually chosen to correspond to such values of m for the majority of the cases considered herein.

We can now relate the above wall dynamics to our kinematic results by using the concept of admittance. This concept is used in acoustics to quantify the motion of the surface of a solid material in response to an in coming sound wave. As mentioned in chapter 1, Landahl [49] was the first to propose its use in the stability theory of flow over a compliant surface. The admittance, Y, is defined as the ratio of minus the normal wall velocity perturbation to the wall pressure perturbation, i.e. $Y = -(u'_{y_*})_w/p'_w$.

We may calculate the admittance from the fluid side of the wall, Y, by using the solutions of the kinematic problem. Since the kinematic solutions are in the form of the normal mode eigensolutions given by equation (2.2), this tells us that the admittance must be independent of the normalisation applied to the solutions. Therefore, we may equate the admittance calculated from the kinematic problem to that which we shall now calculate from the wall dynamics.

Using equations (2.2), (2.7), (2.10) and (2.19), we can deduce the expression for the admittance from the wall side, Y_0, given by Sen and Arora [67],

$$Y_0 = -\frac{ic}{m\alpha\left(c_0^2 - c^2 - i\frac{cd}{\alpha}\right)}. \tag{2.20}$$

Here, $c_0^2 = T/m$ and $d = \bar{d}/m$. Then the dynamics can be formally introduced into the problem now by considering one of the kinematic solutions and imposing the extra wall condition $Y_0 = Y$ at $y_* = y_0$. This enables us to back calculate the wall parameters, m, c_0^2 and d, which would give rise to this mode. Interpretations of such parameters are given in the next subsection.

2.3.2 Physical Realisability Conditions

Now that we have introduced the dynamic conditions which also must be satisfied by the solutions, we can make the necessary reduction of the set of kinematic solutions to those that may be physically realised. This we do by imposing

certain constraints on the back calculated wall parameters found by the method mentioned above.

The physical realisability constraints that we need to impose for a passive compliant surface are certainly m, d, $c_0^2 \geq 0$ and in practice these should be strict inequalities, since the wall must have some mass, it must be under tension for waves to propagate and there will be some damping effects.

From our expression for the admittance from the wall-side (2.20), we can obtain expressions for two of the wall parameters in terms of c, Y_0 and the remaining wall parameter. If we do this for d and c_0^2 in terms of m (and c and Y_0) we obtain

$$d = -2\alpha c_i + \frac{Y_r c_r + Y_i c_i}{m c_r \left(Y_r^2 + Y_i^2\right)}, \tag{2.21a}$$

$$c_0^2 = \left(c_r^2 + c_i^2\right)\left(1 - \frac{Y_i}{m\alpha c_r \left(Y_r^2 + Y_i^2\right)}\right), \tag{2.21b}$$

where $c = c_r + ic_i$ and $Y_0 = Y_r + iY_i$.

We could now choose a physically realisable value for m and calculate the corresponding values of d and c_0^2 to see if they too were physically realistic (i.e. greater than zero). However, we can use the physical realisability inequalities and equations (2.21) to find a single condition which determines whether any particular unstable mode can be realised by some set of wall parameters. We can also deduce upper and lower bounds for all three of the wall parameters, for which the given unstable modes can be found in practice.

In order to find the above condition and bounds we must also restrict ourselves to non-rigid modes, i.e. those modes where $Y_0 \neq 0$. Since we are concerned with the effect of compliance on the rigid case, in which $m, d, c_0^2 \to \infty$, this is not a severe restriction to make. In the case of the basic flow being Hagen-Poiseuille flow in a pipe, the rigid modes are stable and so the above restriction actually has no effect upon the generality of the results.

Now for physically realisable modes we have already stated that we must require $d \geq 0$. This immediately allows us to obtain an upper bound for m, since equation (2.21a) then gives

$$\frac{Y_r c_r + Y_i c_i}{m c_r \left(Y_r^2 + Y_i^2\right)} \geq 2\alpha c_i \,.$$

Hence,

$$\frac{Y_r c_r + Y_i c_i}{2\alpha c_r c_i \left(Y_r^2 + Y_i^2\right)} \geq m \,,$$

since $\alpha > 0$ and for unstable modes, $c_i > 0$. In a similar fashion, the lower bound for m can be obtained from equation (2.21b), since $c_0^2 \geq 0$ requires

$$1 - \frac{Y_i}{m\alpha c_r \left(Y_r^2 + Y_i^2\right)} \geq 0 \,,$$

because $c_r^2 + c_i^2 > 0$ for unstable modes. Thus,

$$m \geq \frac{Y_i}{\alpha c_r \left(Y_r^2 + Y_i^2\right)} \,,$$

but we must also have $m \geq 0$ and so we may write our limits for m in the form

$$\frac{Y_r c_r + Y_i c_i}{2\alpha c_r c_i \left(Y_r^2 + Y_i^2\right)} \geq m \geq \max\left\{\frac{Y_i}{\alpha c_r \left(Y_r^2 + Y_i^2\right)}, 0\right\} . \tag{2.22}$$

From this inequality we can deduce the single condition for determining whether an unstable mode is physically realisable for some set of wall parameters or not. To do this, first we note that $2\alpha\left(Y_r^2 + Y_i^2\right)$ is strictly greater than zero, since $\alpha > 0$ and for non-rigid modes $\left(Y_r^2 + Y_i^2\right) > 0$. Hence, multiplying through by the above noted quantity, we obtain the inequality

$$\frac{Y_r}{c_i} + \frac{Y_i}{c_r} \geq 2\alpha\left(Y_r^2 + Y_i^2\right) m \geq \max\left\{2\frac{Y_i}{c_r}, 0\right\} . \tag{2.23}$$

So, ignoring the middle term of the above inequality and subtracting Y_i/c_r from both sides yields

$$\frac{Y_r}{c_i} \geq \max\left\{\frac{Y_i}{c_r}, -\frac{Y_i}{c_r}\right\} ,$$

and hence

$$\frac{Y_r}{c_i} \geq \left| \frac{Y_i}{c_r} \right| . \tag{2.24}$$

We may reverse all the steps of the above argument, noting that given inequality (2.24) and that $2\alpha\left(Y_r^2 + Y_i^2\right) > 0$, for non-rigid modes, then we can find a positive m such that inequality (2.23) is obeyed and hence we may recover the conditions $d, c_0^2 \geq 0$. Therefore, expression (2.24) is a necessary and sufficient condition for non-rigid unstable modes to be physically realisable in flow past a stretched-membrane wall.

Equation (2.24) is consistent with Benjamin's result [3] that Y_i should be large and negative and that Y_r should be as small as possible in order for a flexible wall to be effective at stabilising flows. However, the above result also leaves the possibility that if Y_i is large and positive with Y_r still small then the flow may be stabilised.

We can now use our inequalities for m to find further restrictions on the values of d and c_0^2 that give rise to the unstable mode under consideration. This we must do for the two different cases, $Y_i/c_r \leq 0$ and $Y_i/c_r > 0$:

Case 1:

Here, $Y_i/c_r \leq 0$ and so

$$\max\left\{ \frac{Y_i}{\alpha c_r \left(Y_r^2 + Y_i^2\right)}, 0 \right\} = 0 .$$

Hence, inequality (2.22) yields

$$\frac{1}{m} \geq \frac{2\alpha c_r c_i \left(Y_r^2 + Y_i^2\right)}{Y_r c_r + Y_i c_i} \geq 0 ,$$

for unstable modes of this type. Now, multiplying through by the quantity, $\left(Y_r c_r + Y_i c_i\right)/c_r \left(Y_r^2 + Y_i^2\right) > 0$ and subtracting $2\alpha c_i$ yields

$$d \geq 0 ,$$

and so we do not gain any extra information about d. However, if we multiply through by $-Y_i/\alpha c_r\left(Y_r^2+Y_i^2\right)$ instead and use $-Y_i/c_r \geq 0$, then we find that

$$\frac{-Y_i}{m\alpha c_r\left(Y_r^2+Y_i^2\right)} \geq \frac{-2Y_i c_i}{Y_r c_r + Y_i c_i} \geq 0\,.$$

Adding one to each term in the inequality and then multiplying through by $c_r^2+c_i^2>0$ we obtain an extra set of conditions on c_0^2:

$$c_0^2 \geq \left(c_r^2+c_i^2\right)\left(\frac{Y_r c_r - Y_i c_i}{Y_r c_r + Y_i c_i}\right) \geq \left(c_r^2+c_i^2\right) > 0\,.$$

Case 2:

Here, $Y_i/c_r > 0$ and so

$$\max\left\{\frac{Y_i}{\alpha c_r\left(Y_r^2+Y_i^2\right)}, 0\right\} = \frac{Y_i}{\alpha c_r\left(Y_r^2+Y_i^2\right)} > 0\,.$$

Hence, inequality (2.22) yields

$$\frac{\alpha c_r(Y_r^2+Y_i^2)}{Y_i} \geq \frac{1}{m} \geq \frac{2\alpha c_r c_i\left(Y_r^2+Y_i^2\right)}{Y_r c_r + Y_i c_i} \geq 0\,,$$

for unstable modes of this type. If, again, we multiply through by the quantity, $(Y_r c_r + Y_i c_i)/c_r\left(Y_r^2+Y_i^2\right) > 0$ and subtract $2\alpha c_i$, as before, then this time we obtain

$$\alpha Y_r\left(\frac{c_r}{Y_i} - \frac{c_i}{Y_r}\right) \geq d \geq 0\,.$$

Hence we get an upper bound for the damping that we can apply and still obtain the unstable mode under consideration. If we follow the procedure for obtaining the bounds on c_0^2, i.e. we multiply the inequality for m through by $-Y_i/\alpha c_r\left(Y_r^2+Y_i^2\right)$, using $-Y_i/c_r < 0$, and then we add one and multiply through by $c_r^2+c_i^2>0$, we obtain

$$\left(c_r^2+c_i^2\right) \geq \left(c_r^2+c_i^2\right)\left(\frac{Y_r c_r - Y_i c_i}{Y_r c_r + Y_i c_i}\right) \geq c_0^2 \geq 0\,.$$

Summary

We can summarise the above results as follows:

1. if

$$\frac{Y_r}{c_i} \geq -\frac{Y_i}{c_r} \geq 0\,,$$

then we have the following set of bounds on the wall parameters:

$$\begin{aligned}\frac{Y_r c_r + Y_i c_i}{2\alpha c_r c_i \left(Y_r^2 + Y_i^2\right)} \geq & m \geq 0\,,\\ \infty \geq & d \geq 0\,,\\ \infty \geq & c_0^2 \geq \left(c_r^2 + c_i^2\right)\left(\frac{Y_r c_r - Y_i c_i}{Y_r c_r + Y_i c_i}\right) \geq \left(c_r^2 + c_i^2\right) > 0\,. \end{aligned} \tag{2.25}$$

2. if

$$\frac{Y_r}{c_i} \geq \frac{Y_i}{c_r} > 0\,,$$

then we have a different set of bounds on the wall parameters, thus:

$$\begin{aligned}\frac{Y_r c_r + Y_i c_i}{2\alpha c_r c_i \left(Y_r^2 + Y_i^2\right)} \geq & m \geq \frac{Y_i}{\alpha c_r \left(Y_r^2 + Y_i^2\right)}\,,\\ \alpha Y_r \left(\frac{c_r}{Y_i} - \frac{c_i}{Y_r}\right) \geq & d \geq 0\,,\\ \left(c_r^2 + c_i^2\right) \geq \left(c_r^2 + c_i^2\right)\left(\frac{Y_r c_r - Y_i c_i}{Y_r c_r + Y_i c_i}\right) \geq & c_0^2 \geq 0\,. \end{aligned} \tag{2.26}$$

Having formulated the kinematic problem for a generalised geometry and having discussed the general numerical approach to solving the resulting equations, now we can consider the specific cases of flow in channels and pipes bounded by compliant walls.

Chapter 3

Compliant Channel Problem

Using the ideas introduced in chapter 2, now we can approach the specific problems of channel and pipe flow bounded by compliant walls. First, we shall tackle the problem of channel flow bounded by one or more compliant surfaces, since this is the simpler geometry and also because there is a larger array of literature with which to compare our results.

In this chapter, we shall start by formulating the compliant channel problem with reference to the methods employed in chapter 2. Next, we shall proceed to apply the numerical methods, given in the previous chapter, to solving the kinematic compliant channel problem. Then, we shall be in a position to find solutions to the kinematic compliant channel problem and we shall investigate the different classes of modes into which the numerical solutions may be divided. Finally, we shall conclude this chapter by investigating various analytical solutions in some cases where one or other of the problem parameters asymptotically approaches given limits.

3.1 Flow Geometry

We shall start by choosing a Cartesian co-ordinate system in which x^* is the dimensional co-ordinate with axis in the streamwise direction, y^* is the dimensional co-ordinate perpendicular to the compliant channel wall(s) in its/their rest state and the dimensional z^* co-ordinate is measured in the direction of the depth of the channel. The channel is then formed by two pairs of parallel walls whose extent in the x^* direction is infinite: one rigid pair a distance, $2d$ apart at constant values of z^*, which we may take to be $-d$ and d; plus one pair of walls, a distance $2L$ apart, at constant values of y^*, which we may take to be at $-L$ and L. Of this second pair, at least one wall is compliant and hence we need to consider two geometries:

1. the symmetric channel where both walls are compliant;

2. the asymmetric channel where only one wall is compliant.

We will then assume that $d \gg L$ and so we may also assume that the effects of the pair of rigid side walls on the flow are negligible over the bulk of the channel.

With our chosen co-ordinate system, the incompressible flow in a rigid channel is described by the pressure, p^*, and the three velocity components, $u^*_{x^*}$, $u^*_{y^*}$ and $u^*_{z^*}$, in the x^*, y^* and z^* directions respectively. All four of these quantities may depend on x^*, y^*, z^* and t^*, the dimensional time.

We shall now choose to formulate the kinematic compliant channel problem with the non-dimensional quantities x, y, z, t, u_x, u_y, u_z and p which are related to the above dimensional variables via the linear relations $x^* = Lx$, $y^* = Ly$, $z^* = Lz$, $t^* = Lt/U$, $u^*_{x^*} = Uu_x$, $u^*_{y^*} = Uu_y$ and $u^*_{z^*} = Uu_z$. Here, U is the maximum (centreline) velocity of the basic flow. For the remaining relation, that of the pressure, we have two options. These are an inertial scaling and a viscous scaling. However, initially, we shall be concerned with finite Reynolds number

flows and so the inertial scaling $p^* = \rho U^2 p$ is suitable, where ρ is the constant density of the fluid.

In the non-dimensional co-ordinate system, the top and bottom walls of the channel are at $y = -1$ and $y = +1$, respectively and hence the geometry of the symmetric channel is as shown in figure 3.1 and the geometry of the asymmetric channel is as shown in figure 3.2.

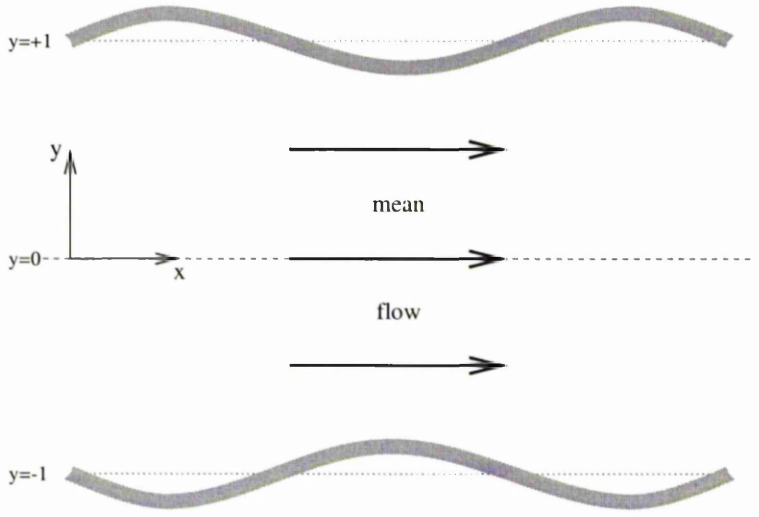

Figure 3.1: The symmetric channel.

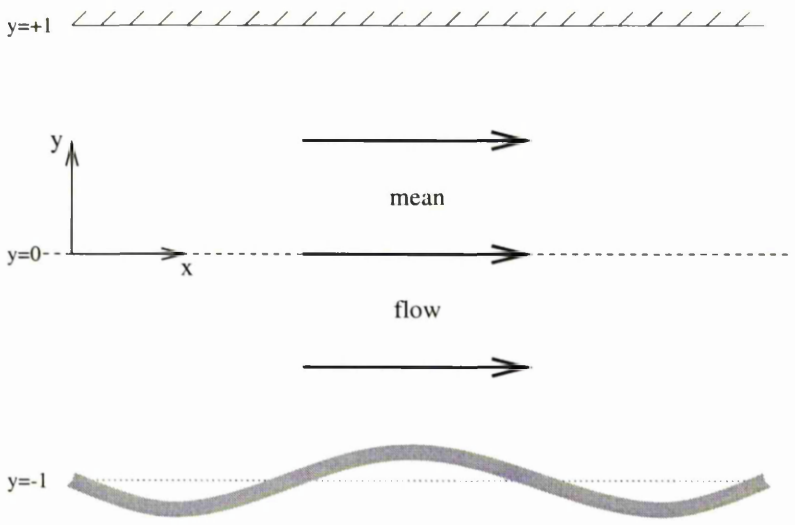

Figure 3.2: The asymmetric channel.

Following chapter 2, we shall consider the incompressible flow of a Newtonian fluid in such a geometry and so the flow is governed by the Navier-Stokes equations, thus:

$$\frac{\partial u_x}{\partial t} + u_x\frac{\partial u_x}{\partial x} + u_y\frac{\partial u_x}{\partial y} + u_z\frac{\partial u_x}{\partial z} = -\frac{\partial p}{\partial x} + \frac{1}{Re}\left(\frac{\partial^2 u_x}{\partial x^2} + \frac{\partial^2 u_x}{\partial y^2} + \frac{\partial^2 u_x}{\partial z^2}\right), \quad (3.1a)$$

$$\frac{\partial u_y}{\partial t} + u_x\frac{\partial u_y}{\partial x} + u_y\frac{\partial u_y}{\partial y} + u_z\frac{\partial u_y}{\partial z} = -\frac{\partial p}{\partial y} + \frac{1}{Re}\left(\frac{\partial^2 u_y}{\partial x^2} + \frac{\partial^2 u_y}{\partial y^2} + \frac{\partial^2 u_y}{\partial z^2}\right), \quad (3.1b)$$

$$\frac{\partial u_z}{\partial t} + u_x\frac{\partial u_z}{\partial x} + u_y\frac{\partial u_z}{\partial y} + u_z\frac{\partial u_z}{\partial z} = -\frac{\partial p}{\partial z} + \frac{1}{Re}\left(\frac{\partial^2 u_z}{\partial x^2} + \frac{\partial^2 u_z}{\partial y^2} + \frac{\partial^2 u_z}{\partial z^2}\right), \quad (3.1c)$$

where $Re = \rho UL/\mu$ is the Reynolds number of the flow and μ is the constant dynamic viscosity of the fluid.

In addition to the Navier-Stokes equations (3.1), the fluid must also obey the continuity equation

$$\frac{\partial u_x}{\partial x} + \frac{\partial u_y}{\partial y} + \frac{\partial u_z}{\partial z} = 0\,, \quad (3.2)$$

which ensures that mass is conserved in the flow.

3.2 Basic Flow

For a rigid channel, the boundary conditions for the Navier-Stokes equations (3.1) are

$$\boldsymbol{u} = (u_x, u_y, u_z) = \mathbf{0} \;\text{ at }\; y = \pm 1\,. \quad (3.3)$$

The x and z components correspond to no-slip at the wall and the y component corresponds to impermeability of the wall.

These conditions, along with the Navier-Stokes equations (3.1) and the continuity equation (3.2), permit a uni-directional solution for all Re. This is the well-known Plane-Poiseuille flow, where:

$$\boldsymbol{u_B} = (1 - y^2)\hat{\boldsymbol{x}}\,, \quad (3.4a)$$

$$p_B(x) = p_0 - \frac{2}{Re}x\,. \quad (3.4b)$$

Here, $\hat{\boldsymbol{x}}$ is a unit vector in the x direction and p_0 is an abitrary constant that corresponds to a background pressure. We can, without loss of generality, take p_0 to be zero.

In practice, this is the flow found for smaller values of the Reynolds number but it becomes unstable as Re is increased and eventually turbulence sets in. We can proceed to considering the effects of compliant walls on the stability of Plane-Poiseuille flow, by looking at small perturbations from the solution given by equations (3.4). This we do in the next section.

3.3 Linear Stability Analysis

Now we shall consider solutions which are small perturbations from Plane-Poiseuille flow (3.4). These may be written in the form $\boldsymbol{u} = \boldsymbol{u_B} + \boldsymbol{u'}$ and $p = p_B + p'$, where $|u'_x|$, $|u'_y|$, $|u'_z|$, $|p'| \ll 1$.

If we substitute this form of solution into the Navier-Stokes equations (3.1) and the continuity equation (3.2) and we ignore all terms of second order in u'_x, u'_y, u'_z or p', since they are much smaller than the remaining terms, then we obtain

$$\frac{\partial u'_x}{\partial t} + u_B \frac{\partial u'_x}{\partial x} + u'_y \frac{du_B}{dy} = -\frac{\partial p'}{\partial x} + \frac{1}{Re}\left(\frac{\partial^2 u'_x}{\partial x^2} + \frac{\partial^2 u'_x}{\partial y^2} + \frac{\partial^2 u'_x}{\partial z^2}\right), \tag{3.5a}$$

$$\frac{\partial u'_y}{\partial t} + u_B \frac{\partial u'_y}{\partial x} = -\frac{\partial p'}{\partial y} + \frac{1}{Re}\left(\frac{\partial^2 u'_y}{\partial x^2} + \frac{\partial^2 u'_y}{\partial y^2} + \frac{\partial^2 u'_y}{\partial z^2}\right), \tag{3.5b}$$

$$\frac{\partial u'_z}{\partial t} + u_B \frac{\partial u'_z}{\partial x} = -\frac{\partial p'}{\partial z} + \frac{1}{Re}\left(\frac{\partial^2 u'_z}{\partial x^2} + \frac{\partial^2 u'_z}{\partial y^2} + \frac{\partial^2 u'_z}{\partial z^2}\right), \tag{3.5c}$$

$$\frac{\partial u'_x}{\partial x} + \frac{\partial u'_y}{\partial y} + \frac{\partial u'_z}{\partial z} = 0, \tag{3.5d}$$

once we have subtracted the equations obeyed by the basic flow quantities (3.4).

By Fourier transforming equations (3.5), using the fact that the boundary conditions and u_B, Du_B are independent of x and t for rigid channel flow, it is possible to show that the solutions must be in the form of normal modes and

hence may be written as

$$(u'_x, u'_y, u'_z, p') = A(u(y), v(y), w(y), p(y))e^{i(\alpha(x-ct)+\beta z)}. \tag{3.6}$$

Here u, v, w and p are $O(1)$ complex amplitude functions and $A \ll 1$ is a real number indicating the small size of the disturbances. Also, α and β are positive real wavenumbers. The quantity $c = c_r + ic_i$ is the complex phase velocity which determines the stability of the solution: if the growth rate, $\omega = \alpha c_i > 0$ then the basic flow is unstable, i.e. the perturbations grow with time; if $\omega < 0$ then the basic flow is stable, i.e. the perturbations decay with time; if $\omega = 0$ then the basic flow is neutrally stable, i.e. the perturbations have a constant magnitude as the time increases.

The phase speed, c_r determines in which direction the disturbance propagates: if $c_r > 0$ then the wave travels downstream; if $c_r < 0$ then the wave travels upstream; if $c_r = 0$ then the wave is stationary.

Substituting this form of solution into the stability equations (3.5), or equivalently performing the necessary Fourier transformation, we obtain a set of equations for the unknowns u, v, w and p:

$$i\alpha Re(u_B - c)u + Re(Du_B)v = -i\alpha Re\, p + \left(D^2 - \gamma^2\right) u\,, \tag{3.7a}$$

$$i\alpha Re(u_B - c)v = -Re\, Dp + \left(D^2 - \gamma^2\right) v\,, \tag{3.7b}$$

$$i\alpha Re(u_B - c)w = -i\beta Re\, p + \left(D^2 - \gamma^2\right) w\,, \tag{3.7c}$$

$$i\alpha\, u + Dv + i\beta\, w = 0\,. \tag{3.7d}$$

Here, $D = d/dy$, $u_B = 1 - y^2$ is the scalar velocity component u_x of the basic flow (3.4) and $\gamma^2 = \alpha^2 + \beta^2$.

In a Cartesian co-ordinate system, we can find the velocity components of a two-dimensional disturbance in terms of a stream function, ψ, which is defined

by:

$$u'_x = \frac{\partial \psi}{\partial y},$$
$$u'_y = -\frac{\partial \psi}{\partial x},$$

whence u'_x and u'_y automatically obey the continuity equation (3.7d). Since u'_y has a normal mode decomposition, the stream function must also have a normal mode decomposition, which we may write as

$$\psi = A\phi(y)e^{i\alpha(x-ct)}.$$

3.3.1 Boundary Conditions

If we now recap and compare with chapter 2, we see that the formulation of the channel problem, so far, is a specific case of the kinematic approach given therein: we have found a set of axes in which $x = x_*$ is the co-ordinate in the direction of the basic flow, with axis parallel to the channel walls; the second, $y = y_*$, axis is perpendicular to the channel walls in their rest state, so that the equation of the lower wall is given by $y = -1$, i.e. $y_0 = -1$ here; similarly, the equation of the upper wall in its rest state is $y = 1$, i.e. $y_0 = 1$ here; also, we have chosen the final, $z = z_*$ axis to form a right-handed set of axes with the x and y axes; the fluid is assumed to be Newtonian and hence the governing equations are the Navier-Stokes equations which, combined with the zero wall velocity boundary conditions, give rise to a basic flow of the type given by equations (2.1), where $u_B(y) = 1 - y^2$; by considering small perturbations from the basic flow, it has been shown that such disturbances may be found in the form of normal modes given by equation (2.2) and also that the equations governing these normal modes are in the form given by equations (2.3), where $L_1(y, u) = (D^2 - \gamma^2)u$, $L_2(y, v, w) = (D^2 - \gamma^2)v$, $L_3(y, v, w) = (D^2 - \gamma^2)w$, $f_1(y) = -i\beta$ and $f_2(y) = i\beta$,

with $D = d/dy$; finally, we have formulated two-dimensional disturbances in terms of a stream function of the form given by equations (2.4), with $f_*(y) = 1$.

Therefore, we have formulated the channel problem in a way which is fully consistent with the kinematic approach described in chapter 2 and hence we may proceed to use the results therein without further justification. We must now use these results to formulate the boundary conditions for and hence close, the channel problem. This we must do for each of the various geometrical possibilities that may arise for the solution modes. There are three cases that we need to consider, which are:

1. Symmetric channel, symmetric modes:

   Here, both walls are compliant and the stream function is symmetric about the centreline of the channel and hence we have $\phi(-y) = \phi(y)$ or equivalently, $D\phi(0) = D^3\phi(0) = 0$.

   The pertubations of the wall from its rest state must take the form of normal modes. This follows from the kinematic condition requiring the normal velocity of the fluid at the fluid-solid interface to be equal to the normal wall velocity at the same point, as discussed in chapter 2. Therefore, the positions of the lower wall, y_{-1} and the upper wall, y_1 may be given as:

$$y_{-1} = -1 + Aa_{-1}e^{i(\alpha(x-ct)+\beta z)},$$
$$y_1 = 1 + Aa_1 e^{i(\alpha(x-ct)+\beta z)},$$

   where a_{-1} and a_1 are the complex amplitudes of the perturbations of the lower and upper walls, respectively. As before, A is the real number indicating the small nature of the perturbations.

   If the values of the stream-function amplitude at the lower and upper walls

are ϕ_{-1} and ϕ_1, respectively, then the anaylsis of chapter 2 shows that:

$$\phi_{-1} = a_{-1}c\,, \tag{3.8a}$$

$$\phi_1 = a_1 c\,. \tag{3.8b}$$

Since ϕ is symmetric, we know that $\phi_{-1} = \phi_1 = \phi_w$ and hence we find that $a_{-1} = a_1 = a$, say.

Hence from equation (2.11), we may immediately write down the boundary conditions for the normal velocity component as:

$$v(-1) = -i\alpha\phi_w\,, \tag{3.9a}$$

$$v(1) = -i\alpha\phi_w\,. \tag{3.9b}$$

The corresponding boundary conditions for the streamwise velocity component are:

$$u(-1) = -\frac{2\phi_w}{c}\,, \tag{3.10a}$$

$$u(1) = \frac{2\phi_w}{c}\,. \tag{3.10b}$$

The remaining boundary conditions, for the transverse velocity, are:

$$w(-1) = 0\,, \tag{3.11a}$$

$$w(1) = 0\,. \tag{3.11b}$$

Finally, a suitable normalisation condition for a symmetric function is to fix its value at zero and hence we shall choose to fix ϕ to be 1 at the centreline of the channel, which may be written alternatively as

$$v(0) = -i\alpha\,. \tag{3.12}$$

This completes the set of conditions required to produce independent eigensolutions of the channel problem.

Now we can choose to further utilise the symmetric nature of the modes under consideration in order to further simplify the problem and ease the numerical calculations. By replacing conditions (3.9b), (3.10b) and (3.11b), with the symmetry conditions

$$u(0) = 0\,, \tag{3.13a}$$

$$D^2u(0) = 0\,, \tag{3.13b}$$

$$w(0) = 0\,, \tag{3.13c}$$

we can halve the size of the domain and hence we can halve the number of points used in calculating the numerical results.

2. Symmetric channel, antisymmetric modes:

   Here, both walls are compliant and the stream function is antisymmetric about the centreline of the channel and hence we have $\phi(-y) = -\phi(y)$ or equivalently, $\phi(0) = D^2\phi(0) = 0$. Following the above case for the symmetric modes, the analysis of chapter 2 gives the equations for the positions of the lower wall, y_{-1} and the upper wall, y_1 as:

$$y_{-1} = -1 + Aa_{-1}e^{i(\alpha(x-ct)+\beta z)}\,,$$

$$y_1 = 1 + Aa_1e^{i(\alpha(x-ct)+\beta z)}\,.$$

   Here again, a_{-1} and a_1 are the complex amplitudes of the perturbations of the lower and upper walls, respectively. As before, A is the real number indicating the small nature of the perturbations.

   If the values of the stream-function amplitude at the lower and upper walls are ϕ_{-1} and ϕ_1, respectively, then the anaylsis of chapter 2 shows that:

$$\phi_{-1} = a_{-1}c\,, \tag{3.14a}$$

$$\phi_1 = a_1c\,. \tag{3.14b}$$

Since now, ϕ is antisymmetric, we know that $\phi_{-1} = -\phi_1 = \phi_w$ and hence we find that $a_{-1} = -a_1 = a$, say.

Hence again from equation (2.11), we may immediately write down the boundary conditions for the normal velocity component as:

$$v(-1) = -i\alpha\phi_w\,, \tag{3.15a}$$

$$v(1) = i\alpha\phi_w\,. \tag{3.15b}$$

The corresponding boundary conditions for the streamwise velocity component are:

$$u(-1) = -\frac{2\phi_w}{c}\,, \tag{3.16a}$$

$$u(1) = -\frac{2\phi_w}{c}\,. \tag{3.16b}$$

The remaining boundary conditions, for the transverse velocity, are again:

$$w(-1) = 0\,, \tag{3.17a}$$

$$w(1) = 0\,. \tag{3.17b}$$

Finally, a suitable normalisation condition for an antisymmetric function is to fix its derivative at zero and hence we shall choose to fix $D\phi$ to be 1 at the centreline of the channel, which may alternatively be written as:

$$u(0) = 1\,. \tag{3.18}$$

This completes the set of conditions required to produce independent eigensolutions of the channel problem.

As for the symmetric modes we can further utilise the antisymmetric nature of the modes under consideration in order to further simplify the problem and ease the numerical calculations. By replacing conditions (3.15b),

(3.16b) and (3.17b), with the antisymmetry conditions

$$v(0) = 0\,, \tag{3.19a}$$

$$D^2 v(0) = 0\,, \tag{3.19b}$$

$$w(0) = 0\,, \tag{3.19c}$$

we can halve the size of the domain and hence we can halve the number of points used in calculating the numerical results.

3. Asymmetric channel modes

Here, only one wall is compliant, which we shall take, without loss of generality, to be the lower wall. In this case there is no symmetry in the stream function for the disturbances. Following the above cases for the symmetric and antisymmetric modes, the results of chapter 2, allow us to write the equation of the lower wall, y_{-1}, as

$$y_{-1} = -1 + Aae^{i(\alpha(x-ct)+\beta z)}\,,$$

where a is the complex amplitude of the perturbations of the lower wall. As before, A is the real number indicating the small nature of the perturbations.

If the value of the stream-function amplitude at the lower wall is ϕ_w, then the anaylsis of chapter 2 shows that

$$\phi_w = ac\,. \tag{3.20}$$

Hence again from equation (2.11), we may immediately write down the boundary conditions for the normal velocity component as:

$$v(-1) = -i\alpha\phi_w\,, \tag{3.21a}$$

$$v(1) = 0\,. \tag{3.21b}$$

The corresponding boundary conditions for the streamwise velocity component are:

$$u(-1) = -\frac{2\phi_w}{c}\,, \tag{3.22a}$$

$$u(1) = 0\,. \tag{3.22b}$$

The remaining boundary conditions, for the transverse velocity, are:

$$w(-1) = 0\,, \tag{3.23a}$$

$$w(1) = 0\,. \tag{3.23b}$$

Finally, a suitable normalisation condition for an asymmetric function is to fix its value at zero and hence we shall choose to fix ϕ to be 1 at the centreline of the channel, which may alternatively be written as:

$$v(0) = -i\alpha\,, \tag{3.24}$$

which completes the set of conditions required to produce independent eigensolutions to the channel. In this case we cannot further simplify the problem since there is no symmetry of which to make use.

Now that we have found the boundary conditions for all the possible modes for the kinematic compliant channel problem, we could find solutions to the system of linearised stability equations (3.7), with the above conditions applied. This we could do by fixing α, β and Re and solving the resulting problem for the eigenvalue, c and the eigenfunctions, u, v, w and p. However, we can make a significant simplification by invoking the theorem due to Squire [72]. This states that for any plane parallel shearing flow in which there exists a three-dimensional instability, that there exists a two-dimensional instability which occurs at a lower Reynolds number. Therefore, to determine the overall stability of the flow, we need only consider two-dimensional disturbances.

3.3.2 Squire's Theorem

Squire's theorem applied originally to flows with rigid boundaries and it is not obvious that it can be extended to a basic flow of a plane parallel shearing type, bounded by compliant walls. However, Rotenberry and Saffman [64] showed that such an extension could be made for the coupled fluid/simple-stretched-membrane system, provided that the governing equation for the membrane was non-dimensionalised in a certain, given way. We shall use the Squire transformation, also given by Lin [53], in order to show that the extension can be made for the kinematic formulation, too.

Suppose we have an unstable three-dimensional disturbance with velocity components, $\tilde{u}$, $\tilde{v}$, $\tilde{w}$ and pressure, $\tilde{p}$ which occurs at a Reynolds number $\tilde{R}e$, with wavenumbers, $\alpha = \tilde{\alpha} \neq 0$ and $\beta = \tilde{\beta} \neq 0$ and phase velocity, $\tilde{c}$. This disturbance must obey the linearised stability equations (3.7), plus the relevant set of boundary conditions from subsection 3.3.1, which may be re-written as

$$\tilde{u} = \frac{-(Du_B)_{\pm 1}(\tilde{\phi}_w)_{\pm 1}}{\tilde{c}}, \quad \tilde{v} = -i\tilde{\alpha}(\tilde{\phi}_w)_{\pm 1}, \quad \tilde{w} = 0\,, \tag{3.25}$$

at $y = \pm 1$, respectively. If the channel is asymmetric then $(\tilde{\phi}_w)_1 = 0$ at the rigid wall, $y = 1$. As stated in section 3.3.1, suitable normalisation conditions are that the eigenfunctions obey are $\tilde{v} = -i\tilde{\alpha}$ at $y = 0$ for symmetric or asymmetric modes and $\tilde{u} = 1$ at $y = 0$ for antisymmetric modes.

Now following Lin [53], we shall construct a two-dimensional disturbance which occurs at a lower Reynolds number by introducing the quantities

$$\hat{u} = \tilde{u} + \frac{\tilde{\beta}}{\tilde{\alpha}}\tilde{w}, \quad \hat{v} = \frac{\tilde{\gamma}}{\tilde{\alpha}}\tilde{v}, \quad \hat{w} = 0, \quad \hat{p} = \frac{\tilde{\gamma}^2}{\tilde{\alpha}^2}\tilde{p}\,,$$

where, $\tilde{\gamma}^2 = \tilde{\alpha}^2 + \tilde{\beta}^2$.

By adding equation (3.7a) to $\tilde{\beta}/\tilde{\alpha}$ times equation (3.7c) we obtain an equation involving only $\hat{u}$, $\hat{v}$ and $\hat{p}$. Equation (3.7b) can immediately be rewritten in terms

of $\hat{v}$ and $\hat{p}$ and similarly, equation (3.7d) can be rewritten in terms of $\hat{u}$ and $\hat{v}$. Hence, we obtain the set of equations:

$$i\tilde{\gamma}(u_B - \tilde{c})\hat{u} + (Du_B)\hat{v} = -i\tilde{\gamma}\hat{p} + \frac{1}{\hat{Re}}\left(D^2 - \tilde{\gamma}^2\right)\hat{u}\,, \tag{3.26a}$$

$$i\tilde{\gamma}(u_B - \tilde{c})\hat{v} = -D\hat{p} + \frac{1}{\hat{Re}}\left(D^2 - \tilde{\gamma}^2\right)\hat{v}\,, \tag{3.26b}$$

$$i\tilde{\gamma}\hat{u} + D\hat{v} = 0\,, \tag{3.26c}$$

where $\hat{Re} = \tilde{\alpha}\tilde{Re}/\tilde{\gamma}$. The boundary conditions (3.25) then imply that:

$$\tilde{u} = \frac{-(Du_B)_{\pm 1}(\tilde{\phi}_w)_{\pm 1}}{\tilde{c}}, \quad \tilde{v} = -i\tilde{\gamma}(\tilde{\phi}_w)_{\pm 1}, \quad \tilde{w} = 0\,, \tag{3.27}$$

at $y = \pm 1$, respectively.

If we now consider a disturbance with wavenumbers, $\alpha = \tilde{\gamma}$ and $\beta = 0$, phase velocity, $c = \tilde{c}$ and complex amplitude functions, $\hat{u}$, $\hat{v}$, $\hat{w} = 0$ and $\hat{p}$, for a flow with Reynolds number, $\hat{Re}$, i.e.

$$(u'_x, u'_y, u'_z, p') = A(\hat{u}(y), \hat{v}(y), 0, \hat{p}(y))e^{i(\tilde{\gamma}(x - \tilde{c}t))}\,,$$

then we see that this must obey equations (3.26), along with the boundary conditions (3.27). The normalisation conditions, $\tilde{v} = -i\tilde{\alpha}$ at $y = 0$ for symmetric or asymmetric modes and $\tilde{u} = 1$ at $y = 0$ for antisymmetric modes, are consistent since, from equation (3.19c), $w(0) = 0$ on the channel centreline and hence $\hat{u} = \tilde{u} = 1$ here.

It is easy to verify that the dynamic condition equating fluid and solid admittances , $Y = Y_0$, at a compliant wall, is also consistent, provided that the damping coefficient is non-dimensionalised such that $\bar{d} = d_0/Re$, where d_0 is independent of the Reynolds number. This assumes that c_0^2 is a constant. However, it is not the case for plates, where $c_0^2 \propto \alpha^{-2}$ for low wave numbers. A simple extension using the scalings employed by Rotenberry and Saffman [64] can be made in order to incorporate this type of wall.

Since the phase velocity is the same for both disturbances, we have constructed an unstable two-dimensional solution to the kinematic linearised stability equations. Also, since $\tilde{\alpha} < \tilde{\gamma}$, this instability occurs at a Reynolds number, $\hat{Re} = \tilde{\alpha}\tilde{Re}/\tilde{\gamma}$, which is strictly less than the Reynolds number at which the three-dimensional disturbance occurs. Hence, for any unstable three-dimensional disturbance in the compliant channel, we can find an unstable two-dimensional disturbance at a lower Reynolds number. Therefore we can limit ourselves to looking at two-dimensional disturbances in order to determine the overall stability of compliant channel flow.

3.4 Application Of Numerical Methods

Now we shall use the ideas of section 2.2 to formulate the problem of finding two-dimensional numerical solutions to the linearised stability equations (3.7) with the relevant boundary and normalisation conditions from section 3.3.1.

3.4.1 The Tchebychev Collocation Method

Given that the compliant channel problem is defined on the interval $[-1, 1]$, it is ideally suited to solution by the Tchebychev collocation method which, as stated in chapter 2, is valid over the same domain.

Since we need only look for two-dimensional disturbances, the numerical solutions, must be of the form:

$$u_j = \sum_{k=0}^{N} \tilde{u_k} T_k(y_j)\,, \quad v_j = \sum_{k=0}^{N} \tilde{v_k} T_k(y_j)\,, \quad p_{j+1/2} = \sum_{k=0}^{N} \tilde{p_k} T_k(y_{j+1/2})\,.$$

Here, the y_j are the Tchebychev-Gauss-Lobatto points defined by (2.14), T_k is the k-th Tchebychev polynomial of the first kind, $u_j = u(y_j)$, $v_j = v(y_j)$, for $j = 0, \ldots, N$ and $p_{j+1/2} = p(y_{j+1/2})$, for $j = 0, \ldots, N-1$.

Not only do we gain from the simple nature of the Tchebychev polynomials for the Tchebychev-Gauss-Lobatto points but also the spacing is such that these points are concentrated near the extremes of the interval, $[-1, 1]$. This is advantageous for the problem of compliant channel flow as large variations in the eigenfunctions often occur near the walls, as shown by the asymptotic analyses of Carpenter and Gajjar [10], Gajjar and Sibanda [22] and Kumaran [48]. Hence a concentration of points near the walls enables the detail of the eigenfunctions to be obtained with a lower total number of points than for a uniform discretisation.

Now, we can formulate the numerical problem by expressing the linearised stability equations (3.7) as

$$[i\alpha Re(u_B(y_j) - c) + \alpha^2]u_j - (D_N^2)_{jk}u_k + ReDu_B(y_j)v_j + i\alpha Re(C^{-1})_{jk}(C^{\frac{1}{2}})_{kl}p_l = 0\,, \tag{3.28a}$$

$$[i\alpha Re(u_B(y_j) - c) + \alpha^2]v_j - (D_N^2)_{jk}v_k + Re(D_N)_{jk}(C^{-1})_{kl}(C^{\frac{1}{2}})_{lm}p_m = 0\,, \tag{3.28b}$$

where there is no summation over j and the matrices, C^{-1}, $C^{1/2}$ and D_N, are as defined in section 2.2.1. It is necessary to calculate the pressure at each collocation point, y_j, from the values at the half-points, $y_{j+1/2}$. It is for this reason that the matrix, $C^{1/2}$, converting from the values of p at the half points to Tchebychev space and the matrix, C^{-1}, calculating the values of p at the collocation points from the Tchebychev coefficients, occur in equations (3.28).

The above equations (3.28) are both calculated for $j = 1, \ldots, N-1$, giving $2N - 2$ of the $3N + 2$ equations required to find the eigenfunctions, u_j, v_j and $p_{j+1/2}$.

The continuity equation is applied at the half-points, $y_{j+1/2}$ for $j = 0, \ldots,$ N-1,

as mentioned in section 2.2.1 and hence may be written in the form

$$i\alpha(C^{\frac{1}{2}})^{-1}_{jk}C_{kl}u_l + (C^{\frac{1}{2}})^{-1}_{jk}C_{kl}(D_N)_{lm}v_m = 0\,. \tag{3.29}$$

The remaining four required equations are obtained from the boundary and normalisation conditions and must be considered for the three cases:

1. Symmetric channel, symmetric modes.

   Here we can use the symmetry conditions (3.13) to reduce the calculation domain to $[-1, 0]$. We do this by introducing the new co-ordinate, $y' = 2y + 1$, which maps the interval $[-1, 0]$, representing the lower half-channel, to the interval $[-1, 1]$, which is required to use the transformation matrices, C and $C^{1/2}$. Then we evaluate each of the numerical stability equations (3.28) and (3.29) at the points y'_j, where $y'_0 = 1$ corresponds to $y_0 = 0$ and $y'_N = -1$ corresponds to $y_N = -1$.

   With this transformation of co-ordinate, the derivative operator, D_N, is modified to $D'_N = D_N/2$, where differentiation is now with respect to y'.

   Hence, now the boundary and normalisation conditions can be applied at the lower wall and the centreline of the channel only. Thus,

$$u_0 = 0\,, \tag{3.30a}$$

$$(D'^2_N)_{0k}u_k = 0\,, \tag{3.30b}$$

$$v_N = -i\alpha\phi_w\,, \tag{3.30c}$$

$$v_0 = -i\alpha\,, \tag{3.30d}$$

   where, as in chapter 2, the streamwise velocity condition, $u_N = 2\phi_w/c$, is relaxed here and used later to find the eigenvalue, c.

2. Symmetric channel, antisymmetric modes.

   Here also, we can use symmetry conditions, in this case conditions (3.19),

to reduce the calculation domain to $[-1, 0]$ using the change of co-ordinate, $y' = 2y + 1$. Again, with this transformation of co-ordinate, the derivative operator, D_N, is modified to $D'_N = D_N/2$, where differentiation is now with respect to y'.

Hence, now the boundary and normalisation conditions can be applied at the lower wall and the centreline of the channel only. Thus

$$v_0 = 0\,, \tag{3.31a}$$

$$(D'^2_N)_{0k} v_k = 0\,, \tag{3.31b}$$

$$v_N = -i\alpha\phi_w\,, \tag{3.31c}$$

$$u_0 = 1\,, \tag{3.31d}$$

where again the streamwise velocity condition, $u_N = 2\phi_w/c$, is relaxed here and used later to find the eigenvalue, c.

3. Asymmetric channel modes.

   In this case there are no symmetry conditions of which we can make use in order to simplify the numerical calculations. Therefore, we have to use the full set of normalisation and boundary conditions, which are

$$u_0 = 0\,, \tag{3.32a}$$

$$v_0 = 0\,, \tag{3.32b}$$

$$v_N = -i\alpha\phi_w\,, \tag{3.32c}$$

$$v_{N/2} = -i\alpha\,, \tag{3.32d}$$

   where N must be even for the normalisation condition (3.32d) to be applied at the channel centreline, $y = y_{N/2} = 0$. Again the streamwise velocity condition, $u_N = 2\phi_w/c$, is relaxed here and used later to find the eigenvalue, c. For later simplicity of notation we shall also introduce primed variables here, where $y' = y$ and hence $D'_N = D_N$.

Hence, for all three types of channel mode, we have now found the $3N+2$ conditions required to calculate the numerical solutions, u_j, v_j for $j = 0, \ldots, N$ and $p_{j+1/2}$ for $j = 0, \ldots, N-1$. These may be re-written in the form:

$$\begin{aligned} X1\boldsymbol{u} + Y1\boldsymbol{v} + W1\boldsymbol{p} &= \boldsymbol{r1}, \\ Y2\boldsymbol{v} + W2\boldsymbol{p} &= \boldsymbol{r2}, \\ X4\boldsymbol{u} + Y4\boldsymbol{v} &= \boldsymbol{r4}, \end{aligned}$$

where the solutions have now been written as vectors, $\boldsymbol{u}$, $\boldsymbol{v}$ and $\boldsymbol{p}$ with the jth element corresponding to the value of the functions, u, v, at y'_j and p at $y'_{j+1/2}$, respectively. Rows 1 to $N-1$ of matrices $X1$, $Y1$ and $W1$ are obtained from equation (3.28a), rows 1 to $N-1$ of matrices $Y2$ and $W2$ are obtained from equation (3.28b) and all rows (0 to $N-1$) of matrices $X4$ and $Y4$ are obtained from equation (3.29). The elements of the rows 0 and N of matrices, $W1$ and $W2$, are all zero and the elements of the same rows of matrices, $X1$, $Y1$ and $Y2$, are determined by the relevant set of conditions (3.30), (3.32) or (3.32). Thus, all the elements of the right-hand-side vectors, $\boldsymbol{r1}$, $\boldsymbol{r2}$ and $\boldsymbol{r4}$, are zero except those which correspond to normalisation conditions or the compliant condition, $v_N = -i\alpha\phi_w$.

Therefore, we may re-write the stability equations for calculating numerical solutions in the form given by equation (2.16), i.e.

$$L\boldsymbol{\phi} = \boldsymbol{r}\,,$$

where here

$$L = \begin{pmatrix} X1 & Y1 & W1 \\ 0 & Y2 & W2 \\ X4 & Y4 & 0 \end{pmatrix}, \boldsymbol{\phi} = \begin{pmatrix} \boldsymbol{u} \\ \boldsymbol{v} \\ \boldsymbol{p} \end{pmatrix}, \boldsymbol{r} = \begin{pmatrix} \boldsymbol{r1} \\ \boldsymbol{r2} \\ \boldsymbol{r4} \end{pmatrix},$$

since we need only consider two-dimensional disturbances.

3.4.2 The Newton-Raphson Iterative Method

As mentioned in chapter 2, unless c is an eigenvalue of the problem, the relaxed boundary condition for the streamwise velocity at the compliant wall, will not be obeyed. Now since the numerical problem has been formulated in such a way that the calculations, for all mode types, only have one set of compliant wall conditions, namely those at $y = -1$, this is equivalent to

$$\chi(c) = c\, u(-1) - \frac{2}{i\alpha} v(-1) \neq 0\,.$$

Following section 2.2.2, if c is sufficiently close to the eigenvalue, then we can use a Newton-Raphson method to find successively closer approximations to the eigenvalue. So we want to find Δc such that $\chi(c + \Delta c) = 0$ and therefore to leading order in Δc

$$\Delta c = -\frac{\chi}{\frac{\partial \chi}{\partial c}}\,,$$

where

$$\frac{\partial \chi}{\partial c} = u(-1) + c\frac{\partial u}{\partial c}(-1) - \frac{2}{i\alpha}\frac{\partial v}{\partial c}(-1)\,.$$

The values of $\partial u/\partial c|_{y=-1}$ and $\partial v/\partial c|_{y=-1}$ are found using equation (2.18), where the elements of $\partial L/\partial c$ are calculated from equations (3.28). The relevant elements of $\partial \boldsymbol{\phi}/\partial c$ are then $(\partial u/\partial c)_N$ and $(\partial v/\partial c)_N$.

By iteratively using this whole procedure, we should find successively more accurate approximations to the phase velocity eigenvalue, c and the associated numerical eigenfunction vector, $\boldsymbol{\phi}$. When the size of the adjustment to the phase velocity, $|\Delta c|$ is smaller than a tolerance of $10^{-6}|c|$, the solution is assumed to be suitably accurate.

Finally in this section, the number of points, N, was chosen so that no change in the profiles of the eigenfunctions was observed if it were increased. Taking $N = 49$ for the modes in the symmetric channel and $N = 100$ for the asymmetric channel modes usually sufficed.

3.5 Numerical Results

We have been able to identify four distinct classes of mode and a further class of transitional modes, in which two or more of the modes of the distinct classes coalesce. The four identified distinct mode classes appear to be the same as those identified by Sen and Arora [67] as the Tollmien-Schlichting (TS) class, the Kelvin-Helmholtz (KH) class, the low speed stable (LSS) class and the Resonant (R) class.

The low-speed stable modes are obviously of least interest when considering the stabilisation and control of the flow as a whole and so we shall start this section with a description of each of the four remaining, potentially unstable mode classes.

3.5.1 Tollmien-Schlichting (TS) Modes

The Tollmien-Schlichting class of modes are modes of the same type that exist for the rigid-walled channel and other parallel flows past rigid walls [74], [75], [66]. These modes are induced by the viscosity of the fluid and exist in the limit as $a \to 0$. The relevant condition from (3.8a), (3.14a) or (3.20) then implies that $\phi_w \to 0$. In this limit $c \to c^*$, the eigenvalue for the rigid-walled channel.

For non-zero but small values of a and ϕ_w, i.e. for $|a|, |\phi_w| \ll 1$, the phase velocity eigenvalue then takes the form $c = c^* + \delta c$, where $|\delta c| \ll |c^*|$.

Symmetric Channel, Symmetric Modes

A typical symmetric TS mode for the symmetric channel can be found for a Reynolds number, $Re = 8000.0$ and a wave number, $\alpha = 1.0$. Here, the least-stable, rigid TS mode has a phase velocity, $c = 0.24708 + 0.00267i$. Hence, this mode grows slowly with time and the overall flow is linearly unstable. The effect that compliance has on this mode, i.e. the effects of introducing non-zero ϕ_w,

can be seen in figures 3.3(a) and 3.3(b). These plot the phase speed, c_r and the growth-rate, $\omega = \alpha c_i$, against θ_w, respectively, for various values of $|\phi_w|$. Here, $\phi_w = |\phi_w| \exp(i\theta_w)$ is the decomposition introduced in chapter 2.

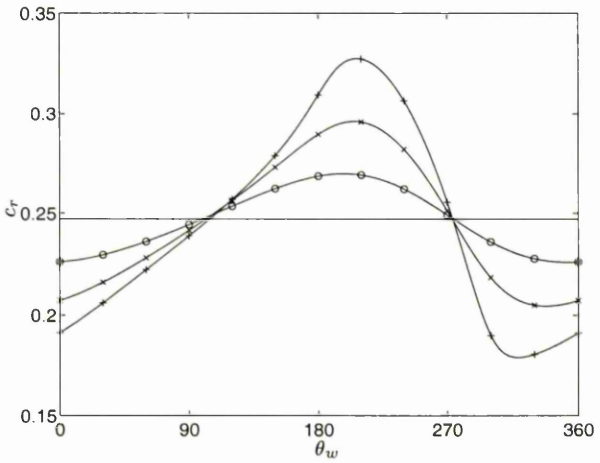

(a) Phase Speed

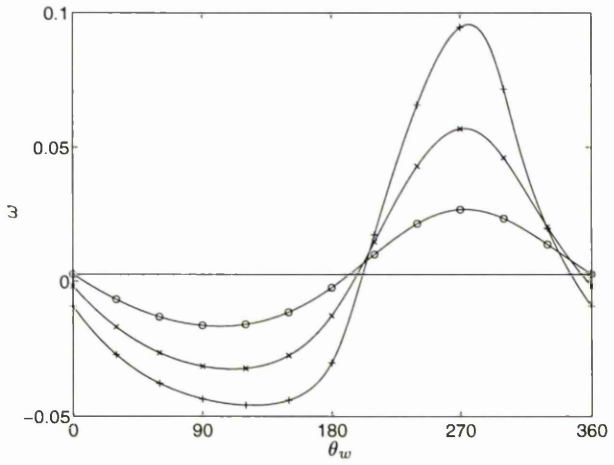

(b) Growth Rate

Figure 3.3: Symmetric TS modes for the symmetric channel.
—, $|\phi_w| = 0$; -o-, $|\phi_w| = 0.1$; -×-, $|\phi_w| = 0.2$; -+-, $|\phi_w| = 0.3$.

For non-zero values of $|\phi_w|$, the phase velocity oscillates about the rigid value

when θ_w is varied from 0 to 360°. The profiles of the graphs for both c_r and ω are very similar in shape to those obtained by Sen and Arora [67] for TS modes in boundary-layer flow.

From figure 3.3(b) it can be seen that for values of θ_w in the approximate range 180° to 360°, the effect of the compliance is to destablise the rigid mode and hence the flow remains unstable. However, for the remaining values of θ_w, the effect of compliance is beneficial with regard to flow stabilisation. Above a certain critical value of $|\phi_w|$, a range of values of θ_w give rise to negative values of the growth rate, ω. As $|\phi_w|$ is increased further, the stable region continues to grow until the point where the TS mode coalesces with a mode from the KH class to form a mode of the transitional class, as can be seen in section 3.5.3. Hence, by using wall parameters which to correspond to such values of ϕ_w, where the growth rate, ω, is negative, we may stabilise the given rigid TS mode, according to the linear stability theory.

This leads us to the question of the physical realisability of the modes in the above examples. As stated in chapter 2 we shall consider the physical realisability of the kinematic modes by wall which can be modelled by the simple stretched membrane. Then, we can follow one of the approaches employed by Sen and Arora [67] in which a physically realisable value of the mass per unit area area of the wall, m, is chosen and then the quantities, d and c_0^2, are back-calculated. This we can do for the case $|\phi_w| = 0.2$, with $m = 2.0$, the results of which are given in figure 3.4. Now, for passive walls we have the conditions, $d, c_0^2 > 0$, which then require that θ_w lies in the region between 180° and 270°, approximately. In this physically realisable region, ω is mainly positive but there is a small range of values of θ_w close to 180° for which ω is negative. This is the channel equivalent of the "stable pocket" found by Sen and Arora [67] for the TS modes in boundary-layer flow. By using wall parameters corresponding to values of ϕ_w in the stable

pocket, the mode under consideration may be stabilised using a simple stretched membrane.

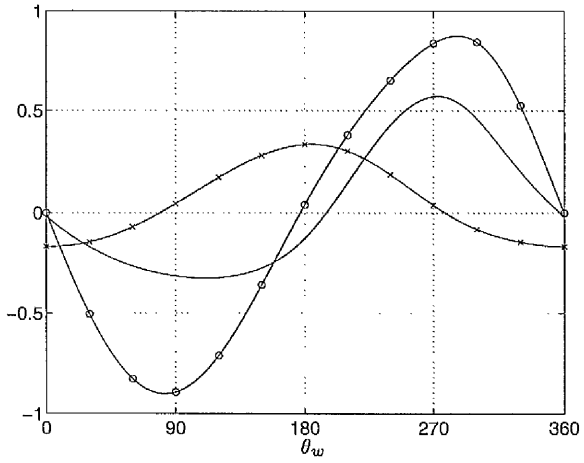

Figure 3.4: Physical realisability for $m = 2.0$.
—, $10 \times \omega$; -o-, d; -×-, c_0^2.

For values of m smaller than 2, the wall parameters, d and c_0^2, vary like $1/m$ for each θ_w, as might be expected from equations 2.21. Hence, there is little qualitative change in the profiles of d and c_0^2. This includes little change in the size and position of the "stable pocket". However, as m is increased beyond 2, c_0^2 increases for each value of θ_w and hence the region of physically realisable modes grows in size. Unfortunately, for smaller increases in m, this growth in the size of the physically realisable region occurs initially where the growth rate is positive. Therefore, it is not particularly useful with respect to flow stabilisation.

For $m \gtrsim 10$ (see figure 3.5(a)), c_0^2 is positive for all θ_w and hence physical realisability depends only on the sign of d. At $m \approx 10$, another small "stable pocket" appears near $\theta_w = 0°$. As m is increased beyond 10, the profiles of d and c_0^2 undergo a significant qualitative transformation, given in figures 3.5(b) and 3.5(c), such that for sufficiently dense walls, the vast majority of physically realisable modes are stable, with only two small "unstable pockets", as illustrated

by figure 3.5(d). This is not unexpected since equations 2.21 imply that $d \to -2\omega$ and $c_0^2 \to c_r^2 + c_i^2$ as $m \to \infty$.

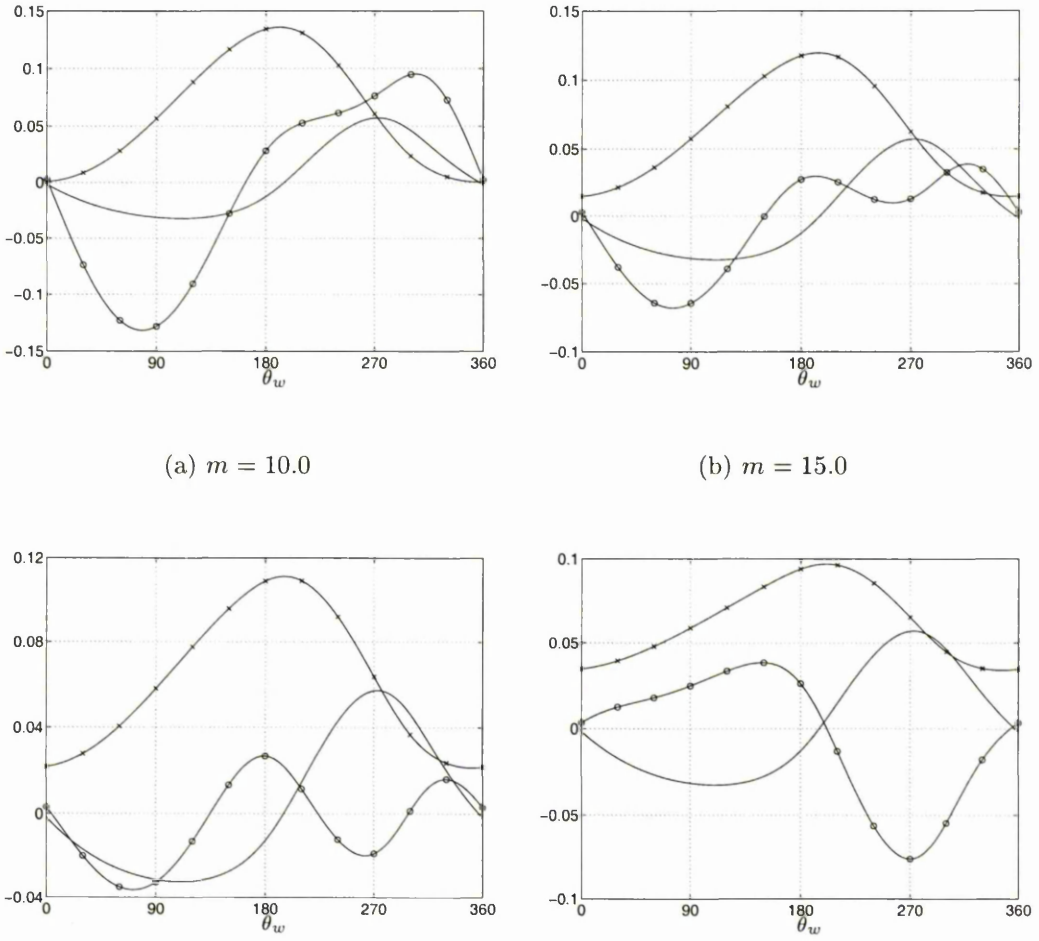

(a) $m = 10.0$ (b) $m = 15.0$

(c) $m = 25.0$ (d) $m = 50.0$

Figure 3.5: The effect of varying m on physical realisability.

—, ω; -o-, d; -×-, c_0^2.

Hence, we can conclude that an increase in the mass per unit area of the wall, m, of about one or two orders of magnitude, should greatly increase the range of the remaining wall parameters which will stabilise the TS mode. This is consistent with previous studies, for example Carpenter and Garrad [11], which

have shown that an increase in the mass per unit area of Kramer-type walls (of which the simple stretched membrane is a specific case) is generally stabilising towards symmetric TS modes. Manufacturing walls of this considerably greater density may be no trivial matter, however but is beyond the scope of this thesis.

In chapter 2, we showed that the physical realisability conditions lead to bounds on the quantities, m, d and c_0^2, for which a particular unstable mode can occur. These bounds allow us to confirm the above result, as follows.

If we plot the bounds against θ_w for the above mode where $|\phi_w| = 0.2$, as in figure 3.6, then we see that the physically realisable unstable region is divided into two parts. For lower values of θ_w, the bounds correspond to those for case 1

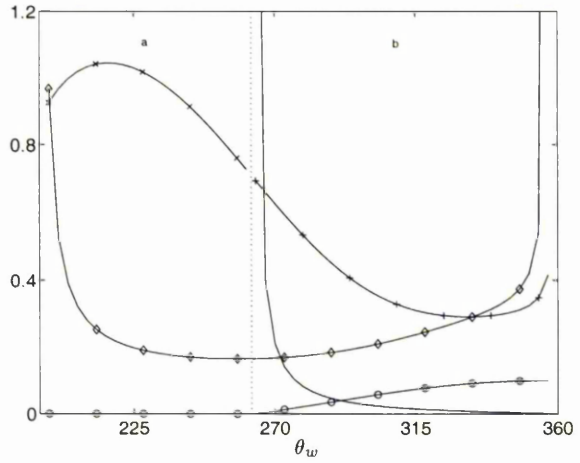

Figure 3.6: Physical realisability bounds on m, d and c_0^2.
—, $10^{-1} \times d$ lower bound;
-o-, $10^{-2} \times m$ lower bound; -◇-, $10^{-2} \times m$ upper bound;
-×-, $10^2 \times c_0^2$ lower bound; -+-, $10^2 \times c_0^2$ upper bound.

in section 2.3.2, whereas for higher values of θ_w, the bounds correspond to those for case 2. We see also that the upper bound for m only exceeds 40 in two small regions where θ_w lies between 198° and 204° or between 351° and 357°, approximately. However, in the first of these two regions the lower bound for c_0^2 is never below 0.092 and in the second region the upper bound never exceeds 0.042. Therefore, if we were to choose any combination of wall parameters where

$m > 40$ and $0.042 < c_0^2 < 0.092$, which correspond to a wall stream function with $|\phi_w| = 0.2$ (e.g. take $m = 50$ with the values of d and c_0^2 at $\theta_w = 90°$, namely 0.0246 and 0.0588 respectively), then we eliminate the possibility of an unstable TS mode. This is consistent with figure 3.5(d), since the two "unstable pockets"

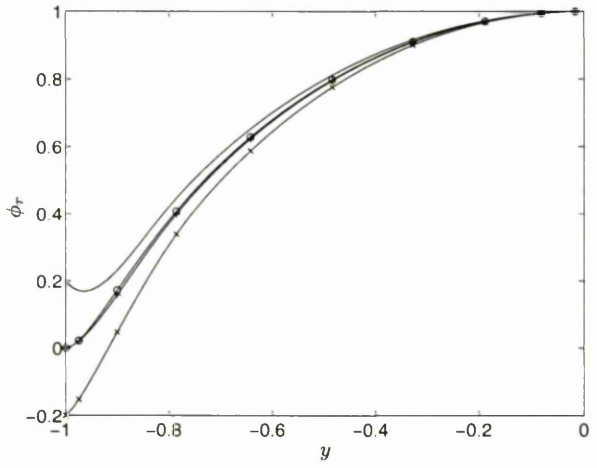

(a) Real Part

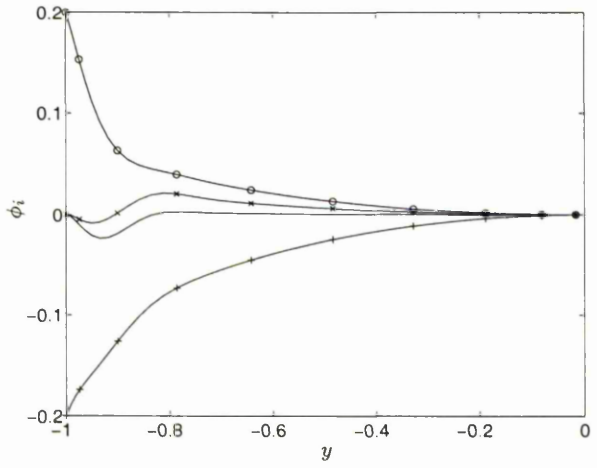

(b) Imaginary Part

Figure 3.7: Eigenfunctions for the symmetric TS modes.
—, $\theta_w = 0°$; -○-, $\theta_w = 90°$; -×-, $\theta_w = 180°$; -+-, $\theta_w = 270°$.

occur close to the extrema for c_0^2. The required variations in the wall parameters

may be achieved by using different membrane materials to vary the wall density, changing the tension applied to the membrane in order to vary the free-wave speed, c_0 and using different substrate fluids in order to vary the damping.

Sample eigenfunctions are given in terms of the stream function, ϕ, in figure 3.7. Again there are similarities when compared with boundary-layer flow. However, the similarities between the eigenfunctions are confined to the region close to the compliant wall, where the velocity disturbances and their gradients are greatest, since there is a significant difference in the domains and hence where the boundary conditions are applied.

Symmetric Channel, Antisymmetric Modes

The phase speed and growth rate of typical antisymmetric TS modes for the symmetric channel are given in figures 3.8. The same values of the parameters, Re, α and $|\phi_w|$ were used as for the symmetric TS modes in figure 3.3. The

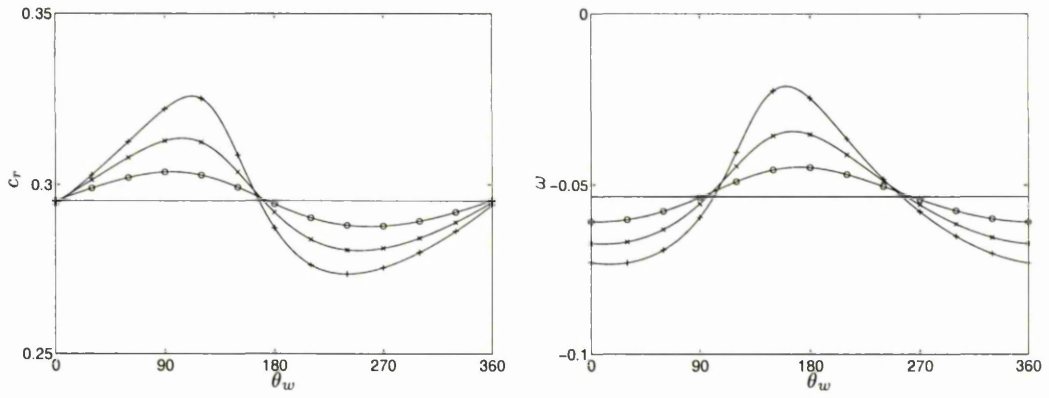

(a) Phase Speed (b) Growth Rate

Figure 3.8: Antisymmetric TS modes for the symmetric channel.
—, $|\phi_w| = 0$; -o-, $|\phi_w| = 0.1$; -×-, $|\phi_w| = 0.2$; -+-, $|\phi_w| = 0.3$.

value of the phase velocity for the least stable antisymmetric rigid TS mode is $0.29521 - 0.00535i$. As for the symmetric modes, the phase velocity oscillates

about the rigid value for non-zero $|\phi_w|$, as θ_w is varied.

Figures 3.3(b) and 3.8(b) suggest the possible existence of antisymmetric modes which may be less stable than their symmetric counterparts (see, for example, the regions about $\theta_w = 180°$ for $|\phi_w| = 0.2, 0.3$). However, back calculating d and c_0^2 for fixed m shows that these modes correspond to different wall parameters. This is illustrated by figure 3.9 where, $|\phi_w| = 0.2$ and $m = 2.0$.

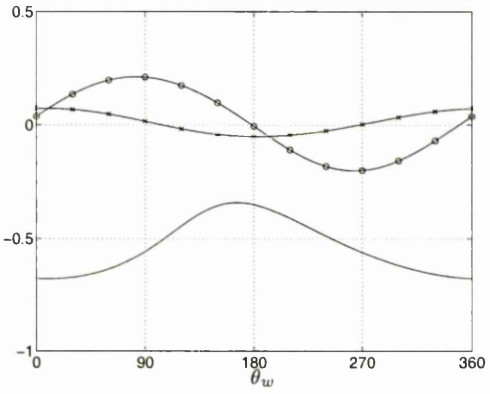

Figure 3.9: Physical realisability for $m = 2.0$.
—, $10 \times \omega$; -o-, $10^{-1} \times d$; -×-, $10^{-1} \times c_0^2$.

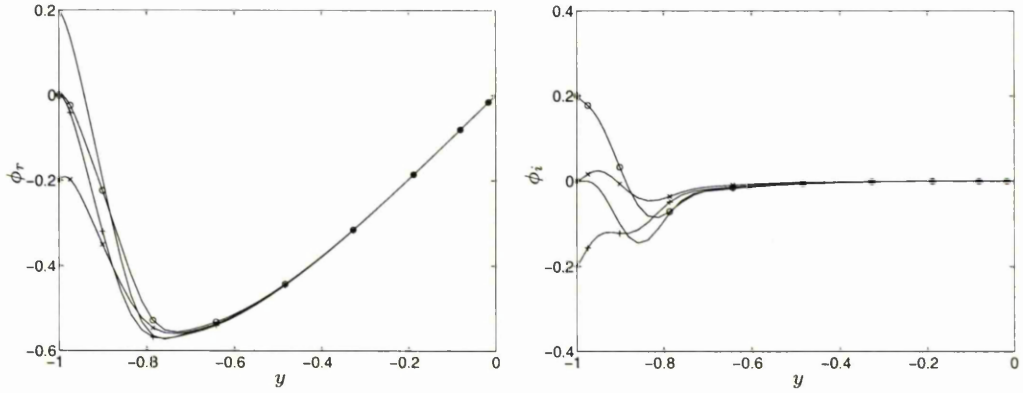

(a) Real Part (b) Imaginary Part

Figure 3.10: Eigenfunctions for the antisymmetric TS modes.
—, $\theta_w = 0°$; -o-, $\theta_w = 90°$; -×-, $\theta_w = 180°$; -+-, $\theta_w = 270°$.

Since we can stabilise a given unstable symmetric TS mode so that its growth rate is greater than the least stable antisymmetric mode, we can afford to ignore the antisymmetric TS modes when considering the overall stablilisation of the flow. This approach has been taken in most previous studies of compliant channel flow, e.g. Davies and Carpenter [15].

For completeness, a sample of the eigenfunctions for the antisymmetric modes is given in figure 3.10, where again the greatest velocity disturbances are found near the walls, where the shear in the mean flow is greatest.

Asymmetric Channel Modes

The most remarkable aspect of the asymmetric TS modes is that the phase velocities seem to be directly related to those for the symmetric modes in the symmetric channel. If the phase velocity of a symmetric TS mode is c_{sym} for a set of

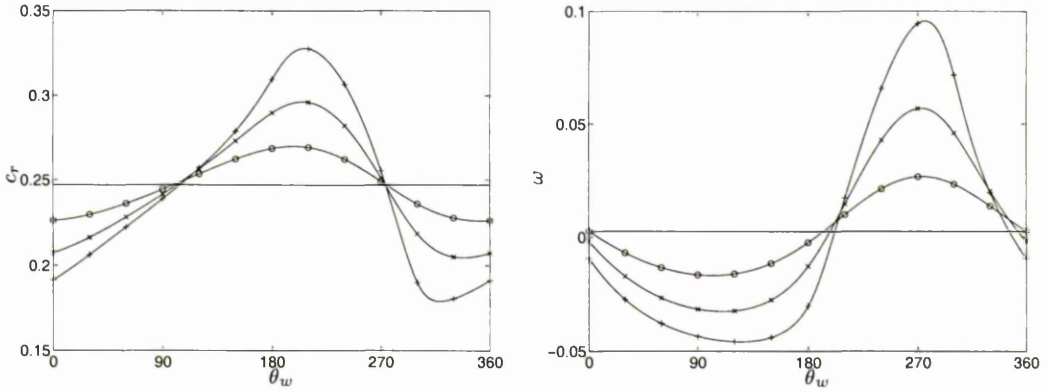

(a) Phase Speed

(b) Growth Rate

Figure 3.11: Asymmetric TS channel modes.
—, $|\phi_w| = 0$; -o-, $|\phi_w| = 0.2$; -×-, $|\phi_w| = 0.4$; -+-, $|\phi_w| = 0.6$.

kinematic parameters Re_{sym}, α_{sym} and $\phi_w = (\phi_w)_{\text{sym}}$, then it appears that there exists an asymmetric TS mode with phase velocity c_{sym} for the set of kinematic

parameters Re_{sym}, α_{sym} and $\phi_w = (\phi_w)_{\text{asym}} = 2(\phi_w)_{\text{sym}}$. Moreover, this hypothesis appears to be true for modes of all classes, as shown in later subsections and is consistent with all of the analytical results given in section 3.6. However, we have been unable to find an explicit form for the connection between the eigenfunctions of the symmetric and asymmetric modes. Hence, this is one potential area for further work. Figure 3.11 illustrates this property of the asymmetric TS modes when it is compared to figure 3.3.

Though there may be a direct link between the phase velocities of the symmetric TS modes in the symmetric channel and the asymmetric channel modes, the eigenfunctions are different, in particular the pressure disturbance. Hence, the wall parameters giving rise to the same phase velocity will be different for the two geomterical cases. This is shown in figure 3.12, where the wall parameters, d and c_0^2, are back-calculated for $m = 2$ and $|\phi_w| = 0.4$, respectively.

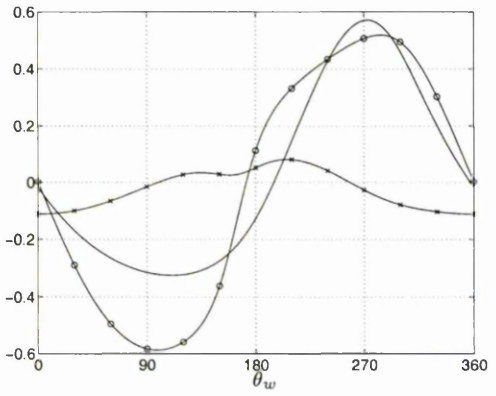

Figure 3.12: Physical realisability for $m = 2.0$.
—, $10 \times \omega$; -o-, d; -×-, c_0^2.

If, also, we plot the physical realisability bounds for the same asymmetric modes (see figure 3.13), we see that here they all correspond to case 2 in section 2.3.2. Hence, these asymmetric TS modes can be stabilised purely by ensuring that the free-wave speed, c_0, is large enough such that c_0^2 is greater than the maximum value of the upper bound for c_0^2 in figure 3.13. Choosing such a value

of c_0^2, the correponding values of m and d can be found using equations (2.21) to obtain a stable asymmetric TS mode where $|\phi_w| = 0.4$.

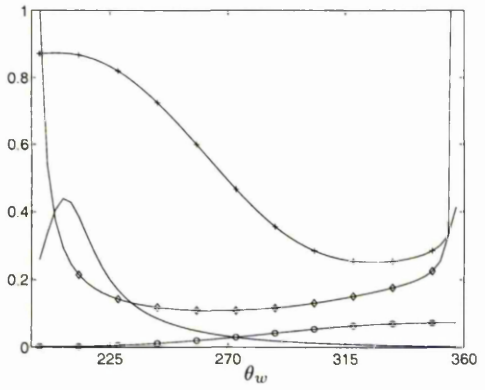

Figure 3.13: Physical realisability bounds on m, d and c_0^2.
—, $10^{-1} \times d$ lower bound; -o-, $10^{-2} \times m$ lower bound; -◇-, $10^{-2} \times m$ upper bound; -+-, $10 \times c_0^2$ upper bound.

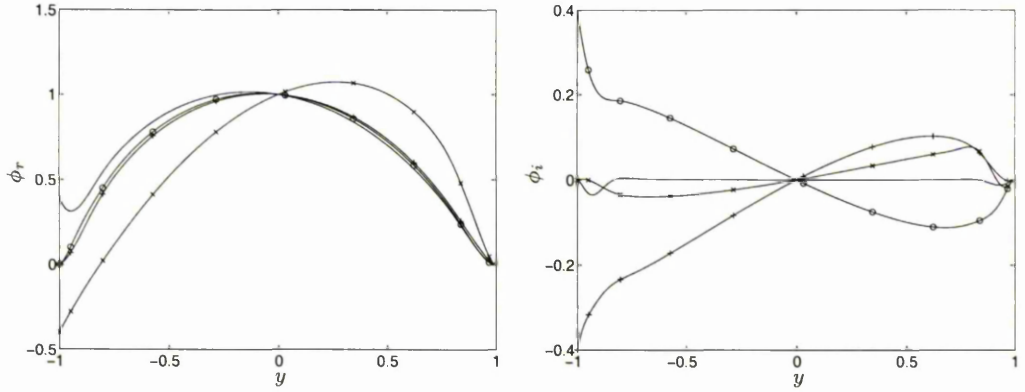

(a) Real Part (b) Imaginary Part

Figure 3.14: Eigenfunctions for the asymmetric TS modes.
—, $\theta_w = 0°$; -o-, $\theta_w = 90°$; -×-, $\theta_w = 180°$; -+-, $\theta_w = 270°$.

The eigenfunctions of the asymmetric channel modes show one marked difference from the modes in the symmetric channel. Although the velocity gradients are still greatest near the walls, both compliant and rigid, the disturbances are significantly larger near the centre of the channel, than for the other geometries. This can be seen in figure 3.14.

Finally in this section on the asymmetric TS modes, we may be able to make use of the above hypothesis relating the asymmetric and symmetric modes. If it can be proven, then we may be better off attempting to stabilise channel flows using only a single compliant wall. This would eliminate the need to consider antisymmetric modes in case any such mode, of any class, is more unstable than its symmetric counterpart. The hypothesis would then make it quicker to compute solutions in the asymmetric channel problem.

We have shown in this section that we can stabilise a given TS mode in a channel with one or more compliant walls. However, in order to stabilise the flow as a whole, we must choose wall parameters which stabilise all unstable TS modes, for each value of α. Also, we must ensure that no stable rigid TS mode is destabilised sufficiently to become unstable and that no other types of instability are introduced to the flow. It is to the latter of these two problems which we shall now turn our attention.

3.5.2 Kelvin-Helmholtz (KH) Modes

The Kelvin-Helmholtz class of modes also exists for $\phi_w \to 0$. However, for KH modes $c \to 0$ and $a \to a^* \neq 0$ in this limit and so we obtain a stationary wave in the compliant surface with amplitude a^*, spatial wave number α and which is neutrally stable. Hence modes of this class are associated with instabilities in the compliant surface itself.

For non-zero but small values of ϕ_w, i.e. for $|\phi_w| \ll 1$, the values of the phase velocity eigenvalues are also small, i.e. $|c| \ll 1$ and so we obtain a surface wave which is either stationary or slow moving. Here also, $a = a^* + \delta a$, where $\delta a \ll a^*$.

There are, therefore, similarities between the KH modes and the static divergence modes of more conventional studies, e.g. Davies and Carpenter [15].

However, the results of section 3.6 show that there are modes in the KH class which obey a purely viscous theory, as opposed to the inviscid theory which is obeyed by the static divergence modes. This lends support to Sen and Arora's hypothesis [67] that the KH class of modes may be a superset of the static divergence modes. There is still, though, the possibility, also put forward by Sen and Arora [67], that the classification of the kinematic modes and those of other studies could be entirely separate endeavours. If this were so, such a comparison between the mode classes of the different approaches would be meaningless.

Symmetric Channel, Symmetric Modes

We can look at the KH modes for the same parameters as for the TS modes, i.e. for $Re = 8000$ and $\alpha = 1.0$. Plots of the phase speed, c_r and the growth-rate, ω, against θ_w, for various values of $|\phi_w|$ can be seen in figures 3.15(a) and 3.15(b), respectively. As predicted, the phase velocity oscillates about zero and as for the TS modes, the similarity of the profiles when compared with boundary-layer flow [67] is quite marked. As for the TS modes, an increase in $|\phi_w|$ leads to an increase in the amplitude of the oscillations, too. Also like the TS modes, as $|\phi_w|$ is increased the range of values of θ_w which lead to unstable modes shrinks.

Again, we seek values of the wall parameters which lead to flows where all modes are stable, for all α and hence we shall now look at the physical realisability of the KH modes.

Back calculating the values of d and c_0^2 for $m = 2.0$ and $|\phi_w| = 0.2$ we obtain the profiles given in figure 3.16. The biggest difference between these and the TS modes is the existence of two singularities, at 98° and 310°. That these singularities correspond to the stationary ($c_r = 0$) modes can be deduced from figure 3.15(a) and equations (2.21). With no stationary TS modes in section 3.5.2 there are no corresponding singularities in the wall parameters, d and c_0^2.

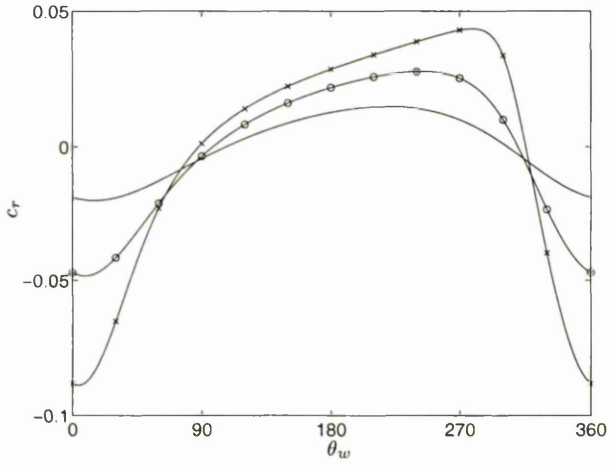

(a) Phase Speed

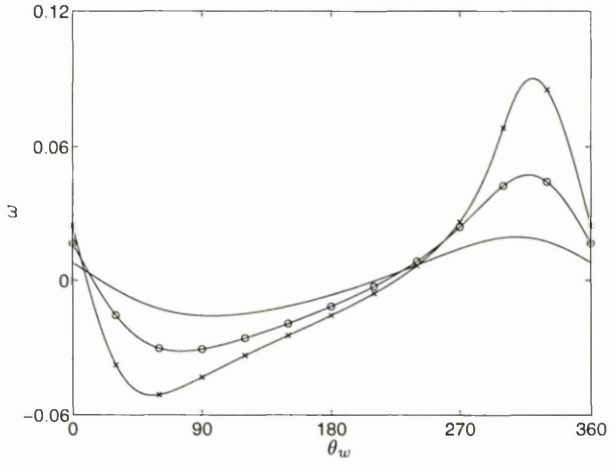

(b) Growth Rate

Figure 3.15: Symmetric KH modes for the symmetric channel.
—, $|\phi_w| = 0.1$; -o-, $|\phi_w| = 0.2$; -×-, $|\phi_w| = 0.3$.

The passive wall conditions, $d, c_0^2 > 0$, require that θ_w lies in the region between the singularity at 98° and 270°, approximately. In this region ω is mainly negative but there is also a significant unstable region too, which exists for the larger values of θ_w. As for the TS modes, for values of m smaller than 2, d and

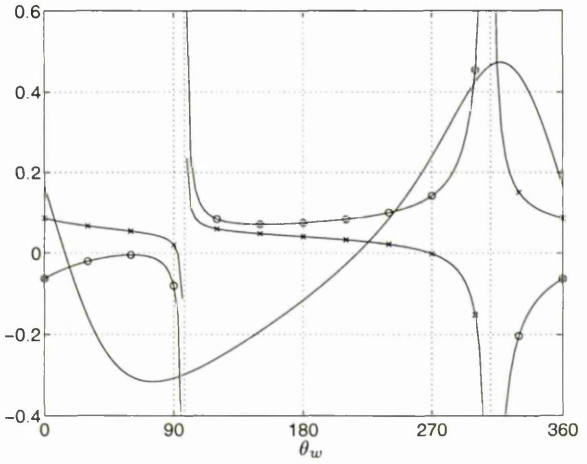

Figure 3.16: Physical realisability for $m = 2.0$.
—, $10 \times \omega$; -o-, $10^{-1} \times d$; -×-, c_0^2.

c_0^2 vary like $1/m$ but there is no qualitative change in the profiles when plotted against θ_w. However, as m is increased from 2, d increases for $\theta_w < 98°$ until another physically realisable region emerges here (see figure 3.17(a)). Fortunately, in terms of flow stabilisation, this physically realisable region occurs where the modes are stable. As $m \to \infty$ the effects of the singularities confined to vanishingly thin regions and $d \to -2\omega$, $c_0^2 \to c_r^2 + c_i^2$. As a result, the unstable region reduces to an "unstable pocket" for large values of m (see figures 3.17), as is the case for the symmetric TS modes.

If we plot the bounds for m, d and c_0^2 against θ_w for $|\phi_w| = 0.2$ (see figure 3.18), we see that, as for the TS modes, the potentially physically realisable unstable region is divided into two. For the modes where $219° < \theta_w < 268°$, the bounds correspond to those for case 1 in section 2.3.2, whereas for $268° < \theta_w < 288°$, the bounds correspond to those for case 2.

The main difference between the bounds for the symmetric KH modes and those for the symmetric TS modes is that as the upper value of θ_w is approached, the upper bound for m tends to a finite limit for the KH modes as opposed to infinity for the TS modes. Linked with this, the lower bound for m tends

to the same limit as for the upper bound and this occurs at the point where $Y_r/c_i = Y_i/c_r$. Also at this point, the upper bounds for c_0^2 and d both tend to zero.

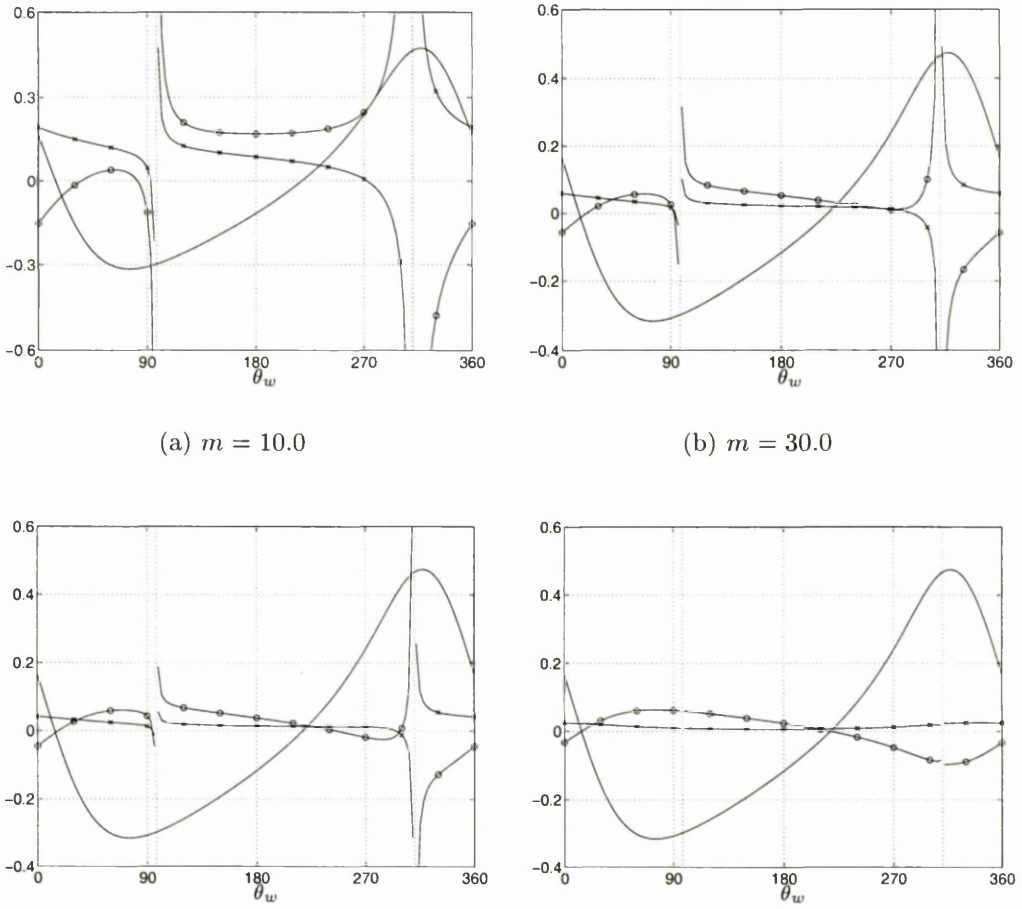

(a) $m = 10.0$

(b) $m = 30.0$

(c) $m = 100.0$

(d) $m = 10000.0$

Figure 3.17: The effect of varying m on physical realisability.
—, $10 \times \omega$; -o-, d; -×-, c_0^2.

These differences actually make it easier for us to choose wall parameters which will eliminate the above unstable modes in the KH class. Choosing a value of m above about 100 will eliminate all unstable modes corresponding to $|\phi_w| = 0.2$, except those in the approximate range $219° < \theta_w < 250°$. However, in order to eliminate modes in this remaining region we can choose c_0^2 below 0.0007.

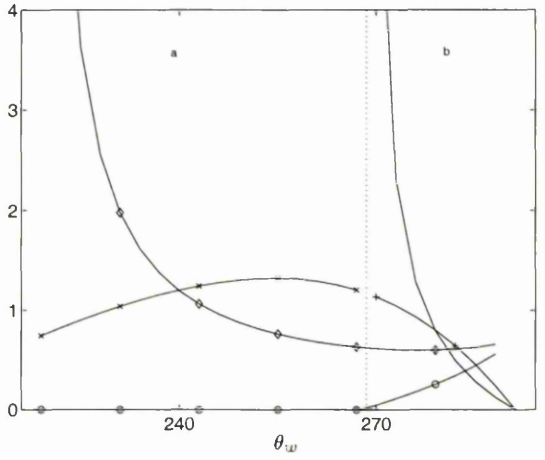

Figure 3.18: Physical realisability bounds on m, d and c_0^2.
—, $10 \times d$ lower bound;
-○-, $10^{-2} \times m$ lower bound; -◇-, $10^{-2} \times m$ upper bound;
-×-, $10^3 \times c_0^2$ lower bound; -+-, $10^3 \times c_0^2$ upper bound.

Therefore, we need only impose two restrictions on the wall parameters in order to eliminate unstable KH modes where $\alpha = 1.0$ and $|\phi_w| = 0.2$. The restriction on the wall density, m, does require an increase in its value of about two orders of magnitude, which again poses questions with regard to the manufacturing of the wall. However, the large range of values of θ_w for which stable physically-realisable modes can be found suggest that it should be possible to find wall parameters for which the symmetric TS modes are stabilised and which also lead to stable symmetric KH modes.

Sample eigenfunctions are given in figures 3.19. These show some similarities with the KH mode eigenfunctions for boundary-layer flow, with the similarities again most marked in the near wall region, where the velocity disturbances are at their greatest.

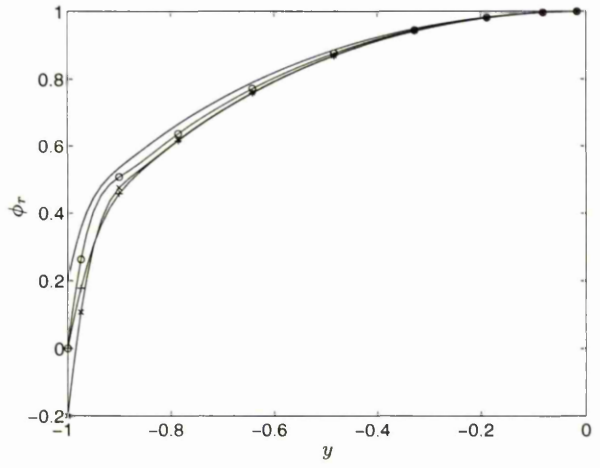

(a) Real Part

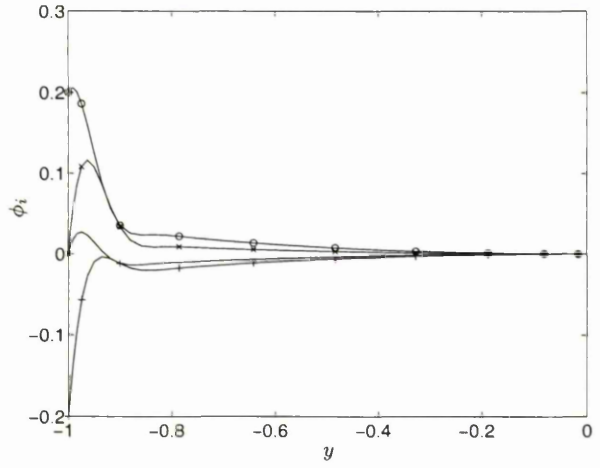

(b) Imaginary Part

Figure 3.19: Eigenfunctions for the symmetric KH modes.
—, $\theta_w = 0°$; -o-, $\theta_w = 90°$; -×-, $\theta_w = 180°$; -+-, $\theta_w = 270°$.

Symmetric Channel, Antisymmetric Modes

The phase speed and growth rate of the antisymmetric KH modes in the symmetric channel are given in figures 3.20(a) and 3.20(b), respectively, where $Re = 8000$

and $\alpha = 1.0$. These show that the antisymmetric modes resemble their symmetric counterparts if θ_w is shifted by 180°. The amplitude of the oscillations of the antisymmetric modes are of smaller magnitude about zero than for the symmetric modes with the same value of $|\phi_w|$. Hence, in some sense, the antisymmetric KH modes are more stable than the symmetric KH modes. However, it is not necessarily the case that the antisymmetric KH mode is more stable than its symmetric counterpart for a given set of wall parameters and hence there is a need to study these modes.

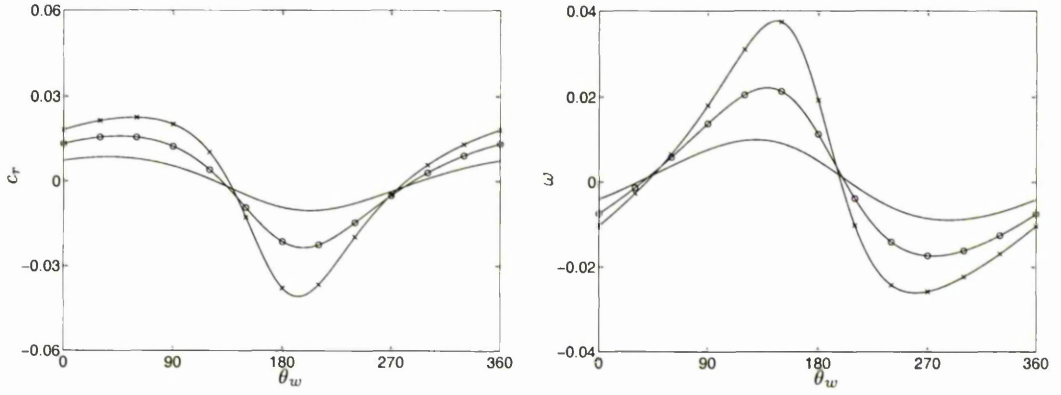

(a) Phase Speed

(b) Growth Rate

Figure 3.20: Antisymmetric KH modes for the symmetric channel.
—, $|\phi_w| = 0.1$; -o-, $|\phi_w| = 0.2$; -×-, $|\phi_w| = 0.3$.

The wall-parameter bounds are plotted in figure 3.21, for a wavenumber, $\alpha = 1.0$ and stream functions where $|\phi_w| = 0.2$. This plot shows the bounds to be qualitatively similar to those for the symmetric KH modes. If a shift in θ_w of 180° is considered, then the physically realisable regions of the antisymmetric KH modes are approximately the same as those for the symmetric KH modes, for both cases of the bounds. However, there is a significant difference in the values of the bounds themselves.

The qualitative similarity between the bounds of the antisymmetric KH modes

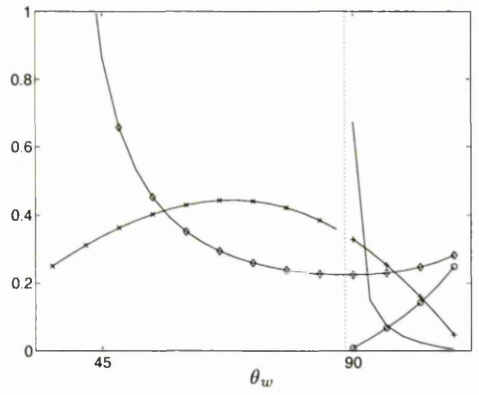

Figure 3.21: Physical realisability bounds on m, d and c_0^2.
—, d lower bound;
-o-, $10^{-3} \times m$ lower bound; -◇-, $10^{-3} \times m$ upper bound;
-×-, $10^3 \times c_0^2$ lower bound; -+-, $10^3 \times c_0^2$ upper bound.

and those of the symmetric KH modes implies that we need only apply two restrictions in order to eliminate unstable antisymmetric KH modes corresponding to $|\phi_w| = 0.2$. These two restrictions are that m must be large enough to eliminate all of the case 2 instabilities and most of the case 1 instabilities. If the free-wave speed, c_0, is then made small enough, the remaining case 1 instabilities will be eliminated, too. However, the required value of m is at least twice that used for the symmetric case, which poses further practical questions.

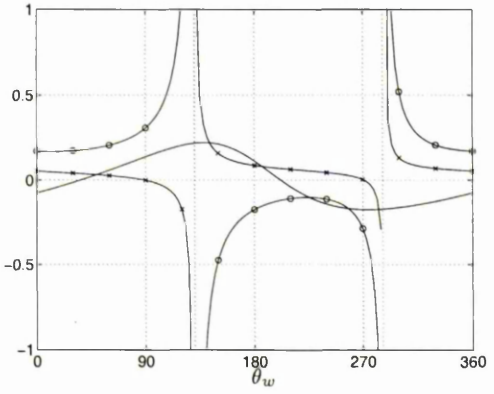

Figure 3.22: Physical realisability for $m = 2.0$.
—, $10 \times \omega$; -o-, $10^{-1} \times d$; -×-, c_0^2.

The back-calculated values of d and c_0^2 are plotted in figure 3.22 against θ_w,

for $\alpha = 1.0$, $|\phi_w| = 0.2$ and $m = 2.0$. These, too, are qualitatively similar to their symmetric counterparts, if θ_w is shifted by 180°. There is a small region, $36° < \theta_w < 90°$, approximately, where unstable physically-realisable modes exist, as can be predicted from figure 3.21.

A sample of the eigenfunctions for the antisymmetric KH modes is given in figure 3.23 and shows that, like all of the modes previously encountered, the largest velocity disturbances and their gradients are to be found in a small region nearest the walls.

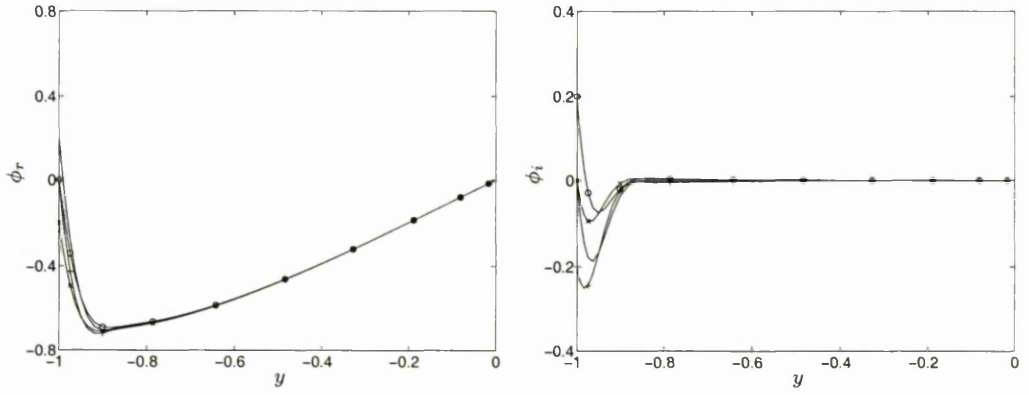

(a) Real Part (b) Imaginary Part

Figure 3.23: Eigenfunctions for the antisymmetric KH modes.
—, $\theta_w = 0°$; -o-, $\theta_w = 90°$; -×-, $\theta_w = 180°$; -+-, $\theta_w = 270°$.

Asymmetric Channel Modes

As stated in section 3.5.1, some relief from the problem of needing to consider modes of different symmetries could be obtained by using an asymmetric channel where no symmetry considerations need to be made. The observation that there appears to be a one-to-one correspondence between the symmetric TS modes for the symmetric channel and the asymmetric TS channel modes shows that studying the former is also tantamount to studying the latter. The same observation

holds for the asymmetric KH modes. This is illustrated in figure 3.24 where the phase speed and growth rate are plotted against θ_w for values of $|\phi_w|$ which are twice those of the symmetric KH modes in the symmetric channel.

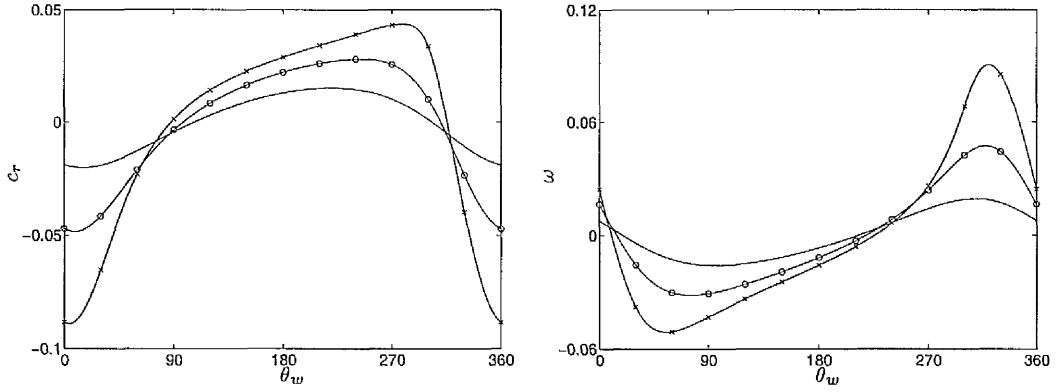

(a) Phase Speed (b) Growth Rate

Figure 3.24: Asymmetric KH channel modes.
—, $|\phi_w| = 0.2$; -o-, $|\phi_w| = 0.4$; -×-, $|\phi_w| = 0.6$.

The bounds on the wall parameters are plotted in figure 3.25, for $\alpha = 1.0$ and $|\phi_w| = 0.4$. The quantitative difference between these and the bounds for the symmetric KH modes with $\alpha = 1.0$ and $|\phi_w| = 0.2$ is very small. Plots of the

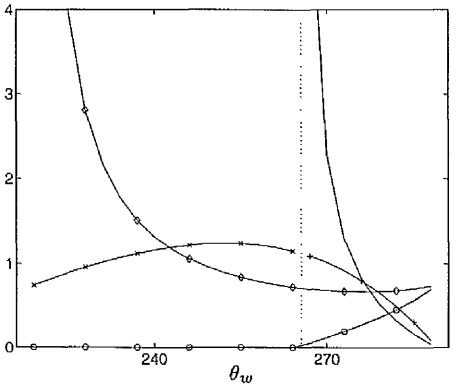

Figure 3.25: Physical realisability bounds on m, d and c_0^2.
—, $10 \times d$ lower bound;
-o-, $10^{-2} \times m$ lower bound; -◇-, $10^{-2} \times m$ upper bound;
-×-, $10^3 \times c_0^2$ lower bound; -+-, $10^3 \times c_0^2$ upper bound.

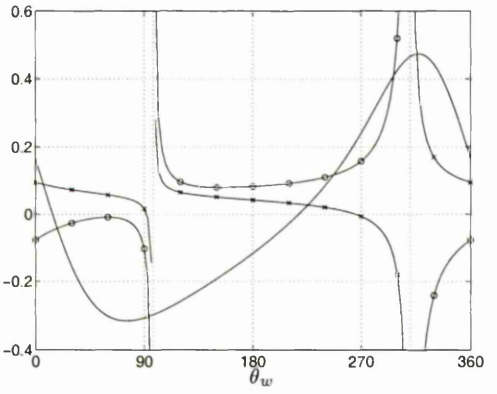

Figure 3.26: Physical realisability for $m = 2.0$.
—, $10 \times \omega$; -o-, $10^{-1} \times d$; -×-, c_0^2.

back-calculated values of d and c_0^2 against θ_w also appear to exhibit this same property, as shown in figure 3.26. Further investigation is required to determine exactly why this is so, since the eigenfunctions differ. Most importantly, this difference is significant for the pressure at the wall, which differs by about one part in ten. Hence, one would expect the admittance and the wall parameters should differ significantly, as is the case for the TS modes.

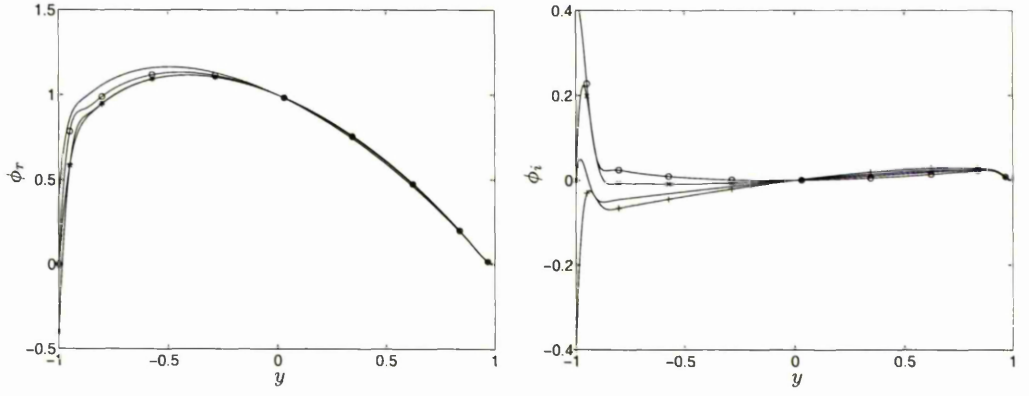

(a) Real Part (b) Imaginary Part

Figure 3.27: Eigenfunctions for the asymmetric KH modes.
—, $\theta_w = 0°$; -o-, $\theta_w = 90°$; -×-, $\theta_w = 180°$; -+-, $\theta_w = 270°$.

The stream function is given in figure 3.27, for $|\phi_w| = 0.4$. Unlike the asymmetric TS modes, the velocity disturbances and their gradients are not particularly pronounced at the centre of the channel. There is, though, the same region near the compliant wall where the disturbances are at their greatest.

3.5.3 Transitional modes

Modes of the above two classes occur for smaller values of $|\phi_w|$. However, as $|\phi_w|$ is increased from zero, the phase velocities for the Tollmien-Schlichting and Kelvin-Helmholtz classes become closer until they coalesce at a critical value of $|\phi_w|$. Thus, a solution is then formed, with two branches in the complex ϕ_w plane. Further increasing of $|\phi_w|$, leads to the occurence of more solution branches. The resulting set of multi-valued solutions for mid range $|\phi_w|$ in boundary-layer flow was termed the transitional class of modes by Sen and Arora [67].

Symmetric Channel, Symmetric Modes

This class of modes is exceedingly complex and further work is necessary to gain a fuller understanding of the relationship between it and the classes given in previous studies. Additionally, numerical difficulties were often encountered in calculating solutions for modes of this class. An increase in N was sometimes necessary. More often though, the distance between adjacent values of θ_w was dramatically reduced. This was necessary since the value of the phase velocity changes much more rapidly with θ_w for the transitional modes than for the modes of any other class.

Given the complex nature of these solutions it is not possible to give an example of a generic transitional mode and so we shall give only a couple of examples with differing numbers of branches. Again, we shall use the parameter values, $\alpha = 1.0$ and $Re = 8000.0$. Then, $|\phi_w| = 0.4$ and $|\phi_w| = 0.6$ give rise to

double- and triple-valued phase velocities, respectively. The phase speed and

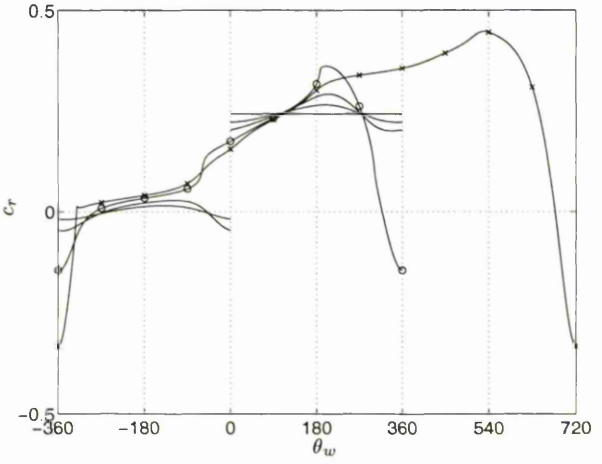

(a) Phase Speed

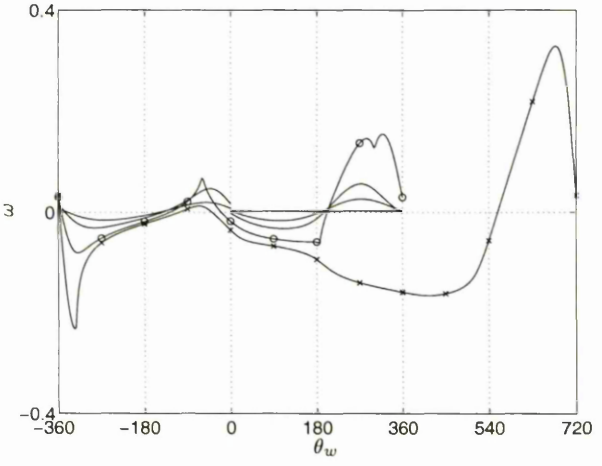

(b) Growth Rate

Figure 3.28: Symmetric Transitional modes for the symmetric channel.
-o-, $|\phi_w| = 0.4$; -×-, $|\phi_w| = 0.6$.

growth rate are plotted against θ_w for both of these modes in figure 3.28. The first branch of each mode lies in the region $-360° < \theta_w < 0°$, the second branch in the region $0° < \theta_w < 360°$ and the third branch, of the mode for which $|\phi_w| = 0.6$, lies in the region $360° < \theta_w < 720°$. A selection of the TS and KH modes from

figures 3.3 and 3.15 have been superimposed on figure 3.28. The KH modes have been plotted in the region occupied by the first branch of the transitional modes and the TS modes have been plotted in the region occupied by the second branch. These illustrate how increasing $|\phi_w|$ leads to the formation of the transitional modes via the coalescence of modes from the TS and KH classes.

The modes, here, again bear some similarities to those of the corresponding class for boundary-layer flow, though the similarities are less marked than for the other mode classes. The most notable feature of the transitional modes, is the existence of values of θ_w for which the growth rate is much greater than that of modes of any other class. As for the modes in boundary-layer flow over a compliant surface, the transition from TS to R class modes occurs via a singularity in the phase speed at some critical value of $|\phi_w|$, $|\phi_w|_c$, say. As $|\phi_w| \to |\phi_w|_c^-$,

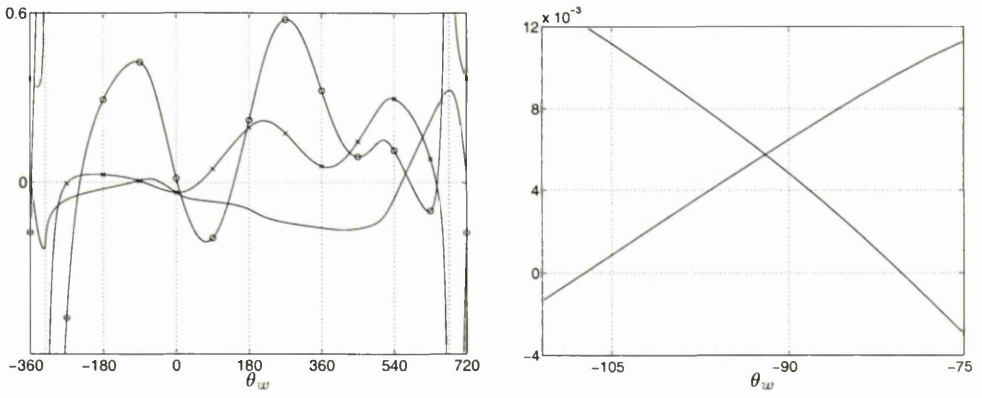

(a) $m = 2.0$ (b) The "unstable pocket"

Figure 3.29: Physical realisability for $m = 2.0$.
—, ω; -o-, $10^{-1} \times d$; -×-, c_0^2.

$c_r \to -\infty$ and as $|\phi_w| \to |\phi_w|_c^+$, $c_r \to +\infty$. In figure 3.28(a), the emergence of a large negative value of c_r can be seen at $\theta_w = -360°$ as $|\phi_w|$ is increased to 0.4 and then to 0.6. Either side of this, the growth rate takes large positive and negative values as θ_w is slightly decreased and increased, respectively. This, too

is in agreement with the results of Sen and Arora [67] for boundary-layer flow over a compliant surface. Although the singularities take a different form for flow in a compliant pipe, that these modes lead to powerful instabilities is illustrated in section 4.5.3.

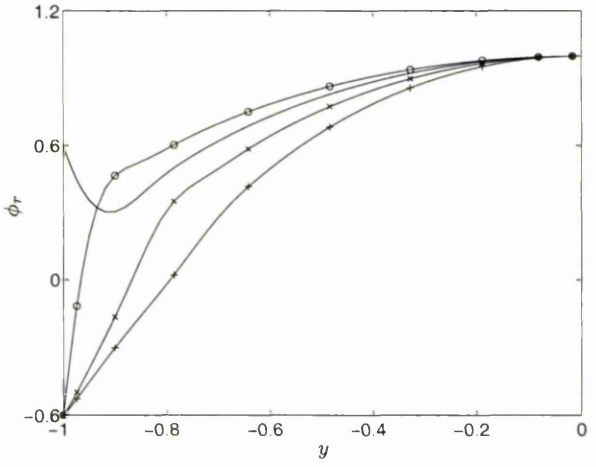

(a) Real Part

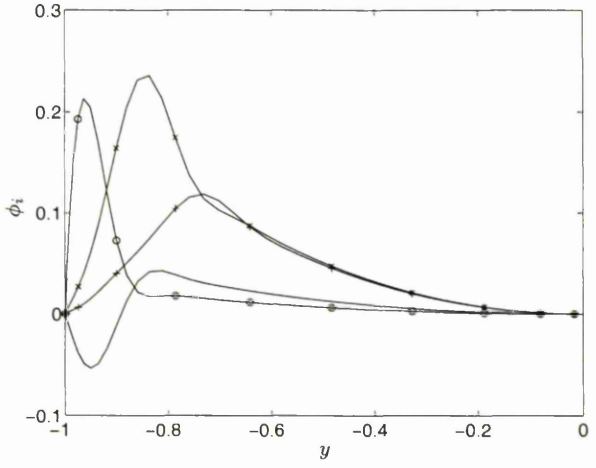

(b) Imaginary Part

Figure 3.30: Eigenfunctions for the symmetric Transitional modes.
—, $\theta_w = -180°$; -o-, $\theta_w = 0°$; -×-, $\theta_w = 180°$; -+-, $\theta_w = 540°$.

As an example of the physical realisability of the transitional modes, back

calculated values of the wall parameters, d and c_0^2, are given in figure 3.29(a). The parameters used are those of the triple-valued mode, where $|\phi_w| = 0.6$. There are two physically realisable unstable regions, one in the third branch and the other a relatively small region in the first branch. This small region has been magnified in figure 3.29(b) to show more clearly that both the growth rate and the free-wave speed, c_0 are greater than zero for $-96° < \theta_w < -87°$. These modes must then be taken into consideration when attempting to stabilise the flow.

Sample eigenfunctions are given in figure 3.30 for $\alpha = 1.0$ and $|\phi_w| = 0.6$. This shows that although the greatest velocity disturbances and their gradients are found in the region nearest the wall, this region covers much more of the channel than for the TS and KH modes.

Symmetric Channel, Antisymmetric Modes

Antisymmetric Transitional modes also occur in the symmetric channel. Examples of these are given in figure 3.31, where the phase speed and growth rate are plotted for $\alpha = 1.0$ and $Re = 8000.0$. Here again, double- and triple-valued

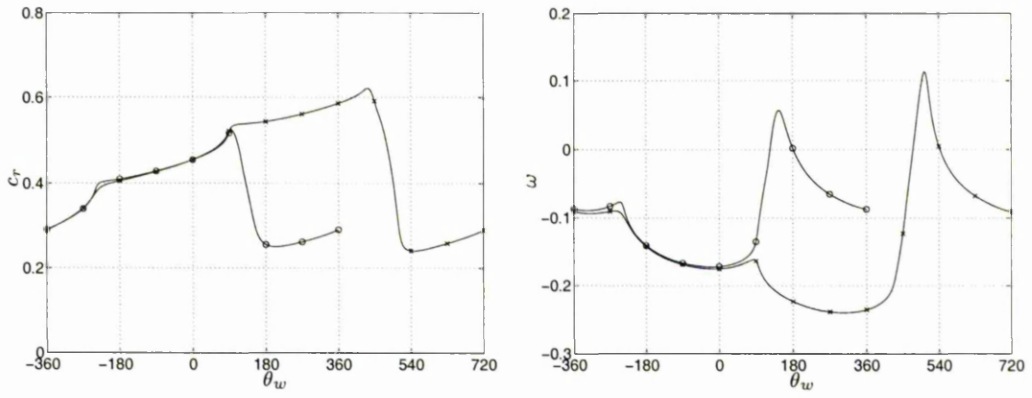

(a) Phase Speed (b) Growth Rate

Figure 3.31: antisymmetric Transitional modes for the symmetric channel. -o-, $|\phi_w| = 0.6$; -×-, $|\phi_w| = 0.7$.

solutions are given. Transition to R class modes occurs again via a singularity, which this time forms at $\theta_w = 180°$, if a suitable transformation is applied to θ_w so that the relevant branch of the solution occurs in the range, $0° < \theta_w < 360°$. Figure 3.31 shows that the growth rate exhibits a markedly more positive value for some values of θ_w when compared to the TS and KH class modes. In this case, though there is only one region where instabilities occur because the TS modes are all stable for these values of α and Re.

Figure 3.32 gives plots of d and c_0^2 for $m = 2$, $\alpha = 1.0$ and $|\phi_w| = 0.7$. There is a small region in which these unstable modes are physically realisable and so the antisymmetric transitional modes must be taken into consideration, too, when attempting to stabilise the flow.

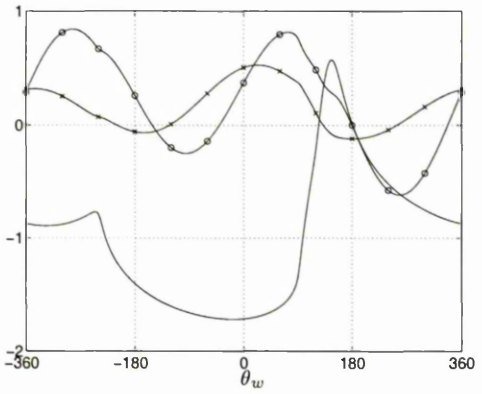

Figure 3.32: Physical realisability for $m = 2.0$.
—, $10 \times \omega$; -o-, d; -×-, c_0^2.

Plots of the eigenfunctions, for the given parameters, can be found in figure 3.33. Only the values at the collocation points have been plotted (and joined together with straight lines) and hence the profiles do not appear to be smooth. Given that the solutions are actually polynomials, it is possible to interpolate using the relevant series of Tchebychev polynomials. This would give a much smoother appearance to the eigenfunctions, though the values at the collocation points would be no more or less valid.

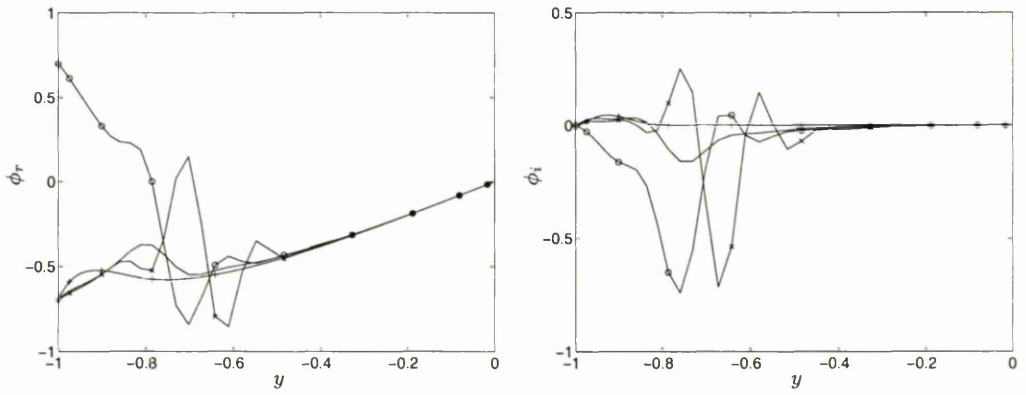

(a) Real Part (b) Imaginary Part

Figure 3.33: Eigenfunctions for the antisymmetric Transitional modes. —, $\theta_w = -180°$; -o-, $\theta_w = 0°$; -×-, $\theta_w = 180°$; -+-, $\theta_w = 540°$.

The most notable feature of these graphs is the extra complexity of the eigenfunctions when compared to any of the others previously encountered. The largest velocities and velocity gradients generally occur away from the wall, which suggests that may be the high shear region of the basic flow is not so important for these modes.

Asymmetric Channel Modes

As for the previously encountered mode classes, the asymmetric modes seem to exhibit the property that the phase velocity is the same as for a symmetric mode with the same kinematic parameters, except for the wall stream function. The value of the wall stream function for the asymmetric modes is twice that for the corresponding symmetric mode with the same phase velocity. Given the rapid changes in c for the Transitional modes, in both numerical values and in the number of solution branches, as $|\phi_w|$ is varied, this is the strongest observational evidence that a link does indeed exist between the symmetric and asymmetric channel modes.

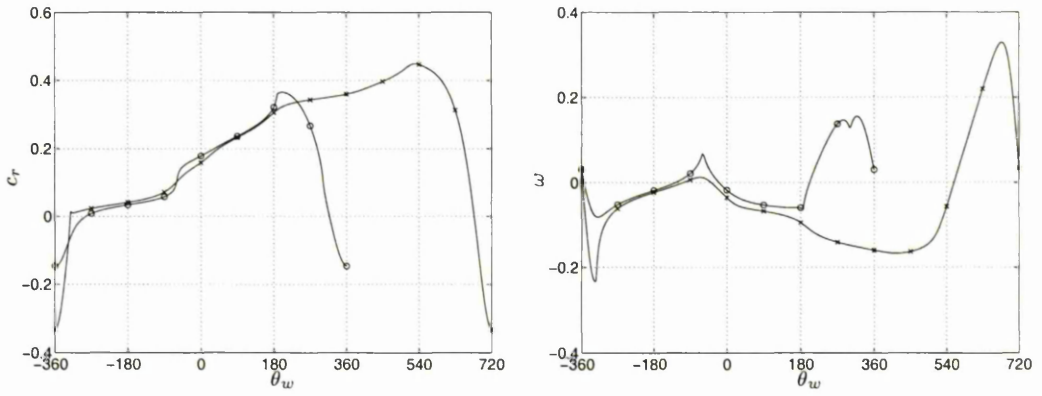

(a) Phase Speed (b) Growth Rate

Figure 3.34: Asymmetric Transitional channel modes.
-o-, $|\phi_w| = 0.8$; -×-, $|\phi_w| = 1.2$.

For the Transitional modes, the suggested link between the symmetric and asymmetric modes requires that the asymmetric phase velocities should agree with those in figure 3.28, if we take $\alpha = 1.0$, $Re = 8000.0$ and $|\phi_w| = 0.8, 1.2$. That the phase velocities agree can be seen in figure 3.34, where the kinematic parameters are as above.

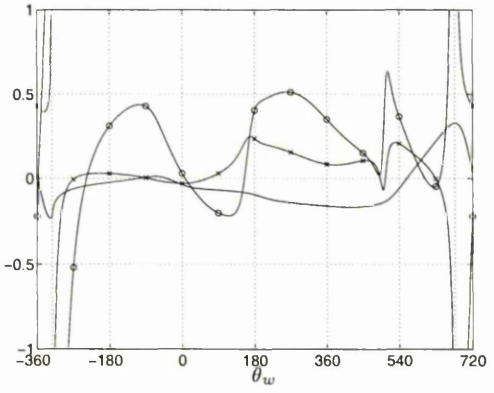

Figure 3.35: Physical realisability for $m = 2.0$.
—, $10 \times \omega$; -o-, $10 \times d$; -×-, $10 \times c_0^2$.

Plots of the back-calculated wall parameters, d and c_0^2, are given in figure 3.35,

for $Re = 8000.0$, $\alpha = 1.0$ and $|\phi_w| = 1.2$. It can be seen that sections of both unstable regions are physically realisable for this value of the wall density, m. For the unstable region at approximately $\theta_w = -90°$ there is an unstable pocket, as for the corresponding symmetric transitional modes. For the unstable region where $540° < \theta_w < 720°$, approximately, the lower values of θ_w are physically realisable and the higher values are not. This is similar to the physical realisability of the corresponding symmetric modes as shown in figure 3.29. However, the physically realisable region is larger here for the asymmetric modes.

Sample eigenfunction plots are given in figure 3.36 for various values of θ_w. For all solution branches the greatest velocity disturbances and their gradients are located nearest the walls. For the first branch solutions, where $\theta_w = -180°, 0°$ and which arise as a result of the KH part of the modal coalescence, only near the wall do any significant velocity gradients exist. However, for the remaining branches significant velocity gradients also exist in regions away from the wall including at the channel centreline.

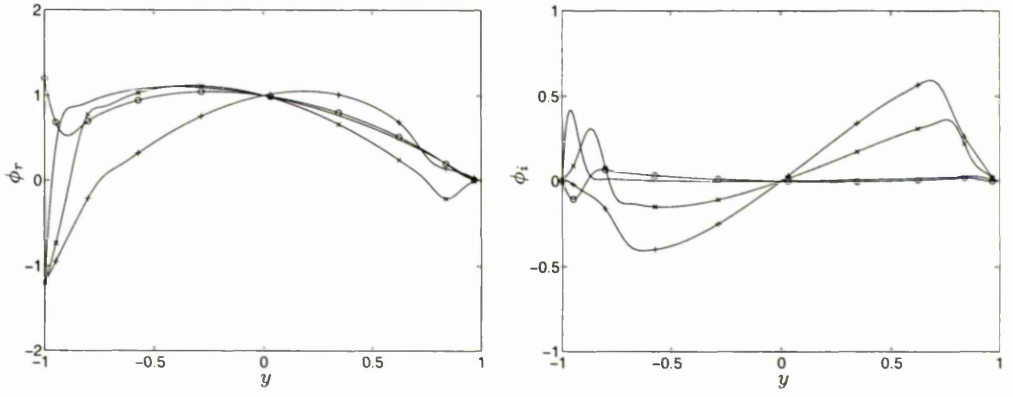

(a) Real Part (b) Imaginary Part

Figure 3.36: Eigenfunctions for the asymmetric Transitional modes.
—, $\theta_w = -180°$; -o-, $\theta_w = 0°$; -×-, $\theta_w = 180°$; -+-, $\theta_w = 540°$.

3.5.4 Resonant (R) modes

The Resonant class of modes exists for large values of $|\phi_w|$. In the limit $|\phi_w| \to \infty$, Carpenter and Garrad [11] have shown, using an inviscid theory, that this type of mode is neutrally stable and that $c \to 1 + 0i$ for boundary-layer flow. The relevant condition from (3.8a), (3.14a) or (3.20) then implies that the surface wave amplitude, a, is then also large. These modes then, like the Kelvin-Helmholtz modes, are associated with instabilities in the compliant surface induced by the flow.

For finite but sufficiently large values of $|\phi_w|$, $c = 1 + \delta c$, where δc is small, i.e. $|\delta c| \ll 1$. This holds until $|\phi_w|$ is decreased to a value close to that at which the transitional modes occur. Alternatively, the above may breakdown if the kinematic parameters are varied so that the inviscid theory breaks down.

As for the KH modes, there are modes of the Resonant class which obey a purely viscous theory. These are given in section 3.6. For these viscous modes, the phase velocity becomes a function of α as $|\phi_w| \to \infty$ and hence do not necessarily tend towards 1. This suggests there is the possibility that the Resonant class of modes is a superset of the "panel flutter" modes of inviscid studies, in the same way that the KH modes may be a superset of the static divergence modes. Alternatively, as for the KH and static divergence classes of mode, the Resonant and "panel flutter" modes may have a common intersection or again there is possibility that the classification of the kinematic and conventional modes comprise entirely separate endeavours.

Symmetric Channel, Symmetric Modes

All the unstable Resonant modes are not physically realisable for the kinematic parameters used in section 3.5.1, for fixed Re. However, for lower wave numbers physically realisable modes do exist and so we shall consider Resonant modes for

which $Re = 8000.0$ and $\alpha = 0.01$. Plots of the phase speed and the growth rate for some of the Resonant modes are given in figure 3.37. Since the Reynolds number

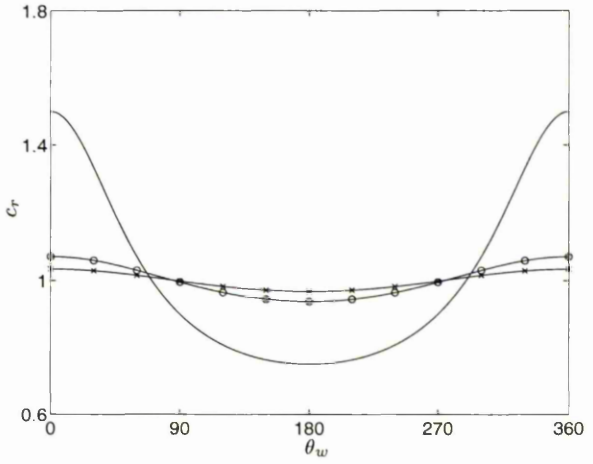

(a) Phase Speed

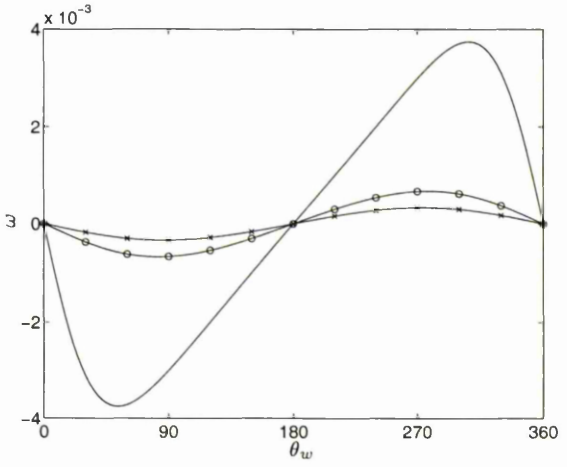

(b) Growth Rate

Figure 3.37: Symmetric R modes for the symmetric channel.
—, $|\phi_w| = 3.0$; -o-, $|\phi_w| = 15.0$; -×-, $|\phi_w| = 30.0$.

is large enough that the inviscid approximation is valid, the phase velocity can be seen to oscillate about 1 as θ_w is varied. As $|\phi_w|$ is increased, the amplitude of the oscillations about 1 decrease in magnitude, which is consistent with the

inviscid theory, too. Again, the profiles of the Resonant modes here and those of boundary-layer flow over a compliant surface are broadly the same qualitatively, in keeping with the other mode classes.

Back-calculated values of the wall parameters, d and c_0^2, are given in figure 3.38(a), for $Re = 8000.0$, $\alpha = 0.01$, $|\phi_w| = 3.0$ and $m = 2.0$. This shows that

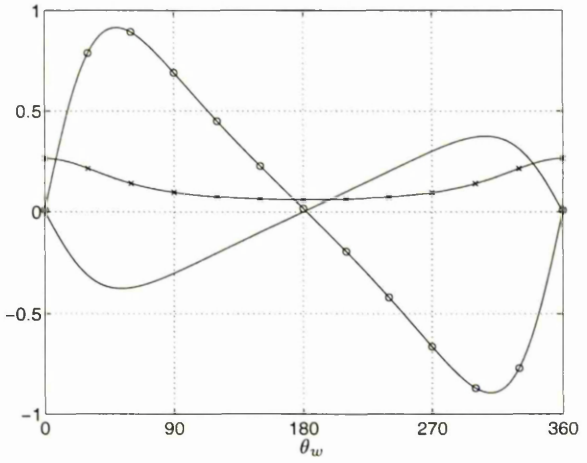

(a) $m = 2.0$

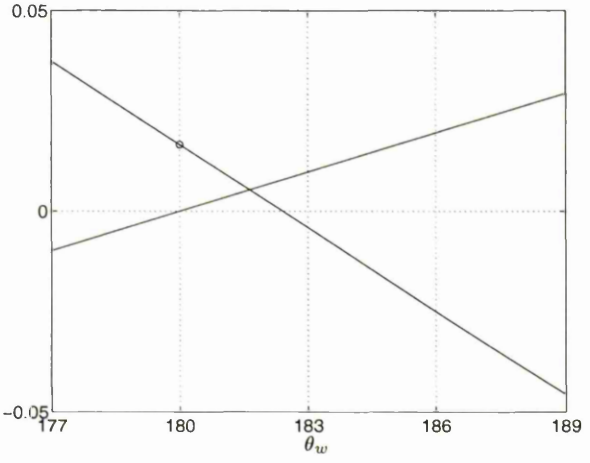

(b) The unstable pocket

Figure 3.38: Physical realisability for $m = 2.0$.
—, $10^2 \times \omega$; -o-, $10^2 \times d$; -×-, $10^{-1} \times c_0^2$.

there is a single "unstable pocket", where the Resonant modes are unstable and physically realisable. This is clarified by figure 3.38(b), which is a close up of the region surrounding the "unstable pocket", which is located at $\theta_w = 180°$, approximately. This is similar to the findings of Sen and Arora for boundary-layer flow over a compliant surface [67].

It also can be seen in figure 3.38(a) that the value of c_0^2 required to obtain the modes oscillates about 1, as θ_w is varied, with a maximum value of about 2.5. Looking at figure 3.37, we can see that the value of c_r^2 must also oscillate about 1 in phase with c_0^2 and with a maximum value of about 2.25. This close direct correlation between c_0 and c_r is an expected property of Resonant modes.

Plots of the wall-parameter bounds are given in figure 3.39 for the stream functions where $|\phi_w| = 3.0$. For these particular kinematic parameter values,

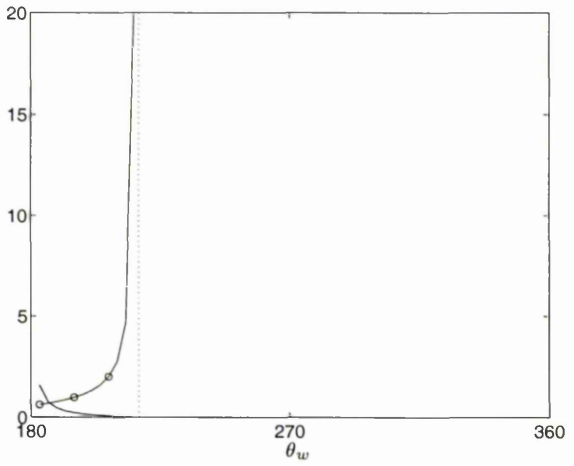

Figure 3.39: Physical realisability bounds on m, d and c_0^2.
—, m upper bound; -o-, c_0^2 lower bound;

the bounds correspond to case 1 of section 2.3.2 and the upper bound for m is greater than 2 only for a small region near $\theta_w = 180°$. This is consistent with the small "unstable pocket" in figure 3.38(a). Since the bounds correspond to case 1 only, we can eliminate all unstable Resonant modes where $|\phi_w| = 3.0$ by choosing the free-wave speed, c_0, so that c_0^2 is less than the minimum of the

lower bound for c_0^2. It is also possible to eliminate the same modes by choosing a suitably large value of m in conjunction with a suitable value of the damping, d. As stated above, $m = 2.0$ reduces the physically realisable unstable region to a pocket. By choosing a large enough value of the damping (anything above the

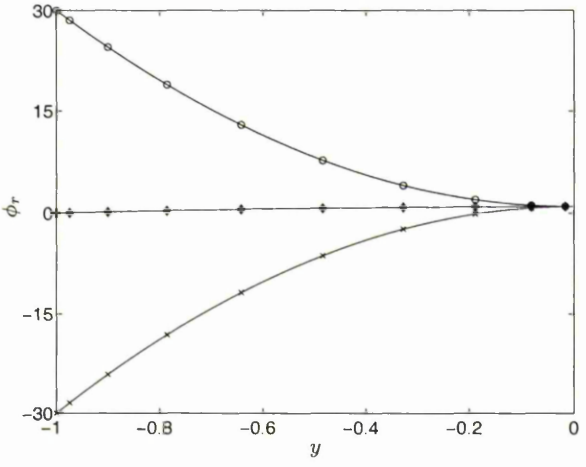

(a) Real Part

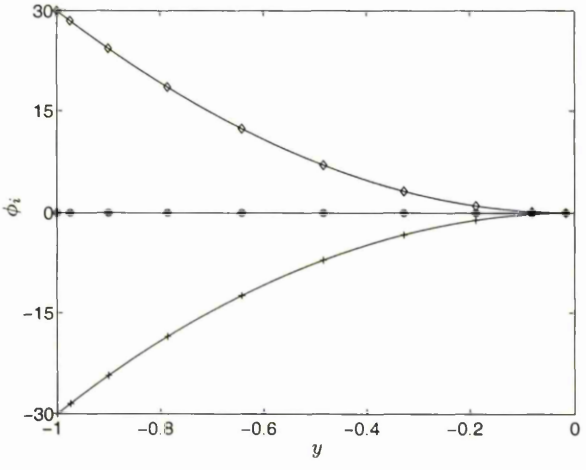

(b) Imaginary Part

Figure 3.40: Eigenfunctions for the symmetric R modes.
-o-, $\theta_w = 0°$; -◇-, $\theta_w = 90°$; -×-, $\theta_w = 180°$; -+-, $\theta_w = 270°$.

value at $\theta_w = 180°$, where $\omega = 0$), will mean that a Resonant mode corresponding

to $|\phi_w| = 3.0$ will be stable.

Plots of the eigenfunctions are given in figure 3.40 for various values of θ_w. These show that although the largest velocity disturbances are to be found nearest the wall, as for most of the mode classes previously encountered, there is no obvious wall region where the gradients are significantly larger than elsewhere. All the previous mode classes (except the antisymmetric transitional modes) exhibit such a wall region, where the velocity gradients are significantly larger than in the remainder of the channel.

Symmetric Channel, Antisymmetric Modes

Profiles of the phase speeds and growth rates of sample antisymmetric Resonant modes are given in figure 3.41 for $Re = 8000.0$ and $\alpha = 1.0$. These show that,

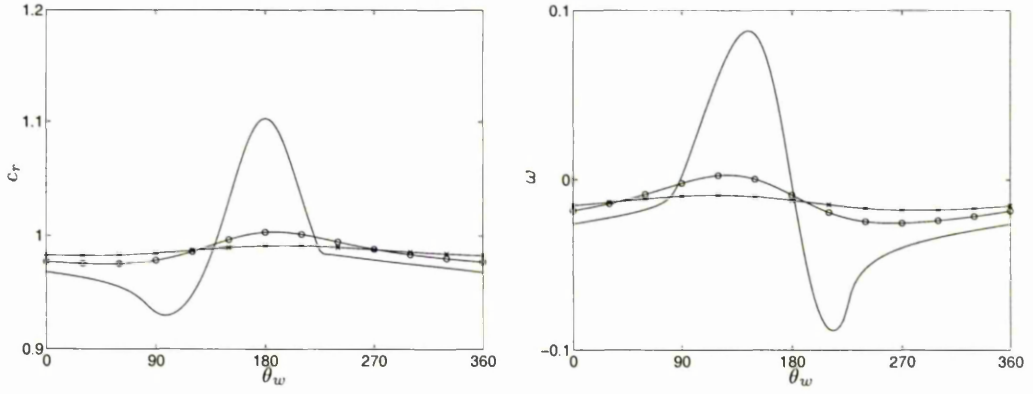

(a) Phase Speed (b) Growth Rate

Figure 3.41: Antisymmetric R modes for the symmetric channel.
—, $|\phi_w| = 3.0$; -o-, $|\phi_w| = 10.0$; -×-, $|\phi_w| = 30.0$.

as for the symmetric modes, the phase velocities oscillate about 1 as θ_w is varied. However, given that the singularity in the transitional mode class occurs at $\theta_w = 180°$, for the antisymmetric modes, it is in the region around $\theta_w = 180°$ where the largest variations in the phase velocity are to be found. As for the

symmetric R modes, when $|\phi_w|$ is increased the amplitude of the oscillations of c about 1, as θ_w is varied, decreases in size.

Plots of the wall-parameter bounds are given in figure 3.42 for $|\phi_w| = 10.0$. As for the symmetric modes, the bounds all correspond to those of case 1 in

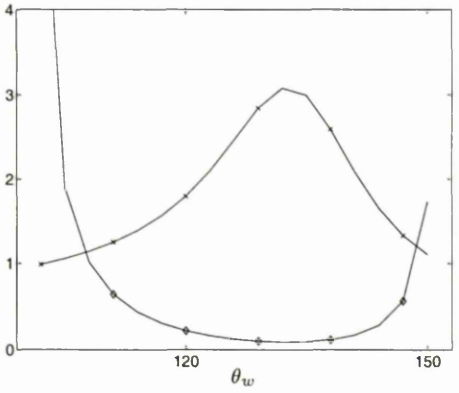

Figure 3.42: Physical realisability bounds on m, d and c_0^2.
-◇-, m upper bound; -×-, c_0^2 lower bound.

section 2.3.2. However, here the upper bound for m tends towards infinity at both extremes of the physically realisable region and the lower bound for c_0^2 always takes finite values with a single maximum. This is similar to the bounds plots for the symmetric R modes when $|\phi_w|$ is taken suitably large ($\gtrsim 30.0$). Hence the same approach to stabilising these modes can be taken as for the symmetric Resonant modes.

Plots of the back-calculated wall parameters, d and c_0^2, can be found in figure 3.43 for $|\phi_w| = 10.0$ and $m = 2$. These show that there are two small physically realisable "unstable pockets", corresponding to the two extreme value of θ_w in figure 3.42. Again it can be ssen that the corresponding value of c_0^2 is close to c_r^2 as would be expected for Resonant modes. A suitably large value of the damping, d should eliminate the unstable antisymmetric R modes with $|\phi_w| = 10.0$, in line with the symmetric R modes, too.

Plots of the eigenfunctions exhibit similarities to the symmetric modes in that

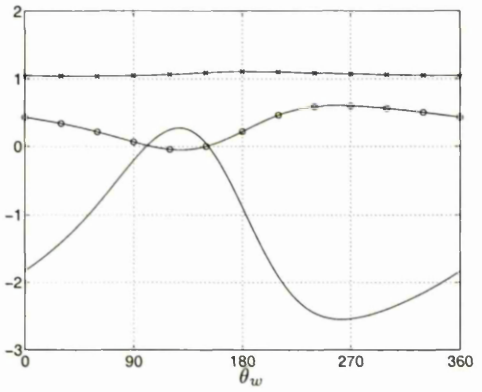

Figure 3.43: Physical realisability for $m = 2.0$.
—, $10 \times \omega$; -o-, $10 \times d$; -×-, c_0^2.

there is no discernable wall layer where the velocity gradients are significantly greater than elsewhere in the channel. This is illustrated by figure 3.44.

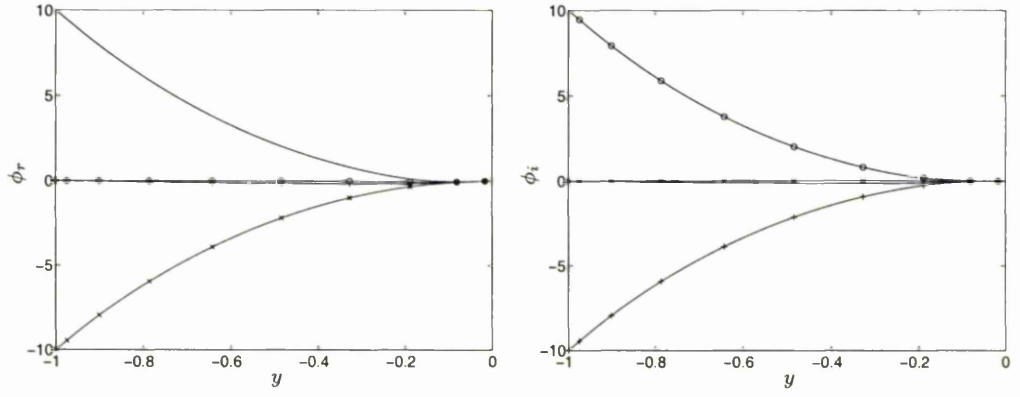

(a) Real Part (b) Imaginary Part

Figure 3.44: Eigenfunctions for the antisymmetric R modes.
—, $\theta_w = 0°$; -o-, $\theta_w = 90°$; -×-, $\theta_w = 180°$; -+-, $\theta_w = 270°$.

Asymmetric Channel Modes

To round off the decriptions of the various mode classes obtained via the numerics, we shall conclude by considering modes of the Resonant class for the asymmetric channel. Examples of the phase speeds and growth rates are given

in figure 3.45, for $Re = 8000.0$, $\alpha = 0.01$ and $|\phi_w| = 6.0, 30.0, 60.0$. As for the previously considered mode classes, the phase velocities are the same as for the symmetric modes of the same class and same parameters, but with a wall stream function which is twice the corresponding value for the symmetric modes.

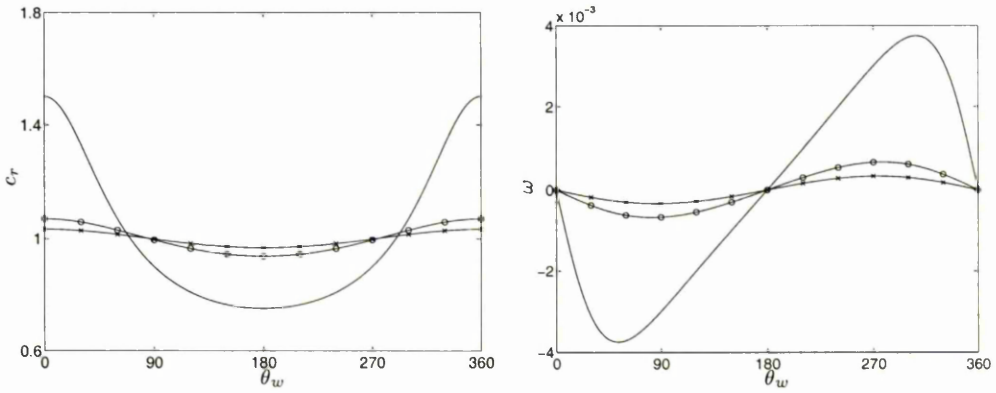

(a) Phase Speed (b) Growth Rate

Figure 3.45: Asymmetric R channel modes.
—, $|\phi_w| = 6.0$; -o-, $|\phi_w| = 30.0$; -×-, $|\phi_w| = 60.0$.

However, there are major differences between the symmetric and asymmetric modes with regard to physical realisability. Plots of the wall-parameter bounds (see figure 3.46) show that whereas the symmetric modes have bounds which correspond to case 1 in section 2.3.2, the asymmetric modes with the same phase velocity have bounds which correspond to case 2. An increase in the free-wave speed of the wall, c_0, should then eliminate any modes of this class.

Back-calculated values of the wall parameters, d and c_0^2, are given in figure 3.47 for $|\phi_w| = 60.0$ and $m = 100.0$. This shows there to be a small unstable physically realisable region below $\theta_w = 360°$. Given that the lower bound for m is strictly greater than zero for all physically realisable unstable modes, all unstable asymmetric R modes, where $|\phi_w| = 60.0$, can be eliminated by a reduction in m. Another way to eliminate these modes would be to choose a value of c_0 such that

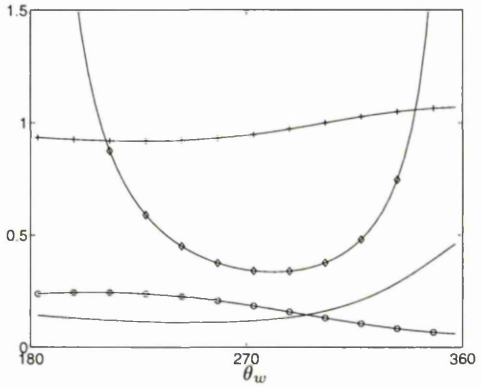

Figure 3.46: Physical realisability bounds on m, d and c_0^2.
—, $10 \times d$ lower bound; -o-, $10^{-3} \times m$ lower bound; -◇-, $10^{-4} \times m$ upper bound; -+-, c_0^2 upper bound.

c_0^2 is greater than the maximum of the upper bound for c_0^2 (which is finite).

The most notable feature of figures 3.47 and 3.45(a) though, is the marked difference between c_0, which oscillates about zero and c_r, which oscillates about one. As explained for the symmetric modes in the symmetric channel, it is expected that c_0 and c_r should be roughly equal for the Resonant modes. However,

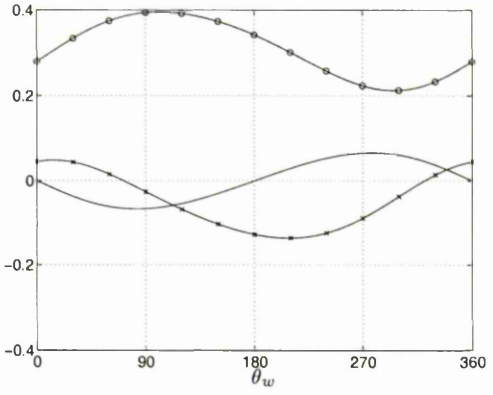

Figure 3.47: Physical realisability for $m = 100.0$.
—, $10 \times \omega$; -o-, d; -×-, c_0^2.

the oscillations are still roughly in phase and one explanation could be that the wave number is low enough such that the asymmetric R mode is in the long-wave

scheme described in section 3.6. Here, the modes are determined by a predominantly viscous theory and the bounds are found to correspond to case 2 of section 2.3.2 to leading order in α. Similarly, the long-wave symmetric R modes, in section 3.6, also have wall-parameter bounds which correspond case 2, to leading order in α. However, the symmetric R modes given in this section have bounds corresponding to case 1 in section 3.6 and hence are probably governed by the established inviscid theory.

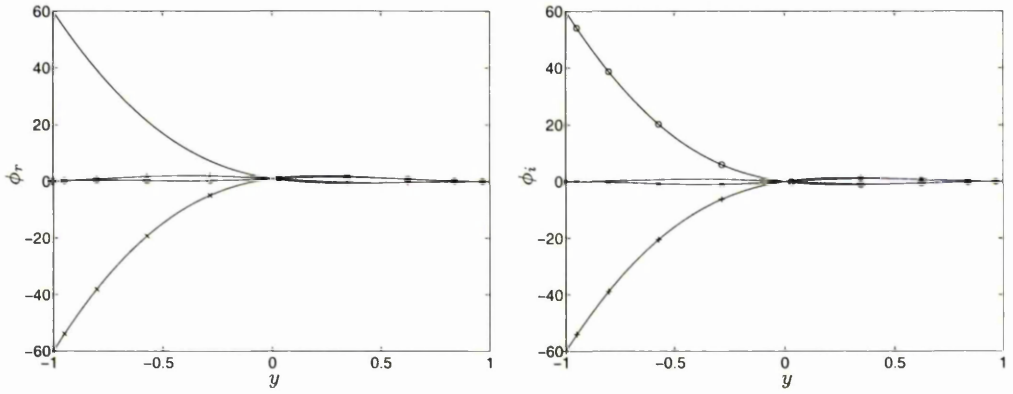

(a) Real Part (b) Imaginary Part

Figure 3.48: Eigenfunctions for the asymmetric R modes.
—, $\theta_w = -180°$; -o-, $\theta_w = 0°$; -×-, $\theta_w = 180°$; -+-, $\theta_w = 540°$.

Finally, example eigenfunctions are given in figure 3.48, for $|\phi_w| = 60.0$. These show that the greatest disturbances occur near the compliant wall with very little activity near the rigid wall, unlike for the modes previously encountered. There is a small amount of activity in the region surrounding the channel centreline, though this is dominated by that which occurs close to the compliant wall.

3.6 Analytical Results

We have been able to find analytical solutions to the governing stability equations for specific kinematic parameter ranges. These may be divided into two main sections, which are given below.

3.6.1 The Viscous Limit

The first set of analytical solutions are for the viscous modes. These occur in the limit $Re \to 0$ where, it can be seen in figures 3.49 and 3.50, that the phase velocities of the KH and R modes tend towards a generally non-zero value for any ϕ_w and any geometry of mode. Kumaran [45] formulated a theory for viscous ($Re \to 0$) modes in a pipe bounded by a visco-elastic continuum of a specified thickness. It was then shown that instabilities could exist provided that the non-dimensional velocity, Γ, exceeded the transitional value, Γ_t, both of which depend on the material parameters of the fluid and solid and on the pipe and wall dimensions.

We aim to follow a similar approach to establishing a viscous theory for the kinematic modes in a channel bounded by one or more compliant walls. Also, the classes of instability will be identified.

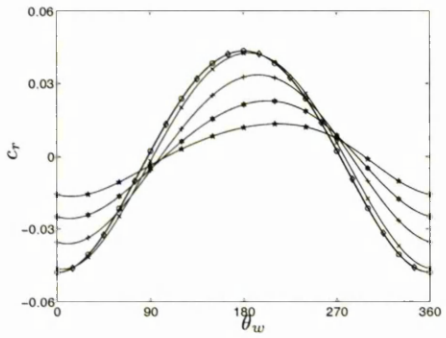

(a) c_r for symmetric modes

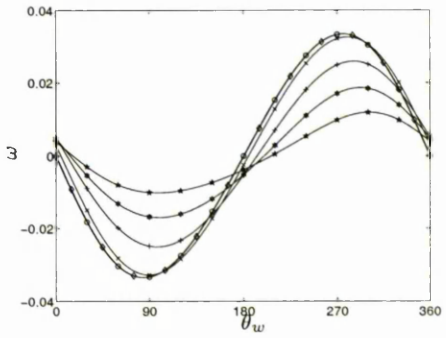

(b) ω for symmetric modes

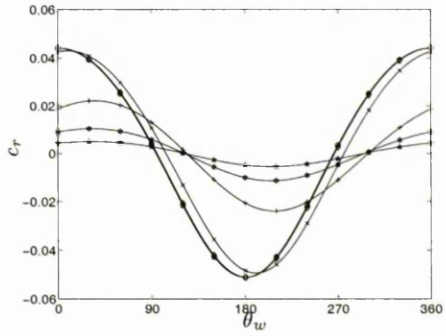

(c) c_r for antisymmetric modes

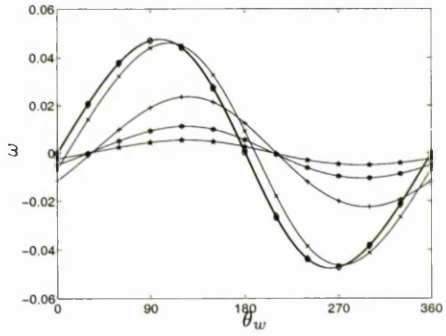

(d) ω for antisymmetric modes

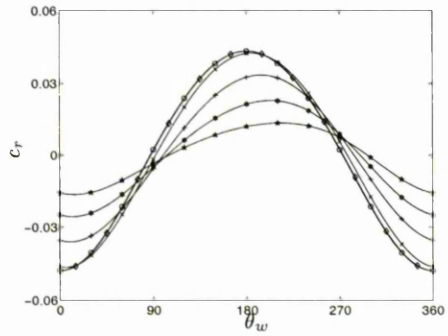

(e) c_r for asymmetric modes

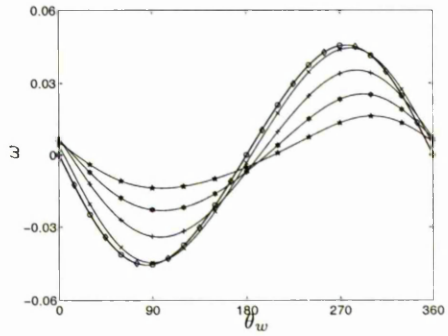

(f) ω for asymmetric modes

Figure 3.49: Phase-Velocities of the KH channel modes as $Re \to 0$.

-○-, $Re = 10^{-6}$; -◇-, $Re = 1$; -×-, $Re = 10$;

-+-, $Re = 10^2$; -∗-, $Re = 10^3$; -⋆-, $Re = 10^4$.

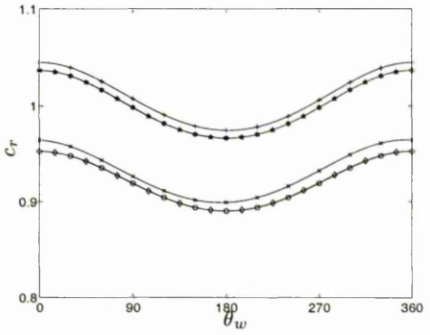

(a) c_r for symmetric modes

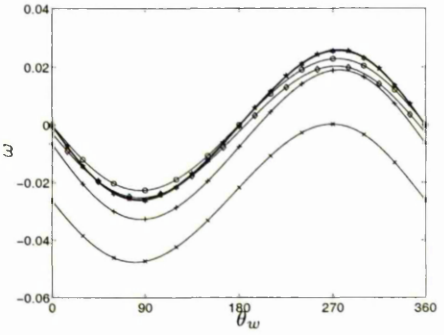

(b) ω for symmetric modes

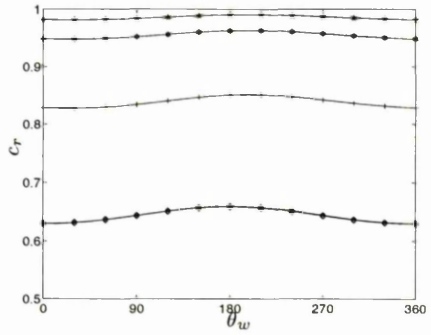

(c) c_r for antisymmetric modes

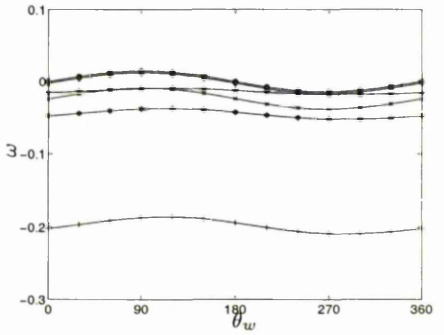

(d) ω for antisymmetric modes

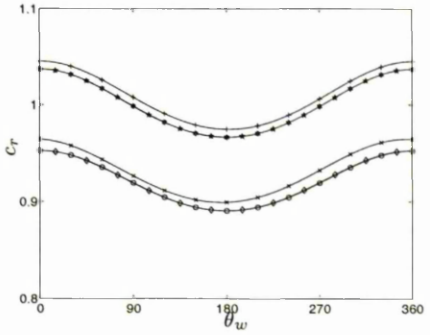

(e) c_r for asymmetric modes

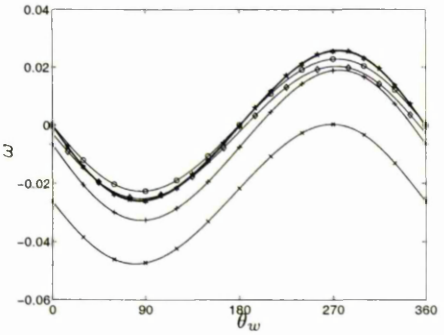

(f) ω for asymmetric modes

Figure 3.50: Phase-Velocities of the R channel modes as $Re \to 0$.

-○-, $Re = 10^{-6}$; -◇-, $Re = 1$; -×-, $Re = 10$;

-+-, $Re = 10^2$; -∗-, $Re = 10^3$; -⋆-, $Re = 10^4$.

In the limit $Re \to 0$ the pressure gradient is balanced by the viscous terms. However, our inertial pressure scaling, $p^* = \rho U^2 p$, implies that the pressure gradient of the basic flow would then become infinite. Hence, we need to rescale the Navier-Stokes equations using the viscous pressure scaling, $p^* = (\mu U/L)p$, to obtain:

$$\frac{\partial u_x}{\partial t} + u_x\frac{\partial u_x}{\partial x} + u_y\frac{\partial u_x}{\partial y} + u_z\frac{\partial u_x}{\partial z} = \frac{1}{Re}\left(-\frac{\partial p}{\partial x} + \frac{\partial^2 u_x}{\partial x^2} + \frac{\partial^2 u_x}{\partial y^2} + \frac{\partial^2 u_x}{\partial z^2}\right), \tag{3.33a}$$

$$\frac{\partial u_y}{\partial t} + u_x\frac{\partial u_y}{\partial x} + u_y\frac{\partial u_y}{\partial y} + u_z\frac{\partial u_y}{\partial z} = \frac{1}{Re}\left(-\frac{\partial p}{\partial y} + \frac{\partial^2 u_y}{\partial x^2} + \frac{\partial^2 u_y}{\partial y^2} + \frac{\partial^2 u_y}{\partial z^2}\right), \tag{3.33b}$$

$$\frac{\partial u_z}{\partial t} + u_x\frac{\partial u_z}{\partial x} + u_y\frac{\partial u_z}{\partial y} + u_z\frac{\partial u_z}{\partial z} = \frac{1}{Re}\left(-\frac{\partial p}{\partial z} + \frac{\partial^2 u_z}{\partial x^2} + \frac{\partial^2 u_z}{\partial y^2} + \frac{\partial^2 u_z}{\partial z^2}\right), \tag{3.33c}$$

where, as before, $Re = \rho UL/\mu$ is the Reynolds number of the flow. With this scaling, the pressure of the basic flow now takes the modified form, $p_B = -2x$, but since it does not appear in the stability equations this change will have no bearing on them.

Following the normal mode analysis of section 3.3, we obtain the revised linearised stability equations for $Re \ll 1$:

$$i\alpha Re(u_B - c)u + Re(Du_B)v = -i\alpha p + \left(D^2 - \alpha^2\right)u, \tag{3.34a}$$

$$i\alpha Re(u_B - c)v = -Dp + \left(D^2 - \alpha^2\right)v, \tag{3.34b}$$

$$i\alpha u + Dv = 0. \tag{3.34c}$$

Here again, α is the positive, real streamwise wavenumber and we have envoked Squire's theorem to reduce the problem to that of studying two-dimensional disturbances. Thus, the normal modes are as for equation (3.6), with $\beta, w = 0$.

Taking the limit $Re \to 0$, of equations (3.34), yields

$$\left(D^2 - \alpha^2\right) u - i\alpha\, p = 0\,, \tag{3.35a}$$

$$\left(D^2 - \alpha^2\right) v - Dp = 0\,, \tag{3.35b}$$

$$i\alpha\, u + Dv = 0\,. \tag{3.35c}$$

From these equations we should recover the solutions for small Reynolds numbers, as given by our numerical scheme.

The general solution to the set of equations (3.35) can be obtained by applying $(D^2 - \alpha^2)$ to equation (3.35c) and then substituting for the velocity components, u and v in terms of the pressure, p. Doing this, we obtain the single second-order linear differential equation for the pressure,

$$(D^2 - \alpha^2)p = 0\,.$$

This has the general solution

$$p(y) = P_c \cosh(\alpha y) + P_s \sinh(\alpha y)\,, \tag{3.36}$$

where P_c and P_s are constants. The x and y momentum equations then yield the following general expressions for the velocities:

$$u(y) = \left(U_c + \frac{i}{2}P_s y\right)\cosh(\alpha y) + \left(U_s + \frac{i}{2}P_c y\right)\sinh(\alpha y)\,, \tag{3.37a}$$

$$v(y) = \left(V_c + \frac{1}{2}P_c y\right)\cosh(\alpha y) + \left(V_s + \frac{1}{2}P_s y\right)\sinh(\alpha y)\,, \tag{3.37b}$$

with the restrictions

$$i\alpha U_c + \alpha V_s + \frac{1}{2}P_c = 0\,, \tag{3.38a}$$

$$i\alpha U_s + \alpha V_c + \frac{1}{2}P_s = 0\,, \tag{3.38b}$$

which must also be imposed in order to satisfy the continuity equation (3.35c). Here, U_c, U_s, V_c and V_s are constants.

These two continuity conditions, along with the three boundary conditions and the normalisation condition, give us the six equations necessary to evaluate the six unknowns U_c, U_s, V_c, V_s, P_c and P_s. We shall proceed by considering the three cases of symmetric modes in the symmetric channel, antisymmetric modes in the symmetric channel and modes in the asymmetric channel, as follows.

The Symmetric Channel: symmetric modes

To summarise, the conditions which must be met in this case are:

$$\begin{aligned} u(0) &= 0\,, \\ D^2u(0) &= 0\,, \\ v(0) &= -i\alpha\,, \\ v(-1) &= -i\alpha\phi_w\,, \\ i\alpha U_c + \alpha V_s + \frac{1}{2}P_c &= 0\,, \\ i\alpha U_s + \alpha v_c + \frac{1}{2}P_s &= 0\,. \end{aligned}$$

It is easy to verify that the values of the unknowns must be, therefore:

$$\begin{aligned} U_c &= 0\,, \\ U_s &= \alpha + \frac{\phi_w - \cosh\alpha}{\sinh\alpha}\,, \\ V_c &= -i\alpha\,, \\ V_s &= 0\,, \\ P_c &= 0\,, \\ P_s &= 2i\alpha\frac{\cosh\alpha - \phi_w}{\sinh\alpha}\,. \end{aligned}$$

This allows us to find an expression for the phase velocity eigenvalue using the condition for the streamwise velocity at the compliant wall, $u(-1) = -2\phi_w/c$ and our expression for $u(-1)$, namely

$$u(-1) = \bar{u}(\alpha)\left(1 + \tilde{u}(\alpha)\phi_w\right)\,,$$

where

$$\bar{u}(\alpha) = \frac{\alpha + \sinh\alpha\cosh\alpha}{\sinh\alpha}, \tag{3.39a}$$

$$\tilde{u}(\alpha) = -\frac{\alpha\cosh\alpha + \sinh\alpha}{\alpha + \sinh\alpha\cosh\alpha}. \tag{3.39b}$$

Hence, our expression for the phase velocity becomes

$$c = -\frac{2\phi_w}{\bar{u}(\alpha)}\left(1 + \tilde{u}(\alpha)\phi_w\right)^{-1}, \tag{3.40}$$

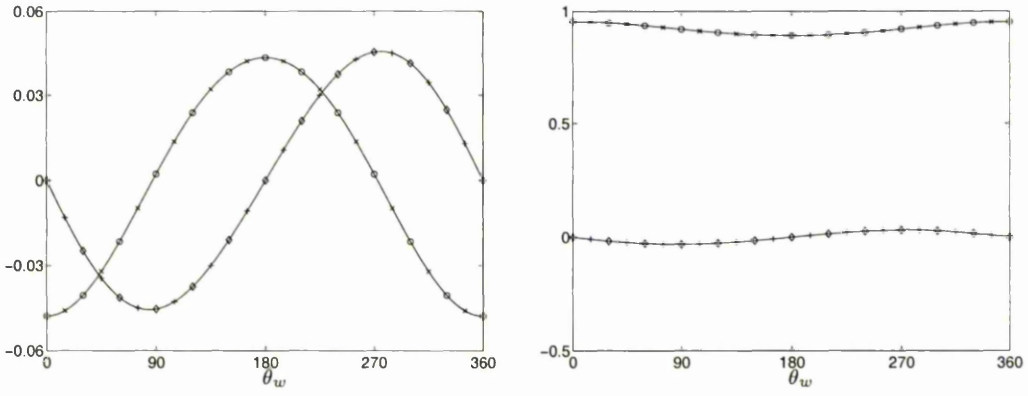

(a) KH modes.

(b) R modes.

Figure 3.51: Analytical-Numerical comparison for the viscous symmetric channel modes.

-o-, analytical c_r; -◇-, analytical c_i; -×-, numerical c_r; -+-, numerical c_i.

For the case $\alpha = 0.733$ the phase velocity was plotted for the KH modes where $|\phi_w| = 0.05$ and compared with the numerical solutions for $Re = 10^{-6}$. Similarly, the phase velocity for the Resonant modes where $\alpha = 0.733$, $|\phi_w| = 30.0$ were plotted and compared with the numerical solutions for $Re = 10^{-6}$. These comparisons can be seen in figures 3.51(a) and 3.51(b), respectively, with excellent agreement between the numerics and analysis.

Contour plots of the phase speed in the θ_w-α plane are given in figure 3.52 for various values of $|\phi_w|$. Corresponding plots of the growth rate are given in

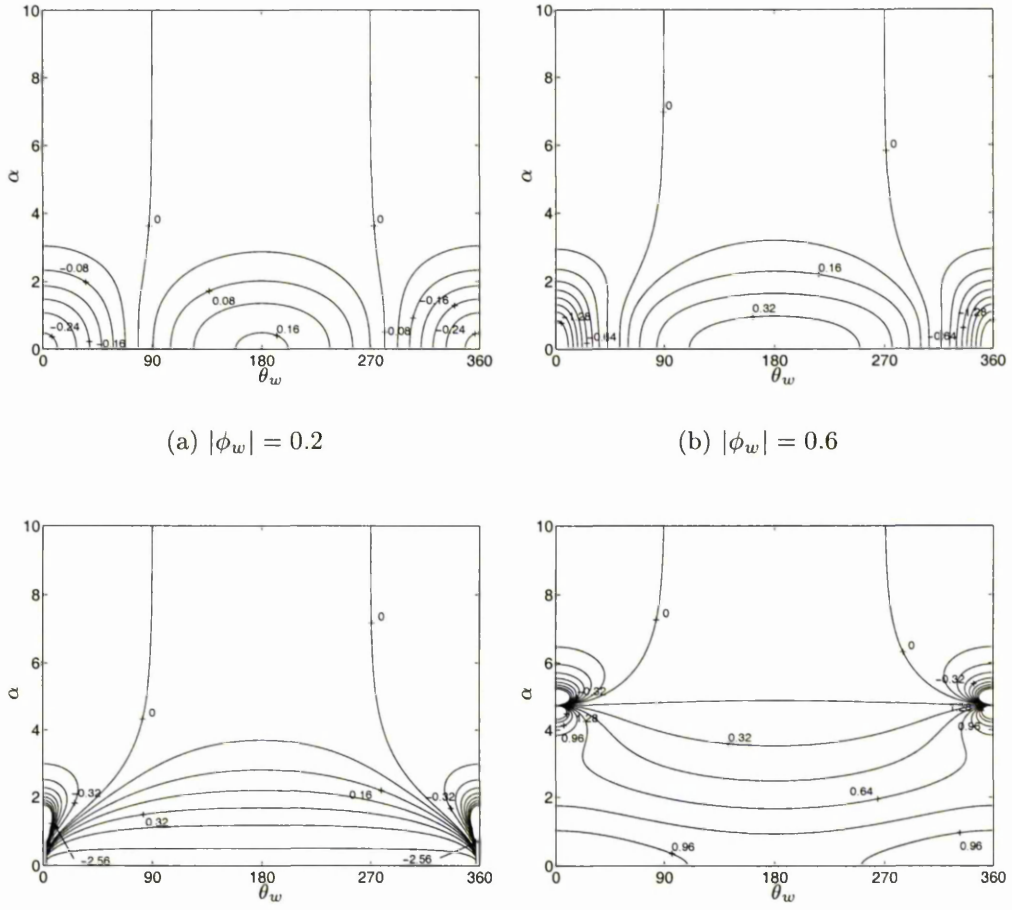

(a) $|\phi_w| = 0.2$

(b) $|\phi_w| = 0.6$

(c) $|\phi_w| = 1.0$

(d) $|\phi_w| = 10.0$

Figure 3.52: Phase-Speeds of the viscous modes.

figure 3.53. These show clearly for smaller values of $|\phi_w|$ (see figures 3.52(a) and 3.52(b)) that the modes belong in the KH class for all values of α. Here, the phase velocities take values oscillating about zero as θ_w is varied. However, as $|\phi_w|$ is increased a singularity appears, initially at $\alpha = 0$ for $|\phi_w| = 1.0$. This singularity occurs at increasing α as $|\phi_w|$ is further increased. For values of α above that at which the singularity occurs the modes remain as members of the KH class. However, for those modes occurring at lower wave numbers than the singularity, the modes belong to the Resonant class and hence the phase velocity

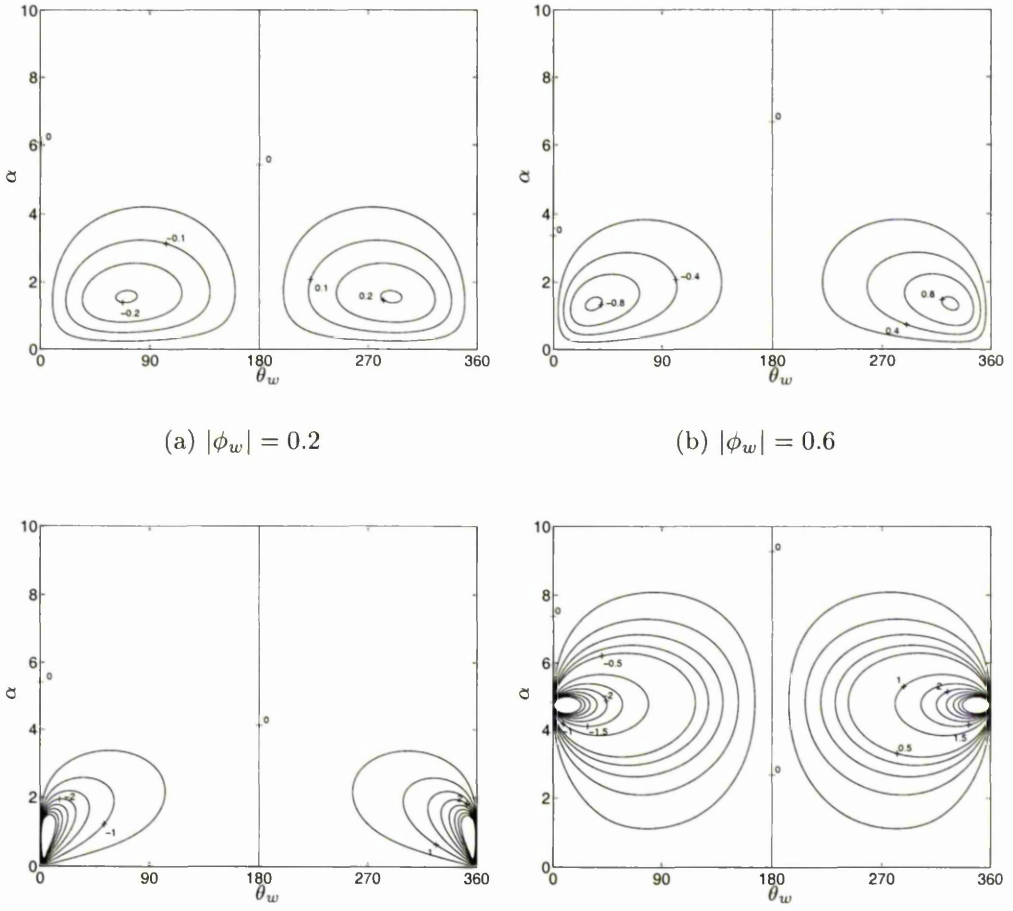

(a) $|\phi_w| = 0.2$

(b) $|\phi_w| = 0.6$

(c) $|\phi_w| = 1.0$

(d) $|\phi_w| = 10.0$

Figure 3.53: Growth-Rates of the viscous modes.

oscillates about a real non-zero value as θ_w is varied.

Therefore, we see that the range of $|\phi_w|$, in which the transitional modes occur, has shrunk to zero in the limit $Re \to 0$. Only the singularity remains of the process by which the transition from TS to R modes and more importantly in this case, from KH to R modes occurs.

All the above can be deduced from expressions (3.39b) and (3.40). If we define α_c as the critical wave number at which the singularity occurs when $\phi_w = (\phi_w)_c$, then $(\phi_w)_c = -1/\tilde{u}(\alpha_c)$. Figure 3.54 plots $\tilde{u}$ against α for $\alpha \geq 0$. This illustrates

three important properties of $\tilde{u}$ which can be deduced analytically from equation (3.39b). The first is that $\tilde{u}$ is -1 when α is zero. The second is that $\tilde{u}$ is a strictly increasing function for $\alpha > 0$. The third is that $\tilde{u} \to 0$ as $\alpha \to \infty$. These imply that $-1/\tilde{u}$ also is a strictly increasing function for $\alpha > 0$, is equal to 1 when $\alpha = 0$ and tends to infinity as $\alpha \to \infty$. Therefore, α_c, can take any value from zero upwards. Hence also, α_c can only exist for $|\phi_w| \geq 1$ and α_c increases as $|\phi_w|$ is increased.

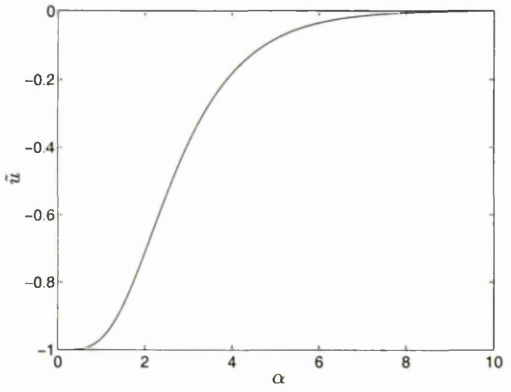

Figure 3.54: $\tilde{u}$ for the viscous symmetric channel modes.

Having identified the kinematic modes which exist in the viscous limit, it is necessary to consider the physical realisability of such modes. Plots of the wall-parameter bounds are given in figure 3.55 for the KH modes with $|\phi_w| = 0.2$ and $\alpha = 1.0$. This shows that the bounds correspond to those of case 2 in section 2.3.2 and it appears that this is the case for any unstable viscous KH mode. Figure 3.56 plots the back-calculated d and c_0^2 for the same kinematic parameters and shows that there is only a small "unstable pocket". Figure 3.55 shows that a small increase in m will increase the size of the unstable region. There is a maximum value for the upper bound of c_0^2 and hence, choosing a value of the tension which corresponds to a value of c_0^2 greater than this, the unstable viscous KH modes for $|\phi_w| = 0.2$ and $\alpha = 1.0$ will be eliminated.

Physical realisability plots for the Resonant modes are shown in figures 3.57

and 3.58. These plot the parameter bounds for $|\phi_w| = 10.0$, $\alpha = 1.0$ and the back-calculated values of d and c_0^2 for $m = 0.2$, $|\phi_w| = 10.0$ and $\alpha = 1.0$, respectively.

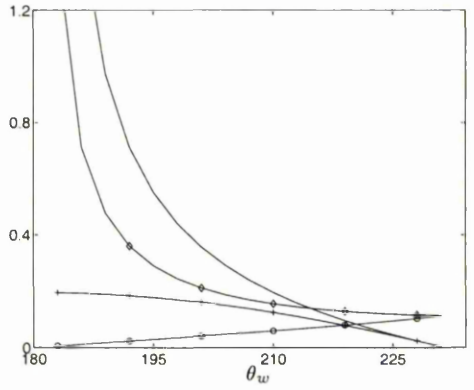

Figure 3.55: Physical realisability bounds on m, d and c_0^2 for the KH modes. —, d lower bound; -o-, $10^{-3} \times m$ lower bound; -◇-, $10^{-3} \times m$ upper bound; -+-, $10 \times c_0^2$ upper bound.

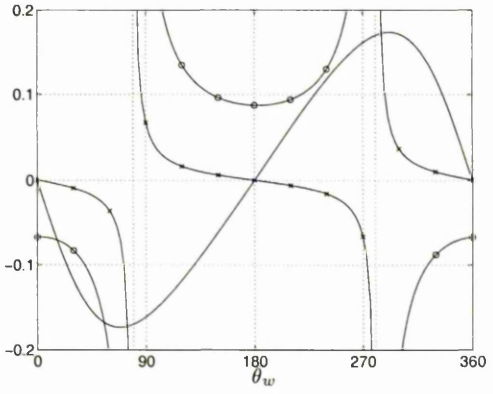

Figure 3.56: Physical realisability of the KH modes for $m = 2.0$. —, ω; -o-, $10^{-2} \times d$; -×-, $10^{-2} \times c_0^2$.

The plots for the upper bounds on m and d have been omitted from figure 3.57 for clarity. This illustrates one important difference between the viscous Resonant and KH modes, namely that between the sizes of the respective physically realisable regions. For the KH modes the physically realisable region covers only

a relatively small subset of the unstable modes, whereas for the Resonant modes any unstable mode can be realised for some set of wall parameters. One notable common property shared by the viscous KH and Resonant modes is that all the physically realisable modes appear to correspond to case 2 in section 2.3.2.

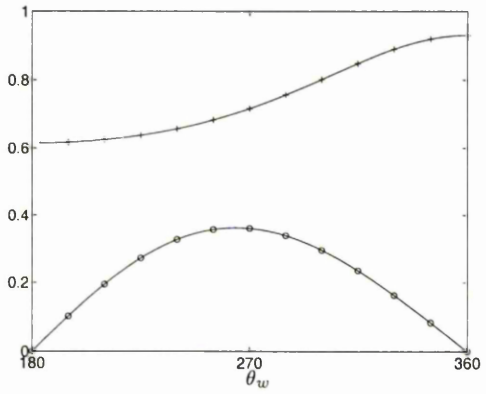

Figure 3.57: Physical realisability bounds on m, d and c_0^2 for the R modes.
-o-, m lower bound; -+-, c_0^2 upper bound.

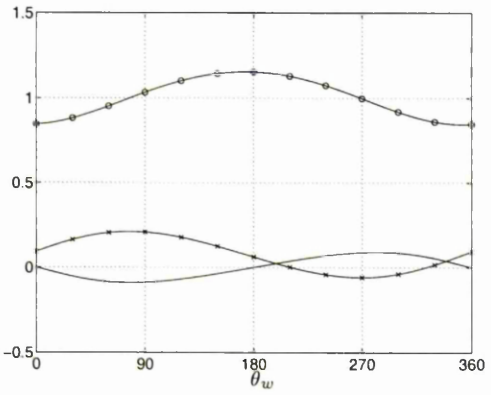

Figure 3.58: Physical realisability of the R modes for $m = 0.2$.
—, ω; -o-, $10^{-1} \times d$; -×-, $10^{-1} \times c_0^2$.

The upper bounds for m and d tend to infinity at the extremes of the physically realisable region with a minimum near the centre of this region. The lower bound for m, however, tends to zero at the extremes of the same region with a maximum

near the centre. If m is chosen such that it lies between the maximum of its lower bound and the minimum of its upper bound, then all the unstable modes for $|\phi_w| = 10.0$ will be physically realisable. At the other extreme, the upper bound for c_0^2 remains finite and so by ensuring that the tension is large enough such that c_0^2 is greater than the maximum of its upper bound, the viscous Resonant modes corresponding to $|\phi_w| = 10.0$ can be eliminated.

Now for a fixed wall density, only a specific value of d will give rise to the instability associated with the singularity ($c_0^2 \to \infty$ as the singularity is approached and hence in practice this mode is unobtainable, anyway). Hence, by choosing other values of the damping and free wave speed, it should be possible to avoid the occurence of this instability and any others in a small region surrounding it in the ϕ_w-α plane. Therefore, it would appear that any unstable symmetric viscous modes can be eliminated by an increase in the free-wave speed, c_0. Davies and Carpenter [15] showed that such an increase was generally stabilising for flow-induced surface instabilities at finite Reynolds numbers.

The Symmetric Channel: antisymmetric modes

To summarise, the conditions which must be met in this case are:

$$
\begin{aligned}
v(0) &= 0\,, \\
D^2 v(0) &= 0\,, \\
u(0) &= 1\,, \\
v(-1) &= -i\alpha\phi_w\,, \\
i\alpha U_c + \alpha V_s + P_c &= 0\,, \\
i\alpha U_s + \alpha v_c + P_s &= 0\,.
\end{aligned}
$$

It is easy to verify that the values of the unknowns must be, therefore:

$$
\begin{aligned}
U_c &= 1\,, \\
U_s &= 0\,, \\
V_c &= 0\,, \\
V_s &= i\alpha \frac{\phi_w + \cosh\alpha}{\sinh\alpha - \alpha\cosh\alpha}\,, \\
P_c &= -2i\alpha \frac{\alpha\phi_w + \sinh\alpha}{\sinh\alpha - \alpha\cosh\alpha}\,, \\
P_s &= 0\,.
\end{aligned}
$$

This allows us to find an expression for the phase velocity eigenvalue using the condition for the streamwise velocity at the compliant wall, $u(-1) = -2\phi_w/c$ and our expression for $u(-1)$, which again takes the form

$$u(-1) = \bar{u}(\alpha)\left(1 + \tilde{u}(\alpha)\phi_w\right)\,.$$

Here,

$$\bar{u} = \frac{\sinh\alpha\cosh\alpha - \alpha}{\sinh\alpha - \alpha\cosh\alpha}\,, \tag{3.41a}$$

$$\tilde{u} = \frac{\alpha^2\sinh\alpha}{\sinh\alpha\cosh\alpha - \alpha}\,. \tag{3.41b}$$

Hence, our expression for the phase velocity again becomes

$$c = -\frac{2\phi_w}{\bar{u}(\alpha)}\left(1 + \tilde{u}(\alpha)\phi_w\right)^{-1}\,. \tag{3.42}$$

For the case $\alpha = 0.733$, the phase velocity was plotted for the KH modes where $|\phi_w| = 0.05$ and compared with the numerical solutions for $Re = 10^{-6}$. Similarly, the phase velocity for the Resonant modes, where $\alpha = 0.733$ and $|\phi_w| = 30.0$, were plotted and compared with the numerical solutions for $Re = 10^{-6}$. These comparisons can be seen in figures 3.59(a) and 3.59(b), respectively, with excellent agreement between the numerics and analysis.

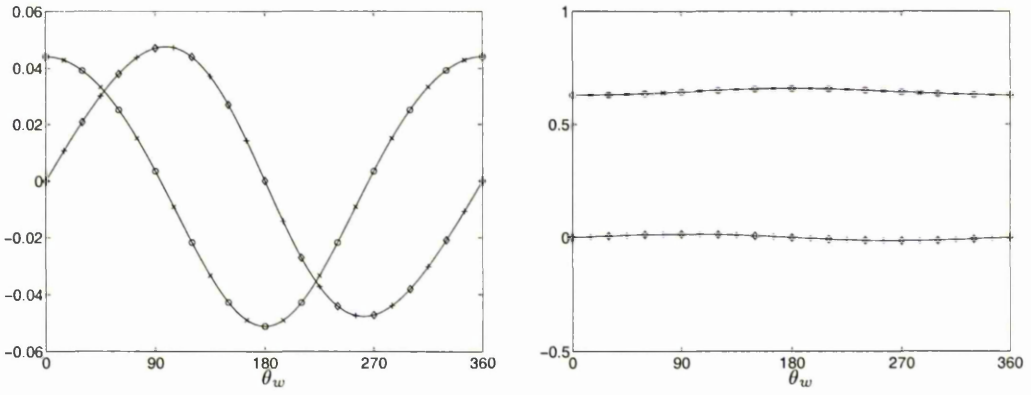

(a) KH modes. (b) R modes.

Figure 3.59: Analytical-Numerical comparison for the viscous antisymmetric channel modes.
-o-, analytical c_r; -$\diamond$-, analytical c_i; -$\times$-, numerical c_r; -+-, numerical c_i.

Contour plots in the θ_w-α plane for the phase speed and growth rates are given in figures 3.60 and 3.61 respectively, for various values of $|\phi_w|$. These show that, as for the symmetric viscous case, the modes belong in the KH class for smaller values of $|\phi_w|$. Similarly, as $|\phi_w|$ is increased, modes of the Resonant class come into existence for smaller values of α. For fixed $|\phi_w|$, modes of the different classes are separated by a singularity associated with the zero of the term, $(1 + \tilde{u}\phi_w)$, in expression (3.42) for the phase velocity.

Now, $\tilde{u}$ is a strictly decreasing function of α for $\alpha > 0$. Also, $\tilde{u} = 3/2$ at $\alpha = 0$ and $\tilde{u} \to 0$ as $\alpha \to \infty$. This is illustrated in figure 3.62. Hence, $-1/\tilde{u}$ is a strictly decreasing function for $\alpha > 0$, which takes all values less than $-2/3$.

Now, if we define α_c as the critical wave number at which the singularity occurs when $\phi_w = (\phi_w)_c$, then $(\phi_w)_c = -1/\tilde{u}(\alpha_c)$. Therefore, $(\phi_w)_c$ takes values less than $-2/3$ and the Resonant modes can only occur for $|\phi_w| > 2/3$.

The physical realisability bounds for the unstable viscous KH modes appear to correspond to case 2 for all ϕ_w and α. Hence, as for the viscous symmetric KH

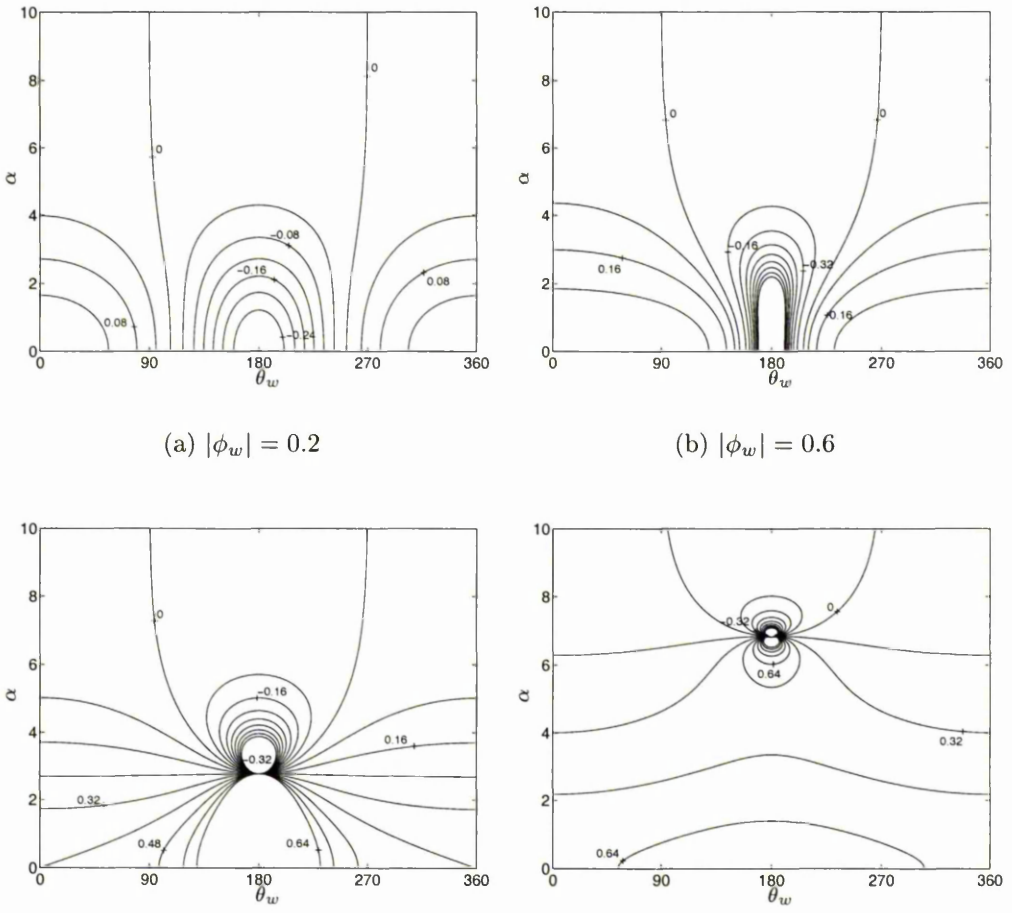

(a) $|\phi_w| = 0.2$

(b) $|\phi_w| = 0.6$

(c) $|\phi_w| = 1.0$

(d) $|\phi_w| = 10.0$

Figure 3.60: Phase-Speeds of the viscous modes.

modes, we may reduce the physically realisable unstable antisymmetric modes to a small "unstable pocket" by making m sufficiently large or small. Furthermore, we may eliminate altogether the unstable viscous KH modes by increasing the free-wave speed, c_0, sufficiently.

The back-calculated values of d and c_0^2 are plotted against θ_w in figure 3.64, for $m = 2$, $\alpha = 1.0$ and $|\phi_w| = 0.2$. Here, the value of m is small enough so that the physically realisable unstable modes do indeed lie in an "unstable pocket".

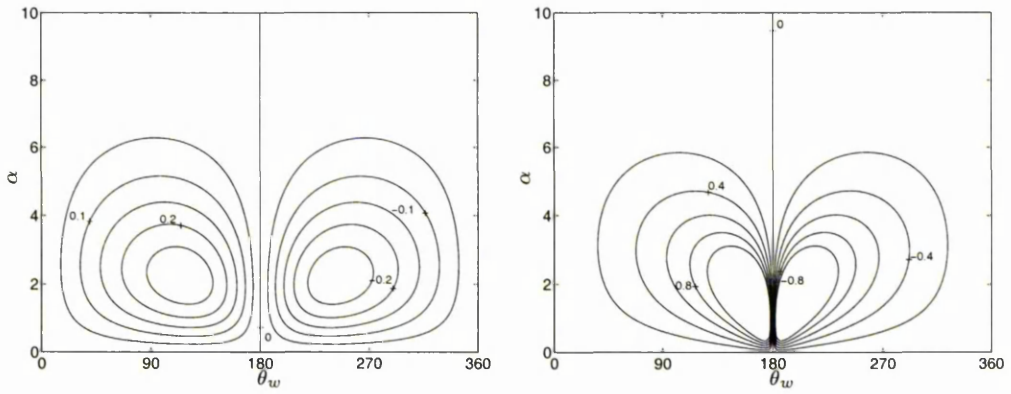

(a) $|\phi_w| = 0.2$ (b) $|\phi_w| = 0.6$

(c) $|\phi_w| = 1.0$ (d) $|\phi_w| = 10.0$

Figure 3.61: Growth-Rates of the viscous modes.

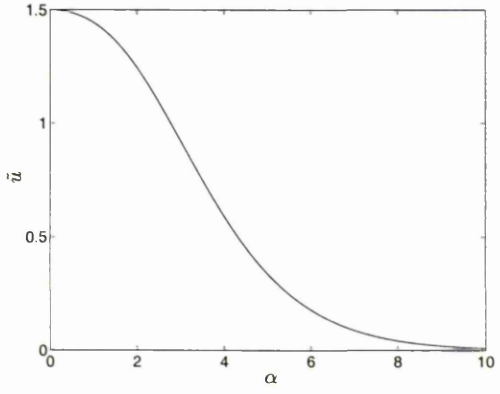

Figure 3.62: $\tilde{u}$ for the viscous antisymmetric channel modes.

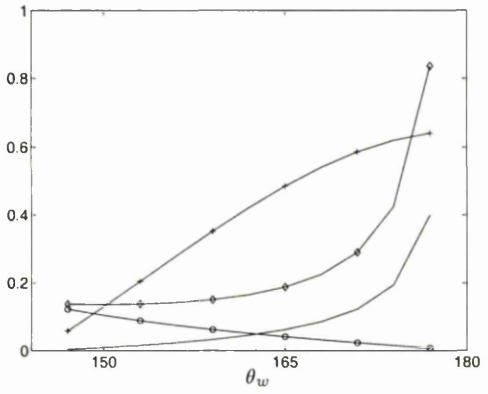

Figure 3.63: Physical realisability bounds on m, d and c_0^2 for the KH modes.

—, $10^{-1} \times d$ lower bound;

-○-, $10^{-3} \times m$ lower bound; -◇-, $10^{-3} \times m$ upper bound;

-+-, $10 \times c_0^2$ upper bound.

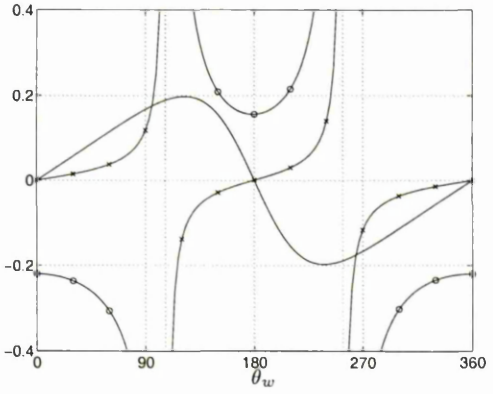

Figure 3.64: Physical realisability of the KH modes for $m = 2.0$.

—, ω; -○-, $10^{-2} \times d$; -×-, $10^{-2} \times c_0^2$.

None of the antisymmetric viscous R modes seem to obey condition (2.24) for an unstable mode being physically realisable for some set of wall parameters. For the mode where $\alpha = 1.0$ and $|\phi_w| = 10.0$, the back-calculated value of the damping coefficient, d, never exceeds zero. This is illustrated in figure 3.65.

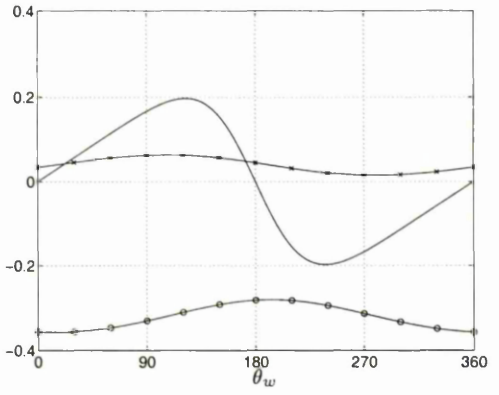

Figure 3.65: Physical realisability of the R modes for $m = 2.0$.
—, ω; -o-, $10^{-1} \times d$; -×-, $10^{-1} \times c_0^2$.

Therefore, like the symmetric viscous modes, the antisymmetric viscous modes can be eliminated by an increase in the free-wave speed of the wall, c_0.

The Asymmetric Channel:

In the case of the asymmetric channel, it is more convenient to write the eigenfunctions in the form:

$$p(y) = P_c \cosh[\alpha(y-1)] + P_s \sinh[\alpha(y-1)]\,,$$
$$u(y) = \left(U_c + \frac{i}{2}P_s(y-1)\right)\cosh[\alpha(y-1)] + \left(U_s + \frac{i}{2}P_c(y-1)\right)\sinh[\alpha(y-1)]\,,$$
$$v(y) = \left(V_c + \frac{1}{2}P_c(y-1)\right)\cosh[\alpha(y-1)] + \left(V_s + \frac{1}{2}P_s(y-1)\right)\sinh[\alpha(y-1)]\,.$$

The continuity conditions remain unaltered by this translation of the independent variable and so the conditions which must be met may be summarised by:

$$\begin{aligned} u(1) &= 0\,, \\ v(1) &= 0\,, \\ v(0) &= -i\alpha\,, \\ v(-1) &= -i\alpha\phi_w\,, \\ i\alpha U_c + \alpha V_s + \frac{1}{2}P_c &= 0\,, \\ i\alpha U_s + \alpha v_c + \frac{1}{2}P_s &= 0\,. \end{aligned}$$

Two of the unknowns are found to be zero using the form of solution given above, which makes the solution easier to establish as:

$$\begin{aligned} U_c &= 0\,, \\ U_s &= \frac{(2\alpha\cosh 2\alpha - \sinh 2\alpha) + (\sinh\alpha - \alpha\cosh\alpha)\phi_w}{\sinh\alpha(\sinh 2\alpha - 2\alpha)}\,, \\ V_c &= 0\,, \\ V_s &= i\alpha\frac{4\cosh\alpha - \phi_w}{\sinh 2\alpha - 2\alpha}\,, \\ P_c &= i\alpha^2\frac{\phi_w - 4\cosh\alpha}{\sinh 2\alpha - 2\alpha}\,, \\ P_s &= i\alpha\frac{(\sinh 2\alpha - 2\alpha\cosh 2\alpha) + (\alpha\cosh\alpha - \sinh\alpha)\phi_w}{\sinh\alpha(\sinh 2\alpha - 2\alpha)}\,. \end{aligned}$$

This allows us to find an expression for the phase velocity eigenvalue using the condition for the streamwise velocity at the compliant wall, $u(-1) = -2\phi_w/c$ and our expression for $u(-1)$, which again takes the form

$$u(-1) = \bar{u}(\alpha)\left(1 + \tilde{u}(\alpha)\phi_w\right)\,.$$

Here

$$\bar{u} = \frac{2\alpha + \sinh 2\alpha}{\sinh\alpha}\,, \tag{3.43a}$$

$$\tilde{u} = -\frac{\alpha\cosh\alpha + \sinh\alpha}{2\alpha + \sinh 2\alpha}\,. \tag{3.43b}$$

Hence again, our expression for the phase velocity becomes

$$c = -\frac{2\phi_w}{\bar{u}(\alpha)} \left(1 + \tilde{u}(\alpha)\phi_w\right)^{-1} . \tag{3.44}$$

By substituting $2\phi_w$ for ϕ_w in the above expression for c, we obtain the phase velocity for the symmetric viscous modes. This lends further support to the hypothesis that the asymmetric and symmetric modes are linked in the way suggested in section 3.5.1.

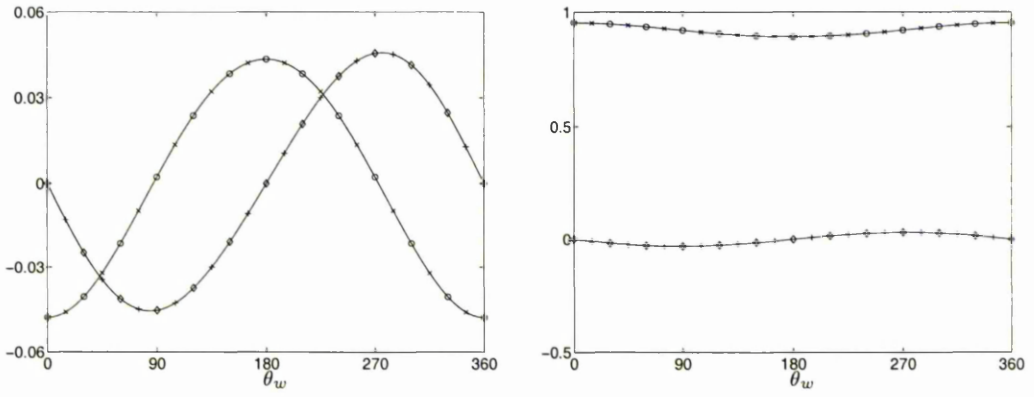

(a) KH modes.

(b) R modes.

Figure 3.66: Analytical-Numerical comparison for the viscous asymmetric channel modes.
-o-, analytical c_r; -◇-, analytical c_i; -×-, numerical c_r; -+-, numerical c_i.

For the case $\alpha = 0.733$ the phase velocity was plotted for the KH modes where $|\phi_w| = 0.1$ and compared with the numerical solutions for $Re = 10^{-6}$. Similarly, the phase velocity for the Resonant modes where $\alpha = 0.733$, $|\phi_w| = 60.0$ were plotted and compared with the numerical solutions for $Re = 10^{-6}$. These comparisons can be seen in figures 3.66(a) and 3.66(b), respectively, with excellent agreement between the numerics and analysis.

Contour plots of the phase speed and the growth rate in the θ_w-α plane are given in figures 3.67 and 3.68. These are identical to those for the symmetric

viscous modes with half the value of the stream function at the wall.

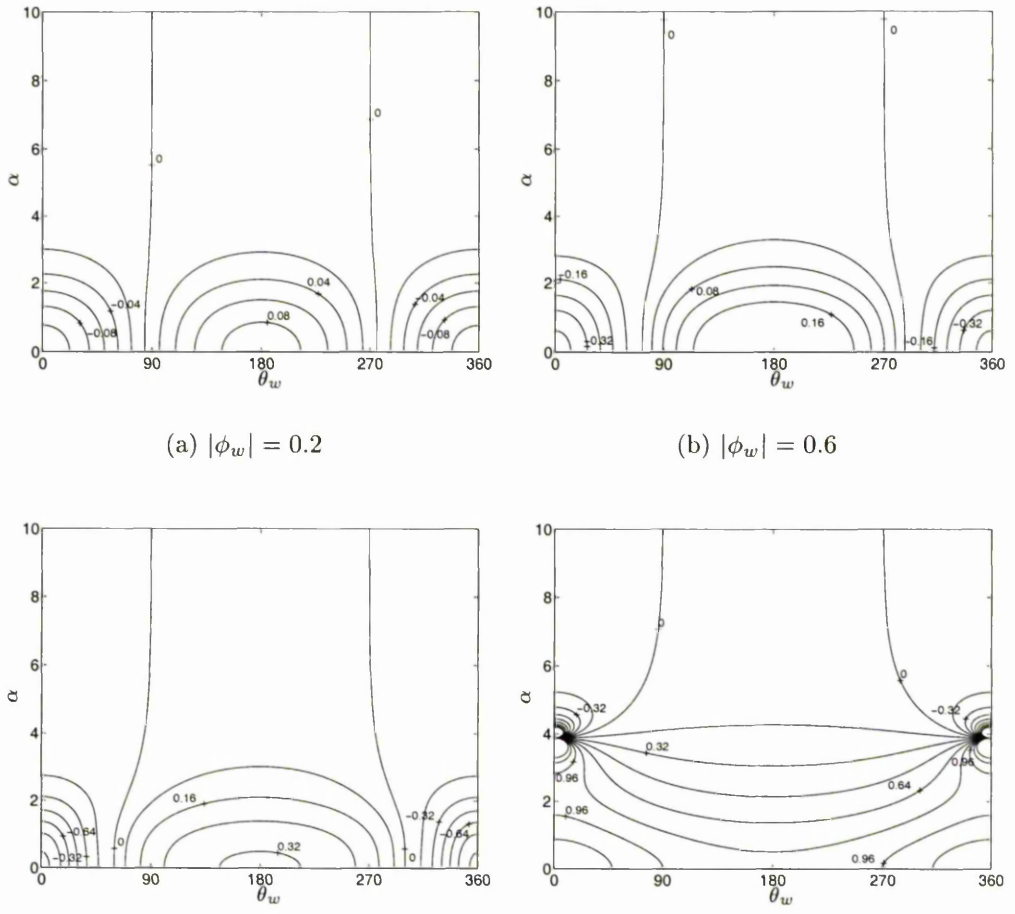

(a) $|\phi_w| = 0.2$

(b) $|\phi_w| = 0.6$

(c) $|\phi_w| = 1.0$

(d) $|\phi_w| = 10.0$

Figure 3.67: Phase-Speeds of the viscous modes.

Plotting $\tilde{u}$ against α for $\alpha > 0$ in figure 3.69, illustrates the property that it takes half the value of that of $\tilde{u}$ for the symmetric modes at the same value of α. This is consistent with the fact that the critical value of ϕ_w (that at which the singularity occurs) for the asymmetric viscous modes, is twice that corresponding to the symmetric viscous modes.

Plots of the wall-parameter bounds for the viscous asymmetric KH modes are given in figure 3.70 for $\alpha = 1.0$ and $|\phi_w| = 0.2$. The bounds correspond to case 2

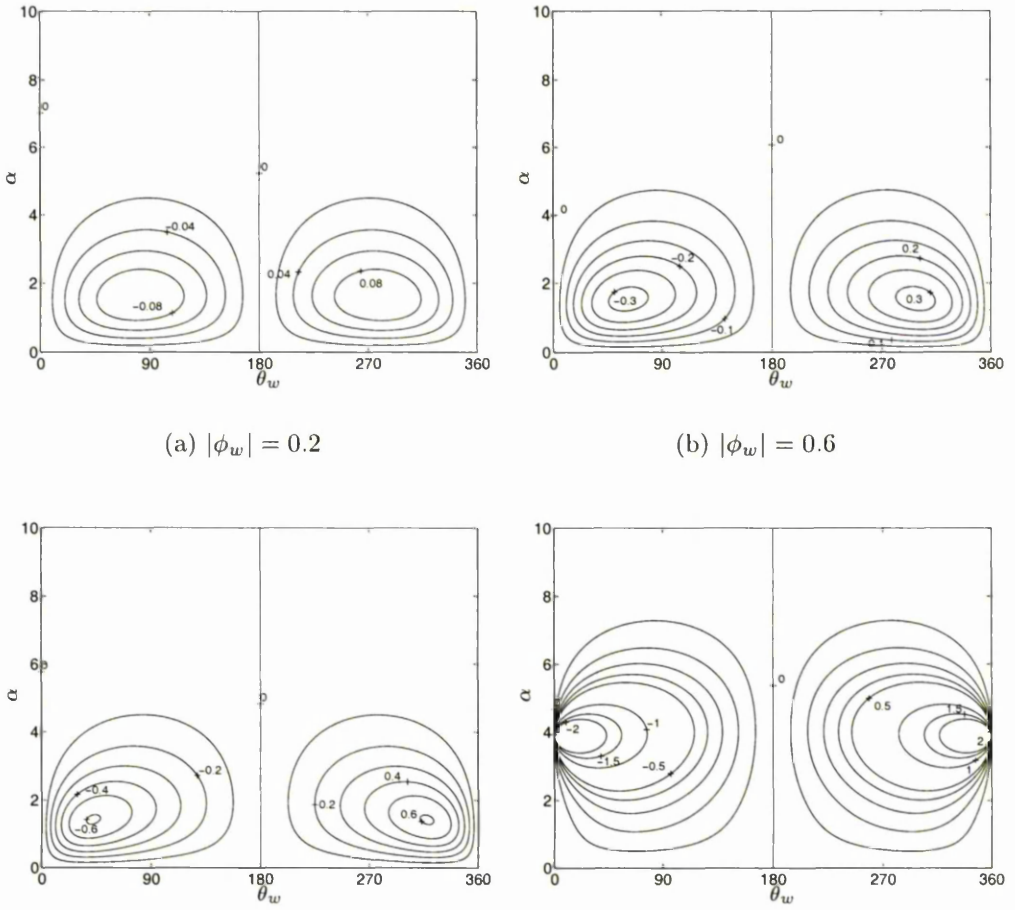

(a) $|\phi_w| = 0.2$

(b) $|\phi_w| = 0.6$

(c) $|\phi_w| = 1.0$

(d) $|\phi_w| = 10.0$

Figure 3.68: Growth-Rates of the viscous modes.

in section 2.3.2, as for the symmetric and antisymmetric cases. All the viscous asymmetric KH modes appear to have wall-parameter bounds corresponding to case 2 in section 2.3.2 and hence we can eliminate instabilities of this type in the same way as for the viscous symmetric KH modes. Therefore, by a sufficiently large increase or decrease in m, we can reduce the physically realisable unstable region to a small "pocket". Alternatively, we can totally eliminate the unstable modes by a suitably large increase in the free-wave speed, c_0. A suitably small value of m to obtain a small "unstable pocket" is 2 for the modes where $\alpha = 1.0$

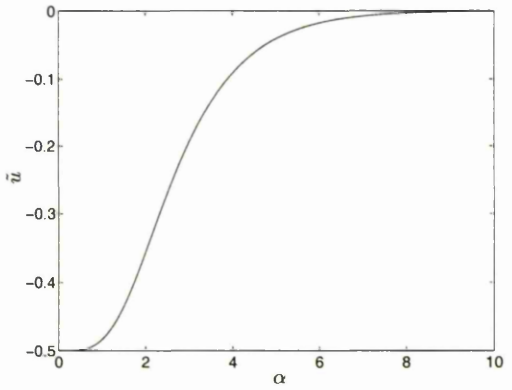

Figure 3.69: $\tilde{u}$ for the viscous asymmetric channel modes.

and $|\phi_w| = 0.2$. This is illustrated in figure 3.71, which plots the back-calculated wall parameters, d and c_0^2 against θ_w for the same values of α and $|\phi_w|$.

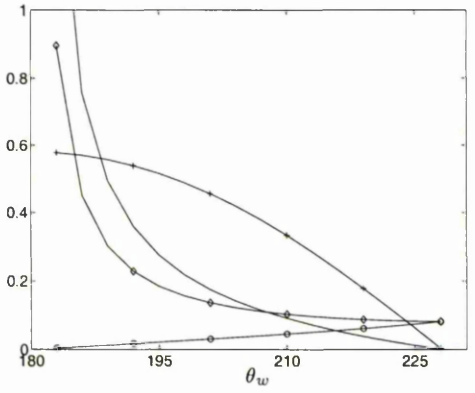

Figure 3.70: Physical realisability bounds on m, d and c_0^2 for the KH modes. —, $10 \times d$ lower bound; -o-, $10^{-3} \times m$ lower bound; -◇-, $10^{-3} \times m$ upper bound; -+-, $10^2 \times c_0^2$ upper bound.

Similarly for the viscous asymmetric Resonant modes, the bounds on the wall parameters always appear to correspond to those of case 2 in section 2.3.2. This is illustrated in figure 3.72 for the case where the parameters take the values $\alpha = 1.0$ and $|\phi_w| = 10.0$. The upper bounds for m and d have been omitted for clarity. Therefore, yet again we can eliminate these unstable modes by a sufficiently large increase in the free-wave speed, c_0.

The back-calculated values of d and c_0^2 are plotted against θ_w in figure 3.73.

The remaining parameters used were $m = 0.1$, $\alpha = 1.0$ and $|\phi_w| = 10.0$. Here, a smaller value of the wall density has been used in order to reduce the size of the unstable region. If $m = 2$ had been used then all of the unstable modes, where $\alpha = 1.0$ and $|\phi_w| = 0.4$, would be physically realisable.

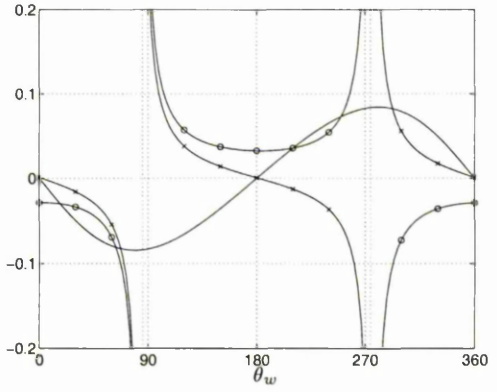

Figure 3.71: Physical realisability of the KH modes for $m = 2.0$.
—, ω; -o-, $10^{-2} \times d$; -×-, $10^{-1} \times c_0^2$.

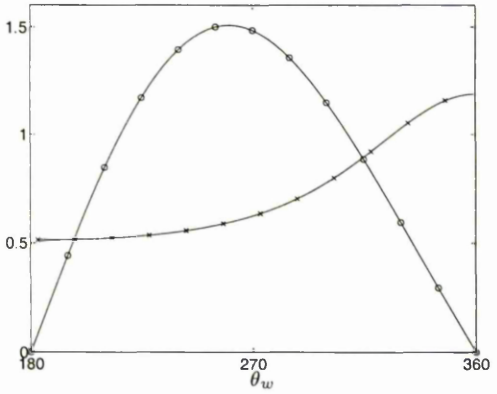

Figure 3.72: Physical realisability bounds on m, d and c_0^2 for the R modes.
-o-, $10 \times m$ lower bound; -+-, c_0^2 upper bound.

In this section we have shown that we can describe the KH and R modes for a compliant channel in terms of a purely viscous theory in the limit $Re \to 0$. Furthermore, the kinematic theory suggests that these are the only classes of

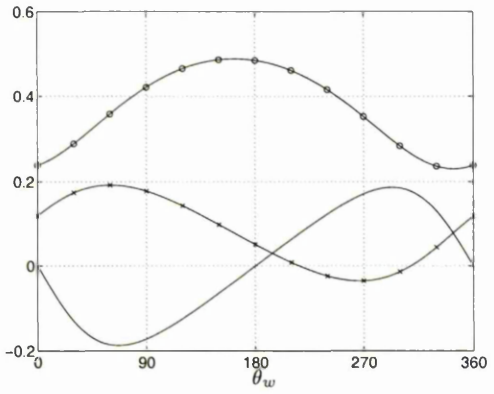

Figure 3.73: Physical realisability of the R modes for $m = 0.1$.
—, ω; -o-, $10^{-1} \times d$; -×-, $10^{-1} \times c_0^2$.

instability that may persist in this limit. The KH modes exist for all values of the wall stream function, ϕ_w but the R modes only exist when $|\phi_w|$ exceeds a critical value determined by the geometry of the modes under consideration.

However, there are questions that arise with regard to the validity and utility of the viscous theory. Our numerical results indicate that the viscous theory is a good leading-order solution, for KH and R modes, for values of αRe of up to $O(1)$ (see figures 3.49 and 3.50). For wave numbers where, $\alpha = O(1)$, this implies that the viscous theory is a good approximation for $Re = O(1)$. However, the kinematic viscosity of water is $O(10^{-6})\text{m}^2/\text{s}$. Hence, the viscous theory would be a good approximation only where the product of the reference velocity and length, UL, were $O(10^{-6})$. For such flow regimes it is possible that any underlying disturbances (e.g. eddies in the fluid as it settled prior to operational flow, or acoustic effects) would be large enough so that the linear stability approximation is not valid. However, the kinematic viscosity is much higher for other fluids, including gels. Hence, in this case it is more likely that the viscous theory will remain valid.

3.6.2 The Long-Wave Limit

The other case in which we may find analytical results is that of long-wave disturbances, where $\alpha \to 0$. Here, we expect from our viscous results that $c = O(1)$, to leading order in α.

As for the viscous limit, $Re \to 0$, we need to use the viscous pressure scaling, $p^* = (\mu U/L)p$. Therefore, with this scaling, equations (3.34) govern long-wave disturbances. Again we have envoked Squire's theorem to reduce the problem to looking at two-dimensional disturbances.

The streamwise velocity wall conditions, (3.10a), (3.16a) or (3.22a), along with the normal velocity wall conditions, (3.9a), (3.15a) or (3.21a) and the continuity equation (3.7d), then allow us the write the solutions in the form:

$$u(y) = u_0(y) + \alpha u_1(y) + O(\alpha^2)\,, \tag{3.45a}$$

$$v(y) = \alpha v_0(y) + \alpha^2 v_1(y) + O(\alpha^3)\,, \tag{3.45b}$$

$$p(y) = \alpha^\sigma p_0(y) + \alpha^{\sigma+1} u_1(y) + O(\alpha^{\sigma+2})\,, \tag{3.45c}$$

$$c = c_0 + \alpha c_1 + O(\alpha^2)\,, \tag{3.45d}$$

as $\alpha \to 0$. Here σ depends on the geometry of the mode under consideration and is found by balancing the terms in the momentum-derived stability equations (3.34a) and (3.34a). In order to proceed, again we shall consider the three cases of symmetric modes in the symmetric channel, antisymmetric modes in the symmetric channel and modes in the asymmetric channel, as follows.

Symmetric channel, symmetric modes.

In this case, $\sigma = 1$ and hence to leading order we have:

$$iu_0 + Dv_0 = 0\,, \tag{3.46a}$$

$$D^2 u_0 = 0\,, \tag{3.46b}$$

$$D^2 v_0 - Dp_0 = 0\,, \tag{3.46c}$$

with boundary conditions which may be written as:

$$\begin{aligned} u_0(0) &= 0\,, \\ p_0(0) &= 0\,, \\ v_0(-1) &= -i\phi_w\,, \\ v_0(0) &= -i\,, \\ c_0 &= -\frac{2\phi_w}{u_0(-1)}\,. \end{aligned}$$

It is easy to verify that the pressure, p_0, must be a linear function of y, as must the streamwise velocity, u_0. The normal velocity, v_0, must be a quadratic function of y. The coefficients of each function can be found and so we obtain

$$\begin{aligned} u_0(y) &= 2(\phi_w - 1)y\,, \\ v_0(y) &= -i + i(1-\phi_w)y^2\,, \\ p_0(y) &= 2i(1-\phi_w)y\,, \\ c_0 &= \frac{\phi_w}{\phi_w - 1}\,. \end{aligned}$$

For the $|\phi_w| = 0.2$, the leading-order solution was plotted alongside the numerical solution where in both cases $Re = 100.0$ and $\alpha = 10^{-4}$. Similarly, the leading-order solution was plotted for $|\phi_w| = 10.0$ alongside the numerical solution for $|\phi_w| = 10.0$, $Re = 100.0$ and $\alpha = 10^{-4}$. These plots can be seen in figures 3.74(a) and 3.74(b), respectively, with good agreement between the analytical solution and the numerics. In these and subsequent plots for the long-wave solutions, Re and Im are functions which take the real and imaginary parts of their arguments, respectively.

For lower values of $|\phi_w|$ we see that the modes belong in the KH class as shown in figures 3.75(a) and 3.75(b), which plot the phase speed and growth rate for modes where $|\phi_w| = 0.2$, assuming that the leading-order solution is valid

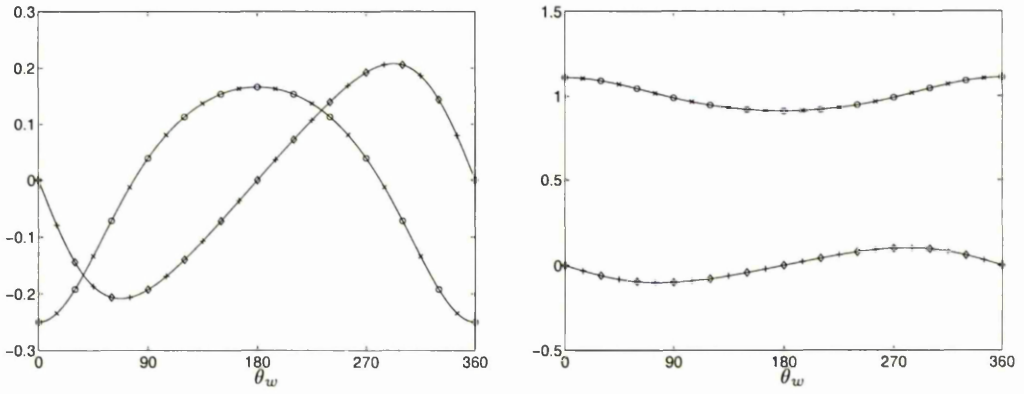

(a) KH modes. (b) R modes.

Figure 3.74: Analytical-Numerical comparison for the long-wave symmetric channel modes.
-o-, analytical c_r, $Re(c_0)$; -◇-, analytical c_i,$Im(c_0)$;
-×-, numerical c_r; -+-, numerical c_i.

for $\alpha = 10^{-4}$. Plots of the wall-parameter bounds show that these correspond to case 2 in section 2.3.2 (see figure 3.76). This is the same as for the viscous modes, as we might expect, since both the viscous and long-wave theories must coincide when both Re and α tend towards zero. Thus, these modes, like the viscous modes, can be eliminated by an increase in the free-wave speed, c_0. It also can be seen that, except near $\theta_w = 180°$, instabilities occur only for very large values of m. This is confirmed in figure 3.77 which plots the back-calculated values of d and c_0^2 for $|\phi_w| = 0.2$ and $m = 2.0$, again assuming the low wave number, $\alpha = 10^{-4}$. Only a very small "unstable pocket" exists and so only a very limited range of values of d and c_0^2 will give rise to these very slowly growing instabilities.

As $|\phi_w|$ is increased a singularity occurs at $\phi_w = 1$, consistent with the occurence of the singularity in the viscous symmetric modes as $\alpha_c \to 0$. Thus, in the long-wave limit, as for the viscous limit, there are no Transitional modes for values of $|\phi_w|$ close to that at which the singularity occurs.

For values of $|\phi_w|$ greater than 1 the modes belong to the Resonant class.

This is illustrated in figures 3.78(a) and 3.78(b) which plot the phase speed and the growth rate for $|\phi_w| = 10.0$, again assuming the low wave number, $\alpha = 10^{-4}$. Like the long-wave KH modes, the wall parameter bounds correspond to case 2 in section 2.3.2. These are plotted in figure 3.79. Therefore, these modes can be eliminated by an increase in the free-wave speed, c_0, too. The physically-realisable unstable long-wave R modes also only exist for large values of m, except near $\theta_w = 180°, 360°$. This is illustrated by figure 3.80 which plots the back calculated values of d and c_0^2 for $|\phi_w| = 10.0$ and $m = 2.0$. Like the long-wave KH modes, there are only very small physically realisable "unstable pockets" and so only a very limited range of values of d and c_0^2 will give rise to these instabilities.

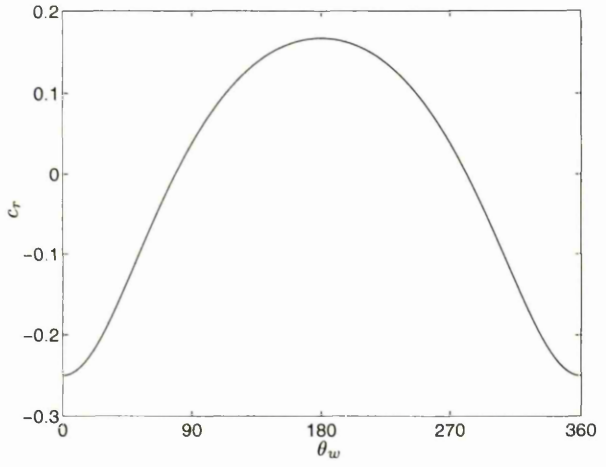

(a) Phase Speed, $Re(c_0)$

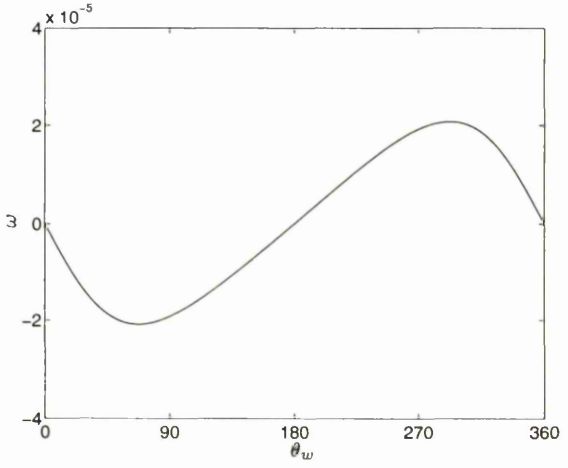

(b) Growth Rate, $\alpha.Im(c_0)$

Figure 3.75: Long-wave symmetric KH modes for the symmetric channel, $|\phi_w| = 0.2$ - leading-order solution.

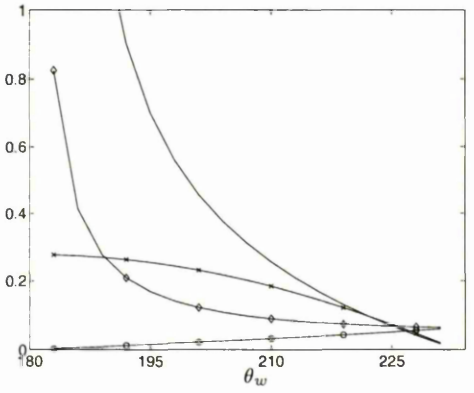

Figure 3.76: Physical realisability bounds on m, d and c_0^2 for the KH modes.
—, $10^4 \times d$ lower bound;
-○-, $10^{-11} \times m$ lower bound; -◇-, $10^{-11} \times m$ upper bound;
-+-, $10 \times c_0^2$ upper bound.

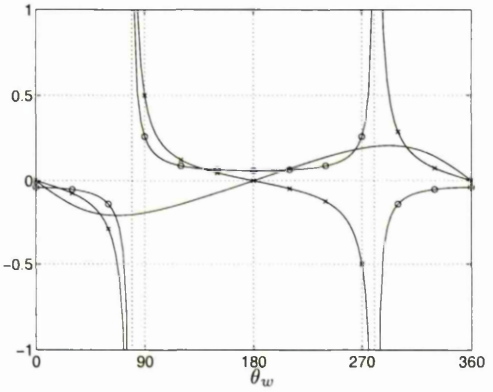

Figure 3.77: Physical realisability of the KH modes for $m = 2.0$.
—, $10^4 \times \omega$; -○-, $10^{-6} \times d$; -×-, $10^{-9} \times c_0^2$.

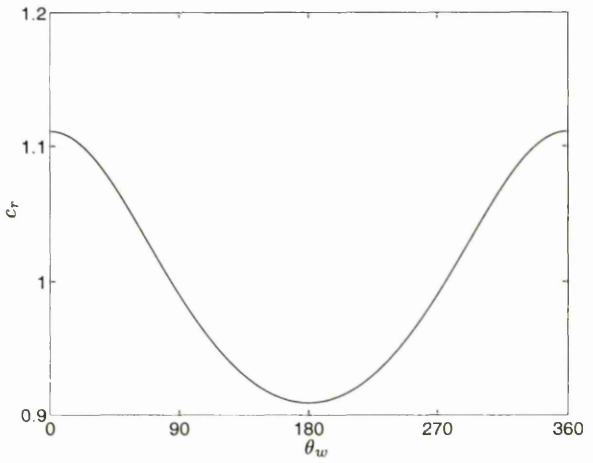

(a) Phase Speed, $Re(c_0)$

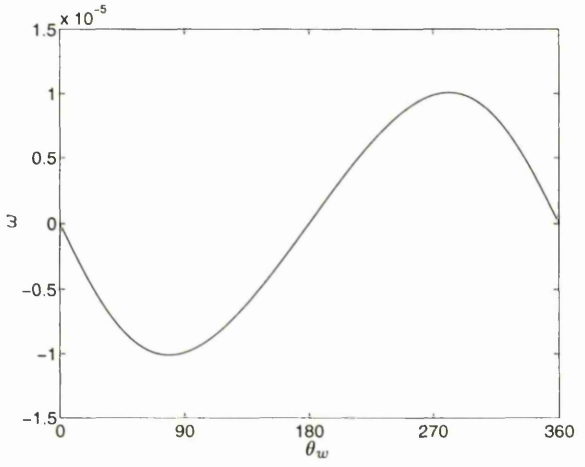

(b) Growth Rate, $\alpha.Im(c_0)$

Figure 3.78: Long-wave symmetric R modes for the symmetric channel, $|\phi_w| = 10.0$ - leading-order solution.

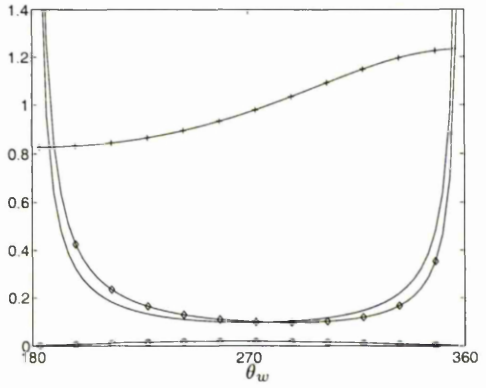

Figure 3.79: Physical realisability bounds on m, d and c_0^2 for the R modes.

—, $10^2 \times d$ lower bound;

-o-, $10^{-9} \times m$ lower bound; -◇-, $10^{-10} \times m$ upper bound; -+-, c_0^2 upper bound.

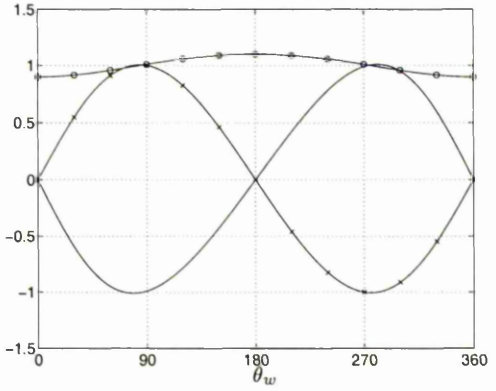

Figure 3.80: Physical realisability of the R modes for $m = 2.0$.

—, $10^5 \times \omega$; -o-, $10^{-4} \times d$; -×-, $10^{-7} \times c_0^2$.

To next order, the stability equations yield:

$$iu_1 + Dv_1 = 0\,, \tag{3.47a}$$

$$D^2u_1 = Re(i(u_B - c_0)u_0 + (Du_B)v_0)\,, \tag{3.47b}$$

$$D^2v_1 - Dp_1 = iRe(u_B - c_0)v_0\,, \tag{3.47c}$$

with boundary conditions which may be written as:

$$\begin{aligned} u_1(0) &= 0\,, \\ p_1(0) &= 0\,, \\ v_1(-1) &= 0\,, \\ v_1(0) &= 0\,, \\ c_1 &= \frac{2\phi_w u_1(-1)}{u_0^2(-1)}\,. \end{aligned}$$

It is easy to verify that, here, the second-order solution is the trivial solution:

$$\begin{aligned} u_1(y) &= 0\,, \\ v_1(y) &= 0\,, \\ p_1(y) &= \frac{Re}{\phi_w - 1}\left[y + \frac{2}{3}(\phi_w - 1)y^3 + \frac{1}{5}(\phi_w - 1)^2 y^5\right]\,, \\ c_1 &= 0\,. \end{aligned}$$

Therefore, there is no second-order correction to the phase velocity for long-wave solutions. However, there is a second-order correction to the pressure disturbance. This is required to balance the inertial terms, due to the leading-order solution, which arise at this order.

Symmetric channel, antisymmetric modes.

In this case, $\sigma = -1$ and hence to leading order we have:

$$iu_0 + Dv_0 = 0\,, \tag{3.48a}$$

$$D^2 u_0 - ip_0 = 0\,, \tag{3.48b}$$

$$Dp_0 = 0\,, \tag{3.48c}$$

with boundary conditions which may be written as:

$$\begin{aligned} u_0(0) &= 0\,, \\ v_0(0) &= 0\,, \\ D^2 v_0(0) &= 0\,, \\ v_0(-1) &= -i\phi_w\,, \\ c_0 &= -\frac{2\phi_w}{u_0(-1)}\,. \end{aligned}$$

It is easy to verify that the pressure, p_0, must be a constant, the streamwise velocity, u_0, must be a quadratic funtion of y and the normal velocity, v_0, must be a cubic function of y. The coefficients of each function can be found easily so that

$$\begin{aligned} u_0(y) &= 1 - 3(1+\phi_w)y^2\,, \\ v_0(y) &= iy((1+\phi_w)y^2 - 1)\,, \\ p_0(y) &= 6i(1+\phi_w)\,, \\ c_0 &= \frac{2\phi_w}{3\phi_w + 2}\,. \end{aligned}$$

For the case $|\phi_w| = 0.05$, the leading-order solution was plotted alongside the numerical solution, where the remaining parameters were $Re = 100.0$ and $\alpha = 10^{-4}$. Similarly, the leading-order solution was plotted for $|\phi_w| = 10.0$, alongside the numerical solution for $|\phi_w| = 10.0$, $Re = 100.0$ and $\alpha = 10^{-4}$. These plots can be seen in figures 3.81(a) and 3.81(b), respectively, with good agreement between the analytical solution and the numerics.

As in the previous section, for lower values of $|\phi_w|$ we see that the modes belong in the KH class as can be seen in figures 3.82(a) and 3.82(b), which plot the phase speed and growth rate for modes where $|\phi_w| = 0.2$, assuming that the leading-order solution is valid for $\alpha = 10^{-4}$. As for the numerical and viscous

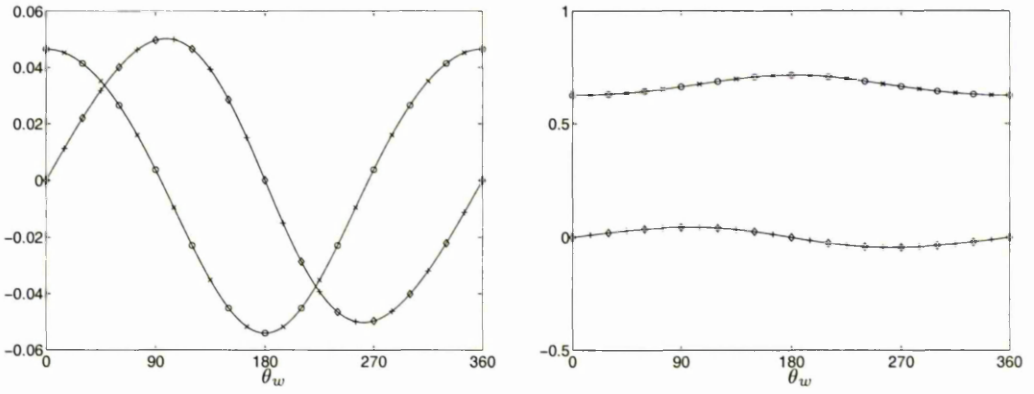

(a) KH modes. (b) R modes.

Figure 3.81: Analytical-Numerical comparison for the long-wave antisymmetric channel modes.
-o-, analytical c_r, $Re(c_0)$; -◇-, analytical c_i, $Im(c_0)$;
-×-, numerical c_r; -+-, numerical c_i.

results, these modes are qualitatively similar to the symmetric KH modes, if θ_w is shifted by 180°. Plots of the wall-parameter bounds show that these correspond to case 2 in section 2.3.2 as for the symmetric long-wave KH modes (see figure 3.83). Hence, these modes, like the viscous modes, can be eliminated by an increase in the free-wave speed, c_0. It also can be seen that, except near $\theta_w = 0°$, instabilities occur only for very large values of m. This is similar to the symmetric long-wave modes and is confirmed in figure 3.84 which plots the back calculated values of d and c_0^2 for $|\phi_w| = 0.2$ and $m = 2.0$, again assuming the low wave number, $\alpha = 10^{-4}$. Only a very small "unstable pocket" exists and so only a very limited range of values of d and c_0^2 will give rise to these instabilities. For both physical realisability plots, the profiles are similar to the symmetric case if θ_w is shifted by 180°.

As $|\phi_w|$ is increased a singularity occurs at $\phi_w = -2/3$, consistent with the occurence of the singularity in the viscous antisymmetric modes as $\alpha_c \to 0$. Hence, in the long-wave limit the antisymmetric Transitional modes are reduced to the

singularity, as is the case for the viscous modes and the symmetric long-wave modes.

For values of $|\phi_w|$ greater than 2/3 the modes belong to the Resonant class.

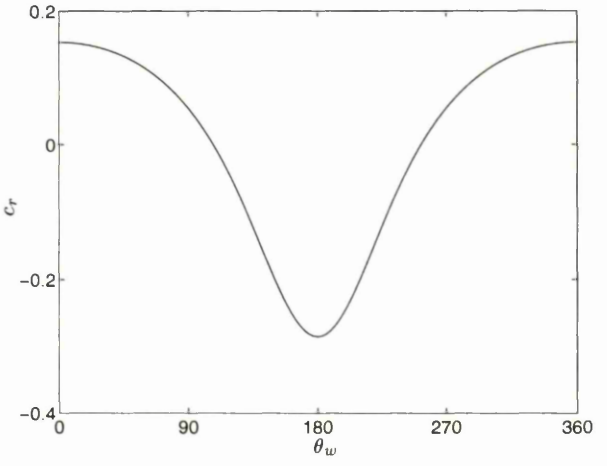

(a) Phase Speed, $Re(c_0)$

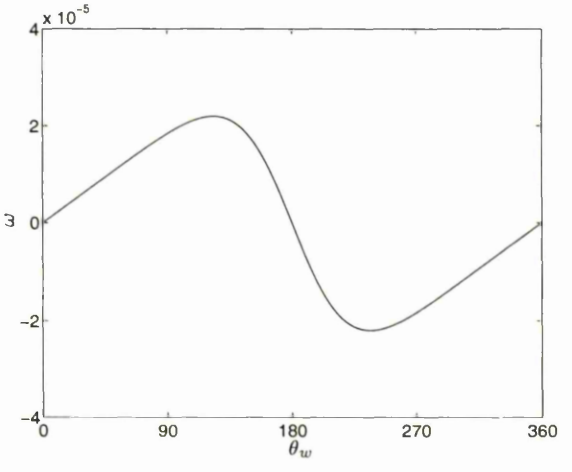

(b) Growth Rate, $\alpha.Im(c_0)$

Figure 3.82: Long-wave antisymmetric KH modes for the symmetric channel, $|\phi_w| = 0.2$ - leading-order solution.

This is illustrated in figures 3.85(a) and 3.85(b) which plot the phase speed and the growth rate for $|\phi_w| = 10.0$, again assuming the low wave number, $\alpha = 10^{-4}$.

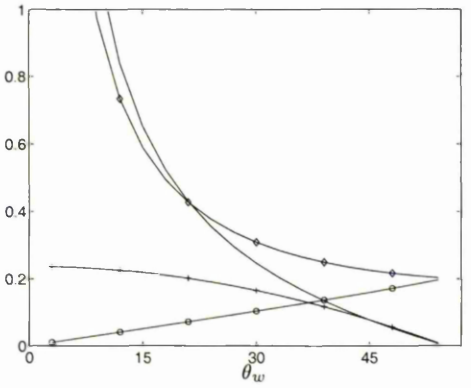

Figure 3.83: Physical realisability bounds on m, d and c_0^2 for the KH modes.
—, $10^4 \times d$ lower bound;
-○-, $10^{-11} \times m$ lower bound; -◇-, $10^{-11} \times m$ upper bound;
-+-, $10 \times c_0^2$ upper bound.

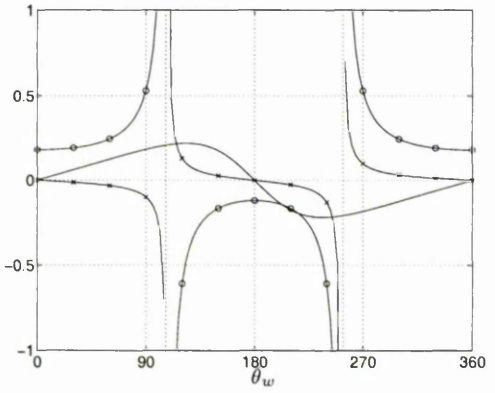

Figure 3.84: Physical realisability of the KH modes for $m = 2.0$.
—, $10^4 \times \omega$; -○-, $10^{-6} \times d$; -×-, $10^{-10} \times c_0^2$.

Like the long-wave KH modes, the wall parameter bounds correspond to case 2 in section 2.3.2. These are plotted in figure 3.86. Therefore, these modes can be eliminated by an increase in the free-wave speed, c_0, too. The physically-realisable unstable long-wave R modes also only exist for large values of m, except near $\theta_w = 0°, 180°$. This is illustrated by figure 3.87 which plots the back-calculated values of d and c_0^2 for $|\phi_w| = 10.0$ and $m = 2.0$. There are only two very small physically realisable "unstable pockets" and so only a very limited range of values of d and c_0^2 will then give rise to these instabilities.

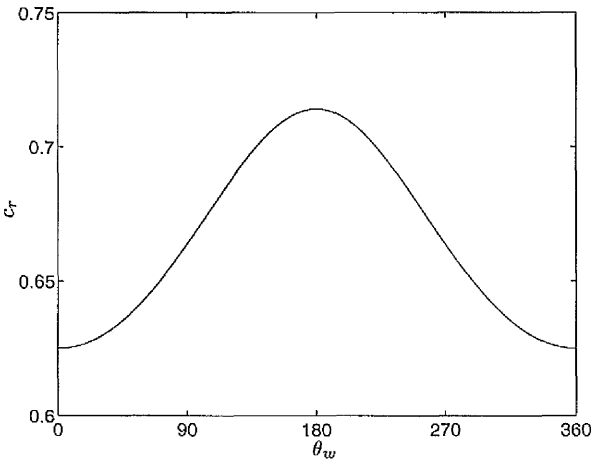

(a) Phase Speed, $Re(c_0)$

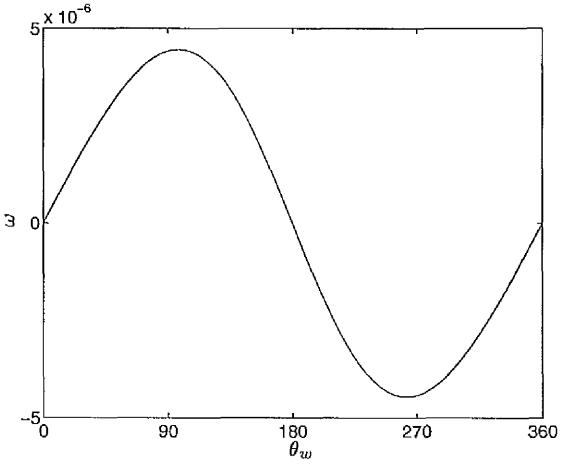

(b) Growth Rate, $\alpha.Im(c_0)$

Figure 3.85: Long-wave antisymmetric R modes for the symmetric channel, $|\phi_w| = 10.0$ - leading-order solution.

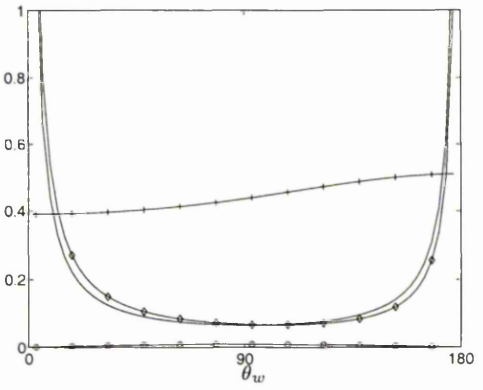

Figure 3.86: Physical realisability bounds on m, d and c_0^2 for the R modes.

—, $10^2 \times d$ lower bound;

-o-, $10^{-10} \times m$ lower bound; -◇-, $10^{-11} \times m$ upper bound; -+-, c_0^2 upper bound.

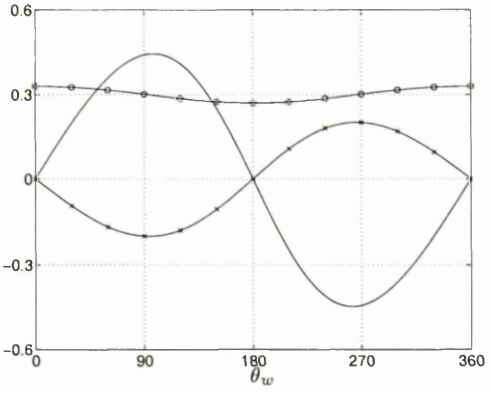

Figure 3.87: Physical realisability of the R modes for $m = 2.0$.

—, $10^5 \times \omega$; -o-, $10^{-5} \times d$; -×-, $10^{-8} \times c_0^2$.

To next order the stability equations yield:

$$iu_1 + Dv_1 = 0\,, \tag{3.49a}$$

$$D^2u_1 - ip_1 = Re(i(u_B - c_0)u_0 + (Du_B)v_0)\,, \tag{3.49b}$$

$$Dp_1 = 0\,, \tag{3.49c}$$

with boundary conditions which may be written as:

$$\begin{aligned} u_1(0) &= 0\,, \\ v_1(0) &= 0\,, \\ D^2 v_1(0) &= 0\,, \\ v_1(-1) &= 0\,, \\ c_1 &= \frac{2\phi_w u_1(-1)}{u_0^2(-1)}\,. \end{aligned}$$

It is easy to verify that the second-order solution is:

$$\begin{aligned} u_1(y) = iRe \Bigg[\left(1 - \frac{3(\phi_w+2)(1+\phi_w)}{3\phi_w+2}\right) \left(\frac{1}{12}y^4 - \frac{1}{20}y^2\right) + \\ (1+\phi_w)\left(\frac{1}{30}y^6 - \frac{1}{70}y^2\right)\Bigg]\,, \\ v_1(y) = Re \Bigg[\left(1 - \frac{3(\phi_w+2)(1+\phi_w)}{3\phi_w+2}\right) \frac{1}{60}y^3(y^2-1) + \\ (1+\phi_w)\,\frac{1}{210}y^3(y^4-1)\Bigg]\,, \\ p_1(y) = -Re \left[\frac{\phi_w+2}{3\phi_w+2} + \frac{1}{10}\left(1 - \frac{3(\phi_w+2)(1+\phi_w)}{3\phi_w+2}\right) + \frac{1}{35}(1+\phi_w)\right]\,, \\ c_1 = -\frac{iRe}{105}\frac{\phi_w}{(3\phi_w+2)^3}\left(9\phi_w^2 + 22\phi_w + 20\right)\,. \end{aligned}$$

Plots of the second-order solutions are given in figures 3.88 and 3.89 for the KH and R modes, respectively. Parameter values are as for the leading-order solutions. It can be seen that in both cases, the largest corrections occur where the leading-order solution is close to its mean value over θ_w.

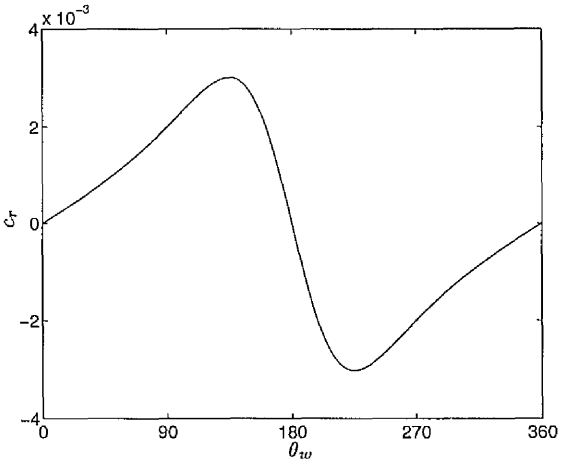

(a) Phase Speed, $Re(c_1)/Re$

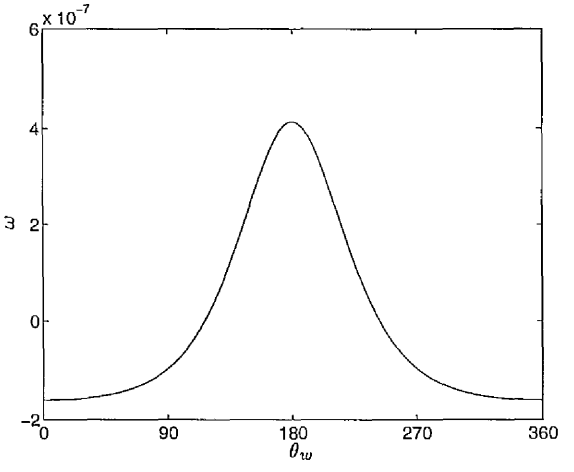

(b) Growth Rate, $\alpha.Im(c_1)/Re$

Figure 3.88: Long-wave antisymmetric KH modes for the symmetric channel, $|\phi_w| = 0.2$ - second-order solution.

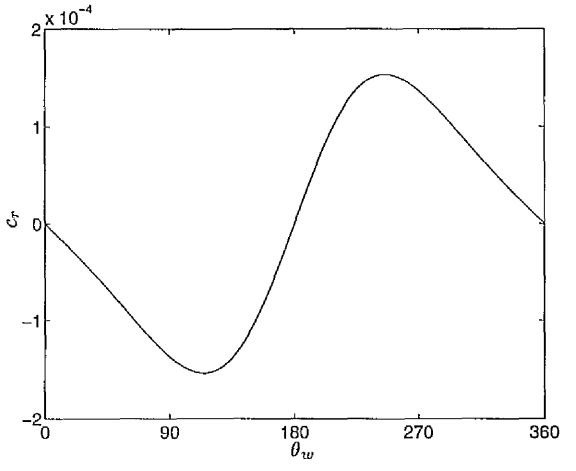

(a) Phase Speed, $Re(c_1)/Re$

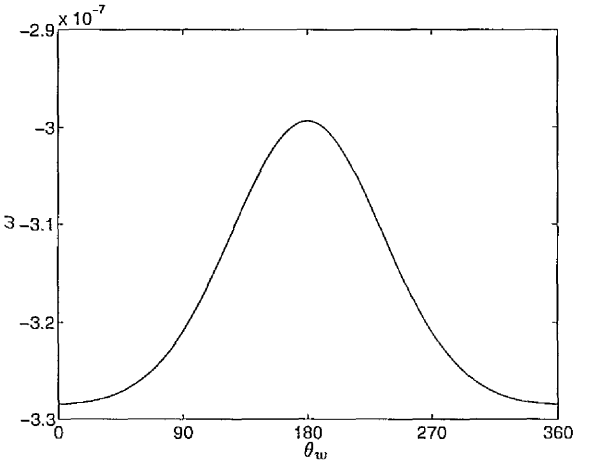

(b) Growth Rate, $\alpha.Im(c_1)/Re$

Figure 3.89: Long-wave antisymmetric R modes for the symmetric channel, $|\phi_w| = 10.0$ - second-order solution.

Asymmetric channel modes.

In this case $\sigma = -1$, as for the antisymmetric modes and hence equations (3.48) govern the leading-order solutions. The boundary conditions may be written as:

$$\begin{aligned} u_0(1) &= 0\,, \\ v_0(1) &= 0\,, \\ v_0(0) &= -i\,, \\ v_0(-1) &= -i\phi_w\,, \\ c_0 &= -\frac{2\phi_w}{u_0(-1)}\,. \end{aligned}$$

It is easy to verify that the pressure, p_0, must be a constant, the streamwise velocity, u_0, must be a quadratic funtion of y and the normal velocity, v_0, must be a cubic function of y. The coefficients of each function can then be found so that

$$\begin{aligned} u_0(y) &= \frac{3}{4}(4-\phi_w)y^2 + (\phi_w - 2)y - \frac{1}{4}(\phi_w + 4)\,, \\ v_0(y) &= \frac{i}{4}(\phi_w - 4)y^3 - \frac{i}{2}(\phi_w - 2)y^2 + \frac{i}{4}(\phi_w + 4)y - i\,, \\ p_0(y) &= \frac{3i}{2}(\phi_w - 4)\,, \\ c_0 &= \frac{\phi_w}{\phi_w - 2}\,. \end{aligned}$$

For the $|\phi_w| = 0.4$, the leading-order solution was plotted alongside the numerical solution, where in both cases $Re = 100.0$ and $\alpha = 10^{-4}$. Similarly, the leading-order solution was plotted for $|\phi_w| = 10.0$, alongside the numerical solution for $|\phi_w| = 10.0$, $Re = 100.0$ and $\alpha = 10^{-4}$. These plots can be seen in figures 3.90(a) and 3.90(b), respectively, with good agreement between the analytical solution and the numerics.

If ϕ_w is replaced by $2\phi_w$ in the above expression for the leading-order phase velocity, the leading-order solution for the symmetric long wave modes is obtained.

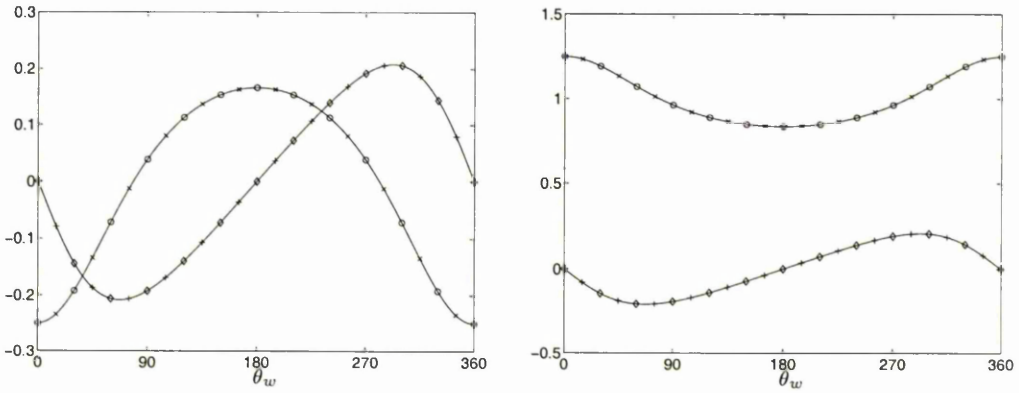

(a) KH modes.

(b) R modes.

Figure 3.90: Analytical-Numerical comparison for the long-wave asymmetric channel modes.
-○-, analytical c_r, $Re(c_0)$; -◇-, analytical c_i,$Im(c_0)$;
-×-, numerical c_r; -+-, numerical c_i.

This lends yet further evidence to the hypothesis first mentioned in section 3.5.1 regarding the link between the symmetric modes in the symmetric channel and the asymmetric channel modes. Therefore, the long-wave asymmetric modes belong to the KH class for $|\phi_w| < 2.0$. This can be seen in figure 3.91 which plots the phase speed and growth rate of the long-wave solutions for $|\phi_w| = 0.2$, again assuming that the leading-order solution is valid for $\alpha = 10^{-4}$. The wall-parameter bounds for these modes correspond to case 2 in section 2.3.2 and are qualitatively similar the other compliant channel long-wave KH modes. These bounds are illustrated in figure 3.92. Therefore, these unstable modes also may be eliminated by an increase in the free-wave speed, c_0 or may be reduced to a very small "unstable pocket" by a suitably small choice of the wall density. As for the other compliant channel modes, choosing $m = O(1)$ will bring about this small "unstable pocket". Figure 3.93 illustrates this for $m = 2.0$, $|\phi_w| = 0.2$ and assuming the leading order solution is valid for $\alpha = 10^{-4}$.

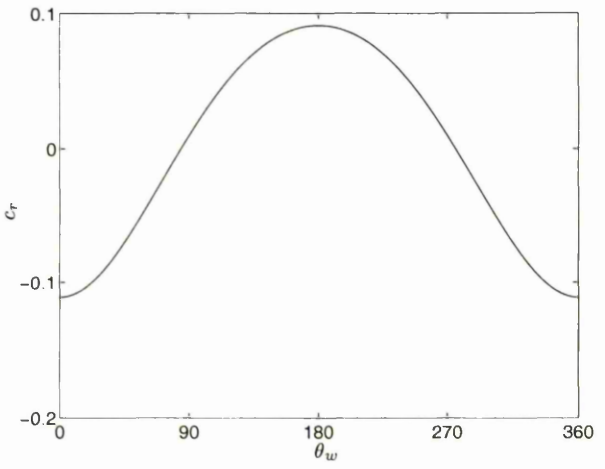

(a) Phase Speed, $Re(c_0)$

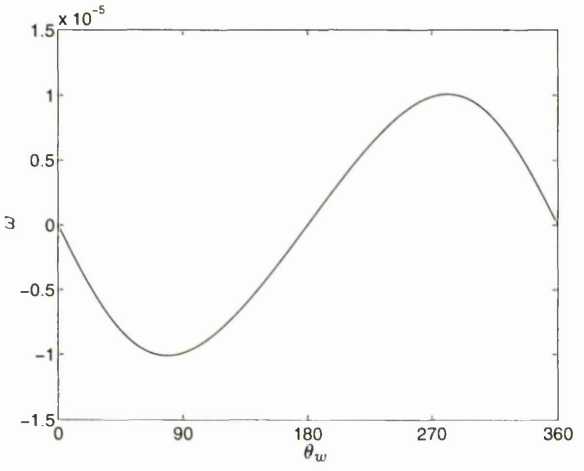

(b) Growth Rate, $\alpha.Im(c_0)$

Figure 3.91: Long-wave KH asymmetric channel modes, $|\phi_w| = 0.2$ - leading-order solution.

The singularity which signifies the transition from KH to R class modes occurs at $|\phi_w| = 2.0$ for the asymmetric modes. For $|\phi_w| > 2.0$ the asymmetric long-wave modes belong to the R class. This can be seen in figure 3.94, which plots the phase speed and growth rate of the R modes for $|\phi_w| = 10.0$, assuming that the

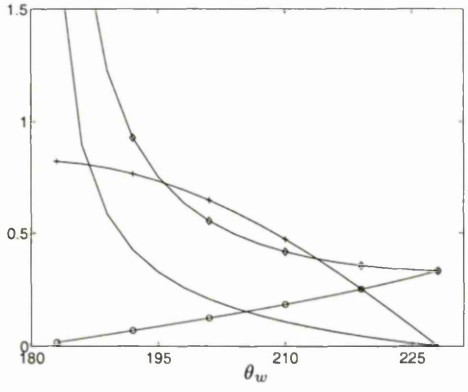

Figure 3.92: Physical realisability bounds on m, d and c_0^2 for the KH modes.
—, $10^4 \times d$ lower bound;
-o-, $10^{-11} \times m$ lower bound; -◇-, $10^{-11} \times m$ upper bound;
-+-, $10 \times c_0^2$ upper bound.

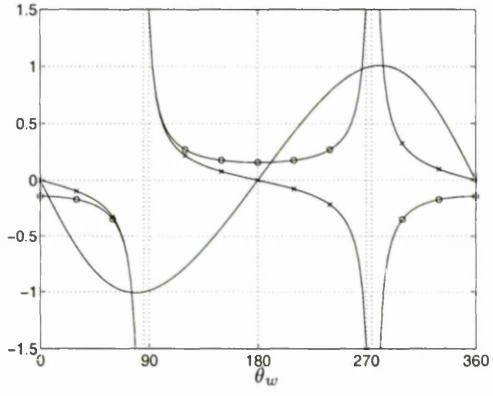

Figure 3.93: Physical realisability of the KH modes for $m = 2.0$.
—, $10^5 \times \omega$; -o-, $10^{-6} \times d$; -×-, $10^{-9} \times c_0^2$.

leading-order long-wave solution is valid for $\alpha = 10^{-4}$. Wall-parameter bounds are given in figure 3.95. This shows that the bounds all correspond to case 2 in section 2.3.2 and are qualitatively similar to the bounds for the long-wave R modes for other channel geometries. This lends support to the claim made in section 3.5.4 that the asymmetric R modes for $Re = 8000.0$ and $\alpha = 0.01$ belong to the long-wave scheme and hence are governed by a viscous theory to leading order. Thus, the unstable asymmetric long-wave R modes can be eliminated by an increase in the free-wave speed, c_0 or can be reduced to small "unstable

pockets" by choosing a suitably low value of m. Taking $m = 2$ is adequate for this purpose, as can be seen in figure 3.96.

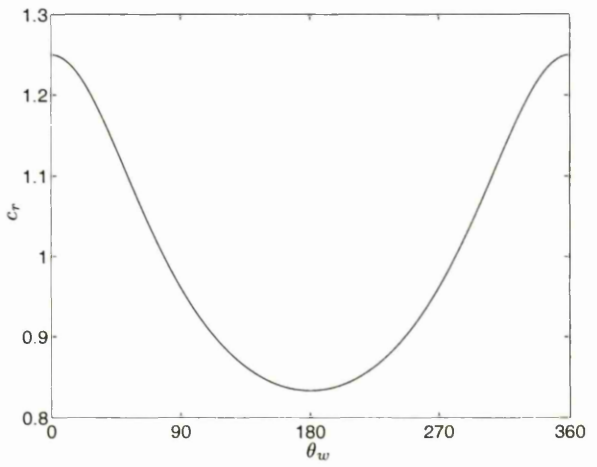

(a) Phase Speed, $Re(c_0)$

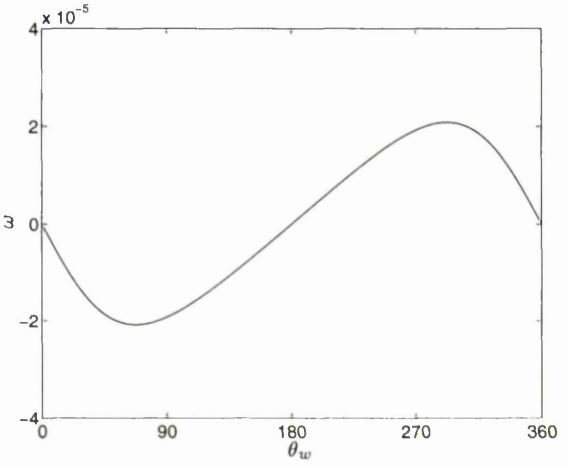

(b) Growth Rate, $\alpha.Im(c_0)$

Figure 3.94: Long-wave R asymmetric channel modes, $|\phi_w| = 10.0$ - leading-order solution.

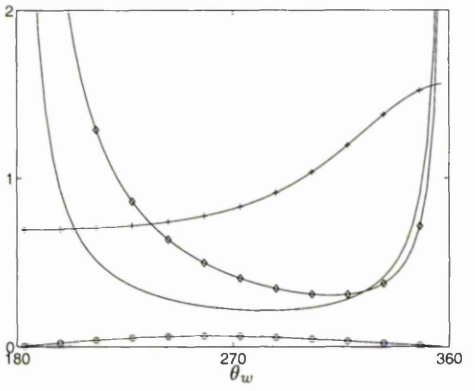

Figure 3.95: Physical realisability bounds on m, d and c_0^2 for the R modes.

—, $10^3 \times d$ lower bound;

-o-, $10^{-9} \times m$ lower bound; -◇-, $10^{-9} \times m$ upper bound; -+-, c_0^2 upper bound.

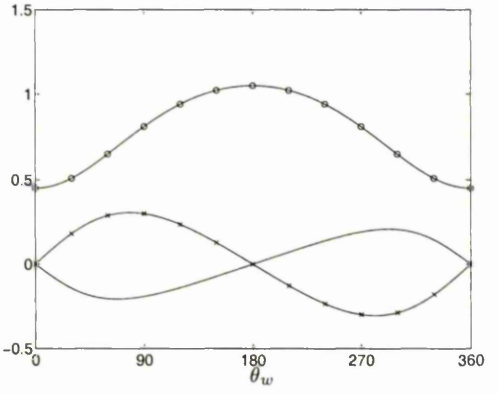

Figure 3.96: Physical realisability of the R modes for $m = 2.0$.

—, $10^4 \times \omega$; -o-, $10^{-4} \times d$; -×-, $10^{-8} \times c_0^2$.

The second-order functions are governed by equations (3.49) with boundary conditions which may be written as:

$$\begin{aligned} u_1(0) &= 0\,, \\ v_1(0) &= 0\,, \\ v_1(0) &= 0\,, \\ v_1(-1) &= 0\,, \\ c_1 &= \frac{2\phi_w u_1(-1)}{u_0^2(-1)}\,. \end{aligned}$$

It then can be verified that the second-order solution is:

$$\begin{aligned} u_1(y) = iRe(1-y^2)\Bigg[\frac{1}{60}\left(\frac{1}{4}(\phi_w+4)+\frac{3}{2}\frac{4-\phi_w}{\phi_w-2}\right)(5y^2-1)+ \\ \frac{1}{140}\left(\frac{1}{4}(4-\phi_w)\right)(7y^4+7y^2-2)\Bigg]\,, \\ v_1(y) = Re(1-y^2)y\Bigg[\frac{1}{60}\left(\frac{1}{4}(\phi_w+4)+\frac{3}{2}\frac{4-\phi_w}{\phi_w-2}\right)(y^2-1)+ \\ \frac{1}{140}\left(\frac{1}{4}(4-\phi_w)\right)(y^4+y^2-2)\Bigg]\,, \\ p_1(y) = Re\left[\frac{1}{5}\left(\frac{1}{4}(\phi_w+4)+\frac{3}{2}\frac{4-\phi_w}{\phi_w-2}\right)+\frac{9}{70}\left(\frac{1}{4}(4-\phi_w)\right)-\frac{1}{2}\frac{\phi_w+4}{\phi_w-2}\right]\,, \\ c_1 = 0\,. \end{aligned}$$

Therefore, as for the symmetric case, there is no second-order correction to the phase velocity for long-wave solutions. However, there is a second-order correction to the pressure and velocity disturbances. These are required to balance the inertial terms, due to the leading-order solution, which arise at this order.

This concludes our study of the flow in channels bounded by compliant walls. A summary of the results found herein for such flows is given in chapter 5.

Chapter 4

Compliant Pipe Problem

In this chapter we consider the problem of flow in a circular compliant pipe. This geometry is by far the more prevalent in practical applications and hence its study is a necessary extension to the simpler geometry of compliant channel flow. Since the flow in a rigid pipe has been shown to be linearly stable by Corcos and Sellars [13], Gill [25], Salwen and Grosch [65], and Garg and Rouleau [23], for example, it is the introduction of compliance itself which is the cause of any instabilities that occur in the pipe problem.

We shall start by formulating the compliant pipe problem with reference to the methods employed in chapter 2. Next, we shall proceed to apply the numerical methods, also given in the same chapter, to solving the kinematic compliant pipe problem. Then we shall be in a position to find solutions to the kinematic compliant pipe problem. Next, we shall investigate the different classes of modes into which the numerical solutions may be divided. Finally, we shall conclude this chapter by investigating various analytical solutions, where one or other of the problem parameters asymptotically approaches given limits.

4.1 Flow Geometry

We shall start by choosing a cylindrical polar co-ordinate system in which x^* is the dimensional co-ordinate with axis parallel to the axis of the pipe, y^* is the dimensional radial co-ordinate perpendicular to the pipe wall in its rest state and the z^* co-ordinate is the polar angle, measured relative to a fixed line in the radial direction. The pipe is then formed by a single curved wall whose extent in the x^* direction is infinite and which in its rest state has equation $y^* = R$, i.e. the pipe has a constant radius, R.

With our chosen co-ordinate system, the incompressible flow in a rigid pipe is described by the pressure p^*, and the three velocity components $u^*_{x^*}$, $u^*_{y^*}$ and $u^*_{z^*}$ in the x^*, y^* and z^* directions respectively. All four of these quantities may depend on x^*, y^*, z^* and t^*, the dimensional time.

We shall now choose to formulate the kinematic compliant channel problem with the non-dimensional quantities x, r, θ, t, u_r, u_r, u_θ and p which are related to the above dimensional variables via the linear relations $x^* = Rx$, $y^* = Rr$, $z^* = \theta$, $t^* = Rt/U$, $u^*_{x^*} = Uu_x$, $u^*_{r^*} = Uu_r$ and $u^*_{z^*} = Uu_\theta$. Here, U is the maximum velocity of the basic flow, i.e. that on the axis of the pipe. For the remaining relation, that of the pressure, we shall use the inertial scaling $p^* = \rho U^2 p$, where ρ is the constant density of the fluid.

In the non-dimensional co-ordinate system, the wall of the pipe is at $r = 1$ and hence the geometry may be given by figure 4.1.

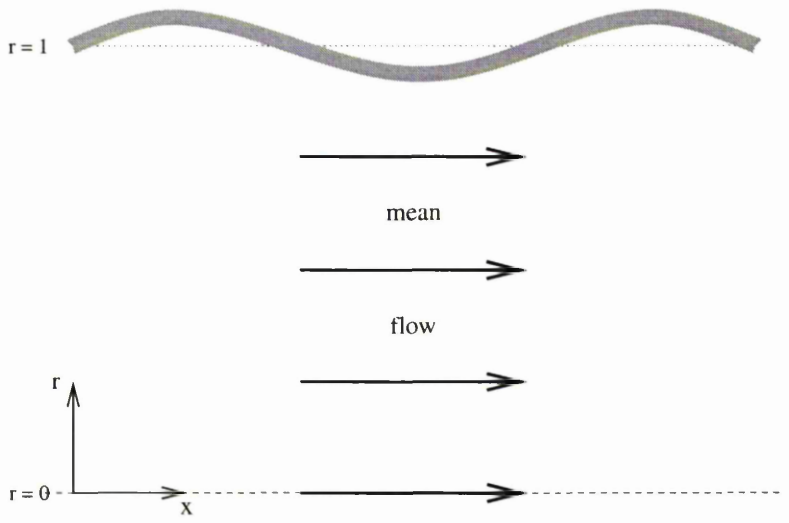

Figure 4.1: The compliant pipe.

Following chapter 2, we shall consider the incompressible flow of a Newtonian fluid in such a geometry and so the governing equations are the Navier-Stokes equations, thus:

$$\frac{\partial u_x}{\partial t}+u_x\frac{\partial u_x}{\partial x}+u_r\frac{\partial u_x}{\partial r}+\frac{u_{\hat{\theta}}}{r}\frac{\partial u_x}{\partial \hat{\theta}}=-\frac{\partial p}{\partial x} + \frac{1}{Re}\left(\frac{\partial^2 u_x}{\partial x^2}+\frac{1}{r}\frac{\partial}{\partial r}\left(r\frac{\partial u_x}{\partial r}\right)+\frac{1}{r^2}\frac{\partial u_x}{\partial \hat{\theta}^2}\right), \tag{4.1a}$$

$$\frac{\partial u_r}{\partial t}+u_x\frac{\partial u_r}{\partial x}+u_r\frac{\partial u_r}{\partial r}+\frac{u_{\hat{\theta}}}{r}\frac{\partial u_r}{\partial \hat{\theta}}-\frac{{u_{\hat{\theta}}}^2}{r}=-\frac{\partial p}{\partial r} + \frac{1}{Re}\left(\frac{\partial^2 u_r}{\partial x^2}+\frac{1}{r}\frac{\partial}{\partial r}\left(r\frac{\partial u_r}{\partial r}\right)+\frac{1}{r^2}\frac{\partial u_r}{\partial \hat{\theta}^2}-\frac{2}{r^2}\frac{\partial u_{\hat{\theta}}}{\partial \hat{\theta}}-\frac{u_r}{r^2}\right), \tag{4.1b}$$

$$\frac{\partial u_{\hat{\theta}}}{\partial t}+u_x\frac{\partial u_{\hat{\theta}}}{\partial x}+u_r\frac{\partial u_{\hat{\theta}}}{\partial r}+\frac{u_{\hat{\theta}}}{r}\frac{\partial u_{\hat{\theta}}}{\partial \hat{\theta}}+\frac{u_r u_{\hat{\theta}}}{r}=-\frac{1}{r}\frac{\partial p}{\partial \hat{\theta}} + \frac{1}{Re}\left(\frac{\partial^2 u_{\hat{\theta}}}{\partial x^2}+\frac{1}{r}\frac{\partial}{\partial r}\left(r\frac{\partial u_{\hat{\theta}}}{\partial r}\right)+\frac{1}{r^2}\frac{\partial u_{\hat{\theta}}}{\partial \hat{\theta}^2}+\frac{2}{r^2}\frac{\partial u_r}{\partial \hat{\theta}}-\frac{u_{\hat{\theta}}}{r^2}\right). \tag{4.1c}$$

Here, $Re = \rho UR/\mu$ is the Reynolds number of the flow and μ is the constant dynamic viscosity of the fluid.

In addition to the Navier-Stokes equations (4.1), the fluid must also obey the continuity equation

$$\frac{\partial u_x}{\partial x}+\frac{1}{r}\frac{\partial\left(ru_r\right)}{\partial r}+\frac{1}{r}\frac{\partial u_\theta}{\partial \theta}=0, \tag{4.2}$$

which ensures that mass is conserved in the flow.

4.2 Basic Flow

For a rigid pipe, the boundary conditions for the Navier-Stokes equations (4.1) are

$$\boldsymbol{u} = (u_x, u_r, u_\theta) = \mathbf{0} \quad \text{at} \quad r = 1\,. \tag{4.3}$$

The x and θ components correspond to no-slip at the wall and the r component corresponds to the impermeability of the wall.

These conditions, along with the Navier-Stokes equations (4.1) and the continuity equation (4.2), permit a uni-directional solution, Hagen-Poiseuille flow, thus:

$$\boldsymbol{u_B} = (1 - r^2)\hat{\boldsymbol{x}}\,, \tag{4.4a}$$

$$p_B(x) = p_0 - \frac{2}{Re}x\,. \tag{4.4b}$$

Here, $\hat{\boldsymbol{x}}$ is a unit vector in the x direction and p_0 is an abitrary constant that corresponds to a background pressure. We can, without loss of generality, take p_0 to be zero.

4.3 Linear Stability Analysis

We shall now consider solutions which are small perturbations from Hagen-Poiseuille flow (4.4). Such solutions may be written in the form $\boldsymbol{u} = \boldsymbol{u_B} + \boldsymbol{u'}$ and $p = p_B + p'$, where $|u'_x|$, $|u'_r|$, $|u'_\theta|$, $|p'| \ll 1$.

If we substitute this form of solution into the Navier-Stokes equations (4.1) and the continuity equation (4.2) and we ignore all terms of second order in u'_x, u'_r, u'_θ or p', since they are much smaller than the remaining terms, then we obtain

$$\frac{\partial u_x'}{\partial t}+u_B\frac{\partial u_x'}{\partial x}+u_r'\frac{du_B}{dr}=-\frac{\partial p'}{\partial x} \tag{4.5a}$$
$$+\frac{1}{Re}\left(\frac{\partial^2 u_x'}{\partial x^2}+\frac{1}{r}\frac{\partial}{\partial r}\left(r\frac{\partial u_x'}{\partial r}\right)+\frac{1}{r^2}\frac{\partial u_x'}{\partial \theta^2}\right),$$
$$\frac{\partial u_r'}{\partial t}+u_B\frac{\partial u_r'}{\partial x}=-\frac{\partial p'}{\partial r} \tag{4.5b}$$
$$+\frac{1}{Re}\left(\frac{\partial^2 u_r'}{\partial x^2}+\frac{1}{r}\frac{\partial}{\partial r}\left(r\frac{\partial u_r'}{\partial r}\right)+\frac{1}{r^2}\frac{\partial u_r'}{\partial \theta^2}-\frac{2}{r^2}\frac{\partial u_\theta'}{\partial \theta}-\frac{u_r'}{r^2}\right),$$
$$\frac{\partial u_\theta'}{\partial t}+u_B\frac{\partial u_\theta'}{\partial x}=-\frac{\partial p'}{\partial z} \tag{4.5c}$$
$$+\frac{1}{Re}\left(\frac{\partial^2 u_\theta'}{\partial x^2}+\frac{1}{r}\frac{\partial}{\partial r}\left(r\frac{\partial u_\theta'}{\partial r}\right)+\frac{1}{r^2}\frac{\partial u_\theta'}{\partial \theta^2}+\frac{2}{r^2}\frac{\partial u_r'}{\partial \theta}-\frac{u_\theta'}{r^2}\right),$$
$$\frac{\partial u_x'}{\partial x}+\frac{1}{r}\frac{\partial (r u_r')}{\partial r}+\frac{1}{r}\frac{\partial u_\theta'}{\partial \theta}=0, \tag{4.5d}$$

once we have subtracted the equations obeyed by the basic flow quantities (4.4).

By Fourier transforming equations (4.5), using the fact that the boundary conditions for the rigid pipe flow are independent of x and t, it is possible to show that the solutions must be in the form of normal modes and may be written thus

$$(u_x', u_r', u_\theta', p') = A(u(r), v(r), w(r), p(r))e^{i(\alpha(x-ct)+n\theta)}. \tag{4.6}$$

Here u, v, w and p are $O(1)$ complex amplitude functions and $A \ll 1$ is a real number indicating the small size of the disturbances. Also, α and n are positive real wavenumbers, where n must be integer valued in order that the solutions remain unchanged as θ is increased by multiples of 2π. The quantity $c = c_r + ic_i$ is the complex phase velocity which determines the stability of the solution: if $\omega = \alpha c_i > 0$ then the basic flow is unstable, i.e. the perturbations grow with time; if $\omega < 0$ then the basic flow is stable, i.e. the perturbations decay with time; if $\omega = 0$ then the basic flow is neutrally stable, i.e. the perturbations have a constant magnitude as the time increases.

Substituting this form of solution into the stability equations (4.5), or equivalently performing the necessary Fourier transformation, we obtain a set of equations for the unknowns u, v, w and p:

$$i\alpha Re(u_B - c)u + Re(Du_B)v = -i\alpha Re\, p + \left(D^2 + \frac{1}{r}D - \left(\frac{n^2}{r^2} + \alpha^2\right)\right)u\,, \quad (4.7a)$$

$$i\alpha Re(u_B - c)v = -Re\, Dp + \left(D^2 + \frac{1}{r}D - \left(\frac{n^2+1}{r^2} + \alpha^2\right)\right)v - \frac{2in}{r^2}w\,, \quad (4.7b)$$

$$i\alpha Re(u_B - c)w = -\frac{in}{r}Re\, p + \left(D^2 + \frac{1}{r}D - \left(\frac{n^2+1}{r^2} + \alpha^2\right)\right)w + \frac{2in}{r^2}v\,, \quad (4.7c)$$

$$i\alpha\, u + \left(D + \frac{1}{r}\right)v + \frac{in}{r}w = 0\,. \quad (4.7d)$$

Here, $D = d/dr$ and $u_B = 1 - r^2$ is the scalar velocity component, u_x, of the basic flow (4.4).

In a cylindrical polar co-ordinate system, we can find the velocity components of a two-dimensional disturbance, where $w = n = 0$, in terms of a stream function, ψ, which is defined by:

$$u'_x = \frac{1}{r}\frac{\partial \psi}{\partial r}\,,$$
$$u'_r = -\frac{1}{r}\frac{\partial \psi}{\partial x}\,,$$

whence u'_x and u'_r automatically obey the continuity equation (4.7d). Since u'_r has a normal mode decomposition, the stream function must also have a normal mode decomposition, which we may write as

$$\psi = A\phi(r)e^{i\alpha(x-ct)}\,.$$

4.3.1 Boundary Conditions

If we now recap and compare with chapter 2, we see that the formulation of the pipe problem, so far, is a specific case of the kinematic approach given therein: we have found a set of axes in which $x = x_*$ is the co-ordinate in the direction

of the basic flow, with axis parallel to the pipe; the second, $r = y_*$, axis is perpendicular to the channel walls in their rest state, so that the equation of the wall is given by $r = 1$, i.e. $y_0 = 1$ here; also, we have chosen the final, $\theta = z_*$ axis to form a right-handed set of axes with the x and r axes; the fluid is assumed to be Newtonian and hence the governing equations are the Navier-Stokes equations which, combined with the zero-wall-velocity boundary conditions, give rise to a basic flow of the type given by equations (2.1), where $u_B(r) = 1 - r^2$; by considering small perturbations from the basic flow, it has been shown that such disturbances may be found in the form of normal modes given by equation (2.2) and also that the equations governing these normal modes are in the form given by equations (2.3), where:

$$
\begin{aligned}
L_1(r,u) &= \left[D^2 + \frac{1}{r}D - \left(\frac{n^2}{r^2} + \alpha^2\right)\right] u\,, \\
L_2(r,v,w) &= \left[D^2 + \frac{1}{r}D - \left(\frac{(n+1)^2}{r^2} + \alpha^2\right)\right] v - \frac{2in}{r^2} w\,, \\
L_3(r,v,w) &= \left[D^2 + \frac{1}{r}D - \left(\frac{(n-1)^2}{r^2} + \alpha^2\right)\right] w + \frac{2in}{r^2} v\,, \\
f_1(r) &= -\frac{in}{r}\,, \\
f_2(y) &= \frac{in}{r}\,,
\end{aligned}
$$

with $D = d/dr$; finally, we have formulated two-dimensional disturbances in terms of a stream function of the form given by equations (2.4), with $f_*(r) = 1/r$.

Therefore, we have formulated the pipe problem in a way which is fully consistent with the kinematic approach described in chapter 2 and hence we may proceed to use the results therein without further justification. Now, we must use these results to formulate the boundary conditions for and hence close, the pipe problem.

Now for the compliant pipe there is only a single wall and hence the equation

describing the wall's position may be written

$$r = 1 + Aae^{i(\alpha(x-ct)+n\theta)}\,.$$

Therefore, following section 2.1, the boundary conditions at the compliant wall are:

$$u(1) = \frac{2\phi_w}{c}\,, \tag{4.8a}$$

$$v(1) = -i\alpha\phi_w\,, \tag{4.8b}$$

$$w(1) = 0 \tag{4.8c}$$

and where also

$$\phi_w = ac\,. \tag{4.9}$$

We may also deal with the normalisation condition at a single stroke by considering a disturbance as $r \to 0$. We can show that a suitable normalisation condition is

$$D^n u(0) = 1\,, \tag{4.10}$$

by considering a region where $r = \epsilon\bar{r}$, with $\epsilon \ll 1$ and $\bar{r} = O(1)$. Dominant balance then yields $u(r) = Cr^n$ from the x-momentum stability equation (4.7a). The pressure, p, is of the same order as u. The remaining velocity components, v and w, are an order ϵ smaller than u. Therefore, $D^n u$ tends to a (generally) non-zero constant, namely $n!C$, as $r \to 0$. So we may choose the normalisation condition (4.10) that fixes $C = 1/n!$.

The conditions for the disturbances on the axis of the pipe are the same as for a rigid pipe and so are probably best dealt with in the following three cases:

1. Axisymmetric modes, $n = 0$ for which:

$$Du(0) = 0\,, \tag{4.11a}$$

$$v(0) = 0\,, \tag{4.11b}$$

$$w(0) = 0\,. \tag{4.11c}$$

2. Non-Axisymmetric modes, $n = 1$ for which:

$$u(0) = 0\,, \tag{4.12a}$$

$$D^2u(0) = 0\,, \tag{4.12b}$$

$$w(0) = 0\,. \tag{4.12c}$$

3. Non-Axisymmetric modes, $n > 1$ for which:

$$u(0) = 0\,, \tag{4.13a}$$

$$v(0) = 0\,, \tag{4.13b}$$

$$w(0) = 0\,. \tag{4.13c}$$

Now that we have found the boundary conditions for all the possible modes for the kinematic compliant pipe problem, we can find solutions to the system of linearised stability equations (4.7), with the above conditions applied, by fixing α, n and Re and solving the resulting problem for the eigenvalue, c and the eigenfunctions, u, v, w and p. However, there is no equivalent of Squire's theorem [72] for pipe flow and so we must consider disturbances in which n is non-zero as well as axisymmetric modes, where $n = 0$.

4.4 Application Of Numerical Methods

Now we shall use the ideas of section 2.2 to formulate the problem of finding numerical solutions to the linearised stability equations (4.7) with the normalisation condition and the relevant boundary conditions from section 4.3.1.

4.4.1 The Tchebychev Collocation Method

The compliant pipe problem is defined on the interval, $[0, 1]$ and hence we must introduce the transformation $r' = 2r - 1$ to map this to the interval, $[-1, 1]$,

so that we can use the Tchebychev collocation method. Therefore, derivatives with respect to r and r' are related by $D' = d/dr' = (1/2)d/dr = (1/2)D$. The numerical solutions then take the form:

$$u_j = \sum_{k=0}^{N} \tilde{u_k} T_k(r'_j)\,, \qquad v_j = \sum_{k=0}^{N} \tilde{v_k} T_k(r'_j)\,,$$
$$w_j = \sum_{k=0}^{N} \tilde{w_k} T_k(r'_j)\,, \qquad p_{j+1/2} = \sum_{k=0}^{N} \tilde{p_k} T_k(r'_{j+1/2})\,,$$

where the r'_j are the Tchebychev-Gauss-Lobatto points (2.14), T_k is the k-th Tchebychev polynomial of the first kind, $u_j = u(r'_j)$, $v_j = v(r'_j)$, $w_j = w(r'_j)$ for $j = 0, \ldots, N$ and $p_{j+1/2} = p(r'_{j+1/2})$, for $j = 0, \ldots, N-1$. Here, $N+1$ is the number of points used.

As for the channel problem, the spacing of the Tchebychev-Gauss-Lobatto points is advantageous for the problem of compliant pipe flow, since the largest variations in the eigenfunctions occur in the regions near the pipe axis and the pipe wall, as shown by Kumaran [48], for example.

We can now formulate the numerical problem by expressing the linearised stability equations (4.7) as

$$[i\alpha Re(u_B(r'_j) - c) + \alpha^2](r'^2)_j u_j + n^2 u_j - (r')_j (D'^2_N)_{jk} u_k \tag{4.14a}$$
$$- (r')_j (D'_N)_{jk} u_k + ReDu_B(r'_j)(r'^2)_j v_j + i\alpha (r'^2)_j Re(C^{-1})_{jk} (C^{\frac{1}{2}})_{kl} p_l = 0\,,$$
$$[i\alpha Re(u_B(r'_j) - c) + \alpha^2](r'^2)_j v_j + n^2 v_j - (r'^2)_j (D'^2_N)_{jk} v_k \tag{4.14b}$$
$$- (r')_j (D'_N)_{jk} v_k + 2inw_j + (r'^2)_j Re(D'_N)_{jk} (C^{-1})_{kl} (C^{\frac{1}{2}})_{lm} p_m = 0\,,$$
$$[i\alpha Re(u_B(r'_j) - c) + \alpha^2](r'^2)_j w_j + n^2 w_j - (r'^2)_j (D'^2_N)_{jk} w_k \tag{4.14c}$$
$$- (r')_j (D'_N)_{jk} w_k - 2inv_j + inr'_j Re(C^{-1})_{jk} (C^{\frac{1}{2}})_{kl} p_l = 0\,.$$

Here, there is no summation over j, the matrix $D'_N = D_N/2$ and the matrices, C^{-1}, $C^{1/2}$ and D_N, are as defined in section 2.2.1. It is necessary to calculate the pressure at each collocation point, r'_j, from the values at the half-points, $r'_{j+1/2}$ and hence the matrix, $C^{1/2}$, converting from the values of p at the half points

to Tchebychev space and the matrix, C^{-1}, calculating the values of p at the collocation points from the Tchebychev coefficients, occur in equations (4.14).

The above equations (4.14) are each calculated for $j = 1, \ldots, N-1$, giving $3N-3$ of the $4N+3$ equations required to find the eigenfunctions, u_j, v_j, w_j and $p_{j+1/2}$.

The continuity equation is applied at each of the half-points, $y_{j+1/2}$, for $j = 0, \ldots, N-1$, as mentioned in section 2.2.1 and hence may be written in the form

$$i\alpha r'_j (C^{\frac{1}{2}})^{-1}_{jk} C_{kl} u_l + [r'_j (C^{\frac{1}{2}})^{-1}_{jk} C_{kl} (D'_N)_{lm} + \delta_{jm}] v_m + in (C^{\frac{1}{2}})^{-1}_{jk} C_{kl} w_l = 0\,, \quad (4.15)$$

where δ_{jm} is the Kronecker tensor.

The remaining six required equations are obtained from the boundary and normalisation conditions. The wall condition for the streamwise velocity, $u_0 = 2\phi_w/c$, is relaxed here and later used to find the eigenvalue, c, as in chapter 2. The normalisation condition and the remaining conditions at the compliant wall may be written:

$$(D'^n_N)_{Nk} u_k = 1\,, \quad (4.16a)$$

$$v_0 = -i\alpha\phi_w\,, \quad (4.16b)$$

$$w_0 = 0\,. \quad (4.16c)$$

The three cases for the conditions on the axis may now be represented as

1. Axisymmetric modes, $n = 0$ for which:

$$(D'_N)_{Nk} u_k = 0\,, \quad (4.17a)$$

$$v_N = 0\,, \quad (4.17b)$$

$$w_n = 0\,. \quad (4.17c)$$

2. Non-Axisymmetric modes, $n = 1$ for which:

$$u_N = 0\,, \tag{4.18a}$$

$$(D'^2_N)_{Nk} u_k = 0\,, \tag{4.18b}$$

$$w_N = 0\,. \tag{4.18c}$$

3. Non-Axisymmetric modes, $n > 1$ for which:

$$u_N = 0\,, \tag{4.19a}$$

$$v_N = 0\,, \tag{4.19b}$$

$$w_N = 0\,. \tag{4.19c}$$

Hence, for all symmetries of pipe mode, we have now found the $4N + 3$ conditions required to calculate the numerical solutions, u_j, v_j, w_j for $j = 0, \ldots, N$ and $p_{j+1/2}$ for $j = 0, \ldots, N-1$. These may be re-written in the form:

$$X1\boldsymbol{u} + Y1\boldsymbol{v} + W1\boldsymbol{p} = \boldsymbol{r1},$$

$$Y2\boldsymbol{v} + Z2\boldsymbol{w} + W2\boldsymbol{p} = \boldsymbol{r2},$$

$$Y3\boldsymbol{v} + Z3\boldsymbol{w} + W3\boldsymbol{p} = \boldsymbol{r3},$$

$$X4\boldsymbol{u} + Y4\boldsymbol{v} + Z4\boldsymbol{w} = \boldsymbol{r4}.$$

Here, the solutions have now been written as vectors, $\boldsymbol{u}$, $\boldsymbol{v}$, $\boldsymbol{w}$ and $\boldsymbol{p}$ with the jth element corresponding to the value of the functions, u, v, w at r'_j and p at $r'_{j+1/2}$, respectively. Rows 1 to $N-1$ of matrices $X1$, $Y1$ and $W1$ are obtained from equation (4.14a), rows 1 to $N-1$ of matrices $Y2$, $Z2$ and $W2$ are obtained from equation (4.14b) rows 1 to $N-1$ of matrices $Y3$, $Z3$ and $W3$ are obtained from equation (4.14c) and all rows (0 to $N-1$) of matrices $X4$, $Y4$ and $Z4$ are obtained from equation (4.15). The elements of the rows 0 and N of matrices, $W1$, $W2$ and $W3$, are all zero and the elements of the same rows of matrices, $X1$, $Y1$, $Y2$, $Z2$, $Y3$ and $Z3$, are determined by equations (4.16), plus the relevant

set of conditions (4.17), (4.18) or (4.19). Thus, all the elements of the right-hand-side vectors, $\boldsymbol{r1}$, $\boldsymbol{r2}$, $\boldsymbol{r3}$ and $\boldsymbol{r4}$, are zero except those which correspond to normalisation condition or the compliant condition, $v_0 = -i\alpha\phi_w$.

Therefore, we may re-write the stability equations for calculating numerical solutions in the form given by equation (2.16), i.e.

$$L\boldsymbol{\phi} = \boldsymbol{r}\,,$$

where here

$$L = \begin{pmatrix} X1 & Y1 & 0 & W1 \\ 0 & Y2 & Z2 & W2 \\ 0 & Y3 & Z3 & W3 \\ X4 & Y4 & Z4 & 0 \end{pmatrix}, \boldsymbol{\phi} = \begin{pmatrix} \boldsymbol{u} \\ \boldsymbol{v} \\ \boldsymbol{w} \\ \boldsymbol{p} \end{pmatrix}, \boldsymbol{r} = \begin{pmatrix} \boldsymbol{r1} \\ \boldsymbol{r2} \\ \boldsymbol{r3} \\ \boldsymbol{r4} \end{pmatrix}.$$

4.4.2 The Newton-Raphson Iterative Method

As mentioned in chapter 2, unless c is an eigenvalue of the problem, the relaxed boundary condition for the streamwise velocity at the compliant wall will not be obeyed. Now since there is only one wall in the compliant pipe problem, the streamwise wall condition can be written as

$$\chi(c) = c\; u(1) - \frac{2}{i\alpha} v(1) \neq 0\,.$$

Following section 2.2.2, if c is sufficiently close to the eigenvalue, then we can use a Newton-Raphson method to find successively closer approximations to the eigenvalue. We want to find Δc such that $\chi(c + \Delta c) = 0$ and therefore to leading order in Δc

$$\Delta c = -\frac{\chi}{\frac{\partial \chi}{\partial c}}\,,$$

where

$$\frac{\partial \chi}{\partial c} = u(1) + c\frac{\partial u}{\partial c}(1) - \frac{2}{i\alpha}\frac{\partial v}{\partial c}(1)\,.$$

The values of $\partial u/\partial c|_{r=1}$ and $\partial v/\partial c|_{r=1}$ are found using equation (2.18), where the elements of $\partial L/\partial c$ are calculated from equations (4.14). The relevant elements of $\partial \boldsymbol{\phi}/\partial c$ are then $(\partial u/\partial c)_0$ and $(\partial v/\partial c)_0$.

By iteratively using this whole procedure, we should find successively more accurate approximations to the phase velocity eigenvalue, c and the associated eigenfunction, $\boldsymbol{\phi}$. When the size of the adjustment to the phase velocity, $|\Delta c|$ is smaller than a tolerance of $10^{-6}|c|$, the solution should be sufficiently accurate.

4.5 Numerical Results

As for the channel problem, we have been able to identify three distinct classes of mode and further transitional modes whereby two or more of the modes of the distinct classes coalesce. The three identified mode classes appear to be equivalent to the classes, identified by Sen and Arora [67], as the Tollmien-Schlichting (TS) class (here these are referred to as the Rigid-Type (RT) modes, as explained below), the Kelvin-Helmholtz (KH) class and the Resonant (R) class, for boundary-layer flow. We shall start by giving descriptions of the four mode classes which may lead to instabilities in the flow.

In theory the circumferential wave number, n, can take any positive integer value. However, it is not possible to consider all such values when seeking numerical solutions. Therefore, concentration has centred on the axisymmetric modes, since these are the simplest in form and also on the non-axisymmetric modes where $n = 1$, since these are generally the least stable modes in the rigid pipe. See for example Salwen and Grosch [65].

4.5.1 Rigid-Type (RT) modes

These modes are of the same type that occur in rigid pipe flow and are the equivalent of the Tollmien-Schlichting modes that occur in both channel and boundary-layer flow. However, since rigid pipe flow is stable, i.e. all modes have a phase velocity with negative imaginary part, the critical layer associated with neutral Tollmien-Schlichting modes does not occur. Hence, the rigid pipe modes are not strictly speaking Tollmien-Schlichting modes and so we shall call these Rigid-Type modes. As for channel and boundary-layer flow these modes are induced by the viscosity of the fluid and exist in the limit as the complex amplitude, $a \to 0$. The condition (4.9) then implies that $\phi_w \to 0$. In this limit $c \to c^*$, the eigenvalue for the rigid-walled pipe.

For non-zero but small values of a and ϕ_w, i.e. for $|a|, |\phi_w| \ll 1$, the phase velocity eigenvalue then takes the form $c = c^* + \delta c$, where $\delta c/c^* \ll 1$.

Axisymmetric Modes

For $\phi_w = 0$ our problem reduces to that of the rigid pipe and so we can compare our results with those of previous rigid pipe studies. For example, we can choose $\alpha = 11.0$, $Re = 6000$, $n = 0$ and then we obtain $c = 0.98899 - 0.012843i$ as did Sen, Venkateswarlu and Maji [68]. Introducing a compliant wall seems to have very little effect on the axisymmetric RT modes for $Re = O(10^3)$. Only for much lower Reynolds numbers is there any noticable deviation from the rigid value of the phase velocity. As $|\phi_w|$ is increased, the Transitional modes occur before the perturbation from the rigid phase velocity is large enough to cause an unstable mode of the RT class and hence no unstable axisymmetric RT modes have been found.

Figure 4.2 demonstrates the resilience of the axisymmetric ($n = 0$) RT modes to compliant effects. The values of Re and α are as above.

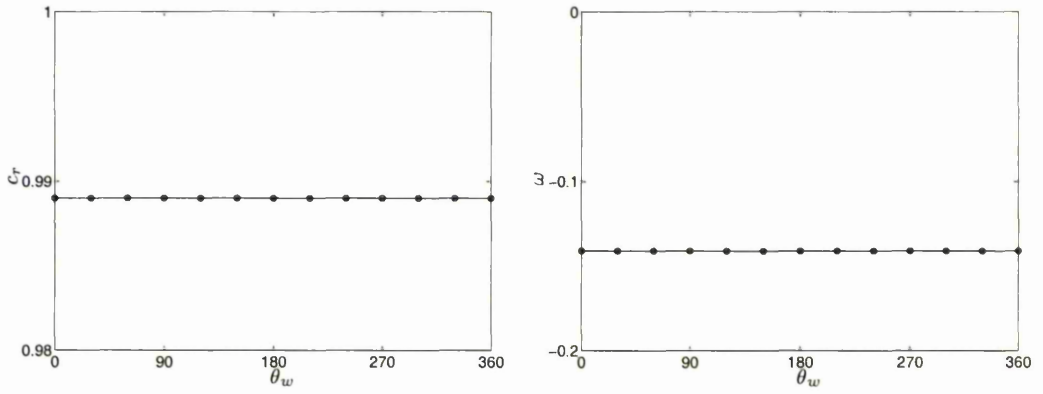

(a) Phase Speed (b) Growth Rate

Figure 4.2: Axisymmetric RT pipe modes.
—, $|\phi_w| = 0.00$; -o-, $|\phi_w| = 0.05$; -×-, $|\phi_w| = 0.10$.

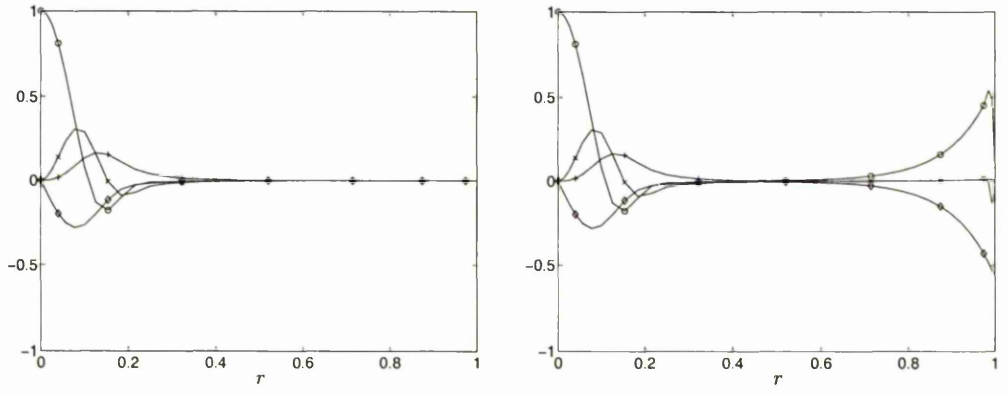

(a) Rigid case (b) $|\phi_w| = 0.05$

Figure 4.3: Eigenfunctions for the axisymmetric RT pipe modes.
-o-, $Re(u)$; -×-, $Im(u)$; -+-, $Re(v)$; -◇-, $Im(v)$.

Components of the eigenfunctions, $u(r)$ and $v(r)$, are given in figures 4.3(a) for the rigid case and 4.3(b) for $|\phi_w| = 0.05$, respectively. Here, $\theta_w = 0°$. These figures show that the rigid solution is a "centre mode", i.e. the largest disturbances

occur near the axis of the pipe. Introducing compliance has very little effect on the eigenfunction near $r = 0$ but another region near the wall arises, where significant disturbances occur.

Since there are no unstable axisymmetric RT modes it is not necessary to consider the physical realisability of such modes. Any set of wall parameters will lead to axisymmetric modes in the RT class which are stable, if they occur.

Non-axisymmetric Modes

For the non-axisymmetric modes with circumferential wave number, $n = 1$, we can choose $\alpha = 4.25$ and $Re = 4000$. Then we obtain $c = 0.96370 - 0.015995i$, which agrees with those obtained by Sen, Venkateswarlu and Maji [68]. Figure 4.4

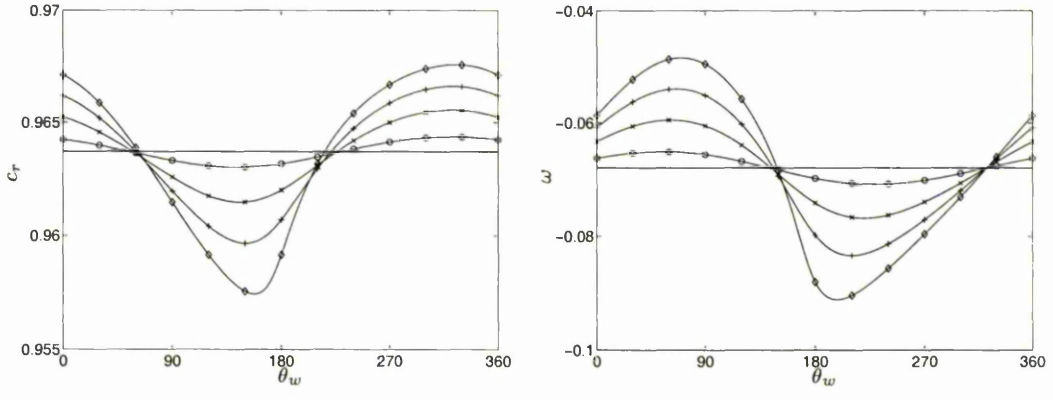

(a) Phase Speed (b) Growth Rate

Figure 4.4: Non-axisymmetric RT pipe modes.
—, $|\phi_w| = 0.00$; -o-, $|\phi_w| = 0.01$; -×-, $|\phi_w| = 0.03$; -+-, $|\phi_w| = 0.05$; -◇-, $|\phi_w| = 0.07$.

illustrates the small perturbation effects of non-zero values of ϕ_w on the given eigenvalue, c. Clearly, the effects of compliance are more marked for the non-axisymmetric ($n = 1$) RT modes than for their axisymmetric counterparts. There is a significant deviation from the rigid eigenvalue for all ranges of the Reynolds number. However, again no unstable RT modes were found, since modes of the

Transitional class arose before $|\phi_w|$ was increased sufficiently to cause the growth rate of the RT modes to become positive.

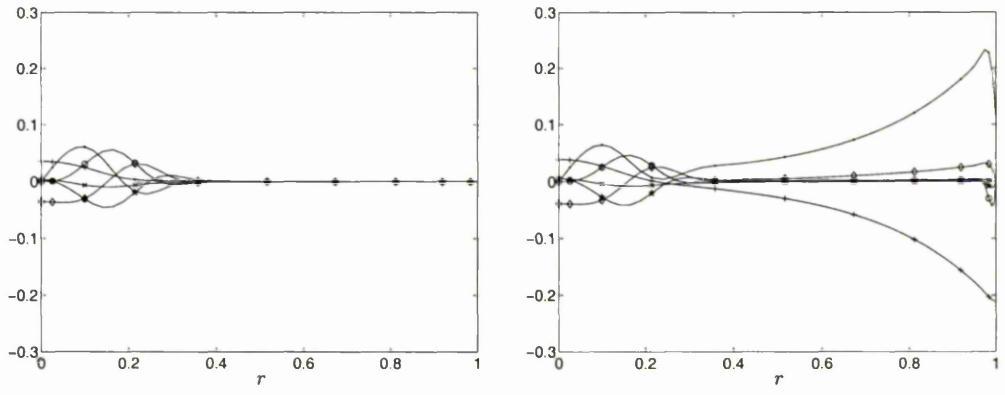

(a) Rigid case

(b) $|\phi_w| = 0.05$

Figure 4.5: Eigenfunctions for the non-axisymmetric RT pipe modes.
-.-, $Re(u)$; -○-, $Im(u)$; -×-, $Re(v)$; -+-, $Im(v)$; -◇-, $Re(w)$; -⋆-, $Im(w)$.

Components of the eigenfunctions, $u(r)$, $v(r)$ and $w(r)$, are given in figures 4.5(a) for the rigid case and 4.5(b) for $|\phi_w| = 0.05$, respectively. Here, $\theta_w = 0°$. These figures show that like the axisymmetric case, the rigid solution is a "centre mode", i.e. the largest disturbances occur near the axis of the pipe. Introducing compliance has more effect on the eigenfunction near $r = 0$ than for the axisymmetric RT modes - take the relative sizes of the eigenfunction extrema near the pipe axis, for example. Like the axisymmetric RT modes another region near the wall arises, where significant disturbances occur and this interacts with the region near the pipe axis.

As for the axisymmetric case, since there are no unstable non-axisymmetric ($n = 1$) RT modes it is not necessary to consider their physical realisability.

4.5.2 Kelvin-Helmholtz (KH) modes

The Kelvin-Helmholtz class of modes also exists for $\phi_w \to 0$. However, as in compliant channel flow, for this class of modes $c \to 0$ and a is non-zero. These modes are associated with instabilities in the compliant surface induced by the flow. In the limit $c \to 0$, $a \to a^* \neq 0$ and so we obtain a stationary wave in the compliant surface with amplitude a^*, streamwise wave number α and which is neutrally stable.

For non-zero but small values of ϕ_w, i.e. for $|\phi_w| \ll 1$, the values of the phase velocity eigenvalues are also small, i.e. $c \ll 1$ and so we obtain a surface wave which is either stationary or slow moving. Therefore, the arguments put forward in section 3.5.2 regarding the similarity of these modes and static divergence modes again hold, since modes exist in the pipe which obey a purely viscous theory (see section 4.6).

Axisymmetric Modes

The phase velocities of axisymmetric modes in the KH class exhibit a more noticeable deviation from the rigid case, i.e. $c = 0$, than the corresponding Rigid-Type modes. This is particularly true for $Re = O(10^3)$, where we have seen in section 4.5.1 that any non-zero ϕ_w seems to have very little effect on the value of the axisymmetric RT eigenvalue. However, the eigenvalue never attains a value close in magnitude to the non-axisymmetric ($n = 1$) or channel KH modes for these values of Re.

Modes of this class seem to persist for large values of $|\phi_w|$, when $Re = O(10^3)$. Linked with this is a difficulty in finding Transitional and Resonant modes for $Re = O(10^3)$, as can be seen in sections 4.5.3 and 4.5.4.

Examples of the phase speed and growth rate of the KH modes are given in figures 4.6(a) and 4.6(b), respectively. Here, $Re = 6000.0$ and $\alpha = 11.0$, as for

the RT modes.

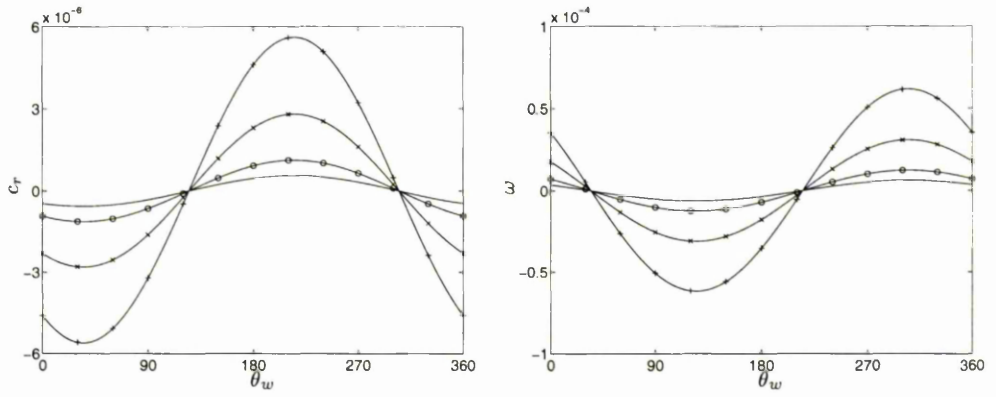

(a) Phase Speed (b) Growth Rate

Figure 4.6: Axisymmetric KH pipe modes.

—, $|\phi_w| = 0.01$; -○-, $|\phi_w| = 0.02$; -×-, $|\phi_w| = 0.05$; -+-, $|\phi_w| = 0.10$.

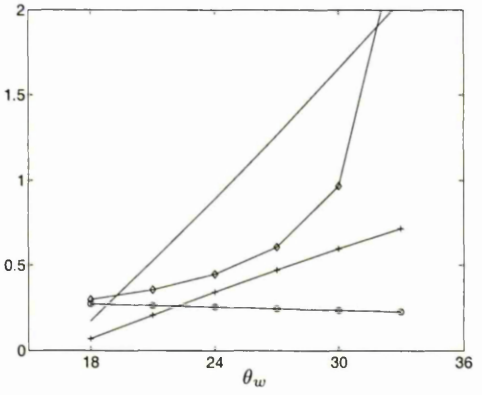

Figure 4.7: Physical realisability bounds on m, d and c_0^2.

—, $10^5 \times d$ lower bound;

-○-, $10^{-8} \times m$ lower bound; -◇-, $10^{-8} \times m$ upper bound;

-+-, $10^{11} \times c_0^2$ upper bound.

The wall parameter bounds for the modes where $Re = 6000.0$, $\alpha = 11.0$ and $|\phi_w| = 0.05$, are given in figure 4.7. Here, the bounds all correspond to case 2 in

section 2.3.2 and hence these modes may be eliminated by an increase in the free wave speed, c_0. Alternatively, given that the lower bound for m is strictly greater than zero for all θ_w, keeping the wall density sufficiently small will eliminate these modes, too. A value of 2 for m is well within this range.

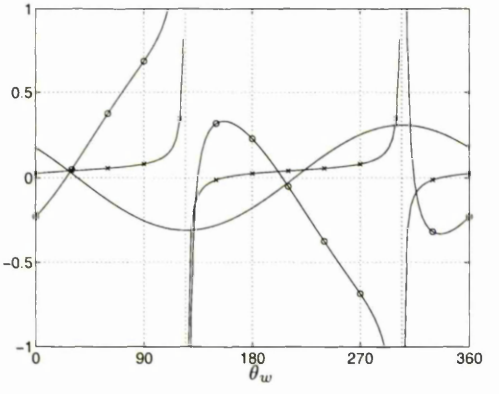

Figure 4.8: Physical realisability for $m = 5.0 \times 10^7$.
—, $10^4 \times \omega$; -o-, $10^4 \times d$; -×-, $10^{10} \times c_0^2$.

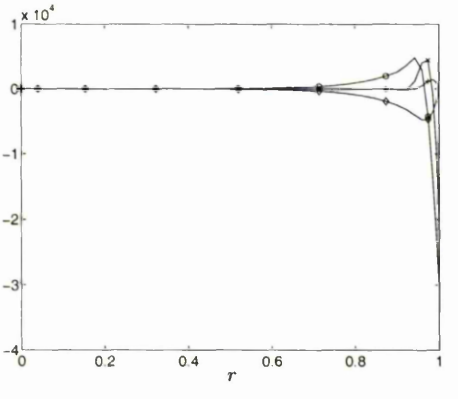

Figure 4.9: Eigenfunctions for the axisymmetric KH pipe modes, $|\phi_w| = 0.05$.
-o-, $Re(u)$; -×-, $Im(u)$; -+-, $Re(v)$; -◇-, $Im(v)$.

Plots of the back-calculated values of d and c_0^2 are given in figure 4.8 for $m = 5.0 \times 10^7$. Obviously, this is an infeasibly large value for m in practice. However, it does demonstrate that the linear stability theory predicts unstable

KH modes for some values of the wall density. A small unstable region can be seen for values of θ_w close to 30°.

A plot of the eigenfunctions for $Re = 6000.0$, $\alpha = 11.0$ and $|\phi_w| = 0.05$ is given in figure 4.9. Here, $\theta_w = 0°$. This shows a very pronounced narrow wall region where the disturbances are much larger than in the remainder of the pipe.

Non-axisymmetric Modes

The magnitude of the eigenvalues for the non-axisymmetric ($n = 1$) KH modes is generally much larger than that of the axisymmetric KH modes with the same values of Re, α and ϕ_w. Examples of the phase speeds and growth rates for the non-axisymmetric ($n = 1$) KH modes are given in figures 4.10(a) and 4.10(b), respectively. Here, $Re = 4000.0$ and $\alpha = 4.25$, as for the RT modes.

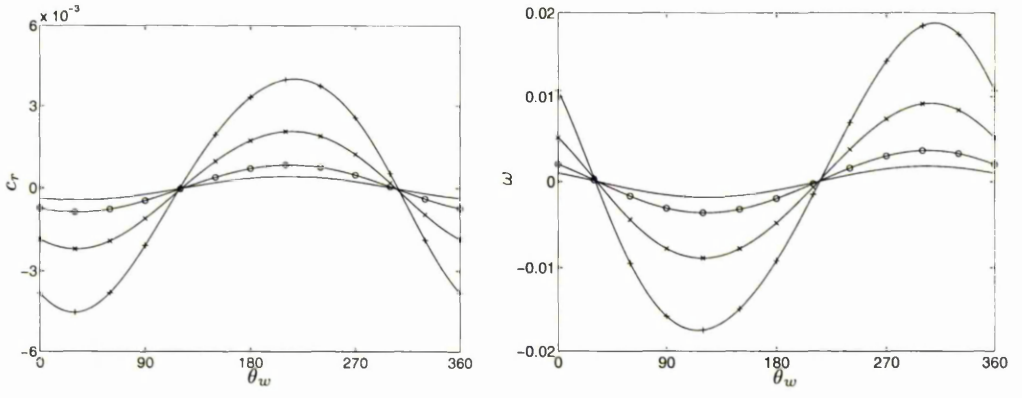

(a) Phase Speed (b) Growth Rate

Figure 4.10: Non-axisymmetric KH pipe modes.
—, $|\phi_w| = 0.01$; -o-, $|\phi_w| = 0.02$; -×-, $|\phi_w| = 0.05$; -+-, $|\phi_w| = 0.10$.

Wall parameter bounds can be found in figure 4.11 for $Re = 4000.0$, $\alpha = 4.25$ and $|\phi_w| = 0.05$. This figure shows that like the axisymmetric modes, the bounds all correspond to case 2 in section 2.3.2 and the lower bound for m is much greater

than zero for all θ_w. Therefore, these unstable modes may be eliminated either by choosing a suitably large free wave speed, c_0 or by choosing a suitably low value of the wall density. Like the axisymmetric modes, a value of 2 for m is well within the range of wall parameters which will eliminate the above unstable modes.

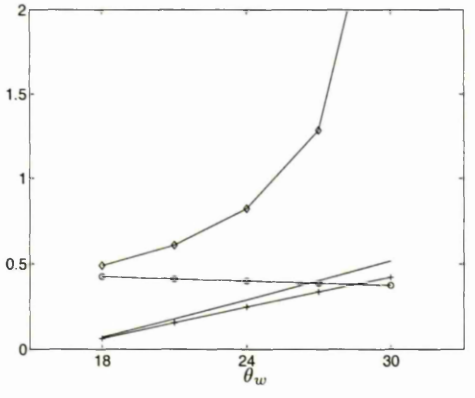

Figure 4.11: Physical realisability bounds on m, d and c_0^2.
—, $10^2 \times d$ lower bound;
-o-, $10^{-3} \times m$ lower bound; -◇-, $10^{-3} \times m$ upper bound;
-+-, $10^5 \times c_0^2$ upper bound.

Plots of the back-calculated values of d and c_0^2 are given in figure 4.12 for $Re = 4000.0$, $\alpha = 4.25$, $|\phi_w| = 0.05$ and $m = 500.0$. As for the axisymmetric KH modes, this value of m is too large to be representative of any walls in practice but it does indicate that the linear theory predicts KH instabilities for sufficiently dense walls. Figure 4.12 shows there to be a small unstable region close to $\theta_w = 30°$.

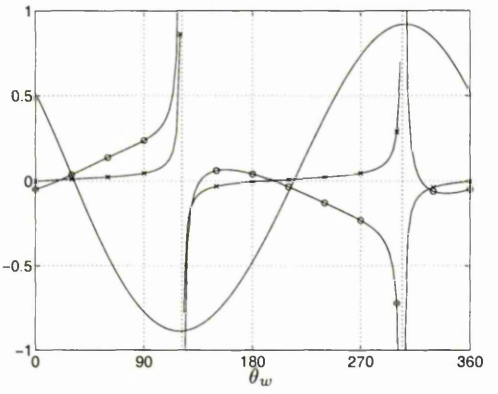

Figure 4.12: Physical realisability for $m = 5.0 \times 10^2$.
—, $10^2 \times \omega$; -o-, $10^2 \times d$; -×-, $10^4 \times c_0^2$.

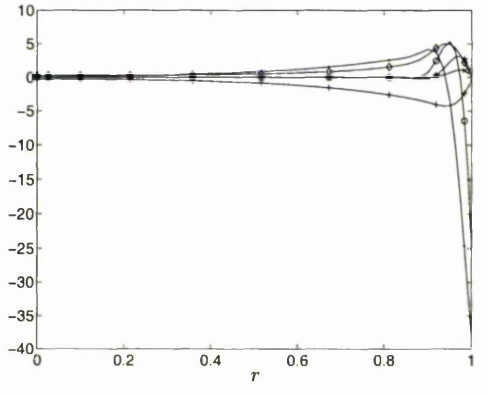

Figure 4.13: Eigenfunctions for the
non-axisymmetric KH pipe modes, $|\phi_w| = 0.05$.
-.-, $Re(u)$; -o-, $Im(u)$; -×-, $Re(v)$; -+-, $Im(v)$; -◇-, $Re(w)$; -⋆-, $Im(w)$.

A plot of the eigenfunctions for $Re = 4000.0$, $\alpha = 4.25$ and $|\phi_w| = 0.05$ is given in figure 4.13. Here, $\theta_w = 0°$. Like the axisymmetric KH modes, this shows there to be a very pronounced narrow wall region where the disturbances are much larger than in the remainder of the pipe.

4.5.3 Transitional modes

Where the Resonant modes can be found, the transition from RT to R modes occurs via a series of modes which can be termed the Transitional modes as they are for boundary-layer flow and channel flow bounded by compliant walls. However, there are certain points which must be addressed with regard to these modes.

The first point is that these modes (and the Resonant modes) are difficult to find numerically for $Re = O(10^3)$. In fact we have been unable to find any Transitional modes for Reynolds numbers much above 100. However, these modes must exist at lower wave numbers for $Re = O(10^3)$, since there are Resonant modes in the long wave limit, $\alpha \to 0$ for all Re (see section 4.6.2). This numerical problem is an outstanding issue which needs to be addressed.

The second point is that where the Transitional modes can be found numerically, the transition from the TS to R classes of modes appears to be very different from that in both boundary-layer and channel flows bounded by compliant walls. It appears that the Transitional modes can themselves be subdivided into three distinct subclasses.

The first subclass is formed as $|\phi_w|$ is increased for modes in the RT class. The RT modes do not coalesce directly with modes in the KH class. Instead the RT modes undergo a series of bifurcations, as $|\phi_w|$ is increased, to form many-valued (possibly infinitely-valued) solutions. The least stable branch of the many-valued solutions corresponds to the least stable RT mode which we can, without loss of generality, call the zeroth branch. We can also fix θ_w so that this branch lies between 0° and 360°. The growth rate appears to decrease monotonically as θ_w is decreased from 0° and ω also appears to decrease montonically as θ_w is increased beyond 360°. In a similar way, the phase speed generally appears to increase as θ_w is decreased and it generally appears to decrease as θ_w is increased. This happens

in such a way that for branches below the zeroth, the modes are all downstream travelling waves and for branches above the zeroth, the modes are all upstream travelling waves.

The second subclass of Transitional modes occur as $|\phi_w|$ is increased further when the first subclass of transitional modes coalesces with the KH modes. This happens in such a way that the branch corresponding to the KH modes can be found at values of θ_w between 360° and 720°. These modes, like those in the first subclass, are many valued but are the first to exhibit unstable regions, as $|\phi_w|$ is increased from zero. These instabilities appear to be found only in the zeroth and first branches, i.e. for θ_w between 0° and 720°.

The third subclass of modes are formed when $|\phi_w|$ is increased yet further and the Resonant modes become distinct from the second subclass of Transitional modes. Effectively, if $|\phi_w|$ is decreased from a very large value, the Resonant modes coalesce with the third subclass of Transitional modes to form the second subclass of Transitional modes. Like the first and second subclasses of modes, these are many-valued and possibly infinitely valued solutions, though only a small region, near 360°, appears to exhibit any instabilities.

As for the Transitional modes in the compliant channel, there is scope for further work to gain a fuller understanding of the nature of transition process from RT to R class modes. Therefore, we shall only give examples of the third subclass of Transitional modes. This particular subclass exhibits some strongly unstable modes which are physically realisable and hence they are important in considering the overall stability of compliant pipe flows.

Axisymmetric Modes

Examples of the third subclass of Transitional modes are given in figure 4.14. These illustrate the strong instability that exists at $\theta_w = 360°$. As $|\phi_w|$ is increased, it can be seen that modes in this subclass become massively damped except in a narrowing region near $\theta_w = 360°$, where the modes become more and more unstable. The kinematic parameters for these modes are $Re = 1.0$ and $\alpha = 4.25$.

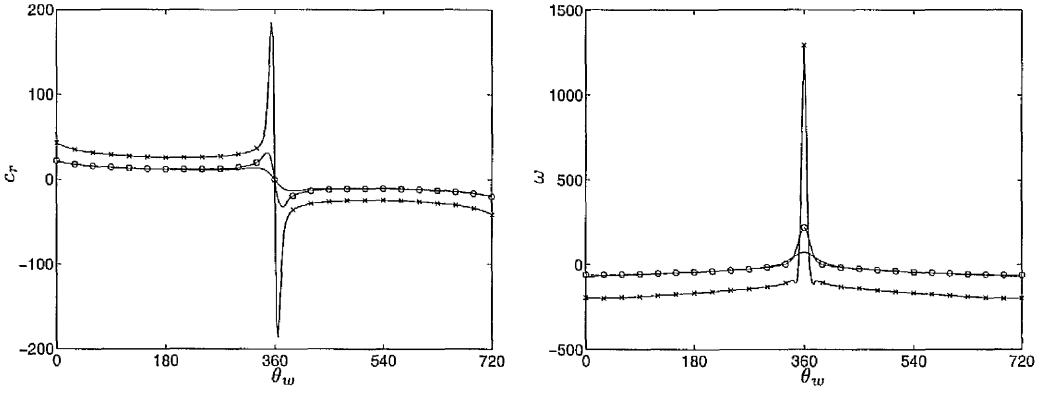

(a) Phase Speed (b) Growth Rate

Figure 4.14: Axisymmetric Transitional pipe modes.
—, $|\phi_w| = 1.5$; -o-, $|\phi_w| = 2.0$; -×-, $|\phi_w| = 2.5$.

Wall parameter bounds for the given modes with $|\phi_w| = 2.0$ are given in figure 4.15. This shows the most unstable mode not to be physically realisable. Where the modes are physically realisable, the bounds all correspond to case 2 in section 2.3.2. Therefore, these unstable modes can be eliminated by a suitably large increase in the free wave speed, c_0. As for the KH modes, the lower bound for m is strictly greater than zero for all θ_w and hence the unstable modes may eliminated by choosing a suitably small value of m. Here, a value of less than about 0.1 would be necessary to ensure elimination of the above mentioned

modes. However, choosing $m = O(1)$ will reduce the unstable region to two "unstable pockets", since such a wall density will be above the upper bound for m for most values of θ_w. This is illustrated in figure 4.16, where back-calculated values of d and c_0^2 are plotted against θ_w for $|\phi_w| = 2.0$ and $m = 1.0$. This confirms the existence of the "unstable pockets" and hence only a very limited range of values of d and c_0^2 will give rise to instabilities with $|\phi_w| = 2.0$ and $m = 1.0$.

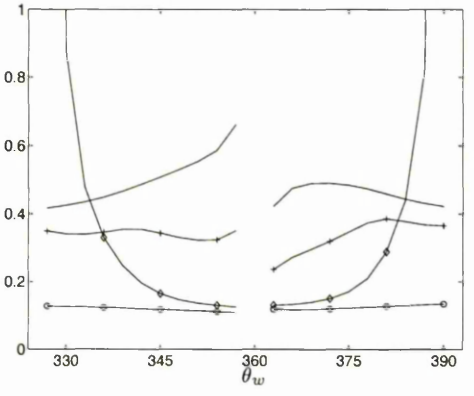

Figure 4.15: Physical realisability bounds on m, d and c_0^2.
—, $10^{-2} \times d$ lower bound; -o-, m lower bound; -◇-, m upper bound;
-+-, $10^{-3} \times c_0^2$ upper bound.

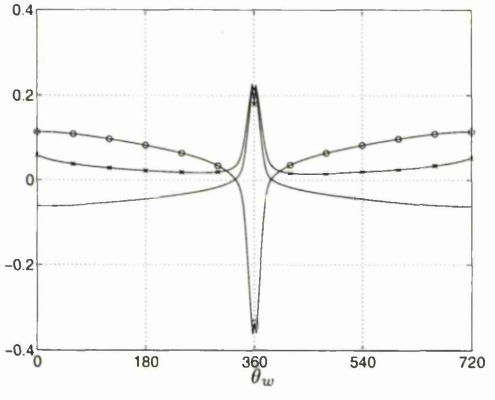

Figure 4.16: Physical realisability for $m = 1.0$.
—, $10^{-3} \times \omega$; -o-, $10^{-3} \times d$; -×-, $10^{-4} \times c_0^2$.

Plots of the eigenfunctions are given in figure 4.17. These show that there is no pronounced wall region for these modes, though there is a tendency for the disturbances to be larger closer to the flexible surface. The kinematic parameters used were $Re = 1.0$, $\alpha = 4.25$, $|\phi_w| = 2.0$ and $\theta_w = 345°$.

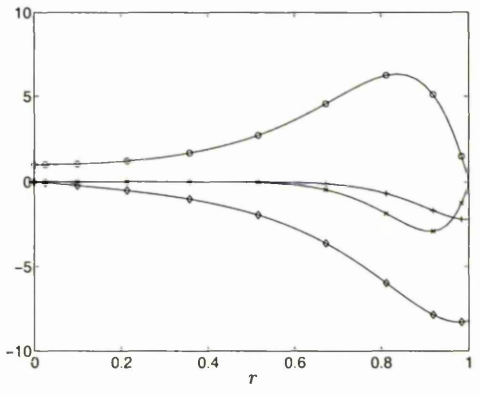

Figure 4.17: Eigenfunctions for the
axisymmetric Transitional pipe modes, $|\phi_w| = 2.0$.
-o-, $Re(u)$; -◇-, $Im(u)$; -×-, $Re(v)$; -+-, $Im(v)$.

Non-axisymmetric Modes

Example modes of the third transitional subclass are given in figure 4.18 for the non-axisymmetric ($n = 1$) case. Here, the remaining kinematic parameters are $Re = 1.0$ and $\alpha = 4.25$. Both the phase speeds and growth rates are qualitatively similar to the axisymmetric modes of the same subclass.

Plots of the wall parameter bounds (see figure 4.19) show these to be qualitatively similar to the axisymmetric case, too. Here, $Re = 1.0$, $\alpha = 4.25$ and $|\phi_w| = 0.8$. Given the noted similarities between the axisymmetric and the non-axisymmetric ($n = 1$) cases, the same approach to eliminating the unstable modes can be taken here, too, i.e. increasing the free wave speed or decreasing the density sufficiently will eliminate these modes and increasing the density sufficiently will reduce the unstable regions to two "small pockets". Using $m = 1.0$, as used

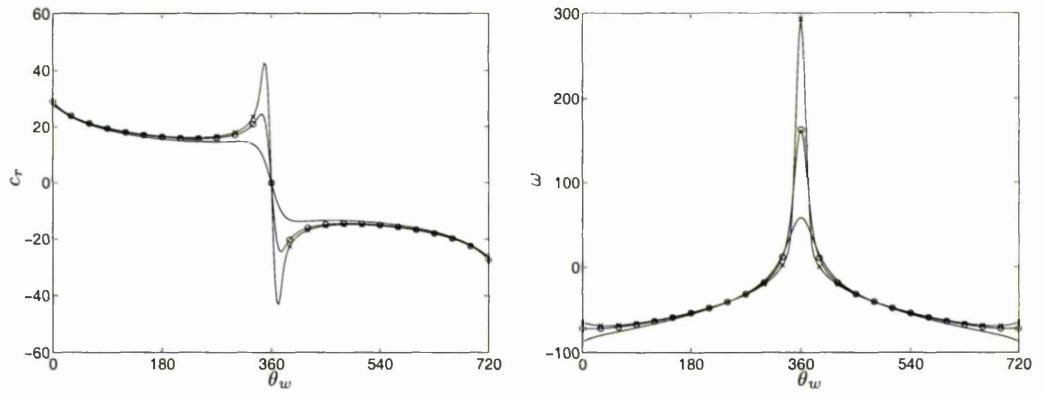

(a) Phase Speed (b) Growth Rate

Figure 4.18: Non-axisymmetric Transitional pipe modes.
—, $|\phi_w| = 0.6$; -o-, $|\phi_w| = 0.8$; -×-, $|\phi_w| = 0.9$.

for the axisymmetric case, back-calculated values of d and c_0^2 are plotted in figure 4.20 for $Re = 1.0$, $\alpha = 4.25$ and $|\phi_w| = 0.8$. This shows the expected "unstable pockets" at values of θ_w close to 330° and 390°.

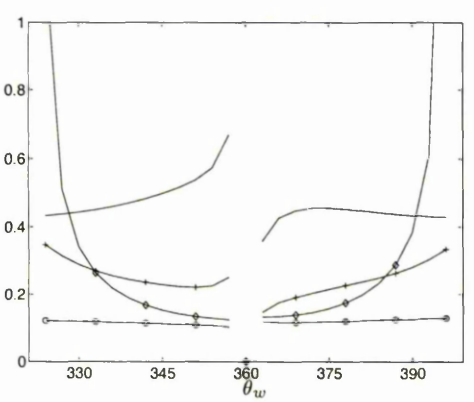

Figure 4.19: Physical realisability bounds on m, d and c_0^2.
—, $10^{-2} \times d$ lower bound; -o-, m lower bound; -◇-, m upper bound;
-+-, $10^{-3} \times c_0^2$ upper bound.

The eigenfunctions for $Re = 1.0$, $\alpha = 4.25$, $|\phi_w| = 0.8$ and $\theta_w = 345°$ are given in figure 4.21. This shows the axial and radial velocity components of the disturbance to be similar to the axisymmetric case. Similarly, the circumferential velocity component has no pronounced wall region but its largest values are close

to the flexible surface.

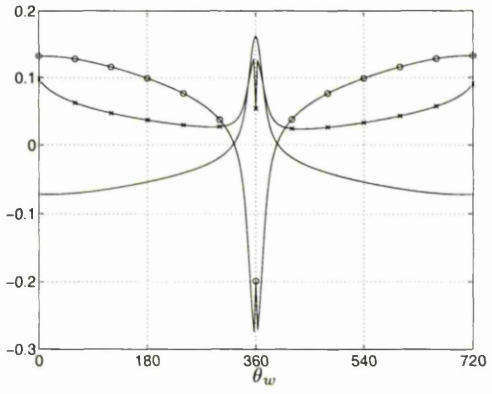

Figure 4.20: Physical realisability for $m = 1.0$.
—, $10^{-3} \times \omega$; -○-, $10^{-3} \times d$; -×-, $10^{-4} \times c_0^2$.

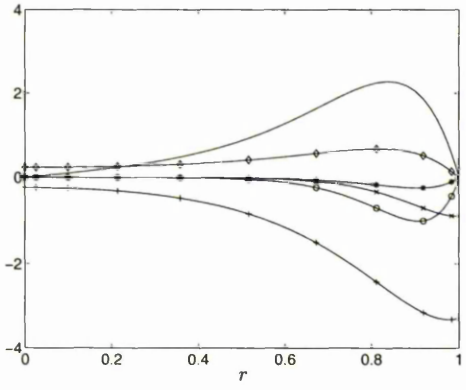

Figure 4.21: Eigenfunctions for the
non-axisymmetric Transitional pipe modes, $|\phi_w| = 0.8$.
—, $Re(u)$; -○-, $Im(u)$; -×-, $Re(v)$; -+-, $Im(v)$; -◇-, $Re(w)$; -⋆-, $Im(w)$.

4.5.4 Resonant (R) modes

As for compliant channel flow, the Resonant class of modes exists for large values of $|\phi_w|$, i.e. generally for more compliant walls. However, as stated above, there has been some difficulty in obtaining numerical solutions in this class. Modes of this class have only been obtained for Re at most $O(10^2)$, where the inviscid

theory is insufficient to describe the solutions and hence the phase velocity is a function of α as $|\phi_w| \to \infty$. Hence, for these modes $c \to c_\infty(\alpha, Re) + 0i$ as $|\phi_w| \to \infty$. The condition (4.9) then implies that the surface wave amplitude, a, is then also large. These modes then, like the KH modes, are associated with instabilities in the compliant surface, induced by the flow.

For finite but sufficiently large values of $|\phi_w|$, $c = c_\infty + \delta c$, where δc is small, i.e. $|\delta c| \ll c_\infty$. This holds until $|\phi_w|$ is decreased to a value close to that at which the Transitional modes occur.

In section 4.5.3 it was mentioned that although no numerical R modes had been found for higher Reynolds numbers (except to confirm the long-wave solutions), they must exist since the long-wave solutions exist. There is, therefore, much scope for further investigation into modes in the R class and into the Transitional modes, too.

Axisymmetric Modes

Phase speeds and growth rates of example axisymmetric Resonant modes can be found in figures 4.22(a) and 4.22(b), respectively. These show that although the oscillations are not about 1, as θ_w is varied, they are qualitatively similar to those of the symmetric Resonant modes in the symmetric channel in section 3.5.4. As expected, when $|\phi_w|$ is increased the amplitude of the oscillations decreases. The kinematic parameters used for figure 4.22 were $Re = 1.0$ and $\alpha = 4.25$. The wall parameter bounds for the above modes where $|\phi_w| = 1.8$ are given in figure 4.23. This shows that the bounds correspond to case 1 in section 2.3.2. Hence, the Reynolds number must be large enough that the leading-order viscous solution (see section 4.6.1) is insufficient to fully describe these modes because the bounds for the viscous R modes are those of case 2.

Back-calculated values of d and c_0^2 are plotted in figure 4.24 for $m = 2$. This

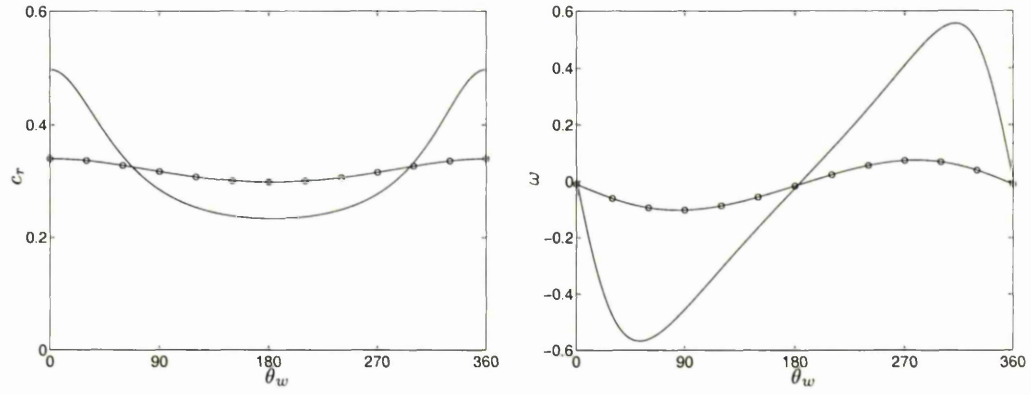

(a) Phase Speed (b) Growth Rate

Figure 4.22: Axisymmetric R pipe modes.
—, $|\phi_w| = 1.8$; -o-, $|\phi_w| = 10.0$.

along with figure 4.23 shows that there is a small unstable region which can be reduced to an "unstable pocket" by a small increase in the wall density. A value of m between 5 and 10 should bring about such a stabilising effect. Only a small range of values of d and c_0^2 would then lead to instabilities of this class with this value of $|\phi_w|$.

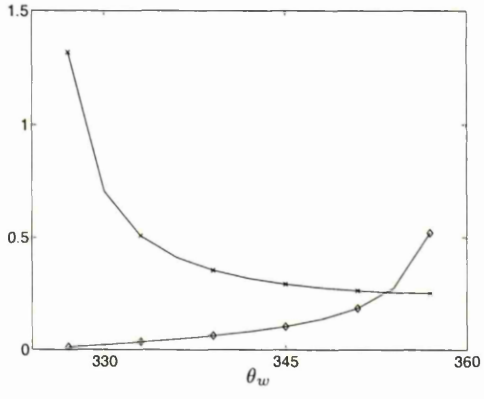

Figure 4.23: Physical realisability bounds on m, d and c_0^2.
-◇-, $10^{-1} \times m$ upper bound; -×-, c_0^2 lower bound.

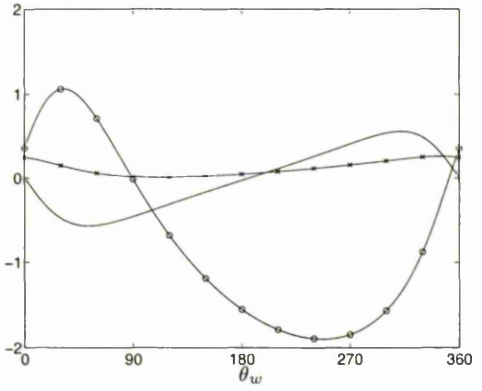

Figure 4.24: Physical realisability for $m = 2.0$.

—, ω; -o-, $\times d$; -×-, c_0^2.

The eigenfunctions for the Resonant modes in the compliant pipe are very similar to those in the compliant channel as can be seen in figure 4.25 for $\theta_w = 0°$. Although this shows only one value of θ_w, it can be seen that the eigenfunctions have no significant wall region. The greatest disturbances do occur closest to the wall though and the normal velocity component, v, is qualitatively similar to $-i\phi$, where here ϕ is the stream function for the symmetric R channel mode for $\theta_w = 0°$ in figure 3.40.

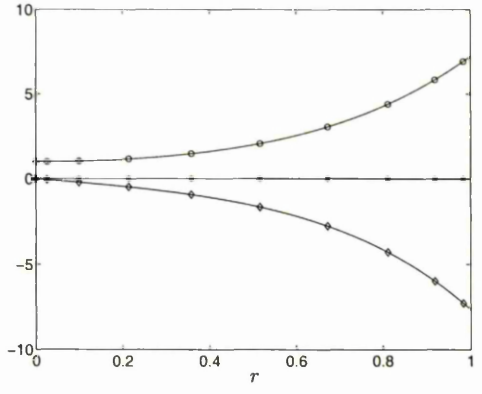

Figure 4.25: Eigenfunctions for the axisymmetric R pipe modes, $|\phi_w| = 1.8$.

-o-, $Re(u)$; -×-, $Im(u)$; -+-, $Re(v)$; -◇-, $Im(v)$.

Non-axisymmetric Modes

The non-axisymmetric ($n = 1$) R modes are remarkably similar to the axisymmetric R modes. This is in contrast to the symmetric and anti-symmetric R modes in the symmetric channel. This can be seen in all of the figures in this section. First, the phase speeds and growth rates are qualitatively similar, as illustrated in figure 4.26. Here, although the magnitudes of the stream functions differ from the axisymmetric case, the profiles are similar to those for the lower value of $|\phi_w|$ in figure 4.22. The remaining parameters used in figure 4.26 were $Re = 1.0$ and $\alpha = 4.25$.

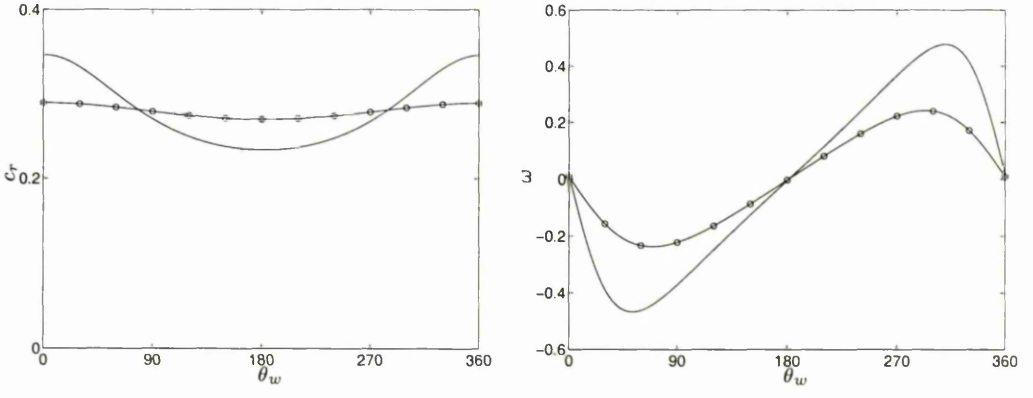

(a) Phase Speed (b) Growth Rate

Figure 4.26: Non-axisymmetric R pipe modes.
—, $|\phi_w| = 1.0$; -o-, $|\phi_w| = 1.8$.

The physical realisability considerations are also very similar to those of the axisymmeric R modes. The wall parameter bounds, like the axisymmetric modes above, correspond to case 1 in section 2.3.2, as can be seen in figure 4.27, where $Re = 1.0$, $\alpha = 4.25$ and $|\phi_w| = 1.0$. Therefore the unstable modes here can be reduced to a small pocket by an increase in the wall density. As for the axisymmetric case, a value of m of about 5 to 10 is large enough to achieve this pocket.

So again, only a very limited range of values of d and c_0^2 would then give rise to instabilities with $|\phi_w| = 1.0$.

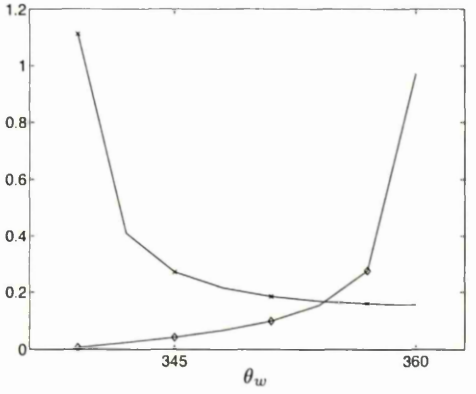

Figure 4.27: Physical realisability bounds on m, d and c_0^2.
-◇-, $10^{-1} \times m$ upper bound; -×-, c_0^2 lower bound.

Taking a lower value of 2 for m, we can see in figure 4.28 that the back-calculated values of d and c_0^2 show there to be a small physically realisable unstable region near $\theta_w = 360°$. This is consistent with the wall parameter bounds as expected. The profiles of d and c_0^2 are again very similar to those of the axisymmetric R modes above.

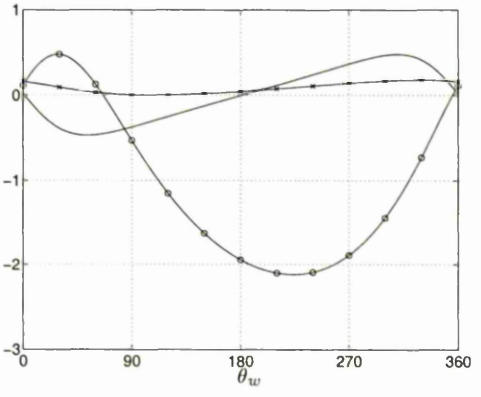

Figure 4.28: Physical realisability for $m = 2.0$.
—, ω; -o-, d; -×-, c_0^2.

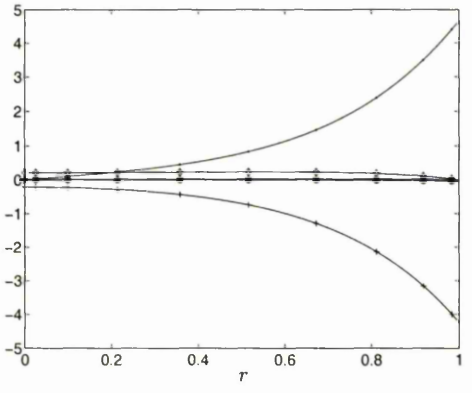

Figure 4.29: Eigenfunctions for the
non-axisymmetric R pipe modes, $|\phi_w| = 0.05$.
-.-, $Re(u)$; -○-, $Im(u)$; -×-, $Re(v)$; -+-, $Im(v)$; -◇-, $Re(w)$; -⋆-, $Im(w)$.

Eigenfunctions for the non-axisymmetric ($n = 1$) R modes are given in figure 4.29 for $\alpha = 4.25$ and $\theta_w = 0°$. These show that the x and r components of the eigenfunctions are very similar qualitatively to the same components of the axisymmetric R modes.

4.6 Analytical Results

We have been able to find analytical solutions to the governing stability equations for specific kinematic parameter ranges. As for the channel problem (see section 3.6), these may be divided into two main sections, which are given below.

4.6.1 The Viscous Limit

The first set of analytical solutions are for the viscous modes. These occur in the limit $Re \to 0$, where it can be seen (in figure 4.30) that the phase velocities of the KH modes tend towards a generally non-zero value for any ϕ_w. This is true for both axisymmetric and non-axisymmetric ($n = 1$) modes. Phase velocities of

modes in the Resonant class also tend to generally non-zero values in this limit but are not plotted given the difficulty in obtaining such modes for larger values of the Reynolds number.

As mentioned in section 3.6, the axisymmetric modes for viscous flow past a visco-elastic wall were found by Kumaran [45]. The present study aims to establish a viscous theory for the kinematic modes in compliant pipe flow. Also, it is intended that the classes of instability will be identified and a comparison made with Kumaran's solutions.

In the limit $Re \to 0$, the pressure gradient is balanced by the viscous terms. However, our inertial pressure scaling, $p^* = \rho U^2 p$ implies that the pressure gradient of the basic flow would then become infinite. Hence we need to rescale the Navier-Stokes equations, using the viscous pressure scaling, $p^* = (\mu U/R)p$, to obtain:

$$\frac{\partial u_x}{\partial t}+u_x\frac{\partial u_x}{\partial x}+u_r\frac{\partial u_x}{\partial r}+\frac{u_\theta}{r}\frac{\partial u_x}{\partial \theta}= \frac{1}{Re}\left(-\frac{\partial p}{\partial x}+\frac{\partial^2 u_x}{\partial x^2}+\frac{1}{r}\frac{\partial}{\partial r}\left(r\frac{\partial u_x}{\partial r}\right)+\frac{1}{r^2}\frac{\partial u_x}{\partial \theta^2}\right), \tag{4.20a}$$

$$\frac{\partial u_r}{\partial t}+u_x\frac{\partial u_r}{\partial x}+u_r\frac{\partial u_r}{\partial r}+\frac{u_\theta}{r}\frac{\partial u_r}{\partial \theta}-\frac{{u_\theta}^2}{r}= \frac{1}{Re}\left(-\frac{\partial p}{\partial r}+\frac{\partial^2 u_r}{\partial x^2}+\frac{1}{r}\frac{\partial}{\partial r}\left(r\frac{\partial u_r}{\partial r}\right)+\frac{1}{r^2}\frac{\partial u_r}{\partial \theta^2}-\frac{2}{r^2}\frac{\partial u_\theta}{\partial \theta}-\frac{u_r}{r^2}\right), \tag{4.20b}$$

$$\frac{\partial u_\theta}{\partial t}+u_x\frac{\partial u_\theta}{\partial x}+u_r\frac{\partial u_\theta}{\partial r}+\frac{u_\theta}{r}\frac{\partial u_\theta}{\partial \theta}+\frac{u_r u_\theta}{r}= \frac{1}{Re}\left(-\frac{1}{r}\frac{\partial p}{\partial \theta}+\frac{\partial^2 u_\theta}{\partial x^2}+\frac{1}{r}\frac{\partial}{\partial r}\left(r\frac{\partial u_\theta}{\partial r}\right)+\frac{1}{r^2}\frac{\partial u_\theta}{\partial \theta^2}+\frac{2}{r^2}\frac{\partial u_r}{\partial \theta}-\frac{u_\theta}{r^2}\right), \tag{4.20c}$$

where, as before, $Re = \rho UR/\mu$ is the Reynolds number of the flow. With this scaling, the pressure of the basic flow takes the form, $p_B = -4x$, but since it does not appear in the stability equations this change will have no bearing on them.

Following the normal mode analysis of section 4.3, we obtain the revised

linearised stability equations for $Re \ll 1$:

$$Re\,[i\alpha(u_B - c)u + (Du_B)v] = -i\alpha\, p + \left(D^2 + \frac{1}{r}D - \left(\frac{n^2}{r^2} + \alpha^2\right)\right) u\,, \quad (4.21a)$$

$$Re\,[i\alpha(u_B - c)v] = -Dp + \left(D^2 + \frac{1}{r}D - \left(\frac{n^2+1}{r^2} + \alpha^2\right)\right) v - \frac{2in}{r^2}\, w\,, \quad (4.21b)$$

$$Re\,[i\alpha(u_B - c)w] = -\frac{in}{r}p + \left(D^2 + \frac{1}{r}D - \left(\frac{n^2+1}{r^2} + \alpha^2\right)\right) w + \frac{2in}{r^2}\, v\,, \quad (4.21c)$$

$$i\alpha\, u + \left(D + \frac{1}{r}\right) v + \frac{in}{r}\, w = 0\,, \quad (4.21d)$$

where again, α is the positive, real, axial wave number and n is the positive integer-valued circumferential wave number. The normal modes are as for equation 4.6.

Taking the limit $Re \to 0$ yields

$$\left(D^2 + \frac{1}{r}D - \left(\frac{n^2}{r^2} + \alpha^2\right)\right) u - i\alpha\, p = 0\,, \quad (4.22a)$$

$$\left(D^2 + \frac{1}{r}D - \left(\frac{n^2+1}{r^2} + \alpha^2\right)\right) v - \frac{2in}{r^2}\, w - Dp = 0\,, \quad (4.22b)$$

$$\left(D^2 + \frac{1}{r}D - \left(\frac{n^2+1}{r^2} + \alpha^2\right)\right) w + \frac{2in}{r^2}\, v - \frac{in}{r}p = 0\,, \quad (4.22c)$$

$$i\alpha\, u + \left(D + \frac{1}{r}\right) v + \frac{in}{r}\, w = 0\,. \quad (4.22d)$$

From these equations we should recover the solutions for small Reynolds numbers given by our numerical scheme.

For simplicity, we shall consider solutions in two separate cases, namely axisymmetric modes and non-axisymmetric modes, as follows.

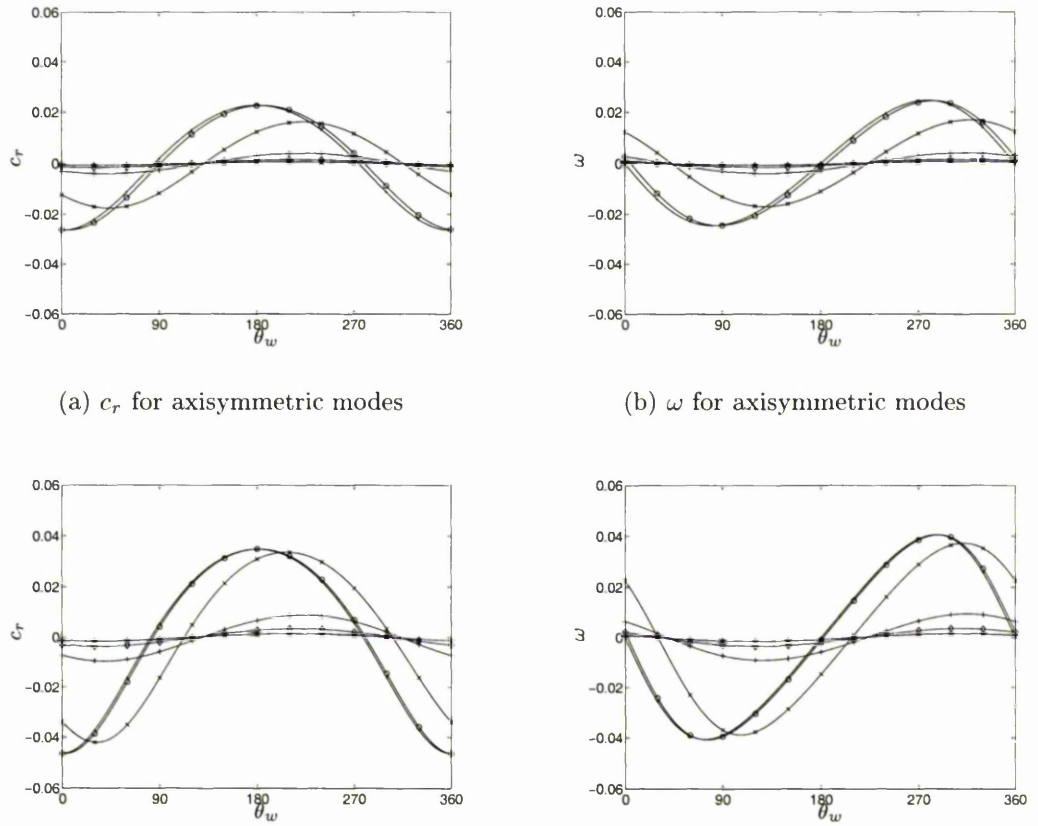

(a) c_r for axisymmetric modes

(b) ω for axisymmetric modes

(c) c_r for modes with $(n = 1)$

(d) ω for modes with $(n = 1)$

Figure 4.30: Phase-Velocities of the KH pipe modes as $Re \to 0$.
-·-, $Re = 10^{-6}$; -○-, $Re = 1$; -◇-, $Re = 10$;
-×-, $Re = 10^2$; -+-, $Re = 10^3$; -⋆-, $Re = 10^4$.

Axisymmetric Modes

For the case $n = 0$, equations (4.22) simplify significantly to

$$L_{(0)}u - i\alpha p = 0\,, \tag{4.23a}$$

$$L_{(1)}v - Dp = 0\,, \tag{4.23b}$$

$$w = 0\,, \tag{4.23c}$$

$$i\alpha u + \left(D + \frac{1}{r}\right)v = 0\,, \tag{4.23d}$$

where $L_{(j)} = D^2 + \frac{1}{r}D - \left(\frac{j^2}{r^2} + \alpha^2\right)$.

By applying $L_{(0)}$ to the continuity equation and using the functional identity $L_{(0)}\,(D + 1/r) = (D + 1/r)\,L_{(1)}$, we can obtain a single second-order o.d.e. for the pressure, thus

$$L_{(0)}p = 0\,. \tag{4.24}$$

Hence the pressure must take the form

$$p(r) = P_0 I_0(\alpha r)\,, \tag{4.25}$$

since it must be finite at $r = 0$. Here, I_0 is the zeroth modified Bessel function of the first kind and P_0 is a constant.

Substituting for the pressure in the stability equations (4.23), we can deduce the following forms for the velocity components:

$$\begin{aligned} u(r) &= U_0 I_0(\alpha r) + \frac{i}{2} P_0 r I_1(\alpha r)\,, \\ v(r) &= V_0 I_1(\alpha r) + \frac{1}{2} P_0 r I_0(\alpha r)\,. \end{aligned}$$

Here, U_0, V_0 are constants and I_1 is the first modified Bessel function of the first kind. We can obtain

$$\begin{aligned} i\alpha U_0 + \alpha V_0 + P_0 &= 0\,, \\ V_0 I_1(\alpha) + \frac{1}{2} P_0 I_0(\alpha) &= -i\alpha\phi_w\,, \\ U_0 &= 1\,, \end{aligned}$$

from the continuity equation (4.23d), the boundary condition, $v = -i\alpha\phi_w$ at $r = 1$ and the normalisation condition, $u = 1$ at $r = 0$, respectively. The above expressions for u, v and p, along with the conditions for finding U_0, P_0 and V_0, form a kinematic equivalent of Kumaran's [45] result.

The equations for P_0 and V_0 can be solved simultaneously, yielding

$$V_0 = i\alpha \frac{I_0(\alpha) - 2\phi_w}{2I_1(\alpha) - \alpha I_0(\alpha)},$$
$$P_0 = 2i\alpha \frac{\alpha\phi_w - I_1(\alpha)}{2I_1(\alpha) - \alpha I_0(\alpha)}.$$

This allows us to find an expression for the phase velocity eigenvalue using equation (4.8a) for $u(1)$, namely

$$u(1) = \bar{u}(\alpha)\left(1 + \tilde{u}(\alpha)\phi_w\right),$$

where

$$\bar{u} = \frac{\alpha I_0^2(\alpha) - 2I_0(\alpha)I_1(\alpha) - \alpha {I_1}^2(\alpha)}{\alpha I_0(\alpha) - 2I_1(\alpha)}, \tag{4.26a}$$
$$\tilde{u} = \frac{\alpha^2 I_1(\alpha)}{\alpha I_0^2(\alpha) - 2I_0(\alpha)I_1(\alpha) - \alpha {I_1}^2(\alpha)}. \tag{4.26b}$$

Hence, our expression for the phase velocity becomes

$$c = \frac{2\phi_w}{\bar{u}(\alpha)}\left(1 + \tilde{u}(\alpha)\phi_w\right)^{-1}. \tag{4.27}$$

For the case $\alpha = 4.25$, the phase velocity was plotted for the KH modes where $|\phi_w| = 0.05$ and compared with the numerical solutions for $Re = 10^{-6}$. This comparison can be seen in figure 4.31, with excellent agreement between the numerics and analysis.

Contour plots of the phase speed in the θ_w-α plane are given in figure 4.32 for various values of $|\phi_w|$. Corresponding plots of the growth rate are given in figure 4.33. These show clearly that, for smaller values of $|\phi_w|$ (see figures 4.32(a) and 4.32(b)), the modes belong in the KH class for all values of α. Here, the phase velocities take values oscillating about zero as θ_w is varied. However, as $|\phi_w|$ is increased a singularity appears, initially at $\alpha = 0$ for $|\phi_w| = 0.25$. This singularity occurs at increasing α as $|\phi_w|$ is further increased. For values of α

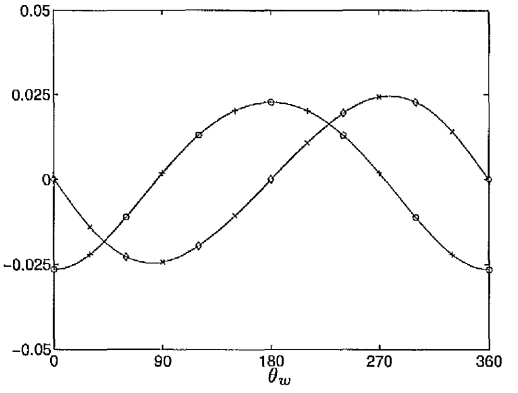

Figure 4.31: Analytical-Numerical comparison for the viscous axisymmetric KH pipe modes.
-o-, analytical c_r; -◇-, analytical c_i; -×-, numerical c_r; -+-, numerical c_i.

above that at which the singularity occurs the, modes remain as members of the KH class. However, for those modes occurring at lower wavenumbers than the singularity, the modes belong to the Resonant class and hence the phase velocity oscillates about a real non-zero value as θ_w is varied.

This is reminscent of the viscous modes for the channel in section 3.6.1 and hence similarly, we see that the range of $|\phi_w|$, in which the transitional modes occur, has shrunk to zero in the limit $Re \to 0$. Only the singularity remains of the process by which the transition from KH to R modes occurs.

As for the channel, the occurence of the singularity and the associated R modes can be deduced from the expressions for c and $\tilde{u}$, which here are (4.27) and (4.26b), respectively. If we define α_c as the critical wave number at which the singularity occurs when $\phi_w = (\phi_w)_c$, then $(\phi_w)_c = -1/\tilde{u}(\alpha_c)$. Figure 4.34 plots $\tilde{u}$ against α for $\alpha \geq 0$. This illustrates three important properties of $\tilde{u}$. The first is that $\tilde{u}$ is -4 when α is zero. The second is that $\tilde{u}$ is a strictly increasing function for $\alpha > 0$. The third is that $\tilde{u} \to 0$ as $\alpha \to \infty$. These imply that $-1/\tilde{u}$ is also a strictly increasing function for $\alpha > 0$, is equal to 0.25 when $\alpha = 0$ and tends to infinity as $\alpha \to \infty$. Therefore, α_c, can take any value from zero upwards. Hence also, α_c can only exist for $|\phi_w| \geq 0.25$ and α_c increases as ϕ_w is increased.

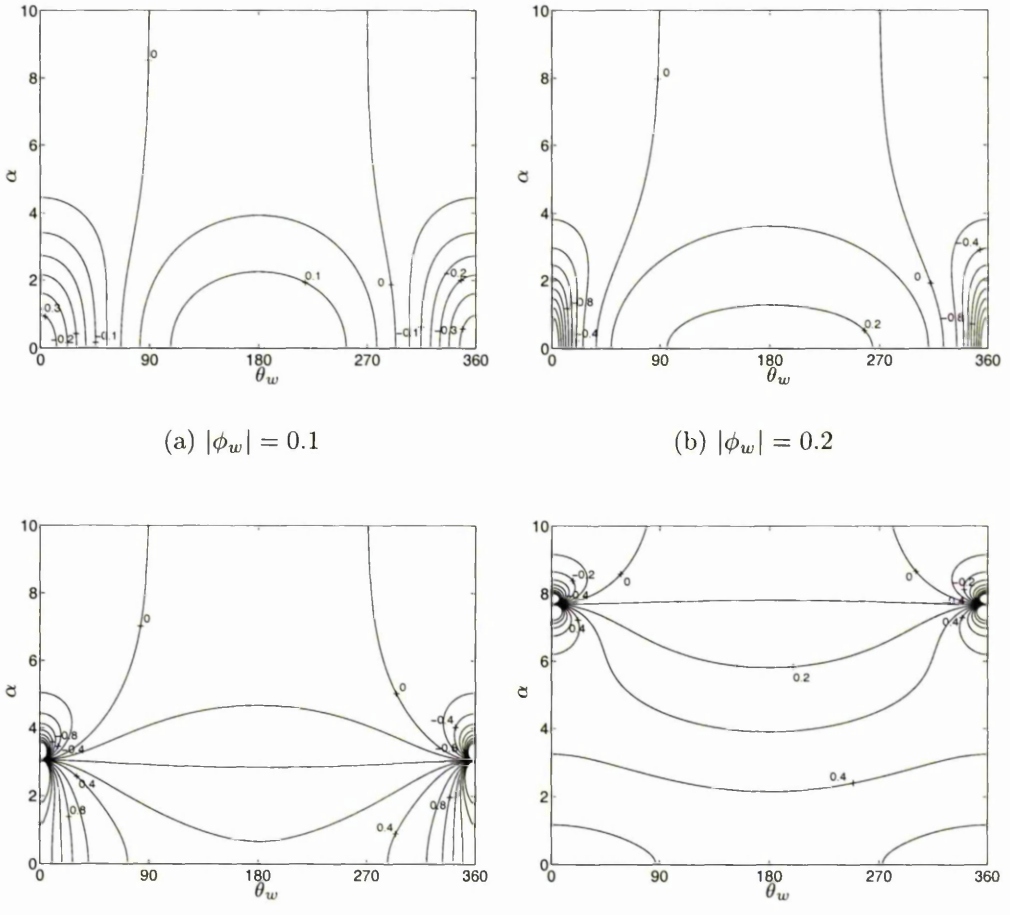

(a) $|\phi_w| = 0.1$

(b) $|\phi_w| = 0.2$

(c) $|\phi_w| = 0.4$

(d) $|\phi_w| = 5.0$

Figure 4.32: Phase-Speeds of the viscous modes.

At the begining of this section it was stated that it was hoped that the modes identified by Kumaran [45] might be classifiable within the kinematic scheme. However, the viscous modes for the visco-elastic wall have a growth rate which tends towards -1 as the wave number becomes large, whereas our kinematic modes have a growth rate which tends towards zero in the same limit. Therefore, Kumaran's modes lie outside the span of the current kinematic formulation. The most likely explanation is that the visco-elastic wall is capable of moving in the direction of the mean flow, whereas the current kinematic formulation is only

valid for walls which move in a direction which is normal to their rest state and the mean flow. An extended kinematic formulation, incorporating streamwise disturbances in the wall position, should be able to catch the differing behaviour.

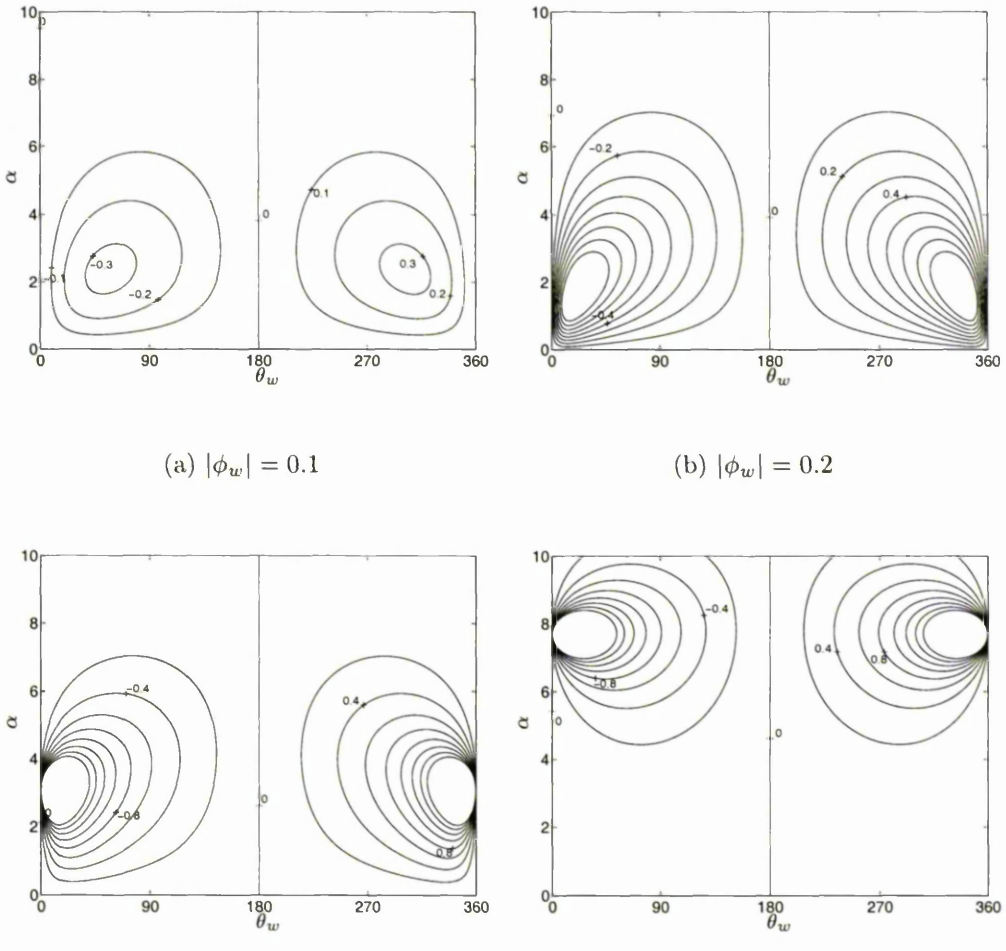

(a) $|\phi_w| = 0.1$ (b) $|\phi_w| = 0.2$

(c) $|\phi_w| = 0.4$ (d) $|\phi_w| = 5.0$

Figure 4.33: Growth-Rates of the viscous modes.

The fact remains though, that streamwise motion of the wall is certainly not a necessity for instabilities in viscous flows in a compliant pipe. This is demonstrated by considering the physical realisability of the kinematic modes. Wall parameter bound plots are given in figure 4.35 for the viscous KH modes

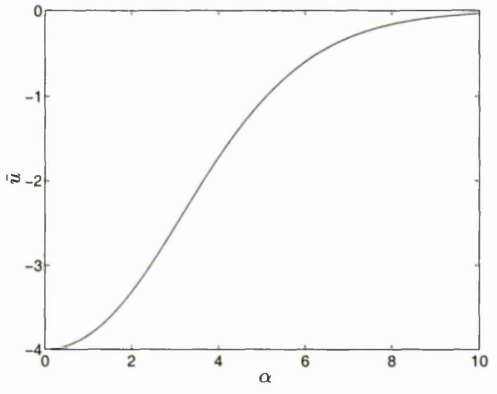

Figure 4.34: $\tilde{u}$ for the viscous axisymmetric pipe modes.

with $\alpha = 4.25$ and $|\phi_w| = 0.1$. These show that, here, all the bounds correspond to case 2 in section 2.3.2. Therefore, these modes may be stabilised by a suitably large increase in the free wave speed, c_0, too.

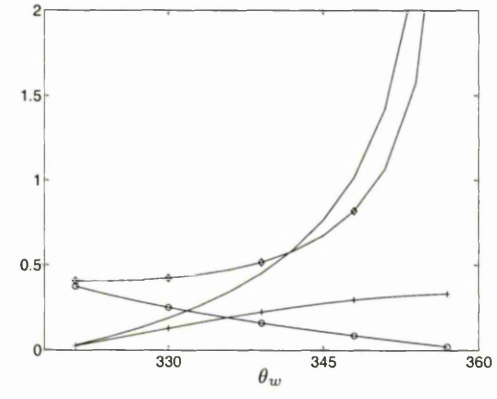

Figure 4.35: Physical realisability bounds on m, d and c_0^2 for the KH modes. —, d lower bound; -o-, $10^{-3} \times m$ lower bound; -◇-, $10^{-3} \times m$ upper bound; -+-, $10^2 \times c_0^2$ upper bound.

The back-calculated values of the wall parameters, d and c_0^2, are plotted in figure 4.36 for $\alpha = 4.25$, $|\phi_w| = 0.1$ and $m = 100.0$. This shows that there is a small physically realisable unstable region, near $\theta_w = 360°$. Figure 4.35 then implies that this region will be shrunk to a very small "unstable pocket" if m is reduced to 2. Similarly, a huge increase in m will have the same effect.

The wall parameter bounds for the R modes with $\alpha = 1.0$ and $|\phi_w| = 0.4$, can

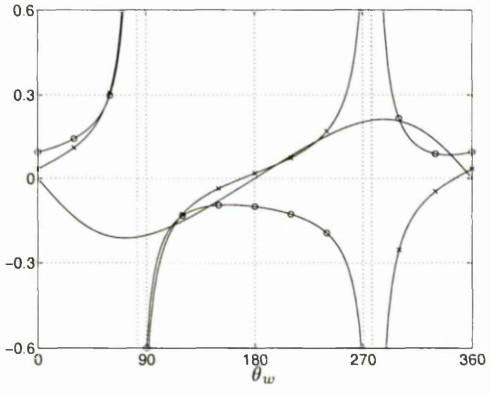

Figure 4.36: Physical realisability of the KH modes for $m = 100.0$.
—, ω; -o-, $10^{-1} \times d$; -×-, $10 \times c_0^2$.

be seen in figure 4.37. These, too, all correspond to case 2 in section 2.3.2 and thus may be stabilised by a suitably large increase in the free wave speed, c_0.

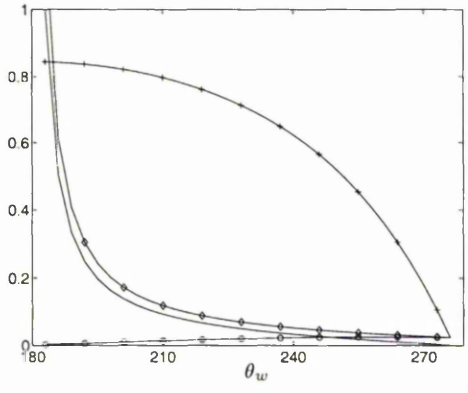

Figure 4.37: Physical realisability bounds on m, d and c_0^2 for the R modes.
—, $10^{-1} \times d$ lower bound;
-o-, $10^{-3} \times m$ lower bound; -◇-, $10^{-3} \times m$ upper bound;
-+-, $10 \times c_0^2$ upper bound.

However, as can be seen in section 4.6.2 the longer wave axisymmetric viscous R modes have bounds corresponding to case 1 and so not all viscous axisymmetric modes may be stabilised in the above way. Back-calculated values of d and c_0^2 can be found in figure 4.38 for $\alpha = 1.0$, $|\phi_w| = 0.4$ and $m = 100.0$. These show, along with figure 4.37, that like the viscous axisymmetric KH modes, there is an unstable physically realisable region, which may be reduced to a small "unstable

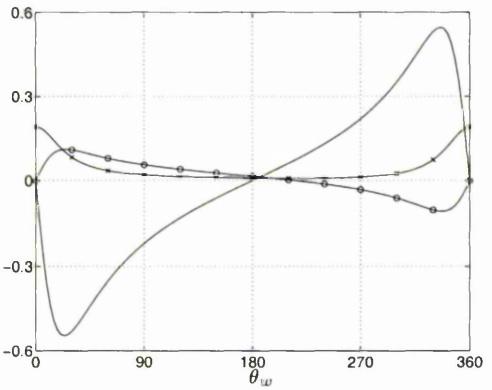

Figure 4.38: Physical realisability of the R modes for $m = 100.0$.
—, ω; -o-, $10^{-1} \times d$; -×-, $10^{-1} \times c_0^2$.

pocket", by a large enough decrease or increase in m.

Therefore, we can eliminate viscous axisymmetric modes of the KH class by a suitably large increase in the free wave speed, c_0, of the wall. Using, the arguments of section 3.6.1, we can choose wall parameters such that the singular modes are avoided and also those in a small region surrounding them. However, eliminating the R modes is not so straightforward as the KH modes, since the wall parameter bounds correspond to both cases in section 2.3.2.

Non-axisymmetric Modes

For the cases where $n \geq 1$, it is convenient to introduce the quantities

$$\psi_{\pm} = v \pm iw\,,$$

which may be inverted by

$$v = \frac{\psi_+ + \psi_-}{2}\,,$$
$$w = \frac{\psi_+ - \psi_-}{2i}\,.$$

Using the above transformations in the limit $Re \to 0$, the stability equations

may be re-written in the form

$$L_0 u - i\alpha p = 0\,, \tag{4.28a}$$

$$L_+ \psi_+ - \left(D - \frac{n}{r}\right) p = 0\,, \tag{4.28b}$$

$$L_- \psi_- - \left(D + \frac{n}{r}\right) p = 0\,, \tag{4.28c}$$

$$i\alpha u + \frac{1}{2}\left(D + \frac{n+1}{r}\right)\psi_+ + \frac{1}{2}\left(D - \frac{n-1}{r}\right)\psi_- = 0\,. \tag{4.28d}$$

Here,

$$L_\pm = D^2 + \frac{1}{r}D - \left(\frac{(n\pm 1)^2}{r^2} + \alpha^2\right)\,,$$

$$L_0 = D^2 + \frac{1}{r}D - \left(\frac{n^2}{r^2} + \alpha^2\right)\,.$$

The approach to solving these equations is, as for the two-dimensional case, to apply L_0 to the continuity equation (4.28d) to obtain a single equation for the pressure. This expression can then be substituted into each of the remaining stability equations (4.28) to obtain equations and then explicit expressions for the quantities u, ψ_+ and ψ_-.

Applying L_0 to the continuity equation (4.28d) yields

$$i\alpha L_0 u + \frac{1}{2}L_0\left(D + \frac{n+1}{r}\right)\psi_+ + \frac{1}{2}L_0\left(D - \frac{n-1}{r}\right)\psi_- = 0\,.$$

Now using the functional identities

$$L_0\left(D + \frac{n+1}{r}\right) = \left(D + \frac{n+1}{r}\right)L_+\,, \tag{4.29a}$$

$$L_0\left(D - \frac{n-1}{r}\right) = \left(D - \frac{n-1}{r}\right)L_-\,, \tag{4.29b}$$

along with each of the remaining stability equations we obtain the single second-order o.d.e. for the pressure,

$$L_0 p = 0\,. \tag{4.30}$$

Hence, the pressure must take the form

$$p(r) = P_n I_n(\alpha r)\,, \tag{4.31}$$

since it must be finite at $r = 0$. Here, I_n is the n-th modified Bessel function of the first kind.

Substituting this expression for the pressure into each of the remaining stability equations (4.28) allows us to deduce the following general form of the solution for $n \geq 1$:

$$\begin{aligned} u(r) &= U_n I_n(\alpha r) + \frac{i}{2} P_n r I_{n-1}(\alpha r)\,, \\ \psi_+(r) &= \Psi_{+n} I_{n+1}(\alpha r) + \frac{1}{2} P_n r I_n(\alpha r)\,, \\ \psi_-(r) &= \Psi_{-n} I_{n-1}(\alpha r) + \frac{1}{2} P_n r I_n(\alpha r)\,. \end{aligned}$$

Here, U_n, Ψ_{+n} and Ψ_{-n} are constants determined by the boundary conditions, the normalisation condition and the continuity condition

$$\alpha \left[iU_n + \frac{1}{2}\left(\Psi_{+n} + \Psi_{-n}\right)\right] + \frac{1}{2} P_n = 0\,. \tag{4.32}$$

For the specific case $n = 1$, the normalisation condition $Du = 1$ at $r = 0$ gives

$$\alpha U_1 + i P_1 = 2\,.$$

The conditions at the compliant wall, $\psi_+ = \psi_- = -i\alpha\phi_w$ at $r = 1$, yield

$$\begin{aligned} \Psi_{+1} I_2(\alpha) + \frac{1}{2} P_1 I_1(\alpha) &= -i\alpha\phi_w\,, \\ \Psi_{-1} I_0(\alpha) + \frac{1}{2} P_1 I_1(\alpha) &= -i\alpha\phi_w\,. \end{aligned}$$

These three equations along with the continuity condition (4.32) can be written in the matrix form $A\boldsymbol{q} = \boldsymbol{s}$, if $\boldsymbol{q} = (\Psi_{+1}, \Psi_{-1}, U_1, P_1)^T$ and

$$A = \begin{pmatrix} \frac{\alpha}{2} & \frac{\alpha}{2} & i\alpha & \frac{1}{2} \\ 0 & 0 & \alpha & i \\ I_2(\alpha) & 0 & 0 & \frac{1}{2} I_1(\alpha) \\ 0 & I_0(\alpha) & 0 & \frac{1}{2} I_1(\alpha) \end{pmatrix}, \quad \boldsymbol{s} = \begin{pmatrix} 0 \\ 2 \\ -i\alpha\phi_w \\ -i\alpha\phi_w \end{pmatrix}.$$

This can be inverted easily to find

$$P_1 = \frac{i}{K}\left(\frac{\alpha^2}{2}\left(\frac{1}{I_0(\alpha)}+\frac{1}{I_2(\alpha)}\right)\phi_w - 2\right),$$
$$U_1 = \frac{1}{\alpha K}\left(1+\frac{\alpha}{2}\left(\alpha\phi_w - I_1(\alpha)\right)\left(\frac{1}{I_0(\alpha)}+\frac{1}{I_2(\alpha)}\right)\right),$$
$$\Psi_{+1} = \frac{i}{I_2(\alpha)K}\left(I_1(\alpha)-\frac{3}{2}\alpha\phi_w\right),$$
$$\Psi_{-1} = \frac{i}{I_0(\alpha)K}\left(I_1(\alpha)-\frac{3}{2}\alpha\phi_w\right),$$

where

$$K = \frac{3}{2} - \frac{\alpha I_1(\alpha)}{4}\left(\frac{1}{I_0(\alpha)}+\frac{1}{I_2(\alpha)}\right). \tag{4.33}$$

We can now find an expression for $u(1)$, similar in form to the case $n = 0$, namely

$$u(1) = \bar{u}(\alpha)\left(1+\tilde{u}(\alpha)\phi_w\right),$$

where in this case

$$\bar{u} = \frac{2I_1(\alpha)}{\alpha}\left(1-\frac{1}{K}\right)+\frac{I_0(\alpha)}{K}, \tag{4.34a}$$
$$\hat{u} = \frac{1}{K}\left[\frac{\alpha^2}{2}\left(\frac{I_1(\alpha)}{\alpha}-\frac{I_0(\alpha)}{2}\right)\left(\frac{1}{I_0(\alpha)}+\frac{1}{I_2(\alpha)}\right)\right] \tag{4.34b}$$

and $\tilde{u} = \hat{u}/\bar{u}$. Thus, our expression for the phase velocity is

$$c = \frac{2\phi_w}{\bar{u}(\alpha)}\left(1+\tilde{u}(\alpha)\phi_w\right)^{-1}. \tag{4.35}$$

For the case $\alpha = 4.25$ the phase velocity was plotted for the KH modes where $|\phi_w| = 0.05$ and compared with the numerical solutions for $Re = 10^{-6}$. This comparison can be seen in figure 4.39, with excellent agreement between the numerics and analysis.

Contour plots of the phase speed in the θ_w-α plane are given in figure 4.40 for various values of $|\phi_w|$. Corresponding plots of the growth rate are given in figure 4.41. These show clearly that, like the axisymmetric modes, for smaller

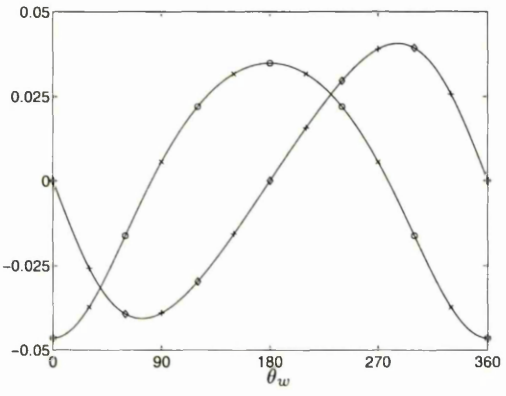

Figure 4.39: Analytical-Numerical comparison for the viscous non-axisymmetric ($n = 1$) KH pipe modes.
-o-, analytical c_r; -◇-, analytical c_i; -×-, numerical c_r; -+-, numerical c_i.

values of $|\phi_w|$ (see figures 4.40(a) and 4.40(b)), the modes belong in the KH class for all values of α. Like the axisymmetric modes, singularities appear as $|\phi_w|$ is increased. However, unlike the viscous axisymmetric modes and the viscous channel modes, the singularity first appears at a non-zero value of the wavenumber $\alpha \approx 3.5$. The corresponding value of $|\phi_w|$ is approximately 0.3. For larger values of $|\phi_w|$ there are two singularities in contrast to the other viscous modes so far considered. One singularity occurs at a wave number less than 3.5, the other at a value greater than 3.5. Modes with wave numbers between those of the singularities belong to the Resonant class. The remaining modes belong to the KH class.

As for all of the previously found viscous modes, the range of $|\phi_w|$ in which the transitional modes occur, has shrunk to zero in the limit $Re \to 0$. Only the singularities remain of the process by which the transition from KH to R modes occurs.

The occurence of the singularities and the associated R modes can be deduced from the expressions for c and $\tilde{u}$. If we define α_l and α_u as the lower and upper critical values of the wave number at which the singularities occur when $\phi_w = (\phi_w)_c$, then $(\phi_w)_c = -1/\tilde{u}(\alpha_l) = -1/\tilde{u}(\alpha_u)$. Figure 4.42 plots $\tilde{u}$ against α

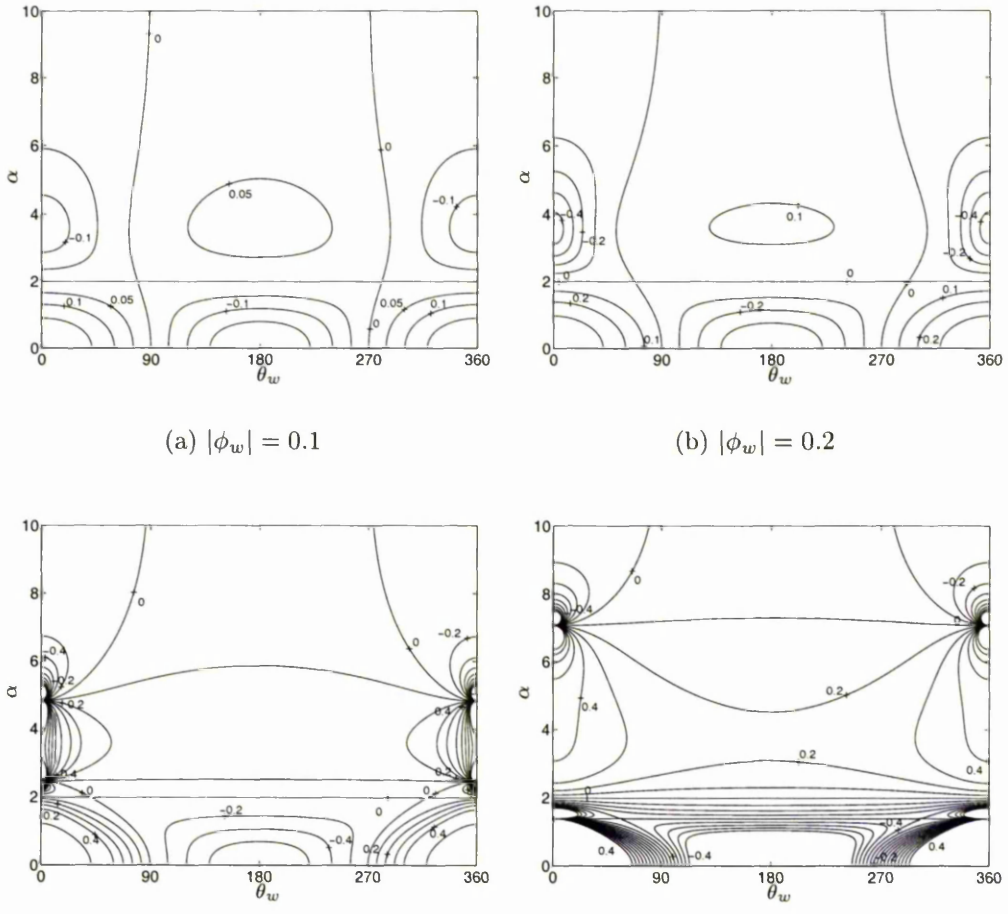

(a) $|\phi_w| = 0.1$

(b) $|\phi_w| = 0.2$

(c) $|\phi_w| = 0.4$

(d) $|\phi_w| = 1.0$

Figure 4.40: Phase-Speeds of the viscous modes.

for $\alpha \geq 0$. This illustrates three important properties of $\tilde{u}$. The first is that $\tilde{u}$ is zero when α is zero. The second is that $\tilde{u} \to 0$ as $\alpha \to \infty$. The third is that $\tilde{u}$ has a single minimum, is a strictly decreasing function for wave numbers less than that at which the minumum occurs and is a strictly increasing function for wave numbers above that at which the minimum occurs. These imply that $-1/\tilde{u}$ also has a single minimum, is also a strictly decreasing function for wave numbers less than that at which the minimum occurs and is also a strictly increasing function for wave numbers above that at which the minimum occurs. Finally, $-1/\tilde{u} \to \infty$

as $\alpha \to 0$.

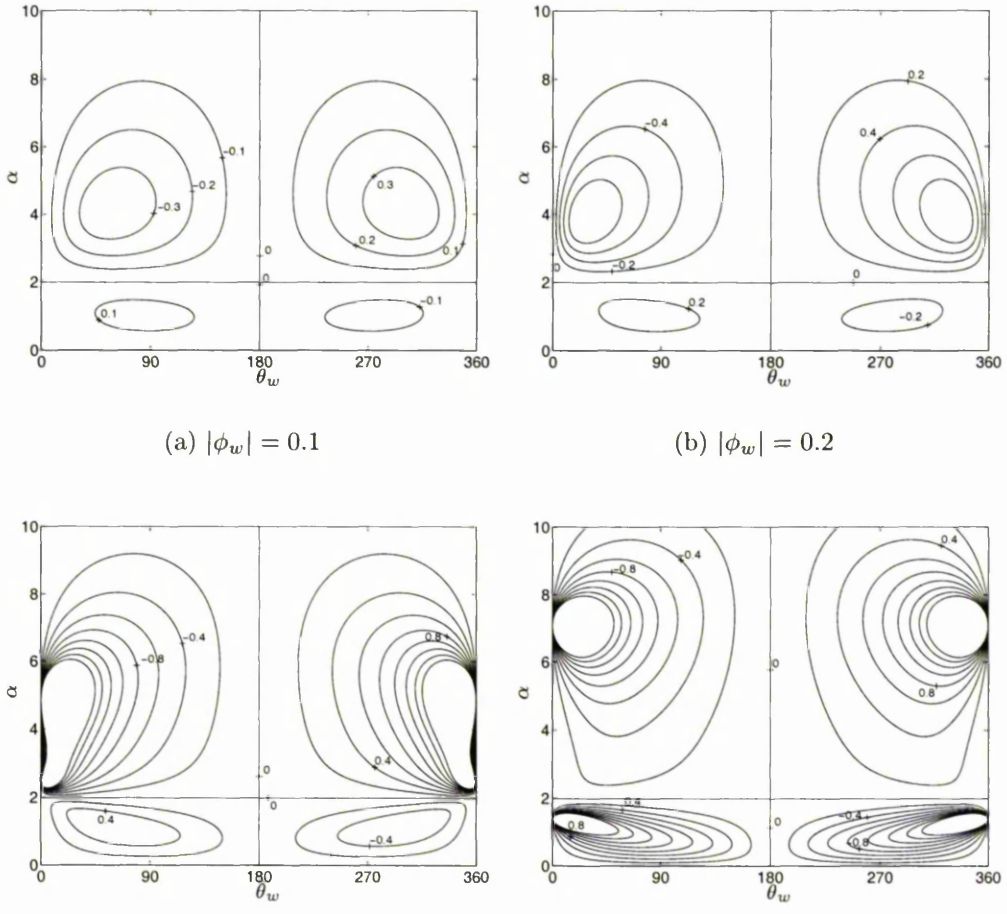

(a) $|\phi_w| = 0.1$

(b) $|\phi_w| = 0.2$

(c) $|\phi_w| = 0.4$

(d) $|\phi_w| = 1.0$

Figure 4.41: Growth-Rates of the viscous modes.

Now, if the minimum of $\tilde{u}$ occurs at α_c, then singularities occur only for wall stream functions, $(\phi_w)_c$, where $|(\phi_w)_c| \geq -1/\tilde{u}(\alpha_c)$. Additionally, for such wall stream functions, there are two values of α which obey $|(\phi_w)_c| = -1/\tilde{u}(\alpha)$. These we may label α_l and α_u, as above. The existence of the two singularities for $|\phi_w| > |(\phi_w)_c|$, can be seen in figures 4.40(c) and 4.40(d).

In figures 4.40 and 4.41 it can be seen that the θ-α plane is divided into two regions by a $c = 0$ contour at an approximate wave number of 2, regardless of the

classes of mode present. There is a change of sign of the growth rate, ω, as α is increased from just below the value at which the $c = 0$ contour occurs, to just above it, with θ_w fixed.

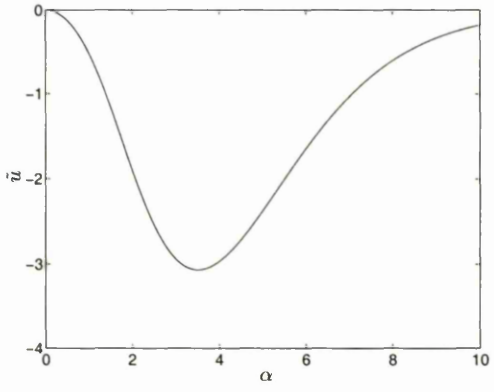

Figure 4.42: $\tilde{u}$ for the viscous non-axisymmetric ($n = 1$) pipe modes.

By considering our expression 4.35 for the phase velocity eigenvalue, we can find the value of α at which this contour occurs. For c to be zero, one of the terms whose product forms c must be zero. The only such term which is dependent on α but not on ϕ_w is $1/\bar{u}_r$. Setting this term equal to zero requires, from equation 4.34, that

$$\frac{\alpha K}{2I_1(\alpha)(K-1) + \alpha I_0(\alpha)} = 0\,.$$

Hence $K = 0$, since

$$\frac{\alpha}{2I_1(\alpha)(K-1) + \alpha I_0(\alpha)} \to 2 \quad \text{as } \alpha \to 0.$$

So, our required value of α is the solution of the equation

$$K = \frac{3}{2} - \frac{\alpha I_1(\alpha)}{4}\left(\frac{1}{I_0(\alpha)} + \frac{1}{I_2(\alpha)}\right) = 0\,.$$

A numerical evaluation of the root, α_1 can be performed, which yields (to 4 d.p.)

$$\alpha_1 = 1.9918\,,$$

which agrees well with figures 4.40 and 4.41.

Therefore, there exists at least one neutral mode for any value of ϕ_w. Furthermore, by showing that, except at $\theta = 0$ and 180°, $\partial c_i/\partial\alpha \neq 0$ at $\alpha = \alpha_1$, there must be an interval, in which α_1 is either the upper or lower bound, where $c_i > 0$.

Now,

$$\frac{\partial c_i}{\partial \alpha} = \frac{2|\phi_w| \sin\theta_w}{1 + \tilde{u}^2 + 2\tilde{u}\cos\theta_w} \left(\frac{d}{d\alpha}\left(\frac{1}{\bar{u}_r}\right) - \frac{2\left(\tilde{u} + \cos\theta_w\right)}{\bar{u}_r\left(1 + \tilde{u}^2 + 2\tilde{u}\cos\theta_w\right)} \frac{d\tilde{u}}{d\alpha} \right) .$$

Since $\tilde{u}$ must be a continuous function, $d\tilde{u}/d\alpha$ is finite for all α. Hence the right-hand term in the brackets will be zero at $\alpha = \alpha_1$. Therefore, to show that $\partial c_i/\partial\alpha \neq 0$ at $\alpha = \alpha_1$, for all ϕ_w, we must show that

$$\frac{d}{d\alpha}\left(\frac{1}{\bar{u}_r}\right) \neq 0 \quad \text{at } \alpha = \alpha_1 .$$

Substituting from equation 4.34, this is equivalent to requiring

$$\frac{dK}{d\alpha} \neq 0 \quad \text{at } \alpha = \alpha_1,.$$

Using equation 4.33,

$$\begin{aligned} \frac{dK}{d\alpha} = & \frac{\alpha I_1(\alpha)}{4}\left(\frac{I_1(\alpha)}{{I_0}^2(\alpha)} + \frac{I_1(\alpha) + I_3(\alpha)}{2{I_2}^2(\alpha)}\right) \\ & - \frac{1}{4}\left(I_1(\alpha) + \frac{\alpha\left(I_0(\alpha) + I_2(\alpha)\right)}{2}\right)\left(\frac{1}{I_0(\alpha)} + \frac{1}{I_2(\alpha)}\right) \\ = & -0.3995(\text{to 4 d.p.}) \text{ at } \alpha = \alpha_1 . \end{aligned}$$

Thus for any non-zero ϕ_w, non-axisymmetric ($n = 1$) viscous modes always appear to have a range of wave numbers, near $\alpha = \alpha_1$, which are unstable. However, in practice the Reynolds number will not be exactly equal to zero and hence the above theory will only be a leading-order approximation to the phase velocity. Therefore, the second-order terms in αRe must be found to determine the overall stability of the non-axisymmetric ($n = 1$) low Reynolds number modes with wave numbers close to $\alpha = \alpha_1$. This is a necessary area for further work.

Another possible explanation for the apparent existence of the above instabilities for all wall types concerns the basic flow. This was assumed to be unidirectional and parallel to the x axis. However, in reality, the driving pressure gradient results in lower pressures downstream and hence the walls will tend to converge, leading to a non-parallel basic flow. For the example of the stretched membrane used herein, the rate of convergence of the walls is proportional to the pressure gradient, i.e. $dr_s/dx \propto dp/dx$. For high Reynolds number flows, $dp/dx = -4/Re$ and hence the convergence of the walls may safely be neglected. However, for low Reynolds number flows, $dp/dx = -4$ and so it is not clear that the parallel-basic-flow assumption can be made.

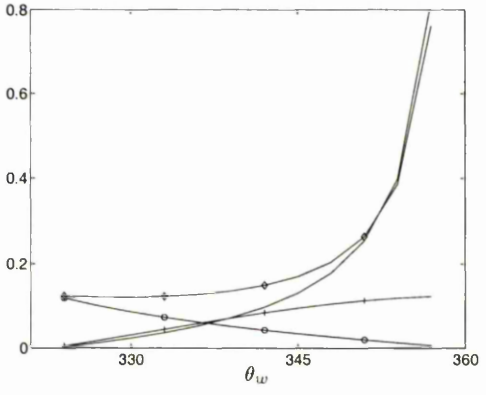

Figure 4.43: Physical realisability bounds on m, d and c_0^2 for the KH modes - high wave number.
—, $10^{-1} \times d$ lower bound;
-o-, $10^{-3} \times m$ lower bound; -◇-, $10^{-3} \times m$ upper bound;
-+-, $10 \times c_0^2$ upper bound.

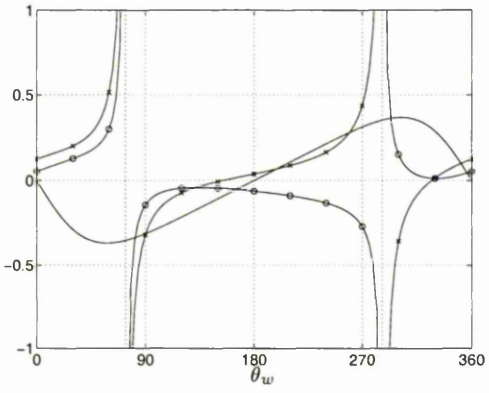

Figure 4.44: Physical realisability of the
KH modes for $m = 100.0$ - high wave number.
—, ω; -o-, $10^{-1} \times d$; -×-, $10^2 \times c_0^2$.

Example plots of the wall parameter bounds away from $\alpha = \alpha_1$ can be found in figure 4.43 for the KH modes where $\alpha = 4.25 > \alpha_1$ and $|\phi_w| = 0.1$. These show that the bounds correspond to case 2 in section 2.3.2 and hence these modes may be stabilised by an increase in the free wave speed, c_0. Similarly, for wave numbers less than α_1, the bounds also correspond to case 2 in section 2.3.2 and so also may be stabilised by an increase in c_0. This is illustrated by figure 4.45, where $\alpha = 1.0$ and $|\phi_w| = 0.1$.

Plots of the back-calculated values of d and c_0^2 are given in figures 4.44 and 4.46 for $\alpha = 4.25$ and $\alpha = 1.0$, respectively. Here also, $|\phi_w| = 0.1$ and $m = 100.0$. These two plots are qualitatively similar if θ_w is shifted by 180° for the lower wave number plots. For higher values of the wave number there is a small physically realisable unstable region for values of θ_w just below 360°. Likewise, for lower values of the wave number there is a small physically realisable region for values of θ_w just below 180°. In both cases a decrease in m leads to the small unstable region being reduced to a very small "unstable pocket", as does a sufficiently large increase in m.

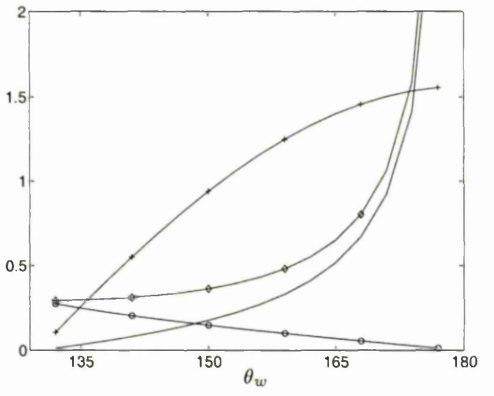

Figure 4.45: Physical realisability bounds on m, d and c_0^2 for the KH modes - low wave number.
—, d lower bound; -o-, $10^{-3} \times m$ lower bound; -◇-, $10^{-3} \times m$ upper bound; -+-, $10^2 \times c_0^2$ upper bound.

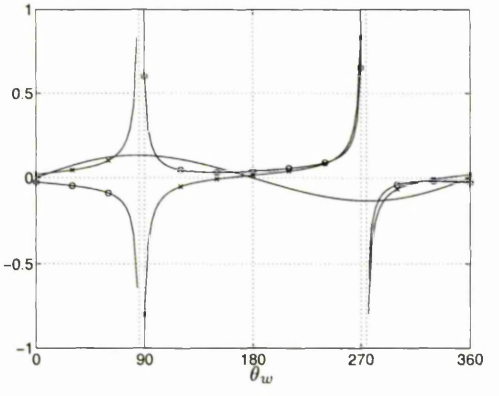

Figure 4.46: Physical realisability of the KH modes for $m = 100.0$ - low wave number.
—, ω; -o-, $10^{-1} \times d$; -×-, $\times c_0^2$.

Figure 4.48 gives the wall parameter bounds for the viscous non-axisymmetric ($n = 1$) modes with $\alpha = 4.25$ and $|\phi_w| = 1.0$. Unlike all of the viscous modes so far considered, these modes have bounds which correspond to case 1 in section 2.3.2 and so an increase in the free wave speed, c_0 will not eliminate these modes.

In fact a decrease in c_0 is needed to eliminate these modes. Alternatively, an increase in m should reduce the region of physically realisble instabilites to a small "pocket". A value of 2 for m yields a relatively small region for physically realisable instabilities with $\alpha = 4.25$ and $|\phi_w| = 1.0$, as illustrated in figure 4.47. Figure 4.48 shows that an increase in m of no more than an order of magnitude should reduce this unstable region to a small pocket of less than 3° in extent in the θ_w co-ordinate.

In this section we have found that the viscous non-axisymmetric ($n = 1$) modes differ in several ways from the other viscous modes so far encountered in both the compliant pipe and channel. One difference is that the viscous non-axisymmetric ($n = 1$) R modes cannot be stabilised by an increase in the free wave speed. Another is the number and location of the singularities by which transition from the KH to the R modes occur in the viscous limit. The most important remaining difference is that the leading-order solution in the limit $Re \to 0$ suggests that non-axisymmetric viscous modes in a compliant pipe are unstable for any value of ϕ_w, i.e. for any wall parameters. The second-order solution in αRe is thus required to determine the overall stability of these low Reynolds number modes.

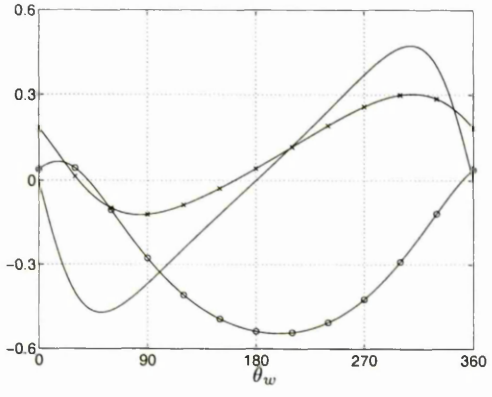

Figure 4.47: Physical realisability of the R modes for $m = 2.0$.
—, ω; -o-, $10^{-1} \times d$; -×-, c_0^2.

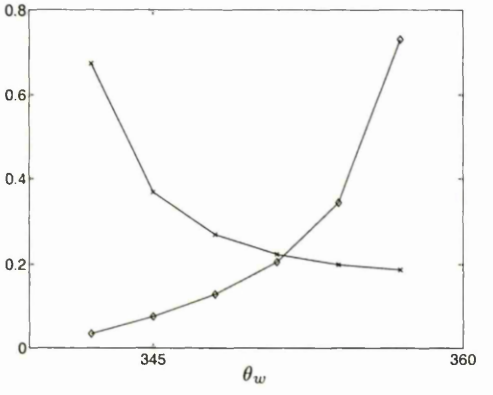

Figure 4.48: Physical realisability bounds on m, d and c_0^2 for the R modes. -◇-, $10^{-1} \times m$ upper bound; -×-, c_0^2 lower bound.

4.6.2 The Long-Wave Limit

The other case in which we may find analytical results is that of long-wave disturbances where $\alpha \to 0$. Here, we expect from the viscous solutions that $c = O(1)$, to leading order in α.

As for the viscous limit, $Re \to 0$, we need to use the viscous pressure scaling, $p^* = (\mu U/L)p$, for the pressure. Therefore, with this scaling equations (4.21) govern long-wave disturbances. Again, for simplicity's sake, we shall consider solutions for the two separate cases of axisymmetric and non-axisymmetric modes.

The wall conditions (4.8), along with the normalisation condition (4.10) and the governing equations (4.21), then allow us the write the solutions in the form:

$$u(r) = u_0(r) + \alpha u_1(r) + O(\alpha^2)\,, \tag{4.36a}$$

$$v(r) = \alpha v_0(r) + \alpha^2 v_1(r) + O(\alpha^3)\,, \tag{4.36b}$$

$$w(r) = \alpha w_0(r) + \alpha^2 w_1(r) + O(\alpha^3)\,, \tag{4.36c}$$

$$p(r) = \alpha^\sigma p_0(r) + \alpha^{\sigma+1} u_1(r) + O(\alpha^{\sigma+2})\,, \tag{4.36d}$$

$$c = c_0 + \alpha c_1 + O(\alpha^2)\,, \tag{4.36e}$$

as $\alpha \to 0$. Here σ depends on the geometry of the mode under consideration and

is found by balancing terms in the momentum derived stability equations (4.21a), (4.21a) and (4.21a). As stated above, in order to proceed we shall consider the two separate cases, as follows.

Axisymmetric Modes.

In this case, $\sigma = -1$ and hence to leading order we have:

$$iu_0 + \left(D + \frac{1}{r}\right) v_0 = 0\,, \tag{4.37a}$$

$$\left(D^2 + \frac{1}{r}D\right) u_0 - ip_0 = 0\,, \tag{4.37b}$$

$$Dp_0 = 0\,, \tag{4.37c}$$

with boundary conditions which may be written as:

$$\begin{aligned} u_0(0) &= 1\,, \\ Du_0(0) &= 0\,, \\ v_0(0) &= 0\,, \\ v_0(-1) &= -i\phi_w\,, \\ c_0 &= \frac{2\phi_w}{u_0(1)}\,. \end{aligned}$$

It is easy to verify that the pressure, p_0, must be a constant, the streamwise velocity, u_0, must be a quadratic funtion of r and the normal velocity, v_0, must be a cubic function of r. The coefficients of each function can be found easily so that

$$\begin{aligned} u_0(r) &= 1 + 2(2\phi_w - 1)r^2\,, \\ v_0(r) &= -\frac{i}{2}r + \frac{i}{2}(1 - 2\phi_w)r^3\,, \\ p_0(r) &= 8i(1 - 2\phi_w)\,, \\ c_0 &= \frac{2\phi_w}{4\phi_w - 1}\,. \end{aligned}$$

For the $|\phi_w| = 0.1$, the leading-order solution was plotted alongside the numerical solution where in both cases $Re = 100.0$ and $\alpha = 10^{-4}$. Similarly, the leading-order solution was plotted for $|\phi_w| = 0.4$ alongside the numerical solution for $|\phi_w| = 0.4$, $Re = 100.0$ and $\alpha = 10^{-4}$. These plots can be seen in figures 4.49(a) and 4.49(b), respectively, with good agreement between the analytical solution and the numerics.

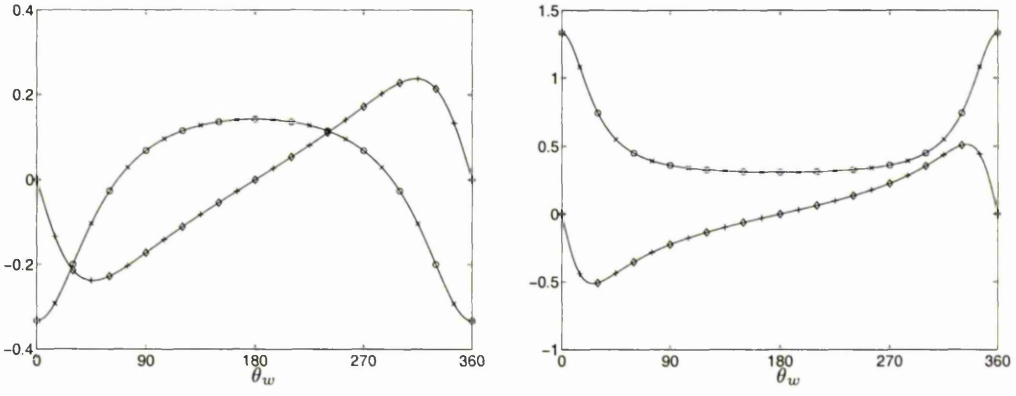

(a) KH modes. (b) R modes.

Figure 4.49: Analytical-Numerical comparison for the long-wave axisymmetric pipe modes.
-o-, analytical c_r, $Re(c_0)$; -◇-, analytical c_i, $Im(c_0)$;
-×-, numerical c_r; -+-, numerical c_i.

For lower values of $|\phi_w|$ the modes belong in the KH class as can be seen in figures 4.50(a) and 4.50(b), which plot the phase speed and growth rate for modes where $|\phi_w| = 0.1$, assuming that the leading-order solution is valid for $\alpha = 10^{-4}$. Plots of the wall parameter bounds show these to correspond to case 2 in section 2.3.2 (see figure 4.51). This is the same as for the viscous modes and the long-wave KH modes in a compliant channel. Thus, these modes can be eliminated by an increase in the free wave speed, c_0. It can also be seen that except near $\theta_w = 360°$, instabilities occur only for very large values of m.

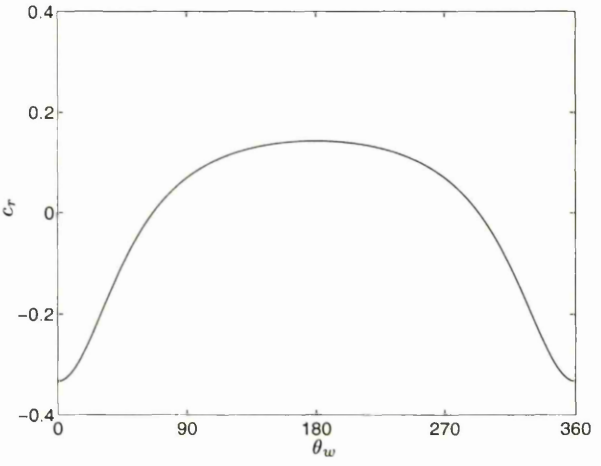

(a) Phase Speed, $Re(c_0)$

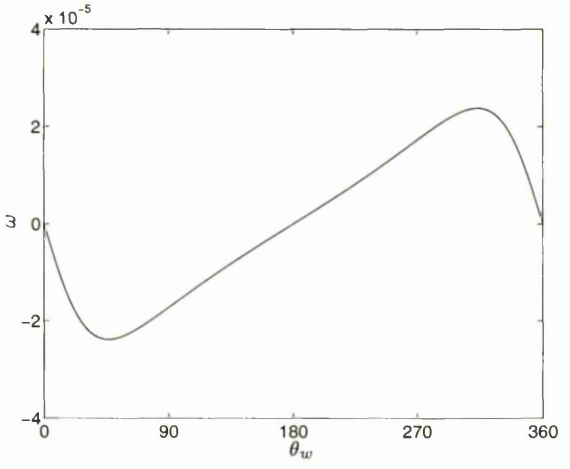

(b) Growth Rate, $\alpha.Im(c_0)$

Figure 4.50: Long-wave KH axisymmetric pipe modes,
$|\phi_w| = 0.2$ - leading-order solution.

This is confirmed in figure 4.52 in which the back-calculated values of d and c_0^2 for $|\phi_w| = 0.1$ and $m = 2.0$ are plotted. Again we have assumed the low wave number, $\alpha = 10^{-4}$. Only a very small "unstable pocket" exists (near $\theta_w = 360°$) and so only a very limited range of values of d and c_0^2 will give rise to these very

slowly growing instabilities.

A singularity occurs at $\phi_w = 0.25$ as $|\phi_w|$ is increased. This is consistent with the occurence of the singularity in the viscous axisymmetric modes as $\alpha_c \to 0$. Hence, the Transitional modes are reduced to the singularity in the long-wave limit, as is the case for the viscous modes and the long-wave modes in a compliant channel

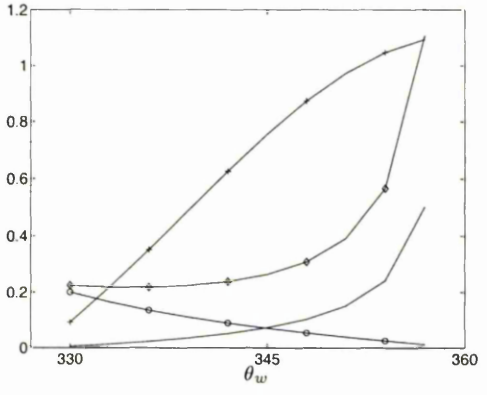

Figure 4.51: Physical realisability bounds on m, d and c_0^2 for the KH modes.
—, $10^3 \times d$ lower bound;
-o-, $10^{-11} \times m$ lower bound; -◇-, $10^{-11} \times m$ upper bound;
-+-, $10 \times c_0^2$ upper bound.

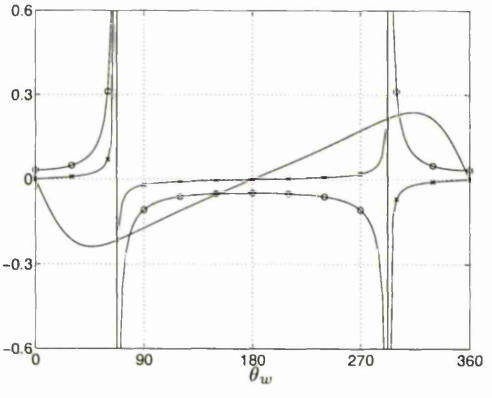

Figure 4.52: Physical realisability of the KH modes for $m = 2.0$.
—, $10^4 \times \omega$; -o-, $10^{-7} \times d$; -×-, $10^{-12} \times c_0^2$.

The modes belong to the Resonant class for values of $|\phi_w|$ greater than 0.25. This is illustrated in figures 4.53(a) and 4.53(b) which plot the phase speed and the growth rate for $|\phi_w| = 0.4$, again assuming the low wave number, $\alpha = 10^{-4}$.

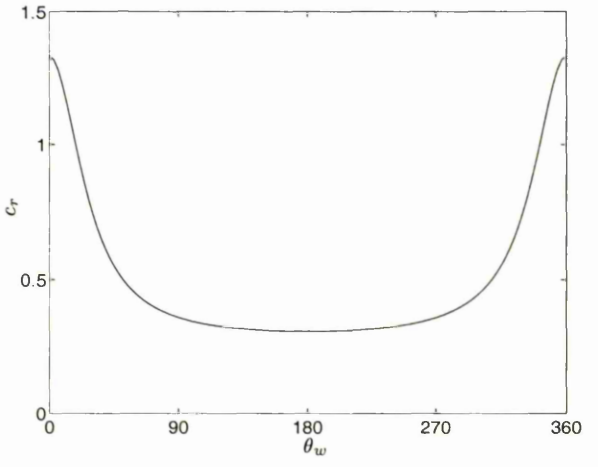

(a) Phase Speed, $Re(c_0)$

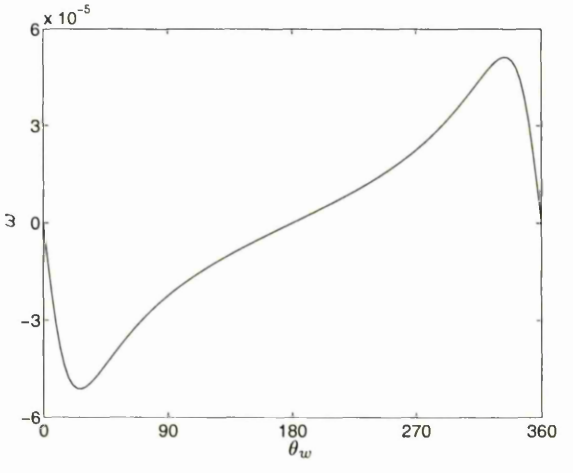

(b) Growth Rate, $\alpha.Im(c_0)$

Figure 4.53: Long-wave R axisymmetric pipe modes,
$|\phi_w| = 0.4$ - leading-order solution.

Unlike the KH long-wave modes and the example axisymmetric viscous R

modes in section 4.6.1, the wall parameter bounds correspond to case 1 in section 2.3.2. These are plotted in figure 4.51. Therefore, these modes cannot be eliminated by a suitable choice of only one of the wall parameters, m, d or c_0^2.

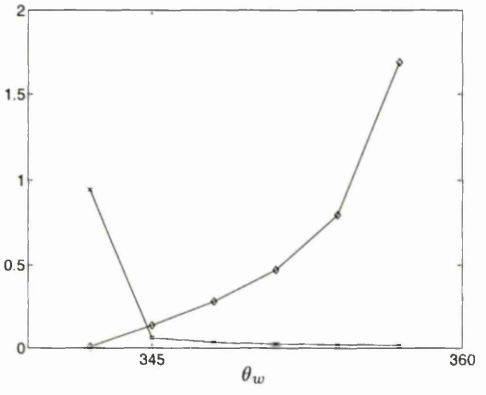

Figure 4.54: Physical realisability bounds on m, d and c_0^2 for the R modes. -◇-, $10^{-9} \times m$ upper bound; -×-, $10^2 \times c_0^2$ lower bound.

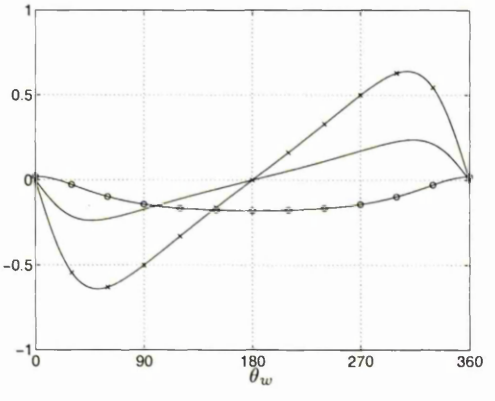

Figure 4.55: Physical realisability of the R modes for $m = 2.0$. —, $10^4 \times \omega$; -o-, $10^{-6} \times d$; -×-, $10^{-9} \times c_0^2$.

A suitable combination of all the wall parameters is necessary to eliminate these modes but the unstable region can be reduced to an "unstable pocket" by choosing a small value of the free wave speed, c_0. Such a choice of c_0 is counter to what is required to eliminate the above axisymmetric long-wave KH modes. Therefore, ensuring all long-wave modes are stable is a much more complex problem than for the channel problem. The physically-realisable unstable long-wave R modes

only exist near $\theta_w = 360°$. This is illustrated by figure 4.55 which plots the back calculated values of d and c_0^2 for $|\phi_w| = 0.4$ and $m = 2.0$.

To next order the stability equations yield:

$$iu_1 + \left(D + \frac{1}{r}\right) v_1 = 0\,, \tag{4.38a}$$

$$\left(D^2 + \frac{1}{r}D\right) u_1 - ip_1 = Re(i(u_B - c_0)u_0 + (Du_B)v_0)\,, \tag{4.38b}$$

$$Dp_1 = 0\,, \tag{4.38c}$$

with boundary conditions which may be written as:

$$\begin{aligned} u_1(0) &= 0\,, \\ Du_1(0) &= 0\,, \\ v_1(0) &= 0\,, \\ v_1(1) &= 0\,, \\ c_1 &= -\frac{2\phi_w u_1(1)}{u_0^2(1)}\,. \end{aligned}$$

It is easy to verify that the second-order solution is:

$$\begin{aligned} u_1(r) &= i\frac{Re}{72}\left(\frac{2\phi_w - 1}{1 - 4\phi_w}\right)\left[(8\phi_w - 5)r^2 - 9(2\phi_w - 1)r^4 + 2(4\phi_w - 1)r^6\right]\,, \\ v_1(r) &= \frac{Re}{288}\left(\frac{2\phi_w - 1}{1 - 4\phi_w}\right)\left[(8\phi_w - 5)r^3 - 6(2\phi_w - 1)r^5 + (4\phi_w - 1)r^7\right]\,, \\ p_1(r) &= \frac{Re}{18}\frac{(2\phi_w - 1)(8\phi_w + 13)}{1 - 4\phi_w}\,, \\ c_1 &= i\frac{Re}{18}\frac{\phi_w(2\phi_w - 1)(1 - \phi_w)}{(1 - 4\phi_w)^3}\,. \end{aligned}$$

Plots of the second-order solutions are given in figures 4.56 and 4.57 for the KH and R modes, respectively. Parameter values are as for the leading-order solutions. As for the long-wave compliant channel modes the second-order solution balances the inertial terms due to the leading-order solution.

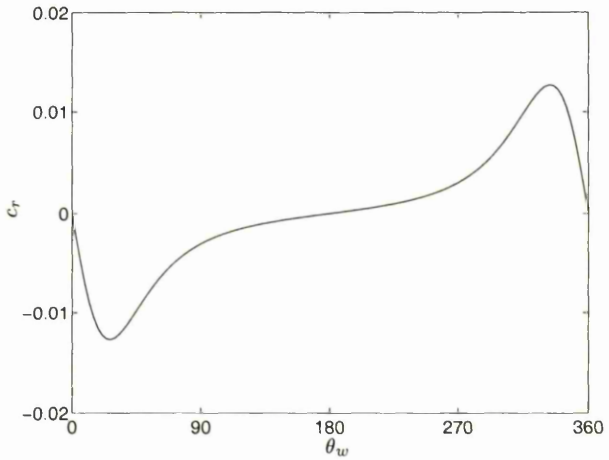

(a) Phase Speed, $Re(c_1)$

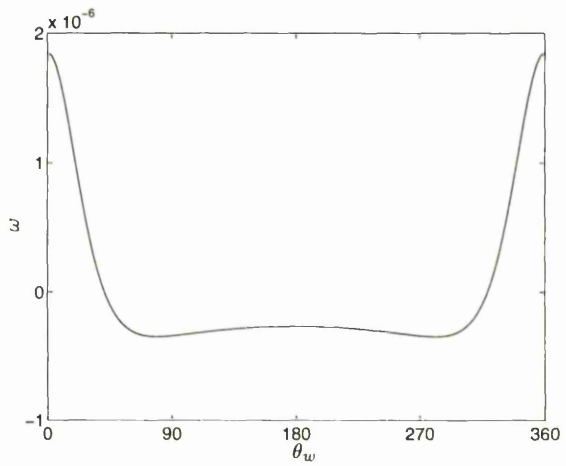

(b) Growth Rate, $\alpha.Im(c_1)$

Figure 4.56: Long-wave KH axisymmetric pipe modes,
$|\phi_w| = 0.1$ - second-order solution.

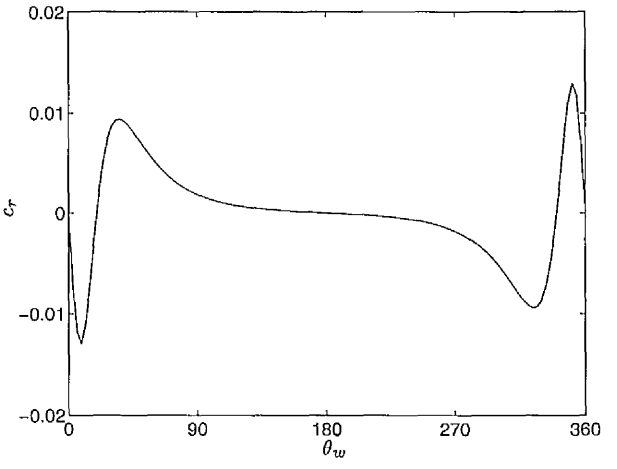

(a) Phase Speed, $Re(c_1)$

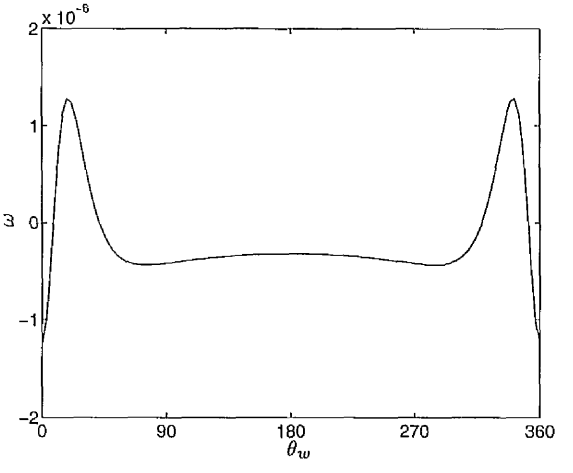

(b) Growth Rate, $\alpha.Im(c_1)$

Figure 4.57: Long-wave R axisymmetric pipe modes,
$|\phi_w| = 10.0$ - second-order solution.

Non-axisymmetric Modes.

Here, it is convenient to use the functions, $\psi_{\pm}$, introduced in section 4.6.1 and then we find that $\sigma = 1$. If, additionally, we now write

$$\psi_+(r) = \alpha\psi_{+0}(r) + \alpha^2\psi_{+1}(r) + O(\alpha^3)\,,$$
$$\psi_-(r) = \alpha\psi_{-0}(r) + \alpha^2\psi_{-1}(r) + O(\alpha^3)\,,$$

where $\psi_{\pm j} = v_j \pm iw_j$, then to leading order we obtain:

$$iu_0 + \frac{1}{2}\left(D + \frac{n+1}{r}\right)\psi_{+0} + \frac{1}{2}\left(D - \frac{n-1}{r}\right)\psi_{-0} = 0\,, \tag{4.39a}$$

$$(L_0 + \alpha^2)u_0 = 0\,, \tag{4.39b}$$

$$(L_+ + \alpha^2)\psi_{+0} - \left(D - \frac{n}{r}\right)p_0 = 0\,, \tag{4.39c}$$

$$(L_- + \alpha^2)\psi_{-0} - \left(D + \frac{n}{r}\right)p_0 = 0\,, \tag{4.39d}$$

with boundary conditions which may be written as:

$$u_0(0) = 0\,,$$
$$Du_0(0) = 1\,,$$
$$\psi_{+0}(0) = 0\,,$$
$$\psi_{+0}(1) = -i\phi_w\,,$$
$$\psi_{-0}(1) = -i\phi_w\,,$$
$$c_0 = \frac{2\phi_w}{u_0(1)}\,,$$

for $n = 1$ and

$$\begin{aligned} u_0(0) &= 0\,, \\ D^n u_0(0) &= 1\,, \\ \psi_{+0}(0) &= 0\,, \\ \psi_{-0}(0) &\text{is finite}\,, \\ \psi_{+0}(1) &= -i\phi_w\,, \\ \psi_{-0}(1) &= -i\phi_w\,, \\ c_0 &= \frac{2\phi_w}{u_0(1)}\,, \end{aligned}$$

for $n > 1$. Here $L_\pm$ and L_0 are defined as in section 4.6.1.

Using identities (4.29), it is easy to verify that the pressure, p_0, must be proportional to r^n, as must the streamwise velocity, u_0. It is then possible to construct the solutions for the functions, ψ_{+0} and ψ_{-0}. Thus, we find that

$$\begin{aligned} u_0(r) &= \frac{1}{n!} r^n\,, \\ \psi_{+0}(r) &= -i\phi_w r^{n+1}\,, \\ \psi_{-0}(r) &= i\left(\frac{1}{n!} - (n+2)\phi_w\right) r^{n-1} + i\left((n+1)\phi_w - \frac{1}{n!}\right) r^{n+1}\,, \\ p_0(r) &= 2i\left((n+1)\phi_w - \frac{1}{n!}\right) r^n\,, \\ c_0 &= 2\phi_w n!\,. \end{aligned}$$

Therefore, the long-wave solutions for $n > 1$ are regular for all values of ϕ_w and the modes belong to the KH class. A comparison of the analytical and numerical solutions for $n = 1$, $|\phi_w| = 1.0$, $Re = 100.0$ and $\alpha = 10^{-4}$ is given in figure 4.58. This shows good agreement between the two solutions.

Figures 4.59(a) and 4.59(b) plot the phase speed and growth rate in isolation for modes where $|\phi_w| = 1.0$, assuming that the leading-order solution is valid

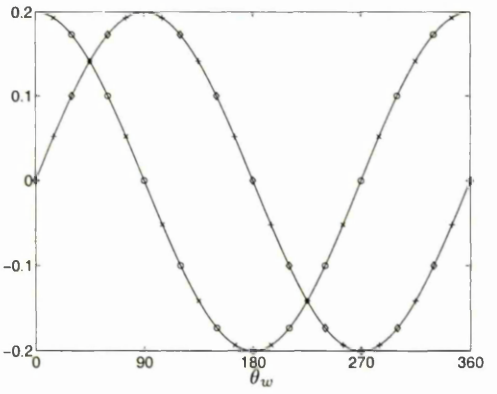

Figure 4.58: Analytical-Numerical comparison for the long-wave non-axisymmetric ($n = 1$) pipe modes. -o-, analytical c_r, $Re(c_0)$; -◇-, analytical c_i,$Im(c_0)$; -×-, numerical c_r; -+-, numerical c_i.

for $\alpha = 10^{-4}$. These confirm the modes to be in the KH class. Plots of the wall parameter bounds show that these correspond to both cases in section 2.3.2 (see figure 4.60). Thus, elimination of these modes cannot be achieved by a simple increase or decrease in one of the wall parameters. These particular modes may be eliminated by choosing $m = O(1)$ and a lower value of c_0. This reduces the two physically-realisable unstable regions to "unstable pockets", with two corresponding small ranges of d which give rise to these modes (see figure 4.61. Choosing any other value of d will thus eliminate the possibility of these particular modes arising.

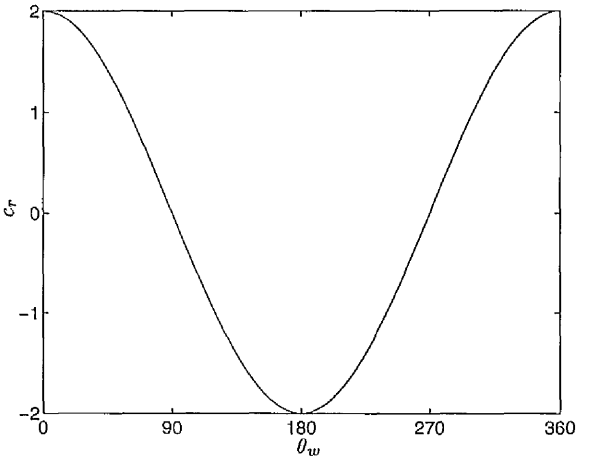

(a) Phase Speed, $Re(c_0)$

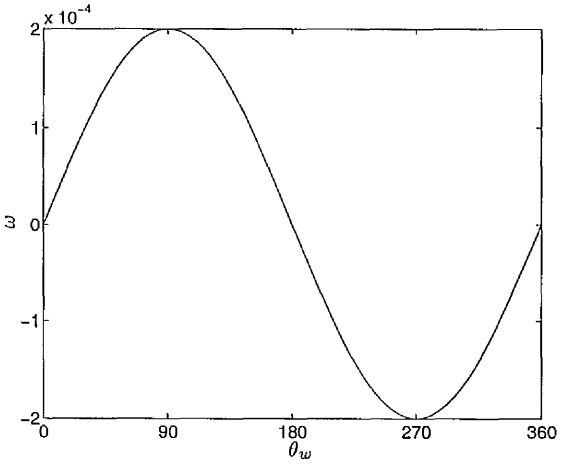

(b) Growth Rate, $\alpha.Im(c_0)$

Figure 4.59: Long-wave KH non-axisymmetric ($n = 1$) pipe modes, $|\phi_w| = 1.0$ - leading-order solution.

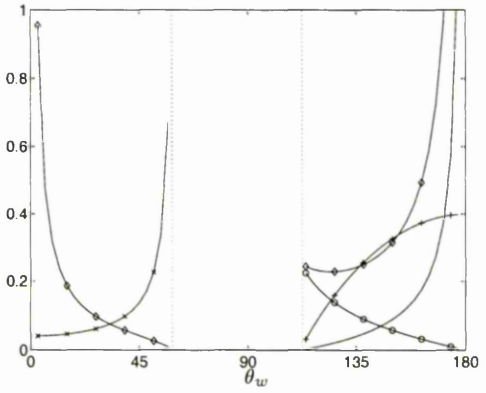

Figure 4.60: Physical realisability bounds on m, d and c_0^2 for the KH modes.

—, $10^2 \times d$ lower bound;

-o-, $10^{-9} \times m$ lower bound; -◇-, $10^{-9} \times m$ upper bound;

-+-, $10^{-2} \times c_0^2$ lower bound; -+-, $10^{-1} \times c_0^2$ upper bound.

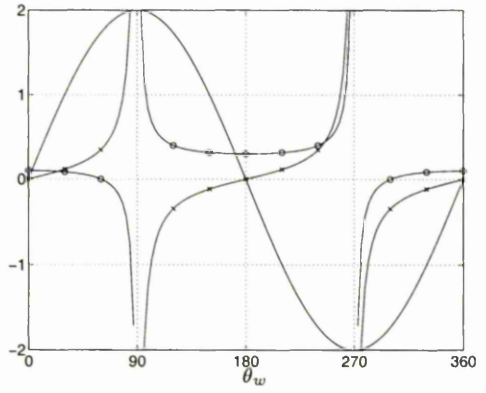

Figure 4.61: Physical realisability of the KH modes for $m = 2.0$.

—, $10^3 \times \omega$; -o-, $10^{-5} \times d$; -×-, $10^{-9} \times c_0^2$.

To next order the stability equations yield:

$$iu_1 + \frac{1}{2}\left(D + \frac{n+1}{r}\right)\psi_{+1} + \frac{1}{2}\left(D - \frac{n-1}{r}\right)\psi_{-1}, = 0 \tag{4.40a}$$

$$\left(D^2 + \frac{1}{r}D - \frac{n^2}{r^2}\right)u_1 = Re\left(i(u_B - c_0)u_0 + (Du_B)\frac{1}{2}\left(\psi_{+1} + \psi_{-1}\right)\right), \tag{4.40b}$$

$$\left(D^2 + \frac{1}{r}D - \frac{(n+1)^2}{r^2}\right)\psi_{+1} - \left(D - \frac{n}{r}\right)p_1 = i.Re(u_B - c_0)\psi_{+0}, \tag{4.40c}$$

$$\left(D^2 + \frac{1}{r}D - \frac{(n-1)^2}{r^2}\right)\psi_{-1} - \left(D + \frac{n}{r}\right)p_1 = i.Re(u_B - c_0)\psi_{-0}, \tag{4.40d}$$

with boundary conditions which may be written as:

$$\begin{aligned}
u_1(0) &= 0\,,\\
D^n u_1(0) &= 0\,,\\
\psi_{+1}(0) &= 0\,,\\
\psi_{-1}(0) &\text{ is finite}\,,\\
\psi_{+0}(1) &= 0\,,\\
\psi_{-0}(1) &= 0\,,\\
c_1 &= -\frac{2\phi_w u_1(1)}{u_0^2(1)}\,.
\end{aligned}$$

Thus, the second-order phase velocity is given by:

$$\begin{aligned}
u_1(r) &= i\frac{Re}{4}\left(n\phi_w - \frac{1}{n!}\right)\left(\frac{1}{n+1} - \frac{r^2}{2(n+2)}\right)r^{n+2}\,,\\
c_1 &= i.Re\frac{(n+3)!}{(n+2)^2(n+1)^2}\phi_w(1 - n.n!\phi_w)\,.
\end{aligned}$$

Plots of the second-order solutions are given in figures 4.62. Parameter values are as for the leading order solution. As for the long-wave compliant channel modes the second-order solution balances the inertial terms due to the leading-order solution.

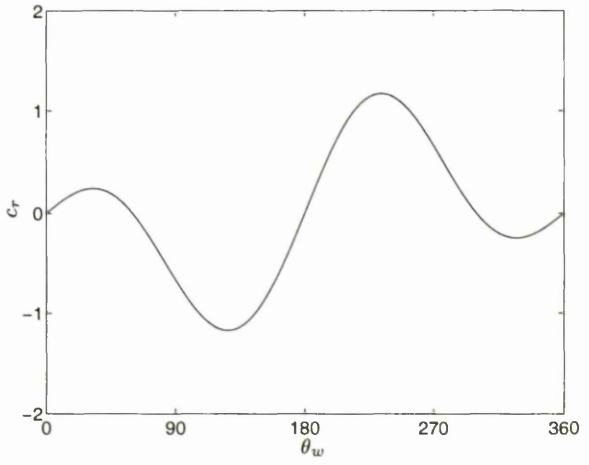

(a) Phase Speed, $Re(c_1)$

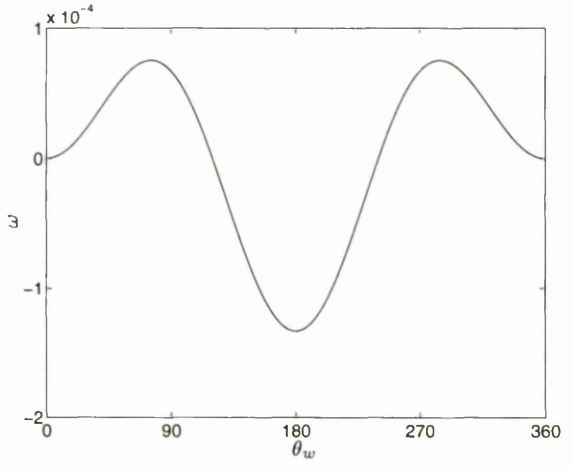

(b) Growth Rate, $\alpha.Im(c_1)$

Figure 4.62: Long-wave KH non-axisymmetric ($n = 1$) pipe modes, $|\phi_w| = 1.0$ - second-order solution.

This concludes our study of the flow in pipes bounded by compliant walls. A summary of the results found herein for such flows is given in the next chapter.

Chapter 5

Conclusions

To conclude this thesis a summary of the work performed and the results obtained will be given in this chapter. Areas for further research are also raised herein.

5.1 Conclusions

The kinematic method pioneered by Sen and Arora [67] has been applied to the problems of flow in a channel and a circular pipe bounded by compliant walls. The resulting set of equations has been solved using a Tchebychev collocation method to calculate the eigenfunctions and a Newton-Raphson method to find the phase-velocity from an initial value.

The unstable solutions obtained in this way can be placed into one of four classes, which are similar to the Tollmien-Schlichting, Kelvin-Helmholtz, Transitional and Resonant classes found by Sen and Arora [67] for boundary-layer flow over a compliant surface. Of the various different geometries studied, the symmetric modes in the symmetric channel exhibit the closest behaviour to the modes obtained in boundary-layer flow over a compliant surface. These similarities extend from the profiles of the phase velocities as θ_w is varied to the eigenfunctions

in the region near the compliant wall(s) and the profiles of the back calculated wall parameters, d and c_0^2, for fixed m.

Another geometrical consideration has been made regarding the symmetric mode in the symmetric channel and the asymmetric channel modes. It has been observed that there appears to be a direct link between these modes. For any symmetric mode with phase velocity, c_{sym} and kinematic parameters, $Re = Re_{\text{sym}}$, $\alpha = \alpha_{\text{sym}}$ and $\phi_w = (\phi_w)_{\text{sym}}$, there exists an asymmetric channel mode with the same phase velocity, c_{sym} and kinematic parameters, $Re = Re_{\text{sym}}$, $\alpha = \alpha_{\text{sym}}$ but which occurs for the wall stream-function, $\phi_w = (\phi_w)_{\text{asym}} = 2(\phi_w)_{\text{sym}}$. This observation is consistent with the analytical results obtained for certain parameter limits.

Instabilites have been found to exist for all Reynolds numbers and all wave numbers in both compliant channel and pipe flows. Physically realisable instabilities in the Kelvin-Helmholtz, Transitional and Resonant classes always can be found for finite Re and α. Modes in the Tollmien-Schlichting class (or in the case of pipe flow, the Rigid-Type class) are heavily damped for low Re and α.

Physically realisable unstable modes in the Kelvin-Helmholtz and Resonant classes persist in the limits $Re \to 0$ and $\alpha \to 0$ for both channel and pipe flows. Analytical solutions have been found in these limits. Transition between the two mode classes occurs via a singularity which can be predicted from the analysis.

In addition to the study of the various mode classes in the channel and pipe problems, progress has been made in extending the kinematic method itself. First, for the case of the simple stretched membrane considered herein, a single necessary and sufficient condition (2.24) has been found for the possible existence of any physically realisable unstable mode in any such walled flow. This links the wall

admittance, $Y = Y_r + iY_i$ and the phase velocity, $c = c_r + ic_i$, thus

$$\frac{Y_r}{c_i} \geq \left| \frac{Y_i}{c_r} \right| .$$

If the the above condition is obeyed by an unstable mode of any class, then at least one set of physically realisable wall parameters, m, d and c_0^2, can be found for which the given mode will arise. Conversely, if a physically-realisable unstable mode can be found, then its admittance and phase velocity must obey the above condition. This is true regardless of the method used to obtain the mode in question, either the kinematic approach used herein or a more conventional approach solving the fully coupled fluid-wall system.

Second, as a consequence of the above condition, the kinematic approach has been extended to include bounds on the wall parameters, m, d and c_0^2, which may give rise to any given unstable kinematic mode. These bounds can be split into the two cases, referred to as case 1 and case 2, depending on whether Y_i/c_r is negative or positive, respectively.

In general, the particular cases of bounds, case 1 and case 2, are not linked specifically to particular mode classes, though all of the Resonant channel modes which obey the inviscid theory appear to have case 1 bounds. Additionally, all of the Kelvin-Helmholtz and Resonant channel modes appear to have case 2 bounds, if Re or α is small enough that the solutions obey a viscous theory.

Using the wall parameter bounds it has been possible to deduce which ranges of m, d and c_0^2 will give rise to the "unstable pockets" observed by Sen and Arora [67]. This is useful since for a fixed value of one wall parameter only very limited ranges of the other wall parameters will then give rise to instabilites. Beyond reducing unstable regions to small pockets it has been shown that for all modes encountered it possible to eliminate instabilites of any class for fixed Re, α and $|\phi_w|$.

It has been found that a sufficiently large increase in m will reduce unstable regions to small pockets and hence is beneficial with regard to flow stabilisation. However, small increases in m can sometimes lead to an increase in the range of values of θ_w for which physically-realisable unstable modes can be found for fixed Re, α and $|\phi_w|$. This increase in the size of the unstable region can cause modes with larger growth rates to become physically realisable.

For the viscous ($Re \ll 1$) and long-wave ($\alpha \ll 1$) modes in the compliant channel, a sufficient increase in the free wave speed, c_0, will lead to no physically-realisable instabilities for any given α and $|\phi_w|$. Hence such an increase in c_0 should lead to a stable flow.

In the compliant pipe the modes in the same parameter limits are much more complex, however. The unstable axisymmetric modes can be eliminated for fixed α and $|\phi_w|$. However, the requirements of the wall parameters to eliminate instabilities is not always the same for different α and $|\phi_w|$. Therefore, it is not a trivial task to find wall parameters which will guarantee stable modes in these limits. The leading order non-axisymmetric ($n = 1$) solutions in the viscous limit, $Re \ll 1$, actually suggest that the flow will be unstable for any set of wall parameters. Therefore, it is necessary to find the second order solution in order to check this and is thus an area for further work, which is considered in the next section.

5.2 Further Work

Some possible areas for further work have been mentioned in chapters 3 and 4 as they have been encountered. There are many other possible areas for further research, too and so a summary of some of the most relevant and important ones are given below.

It has been shown how to find sets of simple stretched membrane parameters, m, d and c_0^2, which stabilise the Tollmien-Schlichting modes in a compliant channel, for a fixed value of $|\phi_w|$. In order to ensure that the overall flow is stabilised all modes of all classes must be stable for the set of wall parameters employed. Therefore, either a further extension to the kinematic approach or a combination of the kinematic method (for finding wall parameters which stabilise the Tollmien-Schlichting modes) and conventional fully-coupled methods (to see if such wall parameters lead to other classes of instability) might enable sets of wall parameters to be found which lead to flow stabilisation. In either case it is likely that multiple values of $|\phi_w|$ will need to be considered at the same time.

The observation of a link between the symmetric modes in the symmetric channel and the modes in the asymmetric channel needs to be proven analytically. Such a link has been found in the limits $Re, \alpha \to 0$ but as yet a general analytical link has not been found. One possible approach to finding such a link might be to use variation of parameters. If a symmetric solution in the symmetric channel $(u, v, p) = (u_s, v_s, p_s)$ with $c = c_s$ can be found for the kinematic parameters, Re, α and $\phi_w = (\phi_w)_s$, then variation of parameters would allow the solution for the asymmetric channel modes to be written in the form $(u, v, p) = (u_a, v_a, p_a) = (U(y)u_s, V(y)v_s, P(y)p_s)$, with $\phi_w = (\phi_w)_a = 2(\phi_w)_s$ and the remaining quantities are unchanged. Substitution into the governing stability equations and boundary conditions should allow $U(y)$, $V(y)$ and $P(y)$ to be found. If the hypothesis regarding a link between modes of the different geometries is true then the normalisation conditions should also be obeyed.

The second order solutions for the viscous modes, for which $Re \ll 1$, need to be found. This is particularly so for the non-axisymmetric $(n = 1)$ pipe modes

where the leading order solution suggests that viscous compliant pipe flow is unstable for all wall parameters.

A further investigation is required for the Transitional modes in both the channel and pipe problems. For the pipe problem this is necessary in order to determine the existence or otherwise of modes in both the Transitional and Resonant classes for larger Reynolds numbers. The long-wave solutions suggest that such modes should exist for higher values of the Reynolds number.

Three final areas where investigations need to be made but have not been undertaken in this thesis are as follows. An investigation into the group velocities of modes in each class needs to be made in order to determine the existence or otherwise of absolute instabilities. This may help in trying to link the mode classes given herein and in the mode classes of fully coupled systems. More work needs to be done in relating the dimensional values of the wall parameters to walls used in experiments. Finally, if an extension of the kinematic problem formulation could be made to incorporate streamwise displacements of the wall, then a direct comparison of the viscous modes could be made with those found by Kumaran [45].

Bibliography

[1] V.V. Babenko and L.F. Kozlov. Experimental investigation of hydrodynamic stability on rigid and elastic damping surfaces. *Izv. Akad. Nauk SSSR, Mekh. Zhidk. i Gaza*, **1**:122–127, 1973.

[2] T.B. Benjamin. Shearing flow over a wavy boundary. *J. Fluid Mech.*, **6**:161–205, 1959.

[3] T.B. Benjamin. The effect of a flexible boundary on hydrodynamic stability. *J. Fluid Mech.*, **9**:513–532, 1960.

[4] T.B. Benjamin. The threefold classification of unstable disturbances in flexible surfaces bounding inviscid flows. *J. Fluid Mech.*, **16**:436–450, 1963.

[5] C.D. Bertram. Unstable equilibrium behaviour in collapsible tubes. *J. Biomech.*, **19**:61, 1986.

[6] C.D. Bertram. The effects of wall thickness, axial strain and end proximity on the pressure area relation in collapsible tubes. *J. Biomech.*, **20**:863, 1987.

[7] C.D. Bertram, C.J. Raymond, and T.J. Pedley. Mapping of instabilities during flow through collapsible tubes. *J. Fluids Struct.*, **4**:125–154, 1989.

[8] C. Canuto, M.Y. Hussaini, A. Quarteroni, and T.A. Zang. *Spectral methods in fluid mechanics.* Springer-Verlag, 1988.

[9] P.W. Carpenter. Optimization of multiple-panel compliant walls for delay of laminar-turbulent transition. *AIAA J.*, **31**:1187–1188, 1993.

[10] P.W. Carpenter and J.S.B. Gajjar. A general theory for the two- and three-dimensional wall mode instabilities in boundary layers over isotropic and anisotropic compliant walls. *Theor. Comput. Fluid. Dyn.*, **1**:349–378, 1990.

[11] P.W. Carpenter and A.D. Garrad. The hydrodynamic stability of flow over Kramer-type compliant surfaces. Part 1. Tollmien-Schlichting instabilities. *J. Fluid Mech.*, **155**:465–510, 1985.

[12] P.W. Carpenter and A.D. Garrad. The hydrodynamic stability of flow over Kramer-type compliant surfaces. Part 2. Flow-induced surface instabilities. *J. Fluid Mech.*, **170**:199–232, 1986.

[13] G.M. Corcos and J.R. Sellars. On the stability of fully developed pipe flow. *J. Fluid Mech.*, **5**:97–112, 1959.

[14] A. Davey, H.P.F. Nguyen, and A.E.) (Gill. Finite-amplitude stability of pipe flow. *J. Fluid Mech.*, **45**:701–720, 1971.

[15] C. Davies and P.W. Carpenter. Instabilities in a plane channel flow between compliant walls. *J. Fluid Mech.*, **352**:205–243, 1997.

[16] C. Davies and P.W. Carpenter. Numerical simulation of the evolution of Tollmien-Schlichting waves over finite compliant panels. *J. Fluid Mech.*, **335**:361–392, 1997.

[17] A.E. Dixon, A.D. Lucey, and P.W. Carpenter. Optimization of visco-elastic compliant walls for transition delays. *AIAA J.*, **32(2)**:256–267, 1994.

[18] U. Ehrenstein and M. Rossi. Nonlinear Tollmien-Schlichting waves for plane

Poiseuille flow with compliant walls. *Eur. J. Mech. B-Fluids*, **12**:789–810, 1993.

[19] C.H. Ellen. The stability of an isolated rectangular surface embedded in uniform subsonic flow. *J. Appl. Mech.*, **44**:1–52, 1950.

[20] M.C. Fischer, L.M. Weinstein, D.M. Bushnell, and R.L. Ash. Compliant wall turbulent skin friction reduction research. *AIAA 8th Fluid and Plasma Dynamics Conference*, **Paper 75-833**, 1975.

[21] R. Fjørtoft. Application of integral theorems in deriving criteria of stability for laminar flows and for the baroclinic circular vortex. *Geofys. Publ.*, **17**:1–52, 1950.

[22] J.S.B. Gajjar and P. Sibanda. The hydrodynamic stability of channel flow with compliant boundaries. *Theor. Comput. Fluid Dyn.*, **8**:105–129, 1996.

[23] V.K. Garg and W.T. Rouleau. Linear spatial stability of pipe Poiseuille flow. *J. Fluid Mech.*, **54**:113–127, 1972.

[24] M. Gaster. Is the dolphin a red herring? *Proceedings IUTAM Symposium on Turbulence Management and Relaminarisation, Bangalore, India*, page 285, 1987.

[25] A.E. Gill. On the behaviour of small disturbances to Poiseuille flow in a circular pipe. *J. Fluid Mech.*, **21**:145–172, 1965.

[26] C.H. Green and C.H. Ellen. The stability of plane Poiseuille flow between flexible walls. *J. Fluid Mech.*, **51**:403–416, 1972.

[27] J.B. Grotberg and S.H. Davis. Fluid-dynamic flapping of a collapsible channel: sound generation and flow limitation. *J. BioMech.*, **13**:219–230, 1980.

[28] J.B. Grotberg and E.L. Reiss. A subsonic flutter anomaly. *J. Sound Vib.*, **80**:444–446, 1982.

[29] J.B. Grotberg and E.L. Reiss. Subsonic flapping flutter. *J. Sound Vib.*, **92**:349–361, 1984.

[30] J.B. Grotberg and T.R. Shee. Compressible-flow channel flutter. *J. Fluid Mech.*, **159**:175–193, 1985.

[31] D. Gyorgyfalvy. Possibilities of drag reduction by the use of flexible skin. *J. Aircraft*, **4**:186–192, 1967.

[32] F.D. Hains and J.F. Price. Effect of a flexible wall on the stability of Poiseuille flow. *Phys. Fluids*, **5(3)**:365, 1962.

[33] E. Høiland. On two-dimensional perturbation of linear flow. *Geofys. Publ.*, **18**:1–12, 1953.

[34] L.N. Howard. Note on a paper of John W. Miles. *J. Fluid Mech.*, **10**:509–512, 1961.

[35] N. Itoh. Non-linear stability of parallel flows with subcritical Reynolds numbers. Part 2. stability of pipe Poiseuille flow to finite axisymmetric disturbances. *J. Fluid Mech.*, **82(3)**:469–479, 1977.

[36] O.E. Jensen and T.J. Pedley. The existence of steady flow in a collapsed tube. *J. Fluid Mech.*, **206**:339, 1989.

[37] A.I. Korotkin. The stability of plane Poiseuille flow in the presence of elastic boundaries. *Prikl. Mat. Mekh.*, **29**:1122–1127, 1965.

[38] M.O. Kramer. Boundary-layer stabilisation by distributed damping. *J. Aero. Sci.*, **24**:459–460, 1957.

[39] M.O. Kramer. Boundary-layer stabilisation by distributed damping. *J. Aero. Sci.*, **27**:69, 1959.

[40] M.O. Kramer. Boundary-layer stabilisation by distributed damping. *ASNE J.*, **72**:25–33, 1960.

[41] M.O. Kramer. The dolphin's secret. *New Scientist*, **7**:1118–1120, 1960.

[42] M.O. Kramer. Boundary-layer stabilisation by distributed damping. *ASNE J.*, **74**:341–348, 1962.

[43] P. Krindel and A. Silberberg. Flow through gel-walled tubes. *J. Colloid Interface Sci.*, **71**:34–50, 1979.

[44] V. Kumaran. Stability of the flow of a fluid through a flexible tube at high Reynolds number. *J. Fluid Mech.*, **302**:117–139, 1995.

[45] V. Kumaran. Stability of the viscous flow of a fluid through a flexible tube. *J. Fluid Mech.*, **294**:259–281, 1995.

[46] V. Kumaran. Stability of inviscid flow in a flexible tube. *J. Fluid Mech.*, **320**:1–17, 1996.

[47] V. Kumaran. Stability of fluid flow through a flexible tube at intermediate Reynolds number. *J. Fluid Mech.*, **357**:123–140, 1998.

[48] V. Kumaran. Stability of wall modes in a flexible tube. *J. Fluid Mech.*, **362**:1–15, 1998.

[49] M.T. Landahl. On the stability of a laminar incompressible boundary-layer over a flexible surface. *J. Fluid Mech.*, **13**:609–632, 1962.

[50] M.T. Landahl and R.E. Kaplan. Effect of compliant walls on boundary-layer stability and transition. *AGARDograph*, **97**:1–353, 1965.

[51] L.D. Landau and E.M. Lifshitz. *Fluid Mechanics.* Butterworth-Heinemann, 1997.

[52] P.G. Larose and J.B. Grotberg. Flutter and long-wave instabilities in compliant channels conveying developing flows. *J. Fluid Mech.*, **331**:37–58, 1997.

[53] C.C. Lin. *The theory of hydrodynamic stability.* Cambridge University Press, 1955.

[54] R.W. Metcalfe, C.J. Rutland, J.H. Duncan, and J.J. Riley. Numerical simulations of active stabilization of laminar boundary layers. *AIAA J.*, **24**, 1986.

[55] M. Nagata and T.R. Cole. On the stability of plane Poiseuille flow between compliant boundaries. *Comput. Meth. Exp. Meas.*, **IX**, 1999.

[56] C.R. Nisewanger. Flow noise and drag measurements of vehicle with compliant coating. *U.S. Naval Ordnance Test Station*, **NAVWEPS Rep. 8518**, 1964.

[57] W.McF. Orr. The instability or instability of the steady motions of a perfect liquid and of a viscous liquid. Part I: A perfect liquid. *Proc. R. Irish Acad.*, **27A**:9–27, 69–138, 1907.

[58] S.A. Orszag. Accurate solution of the orr-sommerfeld stability equation. *J. Fluid Mech.*, 50:689–703, 1971.

[59] F.W. Puryear. Boundary layer control drag reduction by compliant surfaces. *U.S. Dept. of Navy, David Taylor Model Basin*, **Report 1668**, 1962.

[60] J.W. Reyn. Multiple solutions and flow limitation for steady flow through a collapsible tube held by both ends. *J. Fluid Mech.*, **174**:467, 1987.

[61] H. Ritter and L.T. Messum. Water tunnel measurements of turbulent skin friction on six different compliant surfaces of one foot length. *Admiralty Research Laboratory*, **Report ARL/G/N9**, 1964.

[62] H. Ritter and J.S. Porteous. Water tunnel measurements of turbulent skin friction on a compliant coating. *Admiralty Research Laboratory*, **Report ARL/N3/G/HY/9/7**, 1965.

[63] J.M. Rotenberry. Finite amplitude shear waves in a channel with compliant boundaries. *Phys. Fluids A*, 4:270–276, 1992.

[64] J.M. Rotenberry and P.G. Saffman. Effect of compliant boundaries on weakly non-linear shear waves in channel flow. *SIAM J. Appl. Maths*, **50**:259–281, 1990.

[65] H. Salwen and C.E. Grosch. The stability of Poiseuille flow in a pipe of circular cross section. *J. Fluid Mech.*, **54**:93–112, 1972.

[66] H. Schlichting. *Boundary layer theory.* McGraw-Hill, 4th edition, 1960.

[67] P.K. Sen and D.S. Arora. On the stability of laminar boundary-layer flow over a flat plate with a compliant surface. *J. Fluid Mech.*, **197**:201–240, 1988.

[68] P.K. Sen, D. Venkateswarlu, and S. Maji. On the stability of pipe-Poiseuille flow to finite amplitude axisymmetric and non-axisymmetric disturbances. *J. Fluid Mech.*, **158**:289–316, 1985.

[69] V. Shankar and V. Kumaran. Stability of fluid flow in a flexible tube to non-axisymmetric disturbances. *J. Fluid Mech.*, **407**:291–314, 2000.

[70] R.L. Smith and E.F. Blick. Skin friction of compliant surfaces with foamed material substrate. *J. Hydronautics*, **3**:100, 1969.

[71] A. Sommerfeld. Ein Reitrag zur hydrodynamischen Erklörung der turbulenten Flüssigkeitsbewegung. *Proc. 4th Inter. Congr. Maths, Rome*, pages 116–24, 1908.

[72] H.B. Squire. On the stability of the three-dimensional disturbances of viscous flow between parallel walls. *Proc. Roy. Soc.*, **142**:621–628, 1933.

[73] H.L. Swinney and J.P. Gollub. Topics in physics. In *Hydrodynamic instabilities and the transition to turbulence*, volume 45, pages xii, 292. Springer-Verlag, 1981.

[74] W. Tollmien. Über die Enstehung der Turbulenz. *Nachr. Ges. Wiss. Göttingen, Math.-Phys.*, **Klasse 21-44**, 1929.

[75] W. Tollmien. Asymptotische Integration der Störungsdifferentialgleichung ebener laminarer Strömungen bei hohen Reynoldschen Zahlen. *Z. angew. Math. Mech.*, **25/27**:33, 70, 1947.

[76] O. Wiplier and U. Ehrenstein. Numerical simulation of linear and nonlinear disturbance evolution in a boundary layer with compliant walls. *J. Fluids Struct.*, **14**:157–182, 2000.

[77] O. Wiplier and U. Ehrenstein. On the absolute instability in a boundary layer flow with compliant coatings. *Eur. J. Mech. B-Fluids*, **20**:127–144, 2001.

[78] K.S. Yeo. The stability of boundary-layer flow over single- and multi-layer visco-elastic walls. *J. Fluid Mech.*, **196**:359–408, 1988.

[79] K.S. Yeo. The hydrodynamic stability of boundary-layer flow over a class of anisotropic compliant walls. *J. Fluid Mech.*, **220**:125–160, 1990.

[80] K.S. Yeo. Note on the inviscid stability of flow over a compliant wall. *J. Fluid Mech.*, **279**:165–168, 1993.

[81] K.S. Yeo and A.P. Dowling. The stability of inviscid flows over passive compliant walls. *J. Fluid Mech.*, **183**:265–292, 1987.

[82] K.S. Yeo, B.C. Khoo, and W.K. Chong. The linear stability of boundary-layer flow over. *J. Fluid Mech.*, **280**:199–225, 1994.

[83] K.S. Yeo, B.C. Khoo, and A.P. Zhao. The absolute instability of boundary-layer flow over visco-elastic walls. *Theor. Comput. Fluid Dyn.*, **8**:237–252, 1996.